



# Experimental and numerical contribution to heat transfer enhancement in compact plate heat exchangers

F. Vitillo

## ► To cite this version:

F. Vitillo. Experimental and numerical contribution to heat transfer enhancement in compact plate heat exchangers. Modeling and Simulation. Institut Supérieur de l'Aéronautique et de l'Espace, 2014. English. NNT: . tel-01122585

**HAL Id: tel-01122585**

**<https://hal.science/tel-01122585>**

Submitted on 4 Mar 2015

**HAL** is a multi-disciplinary open access archive for the deposit and dissemination of scientific research documents, whether they are published or not. The documents may come from teaching and research institutions in France or abroad, or from public or private research centers.

L'archive ouverte pluridisciplinaire **HAL**, est destinée au dépôt et à la diffusion de documents scientifiques de niveau recherche, publiés ou non, émanant des établissements d'enseignement et de recherche français ou étrangers, des laboratoires publics ou privés.



# THÈSE

En vue de l'obtention du

## DOCTORAT DE L'UNIVERSITÉ DE TOULOUSE

Délivré par :

Institut Supérieur de l'Aéronautique et de l'Espace (ISAE)

---

**Présentée et soutenue par :**

**Francesco VITILLO**

**le** 21 Novembre 2014

**Titre :**

Experimental and Numerical Contribution to  
Heat Transfer Enhancement in  
Compact Plate Heat Exchangers

---

**École doctorale et discipline ou spécialité :**

ED MEGEP : Énergétique et transferts

**Unité de recherche :**

CEA Cadarache DEN/DTN/STCP/LCIT - ONERA Toulouse DMAE/TACT

**Directeur/trice(s) de Thèse :**

M. Pierre MILLAN

**Jury :**

M. Jean-Marie BUCHLIN (Von Karman Institute) - Rapporteur

M. Frédéric PLOURDE (Institut PPrime) - Rapporteur

M. Philippe MARTY (LEGI Grenoble) - Président du Jury

M. Gianfranco CARUSO (Université de Rome "La Sapienza") - Examineur

M. Lionel CACHON (CEA Cadarache) - Encadrant

M. Emmanuel LAROCHE (ONERA Toulouse) - Encadrant





## **PHD THESIS**

# **EXPERIMENTAL AND NUMERICAL CONTRIBUTION TO HEAT TRANSFER ENHANCEMENT IN COMPACT PLATE HEAT EXCHANGERS**

**PHD CANDIDATE: FRANCESCO VITILLO**

**THESIS SUPERVISOR: PIERRE MILLAN**

**THESIS CO-SUPERVISOR: LIONEL CACHON**

**THESIS CO-SUPERVISOR: PHILIPPE REULET**

**THESIS CO-SUPERVISOR: EMMANUEL LAROCHE**



*A NONNA,  
LA MIA PRIMA MAESTRA*

*Tu, che abiti al riparo del Signore  
e che dimori alla sua ombra,  
di al Signore: mio Rifugio,  
mia Roccia in cui confido.*

# Remerciements

Tout d'abord je souhaite remercier les membres du jury de thèse pour avoir accepté d'évaluer ce travail : en particulier merci à M. Jean-Marie Buchlin et M. Frédéric Plourde pour avoir dédié leur temps à la relecture de ce manuscrit et pour l'avoir enrichi avec leurs commentaires ; merci aussi à M. Philippe Marty et M. Gianfranco Caruso pour leur présence et participation.

Je remercie mon directeur de thèse, M. Pierre Millan, pour m'avoir permis de mener ce travail et pour m'avoir motivé pendant ces trois ans.

Je ne remercierai jamais assez mon encadrant au CEA Cadarache, M. Lionel Cachon, pour son soutien quotidien : pour m'avoir choisi, pour m'avoir suivi, pour m'avoir permis de mener à bien ce projet, pour les milliers de pages qu'il a relu, pour toutes les activités faites ensemble et surtout pour son sourire. Au travers son exemple il a confirmé que les vrais leaders sont ceux qui arrivent à vous faire sentir important en tous moments.

Je tiens à remercier aussi mes encadrants de l'ONERA, M. Emmanuel Laroche, pour ses remarques et ses conseils qui m'ont permis d'élargir beaucoup mes connaissances et surtout M. Philippe Reulet, qui, toujours en souriant, m'a supporté pendant les essais LDV, qui a lu des dizaines de fois ce manuscrit et qui a apporté une contribution primordiale à la comparaison de différents motifs d'échange.

Je souhaite remercier aussi M. Sylvain Madeleine, pour m'avoir accueilli au sein du LCIT et pour avoir toujours compris mes besoins et mes requêtes.

Merci tout particulièrement à Thomas Marchiollo, qui a été mon bras droit (et souvent même gauche!) pendant longtemps et notamment lors de la conception et mise-en-service des manips PIV et VHEGAS. Sa motivation a été primordiale pour la réussite de ce travail.

Merci aussi à Chiara Galati et Julien Nave, qui se sont chargés de plusieurs parties importantes de ce travail et qui m'ont permis d'avancer énormément dans des axes de recherche que je n'aurais jamais pu investiguer autrement.

Merci mille fois à Pierre Charvet, pour sa patience infinie avec nous les thésards, toujours en comprenant nos (mes) besoins et pour la bonne humeur qu'il porte toujours avec lui.

Merci à M.Francis Micheli, M.Jean-François Breil (M.Théodolite !) et M.Christian Pelissier pour leurs efforts sur la manip LDV.

Merci également à Mme Isabelle Tkatschenko, Mme Fabienne Bazin et Mme Valerie Biscay pour leur soutien lors de la mise-en-place de la manip PIV. Sans leur engagement il n'aurait pas été possible de mener à bien ces mesures.

Merci à Pascal Defrasne, pour son soutien primordial à l'instrumentation des manips PIV et VHEGAS.

Merci à M. Jean Stefanini pour l'assistance lors de la conception et mise-en-place de la manip PIV.

Merci à M. Denis Tschumperlé pour la patience et le support de toute l'équipe d'ANSYS Fluent.

Merci à M.Emilio Baglietto qui, avec seulement à deux ou trois conversations de dix minutes, a été capable, grâce à sa grande compétence, de me donner énormément d'inspiration pour ce travail.

Je n'aurais pas pu mener à bien ce travail sans la présence et le soutien de toutes les personnes du LCIT, en particulier : Christine Biscarrat, elle m'a vraiment compris et apprécié pendant nos discussions, pas que sur le travail. Je remercie Christophe Garnier pour son amitié et pour son attention ; Sebastien Christin, qui m'a aidé lorsque j'étais en difficulté et qui m'a toujours donné son amitié ; Xavier Jeanningros, qui m'a soutenu et encouragé pendant cette dernière année; Corinne Jaloux, pour son aide continue depuis mon premier jour à Cadarache. Merci aussi à tous les autres membres du LCIT : Alexandre, Aurelien, Damien, Fabrice, Frank, Frédéric, Guilhem, Laurent, Stephan, Xavier, Sebastien, Sylvain.

Merci à tous les thésards du DTN avec qui j'ai partagé ces trois ans, en particulier à Linards, Aurelien, Jeremy.

Merci à Ghislaine et Bruno, qui m'ont accueilli chez eux quand je suis arrivé en France et qui m'ont appris le Français.

Merci à tous mes potes romains, qui de loin m'ont supporté et qui ont toujours été heureux à chaque fois que je rentrais chez moi. Ce n'est ni la distance ni le temps qui passe qui peut changer notre amitié.

Un merci spécial à Daniele Vivaldi, qui a été mon « parrain » au tout début et qui m'a enseigné (beaucoup plus que ce qu'il pense) à ne pas se contenter de ce qui nous est proposé et à aller toujours au-delà. Ceci est exactement le travail d'un chercheur. Merci pour les belles soirées passées ensemble, pour tous les moments vécus dans la salle calcoule et pour sa vraie amitié.

Merci aux « Italiens », qui m'ont fait me sentir chez moi à l'étranger : mes colocs Antonello et Lavinia, Damiano (que je suis sans arrêt, pour l'instant), Nicholas (pour sa capacité à me faire rire une journée entière avec un seul mot), Miro (pour sa joie et pour ses expressions) et surtout Michele, qui a été plus qu'un coloc (coupe du monde), plus qu'un coéquipier, plus que un Copain de non Elucidés : tout simplement il a été là.

Merci à tous ceux qui étaient là au début de cette thèse et qui ne sont plus là aujourd'hui. Dans cette thèse il y a aussi chacun de vous.

Et enfin merci à ma famille, qui après tout m'a supporté toujours durant cette thèse et qui a supporté en même temps le fait d'avoir un fils à l'étranger. C'est difficile pour tous, mais je ne serais pas là aujourd'hui si vous ne m'aviez pas permis de faire ce que je souhaitais de ma vie. C'est pourquoi aujourd'hui c'est grâce à vous qu'on partage ce moment. Merci.

# Table of Contents

<b>Remerciements.....</b>	<b>5</b>
<b>Table of Contents.....</b>	<b>8</b>
<b>List of Figures .....</b>	<b>11</b>
<b>List of Tables.....</b>	<b>16</b>
<b>List of Acronyms .....</b>	<b>17</b>
<b>Chapitre 1: Introduction.....</b>	<b>19</b>
<b>Chapter 1: Introduction.....</b>	<b>22</b>
1. Fission Reactor Energy Production and challenges .....	22
2. French experience with nuclear Power.....	26
2.1 Thermal Reactors.....	26
2.2 Fast Reactors .....	26
3. The ASTRID Project .....	27
4. PhD Thesis outlook.....	30
<b>Chapitre 2: Echangeurs de chaleurs à plaques embouties - (PSHE) Etude technique et bibliographique.....</b>	<b>32</b>
<b>Chapter 2: Plate Stamped Heat Exchanger (PSHE) Technical Bibliographic Review .....</b>	<b>34</b>
1. General Overview.....	34
1.1 PSHE Description.....	34
1.2 Plate geometrical characteristics.....	36
1.3 Hydraulic diameter definition.....	39
1.4 Final definition of the parameters of interest .....	40
2. Flow Characteristics .....	40
2.1 Flow Pattern.....	40
2.2 Local thermal performance of wavy channel corrugation .....	44
3. Correlations.....	51
3.1 Semi-theoretical correlations .....	52
3.2 Non-theoretical correlations .....	53
3.3 Correlations background.....	54
3.4 Heat transfer correlation comparison.....	55
3.5 Friction factor Correlation comparison.....	60
4. Parameters of interest .....	64
4.1 Aspect ratio ( $\lambda/b$ ratio).....	64
4.2 Chevron angle $\beta$ .....	66
4.3 Area enlargement factor .....	68
5. Other Corrugation geometries .....	69
6. CFD Model.....	71
7. Engineering Performance Comparison Methods .....	78
7.1 Area Goodness Factor .....	78
7.2 Volume Goodness Factor .....	78
7.3 Performance Parameters .....	79

8.	<i>Conclusions</i> .....	80
9.	<i>Adopted Strategy for the Present Work</i> .....	83
9.1	<i>Innovative Geometry Description and Motivation</i> .....	83
9.2	<i>Numerical Approach</i> .....	89
9.3	<i>Experimental Approach</i> .....	90
<b>Chapitre 3: Définition du modèle numérique</b> .....		<b>91</b>
<b>Chapter 3: Numerical Model Definition</b> .....		<b>93</b>
1.	<i>Introduction</i> .....	93
1.1	<i>Section Goals and Motivation</i> .....	93
1.2	<i>Selection of the Preliminary Validation Test-Cases</i> .....	94
2.	<i>Turbulence Models Used</i> .....	95
2.1	<i>The Shear Stress Transport (SST) Model</i> .....	95
2.2	<i>The Stress Omega Reynolds Stress Model</i> .....	97
2.3	<i>The Anisotropic Shear Stress Transport (ASST) Model</i> .....	98
2.3.1	<i>Model Background and Formulation</i> .....	98
2.3.2	<i>Logarithmic layer model analysis</i> .....	105
2.4	<i>Thermal modelling approach</i> .....	108
3.	<i>Model Verification and Validation</i> .....	109
3.1	<i>Channel Flow</i> .....	109
3.1.1	<i>Motivation</i> .....	109
3.1.2	<i>Test Configuration</i> .....	110
3.1.3	<i>Numerical discretization</i> .....	110
3.1.4	<i>Mesh convergence evaluation</i> .....	111
3.1.5	<i>Results</i> .....	111
3.1.6	<i>Conclusions</i> .....	116
3.2	<i>Backward Facing Step</i> .....	116
3.2.1	<i>Motivation</i> .....	116
3.2.2	<i>Test configuration</i> .....	117
3.2.3	<i>Numerical Discretization</i> .....	118
3.2.4	<i>Mesh convergence evaluation</i> .....	118
3.2.5	<i>Results</i> .....	119
3.2.6	<i>Conclusions</i> .....	125
3.3	<i>Turbulent Developing Flow in a 90° Bend</i> .....	125
3.3.1	<i>Motivation</i> .....	125
3.3.2	<i>Test Configuration</i> .....	125
3.3.3	<i>Numerical Discretization</i> .....	126
3.3.4	<i>Mesh Convergence Evaluation</i> .....	126
3.3.5	<i>Results</i> .....	128
3.3.6	<i>Conclusions</i> .....	135
3.4	<i>Turbulence-Driven Secondary Motion in Straight-Duct of Square Cross-Section</i> .....	135
3.4.1	<i>Motivation</i> .....	135
3.4.2	<i>Test configuration</i> .....	136
3.4.3	<i>Numerical discretization</i> .....	137
3.4.4	<i>Mesh convergence evaluation</i> .....	137
3.4.5	<i>Results</i> .....	137
3.4.6	<i>Conclusions</i> .....	138
3.5	<i>Secondary Motion in Tight Lattice Rod Bundle</i> .....	138
3.5.1	<i>Motivation</i> .....	138
3.5.2	<i>Test configuration</i> .....	138

3.5.3	Numerical discretization .....	139
3.5.4	Mesh convergence evaluation .....	139
3.5.5	Results .....	140
3.5.6	Conclusions .....	141
4.	<i>Conclusions</i> .....	141
<b>Chapitre 4: Acquisition de la base de données expérimentales .....</b>		<b>143</b>
<b>Chapter 4: Experimental database acquisition .....</b>		<b>145</b>
1.	<i>Laser Doppler Velocimetry measurements</i> .....	145
1.1	Laser Doppler Velocimetry Technique Description .....	145
1.2	Experimental facility and calibration .....	147
1.2.1	Experimental facility description .....	147
1.2.2	Calibration and testing .....	152
1.2.3	Flow stability visualization and control .....	155
1.3	Experimental Campaign Description .....	157
1.3.1	Experimental measurement program definition .....	157
1.3.2	Preliminary tests: Measurement statistical convergence .....	162
1.3.3	Experimental uncertainty evaluation .....	163
1.4	LDV Experimental Measurements .....	167
1.4.1	Flow Inlet Conditions .....	167
1.4.2	Flow Development .....	171
1.4.3	Flow Symmetry .....	173
1.5	Conclusions on the LDV measurements .....	175
2.	<i>Particle Image Velocimetry measurements</i> .....	175
2.1	Particle Image Velocimetry Technique Description .....	175
2.2	Experimental facility and calibration .....	178
2.2.1	Experimental facility description .....	178
2.2.2	Calibration and testing .....	181
2.3	Experimental Campaign Description .....	183
2.3.1	Experimental measurement program definition .....	183
2.3.2	Measurements statistical convergence and experimental uncertainty evaluation .....	185
2.4	PIV Experimental Measurements .....	189
2.4.1	Flow Inlet Conditions .....	189
2.4.2	Flow Development .....	191
2.4.3	Flow Symmetry .....	193
2.5	Conclusions on the PIV measurements .....	194
3.	<i>“VHEGAS” Thermal validation experimental test-section</i> .....	195
3.1	Experimental test section Motivation and Description .....	195
3.2	Experimental Campaign Description .....	201
3.3	Flow Stability Visualization and control .....	202
3.4	Experimental uncertainty evaluation .....	205
3.5	Final global heat transfer coefficient evaluation .....	207
3.5.1	“High Heat Flux” Case .....	207
3.5.2	“Low Heat Flux” Case .....	209
3.6	Conclusions on VHEGAS measurements .....	211
4.	<i>Conclusions</i> .....	211
<b>Chapitre 5: Analyse de l’écoulement .....</b>		<b>212</b>
<b>Chapter 5: Flow Analysis .....</b>		<b>214</b>
1.	<i>Introduction</i> .....	214
2.	<i>Selection of the reference model for the analysis</i> .....	214
3.	<i>Model Validation and Flow Analysis</i> .....	220

3.1	In-bend flow .....	220
3.1.1	Principal flow .....	220
3.1.2	Secondary flow .....	226
3.2	Mixing zone Flow.....	232
3.3	Thermal Model Validation .....	240
3.3.1	VHEGAS channel model description .....	240
3.3.2	VHEGAS “High Heat Flux” case thermal validation .....	242
3.3.3	VHEGAS “Low Heat Flux” case thermal validation.....	244
4.	<i>Heat transfer and pressure drop correlations</i> .....	247
4.1	Introduction .....	247
4.2	Numerical model definition.....	247
4.3	Hydraulic diameter definition.....	250
4.4	Heat transfer and Pressure drop correlations .....	252
5.	<i>Comparison of different heat exchanger technologies</i> .....	259
5.1	Preliminary Considerations .....	259
5.2	Compactness Comparison Strategy .....	262
5.3	Performance Comparison .....	267
6.	<i>Proposed design for ASTRID Na/N<sub>2</sub> heat exchanger</i> .....	269
7.	<i>Conclusions</i> .....	273
<b>Chapitre 6: Conclusions et Perspectives.....</b>		<b>275</b>
<b>Chapter 6: Conclusions and Perspectives.....</b>		<b>279</b>
1.	<i>Conclusions</i> .....	279
2.	<i>Perspectives</i> .....	282
<i>Appendix A – Differently defined PSHE correlation conversion factors.....</i>		<i>285</i>
<i>Appendix B – Anisotropic formulations of the Reynolds stress Tensor .....</i>		<i>286</i>
<i>Appendix C – Example of LDV Calibration File.....</i>		<i>289</i>
<i>Appendix D –LDV mockup dimensions verification .....</i>		<i>291</i>
<i>Appendix E – PIV Mockup plate.....</i>		<i>292</i>
<i>Appendix F – ASST vs Velocity fluctuations measurements comparison .....</i>		<i>293</i>
<i>References .....</i>		<i>303</i>

## List of Figures

Figure 1.1 - Nuclear Energy Production from 1971 to 2010 by Region (TWh) <sup>1</sup> .....	22
Figure 1.2 - Example of a fission chain .....	22
Figure 1.3 - OECD number of units and capacity connected to the grid by type of reactor (2012) <sup>3</sup> .....	23
Figure 1.4 - PWR uranium actinide decay time to natural uranium radiotoxicity level .....	23
Figure 1.5 - Global Clean Energy Need and Supply <sup>4</sup> .....	24
Figure 1.6 - Generations of nuclear reactors .....	25
Figure 1.7 – Pool-type Sodium-cooled Fast Reactor .....	27
Figure 1.8 - Gas Power Conversion System (PCS) Layout .....	29
Figure 1.9 - Cycle net efficiency evaluation versus turbine inlet pressure for the gas PCS .....	29
Figure 2.1 - PSHE assembly.....	34
Figure 2.2 - Different types of plate: (a) Washboard, (b) Zig-zag, (c) Chevron/Herringbone, (d) Protrusions and depressions, (e) Washboard with secondary corrugations, (f) Oblique washboard <sup>14</sup> .....	34
Figure 2.3 - PSHE fluid passages .....	35



Figure 2. 4 - Two of the four plate ports <sup>14</sup> .....	35
Figure 2. 5 - PSHE flow scheme .....	35
Figure 2. 6 - Possible flow arrangement scheme .....	36
Figure 2. 7 - Chevron-type plate .....	36
Figure 2. 8 - Hydraulic channel cross-section at different axial locations .....	37
Figure 2. 9 - Alternative geometrical definitions .....	38
Figure 2. 10 - Furrow and Contact Point visual definition .....	41
Figure 2. 11 - Flow patterns depending on the chevron angle <sup>23</sup> .....	42
Figure 2. 12 - Momentum influence on PSHE flow pattern .....	43
Figure 2. 13 - Flow pattern from CFD simulation for $\beta=60^\circ$ and $Re=1565$ <sup>20</sup> .....	43
Figure 2. 14 - Different single wavy channel flow patterns as a function of Reynolds number <sup>28</sup> .....	45
Figure 2. 15 - Influence of recirculation zone on heat transfer <sup>29</sup> .....	46
Figure 2. 16 - Influence of recirculation zone on local Nusselt number <sup>30</sup> .....	47
Figure 2. 17 - Pressure drop and heat transfer coefficient local distribution <sup>31</sup> .....	48
Figure 2. 18 - Local heat transfer coefficient <sup>32</sup> .....	49
Figure 2. 19 - Local Nusselt number 18 .....	50
Figure 2. 20 - Recommended value of the superscript of Prandtl number in the Nusselt number correlation <sup>59</sup> .....	59
Figure 2. 21 - Comparison of Nusselt number existing correlations for $\beta=60^\circ$ .....	60
Figure 2. 22 - Comparison of friction factor existing correlations for $\beta=60^\circ$ .....	64
Figure 2. 23 - Effect of aspect ratio on PSHE's thermal performance <sup>26</sup> .....	65
Figure 2. 24 - Effect of aspect ratio on thermal-hydraulic performance according to Blomerius and Mitra <sup>60</sup> .....	65
Figure 2. 25 - $\phi$ versus $\lambda/b$ plot .....	66
Figure 2. 26 - Influence of $\beta$ on heat transfer <sup>23</sup> .....	67
Figure 2. 27 - Influence of $\beta$ on friction factor <sup>23</sup> .....	67
Figure 2. 28 - Influence of the area enlargement factor $\phi$ on heat transfer <sup>19</sup> .....	68
Figure 2. 29 - Triangular wavy channels <sup>61</sup> .....	69
Figure 2. 30 - Triangular channel performance <sup>61</sup> .....	69
Figure 2. 31 - Corrugation profiles <sup>62</sup> .....	70
Figure 2. 32 - Thermal-hydraulic performance of the different corrugation profiles <sup>62</sup> .....	70
Figure 2. 33 - Unitary cell approach .....	71
Figure 2. 34 - Unit Cell domain definition with regard to a plate stack .....	72
Figure 2. 35 - Single channel approach .....	72
Figure 2. 36 - Whole plate approach .....	73
Figure 2. 37 - Influence of $\beta$ on Friction factor: CFD vs experimental results in Ciofalo et al. <sup>63</sup> .....	77
Figure 2. 38 - CFD vs experimental results in Kanaris et al. <sup>50</sup> .....	77
Figure 2. 39 - PCHE plate (on the left) and stack (on the right) .....	84
Figure 2. 40 - PCHE performance chart .....	84
Figure 2. 41 - Superposed channels identification .....	85
Figure 2. 42 - Innovative geometry concept .....	85
Figure 2. 43 - Example of the innovative fluid stream configuration (actual cross-section will be defined later) .....	86
Figure 2. 44 - Bend definition for each pair of channel .....	86
Figure 2. 45 - Mixing zone and mixing plane visualization .....	87
Figure 2. 46 - Innovative channel reference cross-section (bottom figure) compared to the reference PCHE reference cross-section (upper figure) .....	88
Figure 2. 47 - Channel main geometrical parameters .....	89
Figure 2. 48 - Superposed channels identification .....	280
Figure 2. 49 - Innovative geometry concept .....	280
Figure 3. 1 - Channel Flow Geometry .....	110
Figure 3. 2 - Channel Flow Mesh .....	111
Figure 3. 3 - Channel Flow law of the wall verification .....	113
Figure 3. 4 - Non-dimensional turbulence kinetic energy distribution for $Re=14000$ (Kim et al.) .....	113
Figure 3. 5 - Fluctuating velocity components compared with experimental data of Laurer for $Re = 14\ 000$ .....	114
Figure 3. 6 - Channel flow mixed Reynolds stress distribution for $Re=5600$ (Kim et al.) .....	115

Figure 3. 7 - Channel Flow anisotropy distribution at $Re = 14\,000$ (Laufer <sup>85</sup> ).....	115
Figure 3. 8 - Concept of Backward Facing Step.....	117
Figure 3. 9 - Backward Facing Step mesh B .....	119
Figure 3. 10 - Backward Facing Step velocity upstream the step at $X/H = -4$ .....	119
Figure 3. 11 - Backward Facing Step mixed Reynolds Stress upstream the step at $X/H = -4$ .....	120
Figure 3. 12 - Backward Facing Step pressure coefficient distribution downstream the step .....	121
Figure 3. 13 - Velocity profiles downstream the step.....	122
Figure 3. 14 - Backward Facing Step skin friction coefficient downstream the step .....	123
Figure 3. 15 - Normalized Stanton number downstream a backward facing step .....	124
Figure 3. 16 - $90^\circ$ bend geometrical configuration.....	126
Figure 3. 17 - $90^\circ$ bend mesh example .....	127
Figure 3. 18 - $90^\circ$ bend studied profiles .....	128
Figure 3. 19 - AA line inlet principal velocity distribution .....	128
Figure 3. 20 - AA line inlet radial velocity distribution .....	129
Figure 3. 21 - AA line inlet principal mixed Reynolds stress distribution .....	129
Figure 3. 22 - AA line outlet principal velocity distribution .....	130
Figure 3. 23 - AA line outlet radial velocity distribution .....	130
Figure 3. 24 - AA line outlet mixed Reynolds stress distribution .....	130
Figure 3. 25 - BB line inlet principal velocity distribution.....	131
Figure 3. 26 - BB line inlet radial velocity distribution.....	132
Figure 3. 27 - BB line inlet Reynolds Stress distribution .....	132
Figure 3. 28 - BB line outlet principal velocity distribution.....	133
Figure 3. 29 - BB line outlet radial velocity distribution.....	134
Figure 3. 30 - BB line outlet mixed Reynolds stress distribution .....	134
Figure 3. 31 - Corner vortices as shown by Speziale <sup>90</sup> .....	136
Figure 3. 32 - Straight duct of squared cross-section configuration .....	136
Figure 3. 33 - Vertical velocity for a straight duct of squared cross-section .....	138
Figure 3. 34 - Tight lattice rod bundle test configuration <sup>88</sup> .....	139
Figure 3. 35 - Tight lattice rod bundle final mesh .....	140
Figure 3. 36 - Non-dimensional wall shear stress versus angular position.....	141
Figure 4. 1 - LDV technique principle .....	145
Figure 4. 2 - Light signal of a single measurement .....	146
Figure 4. 3 - Global view of the LDV test section.....	148
Figure 4. 4 - LDV test section material description.....	148
Figure 4. 5 - General scheme of the LDV experimental facility .....	149
Figure 4. 6 - LDV Laser generator .....	149
Figure 4. 7 - LDV Laser emission .....	150
Figure 4. 8 - LDV displacing system and laser reception.....	150
Figure 4. 9 - LDV volume of measurement (on laser beams crossing point).....	151
Figure 4. 10 - LDV acquisition chain .....	151
Figure 4. 11 - LDV feeding system .....	152
Figure 4. 12 - DEHS droplet size map.....	152
Figure 4. 13 - LDV laser beam measurement domain .....	153
Figure 4. 14 - Laser emission double configuration (upwards and downwards) respectively .....	154
Figure 4. 15 - Theodolite used for laser calibration.....	154
Figure 4. 16 - Flow control station .....	155
Figure 4. 17 - Flow velocity control over a day .....	156
Figure 4. 18 - System of coordinates for LDV measurements .....	158
Figure 4. 19 - Inlet section measured profiles .....	159
Figure 4. 20 - Bend and mixing zone experimental campaign description.....	159
Figure 4. 21 - Measurements of the In-bend flow .....	160
Figure 4. 22 - Measurements in the mixing zone .....	160
Figure 4. 23 - Principal Velocity U convergence tests .....	163
Figure 4. 24 - Principal root-mean-square of the U velocity ( $u'$ ) convergence tests.....	163
Figure 4. 25 - Position uncertainty visual explanation .....	164
Figure 4. 26 - Coincidence criterion with regard to experimental uncertainties.....	166
Figure 4. 27 - Inlet section feeding particle population for y-15 and z50 profiles .....	168

Figure 4. 28 - Inlet Section Measured Velocity profiles along Z direction .....	168
Figure 4. 29 - Inlet Section Measured velocity fluctuations along Z direction.....	168
Figure 4. 30 - Measured W Velocity on a proper visual scale .....	169
Figure 4. 31 - Inlet Section Measured Velocity profiles along Y direction.....	170
Figure 4. 32 - Inlet Section Measured velocity fluctuations along Y direction .....	170
Figure 4. 33 - U and W Velocities and velocity fluctuations profiles on the y0 line with regard to flow development .....	171
Figure 4. 34 - U and W Velocities and velocity fluctuations profiles on the z30 line with regard to flow development .....	172
Figure 4. 35 - U and W Velocities and velocity fluctuations profiles on the y0 line with regard to flow symmetry .....	173
Figure 4. 36 - U and W Velocities and velocity fluctuations profiles on the z30 line with regard to flow symmetry .....	174
Figure 4. 37 - PIV technique principles.....	176
Figure 4. 38 - Example of PIV pixel division.....	177
Figure 4. 39 - Example of PIV pixel cross-correlation.....	177
Figure 4. 40 - PIV experimental PMMA mockup .....	178
Figure 4. 41 - Global view of the PIV test section .....	179
Figure 4. 42 - PIV Laser generator.....	179
Figure 4. 43 - PIV laser and camera configuration.....	180
Figure 4. 44 - PIV feeding system.....	180
Figure 4. 45 - Insight 4G software.....	181
Figure 4. 46 - PIV calibration first method.....	181
Figure 4. 47 - PIV calibration second method .....	182
Figure 4. 48 - System of coordinates for PIV measurements .....	183
Figure 4. 49 - Inlet section measured planes .....	184
Figure 4. 50 - Measurements of the In-bend flow .....	184
Figure 4. 51 - Measurements in the mixing zone .....	184
Figure 4. 52 - PIV number of images convergence test of velocity field .....	186
Figure 4. 53 - PIV accurate measurement statistical convergence evaluation .....	187
Figure 4. 54 - Inlet Flow Velocity field distribution.....	190
Figure 4. 55 - Inlet Flow u' velocity fluctuation field distribution.....	191
Figure 4. 56 - PIV Flow development evaluation: velocity field .....	192
Figure 4. 57 - PIV Flow development evaluation: u' velocity fluctuation .....	192
Figure 4. 58 - PIV Flow symmetry evaluation: velocity field .....	193
Figure 4. 59 - PIV Flow symmetry evaluation: u' velocity fluctuation field .....	194
Figure 4. 60 - LDV/PIV measurements double-check .....	195
Figure 4. 61 - VHEGAS test section .....	196
Figure 4. 62 - VHEGAS innovative channel mockup .....	196
Figure 4. 63 - Holes for TCs position.....	197
Figure 4. 64 - VHEGAS TCs description.....	198
Figure 4. 65 - VHEGAS heating plates .....	198
Figure 4. 66 - VHEGAS heating plates control system.....	199
Figure 4. 67 - VHEGAS insulating box.....	199
Figure 4. 68 - VHEGAS flowmeter .....	200
Figure 4. 69 - VHEGAS acquisition system.....	201
Figure 4. 70 - "High heat flux case" flow stability .....	202
Figure 4. 71 - "High heat flux" case thermal transient evaluation.....	202
Figure 4. 72 - "High Heat Flux" case evaluation of thermal transient by mockup thermal power absorption.....	203
Figure 4. 73 - "Low heat flux case" flow stability .....	204
Figure 4. 74 - "Low heat flux" case thermal transient evaluation.....	204
Figure 4. 75 - "Low Heat Flux" case evaluation of thermal transient by mockup thermal power absorption .....	205
Figure 4. 76 - "High Heat Flux" case fluid temperature distribution inside the channel .....	208
Figure 4. 77 - "Low Heat Flux" case fluid temperature distribution inside the channel .....	210
Figure 5. 1 - Innovative channel computation boundary conditions.....	215

Figure 5. 2 - Innovative channel study reference mesh: bend (on top) and mixing zone (on bottom) .....	216
Figure 5. 3 - Chosen profiles for turbulence model comparison .....	216
Figure 5. 4 - Experimental vs numerical in-bend 45° Y0 profile principal velocity .....	217
Figure 5. 5 - Experimental vs numerical in-bend 45° Y0 profile radial velocity .....	217
Figure 5. 6 - Experimental vs numerical mixing zone central Y profile principal velocity.....	217
Figure 5. 7 - Experimental vs numerical mixing zone central Y profile u'w' mixed Reynolds stress .....	218
Figure 5. 8 - ASST vs SST model computed F1 function in the in-bend 45° Y0 profile .....	219
Figure 5. 9 - ASST vs SST model computed F1 function in the mixing zone central Y profile .....	219
Figure 5. 10 - LDV/ASST Y0 principal velocity profiles for in-bend flow .....	221
Figure 5. 11 - LDV/ASST Y+10 principal velocity profiles for in-bend flow .....	221
Figure 5. 12 - LDV/ASST Y-10 principal velocity profiles for in-bend flow .....	222
Figure 5. 13 - Velocity field on bend middle plane comparison (PIV data on top, ASST computation on PIV channel geometry in the middle and ASST computation on LDV channel on the bottom at Y*=15mm/30mm).....	223
Figure 5. 14 - Velocity field on bend middle plane plus 4 mm comparison (PIV data on top, ASST computation on PIV channel geometry in the middle and ASST computation on LDV channel on the bottom at 24mm/30mm).....	224
Figure 5. 15 - Velocity field on bend middle plane minus 4 mm comparison (PIV data on top, ASST computation on PIV channel geometry in the middle and ASST computation on LDV channel on the bottom at 6mm/30mm).....	225
Figure 5. 16 - LDV/ASST data on radial velocity at bend 0° plane (on the left) and ASST computed secondary motions (on the right) .....	227
Figure 5. 17 - LDV/ASST data on radial velocity at bend 30° plane (on the left) and ASST computed secondary motions (on the right) .....	227
Figure 5. 18 - LDV/ASST data on radial velocity at bend 45° plane (on the left) and ASST computed secondary motions (on the right) .....	228
Figure 5. 19 - LDV/ASST data on radial velocity at bend 60° plane (on the left) and ASST computed secondary motions (on the right) .....	228
Figure 5. 20 - LDV/ASST data on radial velocity at bend 90° plane (on the left) and ASST computed secondary motions (on the right) .....	229
Figure 5. 21 - 90° bend secondary motion according to Adachi et al.....	230
Figure 5. 22 - 30° plane ASST computed principal vorticity profiles .....	231
Figure 5. 23 - In-bend flow ASST computed secondary motion evolution .....	232
Figure 5. 24 - Mixing zone investigated planes.....	233
Figure 5. 25 - LDV/ASST data on principal and radial velocity at mixing zone inlet plane (on the left) and ASST computed secondary velocity vectors (on the right) .....	234
Figure 5. 26 - LDV/ASST data on principal and radial velocity at mixing zone middle plane (on the left) and ASST computed secondary velocity vectors (on the right) .....	235
Figure 5. 27 - LDV/ASST data on principal and radial velocity at mixing zone outlet plane (on the left) and ASST computed secondary velocity vectors (on the right) .....	235
Figure 5. 28 - PIV/ASST velocity field at mixing zone top channel middle + 8 mm plane .....	237
Figure 5. 29 - PIV/ASST velocity field at mixing zone top channel middle + 4 mm plane .....	237
Figure 5. 30 - PIV/ASST velocity field at mixing zone top channel middle plane .....	238
Figure 5. 31 - PIV/ASST velocity field at mixing zone top channel middle - 4 mm plane.....	238
Figure 5. 32 - PIV/ASST velocity field at mixing zone top channel middle - 8 mm plane.....	239
Figure 5. 33 – Example of ASST computed velocity field and vectors at mixing plane and related secondary motion at bend inlet for LDV channel geometry.....	240
Figure 5. 34 - VHEGAS channel study reference mesh: bend (on top) and mixing zone (on bottom) ....	241
Figure 5. 35 - VHEGAS "High Heat Flux" Case channel temperature evaluation comparison .....	242
Figure 5. 36 - VHEGAS "High Heat Flux" case local contribution to the heat transfer.....	244
Figure 5. 37 - VHEGAS "Low Heat Flux" Case channel temperature evaluation comparison .....	245
Figure 5. 38 - VHEGAS "Low Heat Flux" case local contribution to the heat transfer .....	246
Figure 5. 39 - Friction factor as a function of the number of bends for the innovative geometry .....	249
Figure 5. 40 - Heat transfer coefficient as a function of the number of bends for the innovative geometry .....	249
Figure 5. 41 - Innovative channel hydraulic diameter .....	251
Figure 5. 42 - Friction factor correlation for innovative channel with $\alpha=45^\circ$ and $D=2$ mm.....	253
Figure 5. 43 – Nusselt number correlation for innovative channel with $\alpha=45^\circ$ and $D=2$ mm.....	254

Figure 5. 44 - Friction factor correlation for innovative channel with $\alpha=20^\circ$ and $D=3$ mm.....	255
Figure 5. 45 - Nusselt number correlation for innovative channel with $\alpha=20^\circ$ and $D=3$ mm .....	255
Figure 5. 46 - Triple innovative channel description.....	257
Figure 5. 47 - Friction factor correlation for triple innovative channel with $\alpha=45^\circ$ and $D=2$ mm .....	258
Figure 5. 48 - Nusselt number correlation for triple innovative channel with $\alpha=45^\circ$ and $D=2$ mm .....	258
Figure 5. 49 - Compact heat exchanger design process.....	260
Figure 5. 50 - Compact heat exchanger major dimensions.....	261
Figure 5. 51 - Compactness comparison strategy illustration.....	263
Figure 5. 52 - Different technologies performance comparison .....	268
Figure 5. 53 - Single machined plate for innovative channel geometry based ASTRID Sodium-gas heat exchanger .....	270
Figure 5. 54 - ASTRID Sodium-gas heat exchanger design comparison (note that horizontal dimensions are not to scale).....	271
Figure 6. 1 - Possible innovative channel cross-section geometries to be studied .....	284

## List of Tables

Table 1. 1 - Six Generation IV reactor technologies .....	25
Table 1. 2 - French Sodium-cooled Fast Reactors main information .....	26
Table 2. 1 - Correlation preliminary information .....	55
Table 2. 2 - Heat transfer correlation differences .....	58
Table 2. 3 - Friction factor correlation differences .....	63
Table 2. 4 - Turbulence Model Comparison.....	75
Table 3. 1 - List of selected validation test cases .....	95
Table 3. 2 - Examples of non-linear eddy viscosity models .....	99
Table 3. 3 - NLEVM closure coefficient in reference 91 and 96 .....	103
Table 3. 4 - NLEVM closure coefficient in present ASST model.....	103
Table 3. 5 - Channel flow reference flow conditions .....	110
Table 3. 6 - Channel flow used grids.....	111
Table 3. 7 - Channel flow grid convergence evaluation .....	111
Table 3. 8 - Backward Facing Step grid convergence evaluation.....	118
Table 3. 9 - Backward Facing Step calculated reattachment lengths.....	123
Table 3. 10 - 90° bend used grids .....	127
Table 3. 11 - 90° bend mesh convergence evaluation .....	127
Table 3. 12 - Straight duct of squared cross-section grid independence evaluation .....	137
Table 3. 13 - Rod bundle grid convergence evaluation .....	139
Table 4. 1 - LDV channel geometrical characteristics.....	148
Table 4. 2 - Laser Beams major parameters .....	153
Table 4. 3 - LDV local systems of coordinates description .....	158
Table 4. 4 - Experimental campaign description .....	161
Table 4. 5 - Velocity U Uncertainty Analysis .....	165
Table 4. 6 - Velocity W Uncertainty Analysis .....	165
Table 4. 7 - $u'$ Reynolds Stress Uncertainty Analysis .....	165
Table 4. 8 - $w'$ Reynolds Stress Uncertainty Analysis.....	166
Table 4. 9 - PIV channel geometrical characteristics .....	178
Table 4. 10 - PIV measured plane used notation .....	183
Table 4. 11 - Experimental campaign description .....	185
Table 4. 12 - PIV experimental uncertainty evaluation .....	189
Table 4. 13 - VHEGAS channel geometrical description.....	197
Table 4. 14 - "High heat flux" temperature uncertainties .....	206

Table 4. 15 - "Low heat flux" temperature uncertainties .....	207
Table 4. 16 - "High heat flux" derived uncertainties .....	207
Table 4. 17 - "Low heat flux" derived uncertainties .....	209
Table 5. 1 - Innovative channel LDV geometry mesh convergence evaluation .....	215
Table 5. 2 - VHEGAS channel geometry mesh convergence evaluation .....	241
Table 5. 3 - VHEGAS "High Heat Flux" Case numerical vs experimental heat transfer coefficient comparison .....	243
Table 5. 4 - VHEGAS "Low Heat Flux" Case numerical vs experimental heat transfer coefficient comparison .....	245
Table 5. 5 – Reference innovative channel geometry for performance evaluation .....	247
Table 5. 6 – Influence of thermal gradients for 45° innovative channel geometry flow .....	253
Table 5. 7 – Alternative innovative channel geometry for performance evaluation .....	254
Table 5. 8 - Influence of thermal gradients for 20° innovative channel geometry flow .....	254
Table 5. 9 – Friction factor difference between innovative channel with $\alpha = 45^\circ$ and $\alpha = 20^\circ$ .....	255
Table 5. 10 – Heat transfer coefficient difference between innovative channel with $\alpha = 45^\circ$ and $\alpha = 20^\circ$ .....	255
Table 5. 11 - Correlation comparison .....	256
Table 5. 12 - Pressure drop difference between single and triple innovative channel with $\alpha = 45^\circ$ and $\alpha = 20^\circ$ .....	257
Table 5. 13 – Heat transfer coefficient difference between single and triple innovative channel with $\alpha = 45^\circ$ and $\alpha = 20^\circ$ .....	258
Table 5. 14 - Compactness comparison of different geometries for ASTRID Sodium-Has Heat Exchanger conditions .....	268
Table 5. 15 - Design comparison of the ASTRID Sodium-Gas Heat Exchanger (innovative channel geometry on the left and straight tube geometry on the right) <sup>112</sup> .....	272

## List of Acronyms

**OECD:** Organization for Economic Co-operation and Development

**ASTRID:** Advanced Sodium Technological Reactor for Industrial Demonstration

**PSHE:** Plate Stamped Heat Exchanger

**PCHE:** Printed Circuit Heat Exchanger

**Re:** Reynolds number

**Nu:** Nusselt number

**Pr:** Prandtl number

**RANS:** Reynolds-Averaged Navier Stokes

**LES:** Large Eddy Simulation

**DNS:** Direct Numerical Simulation

**RSM:** Reynolds Stress transport Model

**Low-Re:** (referred to a turbulence model) model with modified terms of the turbulent transport equations to take into account near-wall turbulence damping

**High-Re** (referred to a turbulence model) model with no near-wall turbulence damping modification

**SST**: Shear Stress Transport model

**ASST**: Anisotropic Shear Stress Transport model

**RNG** (referred to a k- $\epsilon$  model): Re-Normalization Group k- $\epsilon$  model

**NEWF**: Non-Equilibrium Wall Functions

**U**: Average velocity component of the Reynolds velocity decomposition

**u'**: Fluctuating velocity component of the Reynolds velocity decomposition

$\overline{u'_i u'_j}$ : Reynolds stress tensor

# Chapitre 1: Introduction

L'énergie nucléaire fournit aujourd'hui (données 2012) environ 13% de la consommation d'électricité dans le monde, avec 437 réacteurs nucléaires en exploitation.

Dans le cadre des réacteurs de fission, la technologie nucléaire la plus utilisée pour la production d'énergie est celle des réacteurs à eau pressurisée (REP), suivi par les réacteurs à eau bouillante (REB). L'expérience française avec l'énergie nucléaire commence le 29 Septembre 1956 avec la première génération d'électricité d'origine nucléaire dans le centre de Marcoule. Aujourd'hui, il y a 58 réacteurs en exploitation en France pour une puissance électrique de 36,1 GWe connectée au réseau. Les 58 réacteurs sont tous des réacteurs à eau pressurisée. La France produit environ 77% de sa puissance électrique grâce au nucléaire, en étant le pays le plus «nucléarisé» dans le monde en termes de production nucléaire par rapport aux besoins de puissance électrique totale.

Même si les activités françaises ont été concentrées sur les REP, la France a une expérience importante avec les réacteurs à neutrons rapides refroidis au sodium, RNR-Na. En effet, la France a déjà construit trois RNR-Na. Un RNR-Na se compose de trois boucles: la boucle primaire de sodium, qui refroidit le cœur. Le cœur est confiné dans un grand bassin de sodium, qui contient également l'échangeur intermédiaire de chaleur (IHX), où le transfert de chaleur entre le circuit de sodium primaire et secondaire se produit. La boucle de sodium secondaire, même si l'on peut la considérer comme une perte en termes d'efficacité thermique, permet de découpler deux risques principaux que sont le risque nucléaire du circuit primaire et le risque pression du circuit tertiaire, auquel il faut ajouter le risque chimique (réaction sodium eau) dans le cas d'un tertiaire en eau/vapeur. Enfin, la boucle secondaire de sodium, transfère l'énergie thermique pour le système de conversion de l'énergie (SCE), qui utilise généralement de la vapeur d'eau pour convertir l'énergie thermique en énergie électrique par des turbines à vapeur. La loi française N ° 2006-739 (28 Juin 2006) prévoit un réacteur de génération IV en France pour faire face à la gestion des déchets radioactifs et des actinides mineurs, ainsi que pour accroître son indépendance énergétique avec une meilleure utilisation de son combustible. Dans ce cadre, la Commissariat à l'Energie Atomique et aux Energies



Alternatives (CEA) a pour mission avec des partenaires industriels de développer un réacteur à neutrons rapides en mesure de faire face à cette question. Le projet a été appelé ASTRID, qui est l'acronyme de "Advanced Sodium Technological Reactor for Industrial Demonstration". Ce réacteur devra, entre autre, démontrer qu'un RNR Na pourra atteindre les standards actuels en termes de sûreté et de disponibilité. Pour cela, un système innovant de conversion d'énergie à gaz, étudié au CEA depuis le début des années 2000 se pose comme étant la référence. Son principal intérêt est dû à l'élimination pratique du risque associé à l'interaction sodium-eau présente dans les générateurs de vapeur équipant le système de conversion d'énergie plus classique en eau/ vapeur, en cas de rupture d'un des tubes. Les études préliminaires ont montré que le gaz présentant le meilleur compromis en termes de rendement global, rendement des machines tournantes, taille des composants d'échange, facilité de mise en œuvre, est de l'azote à 180 bar. Dans ce cadre, un des composants présentant un enjeu important est l'échangeur sodium-gaz (ECSG). Il remplacera le GV du SCE eau vapeur, et comme ce dernier permettra de transmettre la chaleur du sodium secondaire au gaz pressurisé. A la sortie de l'ECSG le gaz se détendra dans les turbines. En raison de la faible capacité de transfert de chaleur de l'azote par rapport à celle de l'eau bouillante, les technologies d'échangeur compact sont incontournables pour l'application visée. En effet, l'objectif est d'avoir une installation générale peu impactée par le choix du fluide tertiaire en termes d'encombrement; cela se traduit par la conception d'un composant le plus compact possible. Les études préliminaires effectuées au CEA ont montré que la technologie des Printed Circuit Heat Exchangers (PSHE) est une des plus intéressantes en raison de sa compacité. Par conséquent, l'étude bibliographique (Chapitre 2) commence à étudier la technologie des PSHE, pour évaluer leur comportement thermo-hydraulique et pour comprendre les phénomènes physiques fournissant le transfert de chaleur efficace. La compréhension de la physique sera utilisée pour proposer le motif d'échange qui sera le support du travail de recherche, décrit dans ce document, visant à le caractériser.

L'échange thermique dans cet échangeur étant limité par le côté gaz, ce travail sera focalisé sur ce dernier.

Pour ce faire, un modèle numérique a été développé et proposé afin d'étudier les performances thermo-hydrauliques du motif d'échange innovant (Chapitre 3). Les bancs

d'essai expérimentaux utilisés pour la validation du modèle sont décrits (Chapitre 4), pour pouvoir montrer la validation du modèle numérique ainsi que l'analyse de l'écoulements. Ensuite, les performances d'échange thermique et frottement sont étudiées pour pouvoir comparer le motif innovant à d'autres géométries existantes (Chapitre 5). Enfin, les conclusions et perspectives de ce travail seront discutées (Chapitre 6).

# Chapter 1: Introduction

## 1. FISSION REACTOR ENERGY PRODUCTION AND CHALLENGES

Nuclear energy provides nowadays (as of reported for 2012) around 13% of the world's electricity consumption<sup>1</sup>, with 437 operational nuclear reactors<sup>2</sup>. The percentage rises up to 18.9% in OECD countries and 24.0% in Europe<sup>3</sup>, as also Figure 1.1 shows:

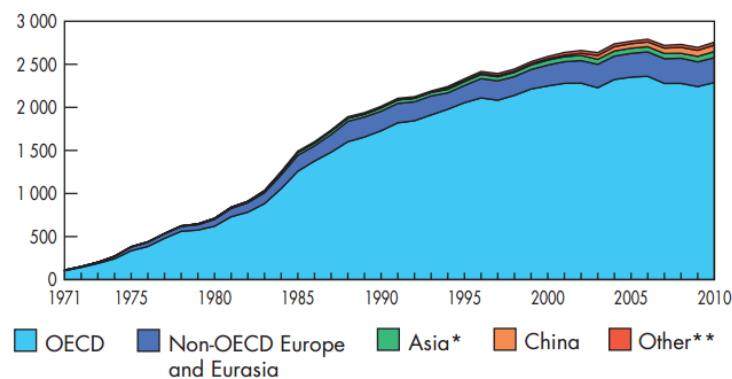


Figure 1.1 - Nuclear Energy Production from 1971 to 2010 by Region (TWh)<sup>1</sup>

Practically all the nuclear electrical energy is produced through nuclear fission, where thermal neutrons (i.e. which energy is around 0.025 eV) can divide the nucleon of a heavy element (typically  $U^{235}$ ) to produce energy thanks to the excess mass. See Figure 1.2 for further explanation.

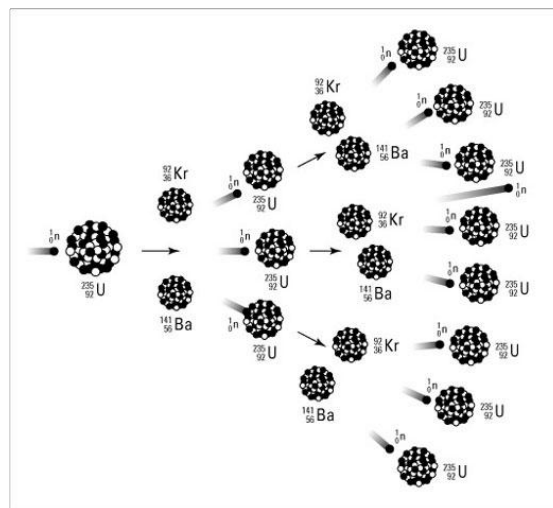
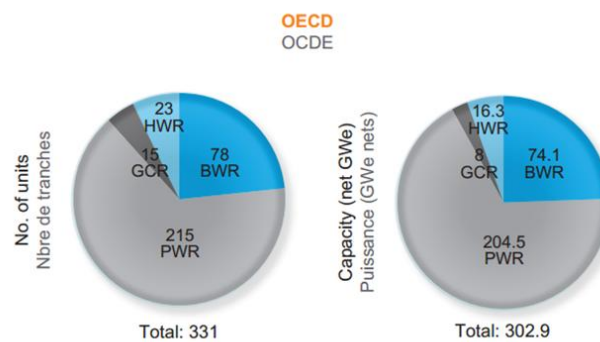


Figure 1.2 - Example of a fission chain<sup>1</sup>

<sup>1</sup> See that the fission products shown in Figure 1.2 are not necessarily the ones shown. In other words, fission products are subjected to statistics: there is a certain probability to have a given fission product. Moreover, fission product statistics changes with neutron energy spectrum.

In the frame of fission reactors and considering OECD statistics, the major nuclear technology employed for energy production is that of Pressurized Water Reactors (PWRs), followed by Boiling Water Reactors (BWRs). Smaller contributes are due to Heavy Water Reactors (HWRs) and to old technology Gas-Cooled Reactors (GCR). See Figure 1.3 for visualisation.



**Figure 1.3 - OECD number of units and capacity connected to the grid by type of reactor (2012)<sup>3</sup>**

The all of them are thermal reactors, hence they all use thermal neutrons to fission the U235. The major difference is instead on the moderator, which is the element used to decrease neutron energy to thermal values. The major issue related to fission reactors is the production of nuclear waste. Indeed thermal reactors typically produce medium and long-life fission products, which are supposed to take some million years to reach natural radioactivity levels (see Figure 1.4).

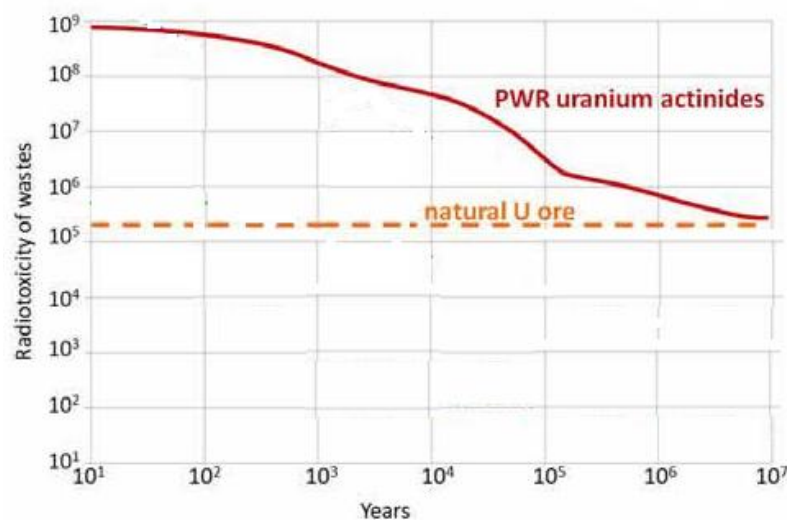


**Figure 1.4 - PWR uranium actinide decay time to natural uranium radiotoxicity level**

Even if nuclear energy debate goes on, nuclear energy is foreseen as one of the principal ways to face global warming. Emerging countries are developing important nuclear plans to produce long-term carbon-free energy. World Nuclear Association estimates two different scenarios related to nuclear energy development in the 21st century, showing that only with a major use of nuclear energy the world will be able to meet the global clean-energy needs, as Figure 1.5 shows:

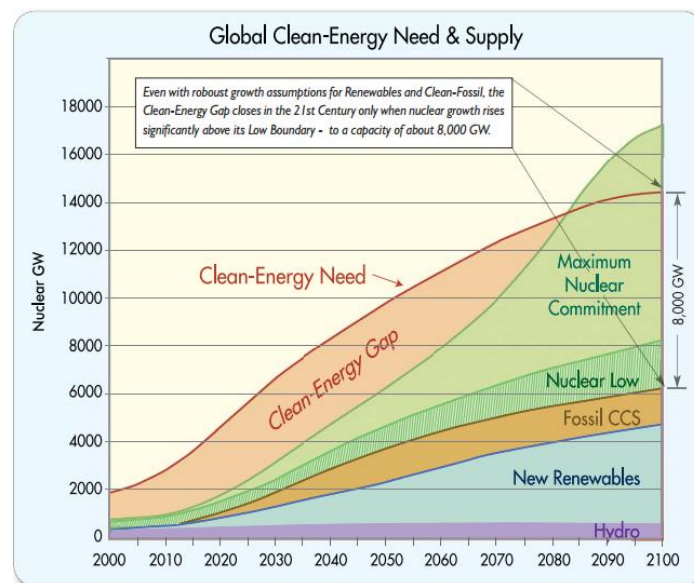


Figure 1.5 - Global Clean Energy Need and Supply [Errore. Il segnalibro non è definito.](#)

In this sense an international cooperation project named “Generation IV International Forum” has been created, aiming to develop new generation (i.e. 4<sup>th</sup>) nuclear fission reactors capable to meet the challenge of a major nuclear energy production with minor produced nuclear waste<sup>II</sup>. See Figure 1.6 for the history of nuclear fission reactor technology:

<sup>II</sup> Indeed principal objectives of Generation IV reactors are also to provide reactors as safe, secure and economical as those of the current (i.e. III+) generation.

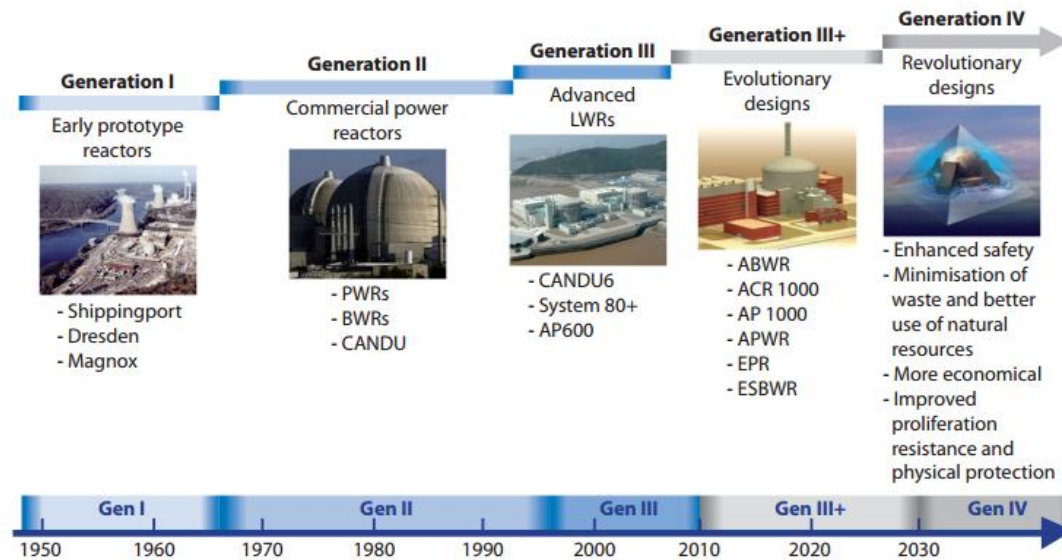


Figure 1.6 - Generations of nuclear reactors<sup>4</sup>

Six technologies have been identified as candidates for further development (Table 1.1):

Abbreviation	Full Designation	Neutron energy Spectrum
<b>GFR</b>	Gas-cooled Fast Reactor	Fast
<b>LFR</b>	Lead-Cooled Fast Reactor	Fast
<b>SCWR</b>	SuperCritical Water-cooled Reactor	Fast/Thermal
<b>SFR</b>	Sodium-cooled Fast Reactor	Fast
<b>MSR</b>	Molten Salt Reactor	Fast (thermal in the past)
<b>VHTR</b>	Very High Temperature Reactor	Thermal

Table 1.1 - Six Generation IV reactor technologies

See that almost all the GenIV reactors are based on a fast neutron energy spectrum. Indeed this is the easiest way to burn high level waste when mixed to nuclear fuel. In this sense the goal of burning long-lived fission product can be met more easily.

## 2. FRENCH EXPERIENCE WITH NUCLEAR POWER

### 2.1 THERMAL REACTORS

French experience with nuclear power starts on September, 29th 1956 with the first electrical power generation in Marcoule G-1 (UNGG) plant<sup>5</sup>. As of 2011, there are 58 operating reactors in France for a 36.1 GWe electrical power connected to the grid. All of the 58 reactors are Pressurized Water Reactors. France produces about 77% of its electrical power needs through nuclear power, being the most “nuclearized” country in the world in terms of nuclear production over total electrical power needs.

A new generation (i.e. III+) European Pressurized Reactor (EPR) is under construction in the site of Flamanville, the first criticality been expected in 2016.

### 2.2 FAST REACTORS

Even though French activities were concentrated on thermal PWRs, France has quite an important experience with fast reactor, in particular with SFRs. In fact, France already built three SFRs: Table 1.2 provides some information about the three French SFRs.

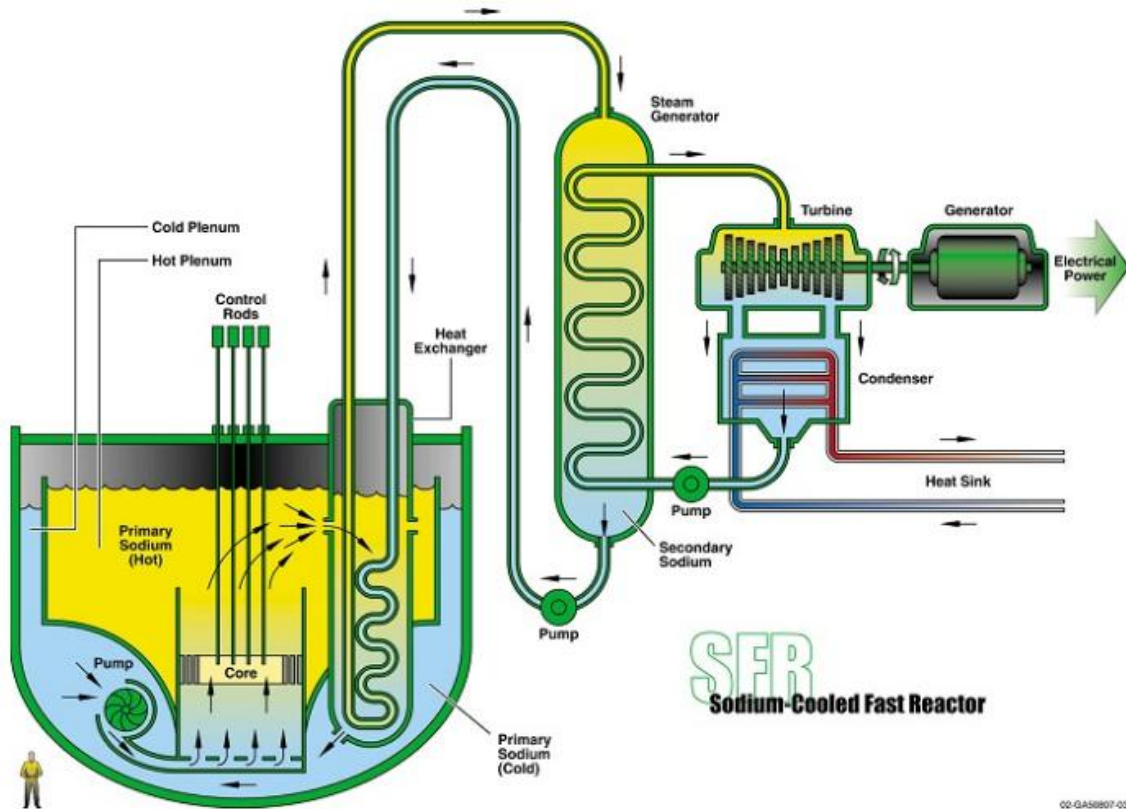
Name	First Criticality	Final Shutdown	Thermal Power [MWth]	Gross Electrical Power [MWe]
Rapsodie	January 1967	April 1983	40	0
Phénix	1973	2010	563 <sup>III</sup>	255
Super-Phénix	1985	1998	2990	1242

Table 1.2 - French Sodium-cooled Fast Reactors main information

All of them are pool-type SFRs, as those shown in Figure 1.7:

---

<sup>III</sup> Since 1993 the Phénix reactor has been used as a support to French CEA R&D Program: hence its thermal power has been limited to 350 MWth corresponding to 145 MWe.



**Figure 1.7 – Pool-type Sodium-cooled Fast Reactor**

In this kind of SFR, we can see three loops: the primary sodium loop, which cools down the core, transferring the produced thermal energy to the secondary sodium loop. The core is confined in a big sodium pool, which contains also the Intermediate Heat eXchanger (IHx), where the heat transfer between primary and secondary sodium loop occurs. The secondary sodium loop, even if can be considered as a loss in terms of plant efficiency, acts as a protection barrier in case of primary circuit leakage. Finally, the secondary sodium loop transfers the thermal energy to the Power Conversion System (PCS), which typically uses steam-water to convert thermal power into electrical power in steam turbines.

### **3. THE ASTRID PROJECT**

The French Act N° 2006-739 (June, 28<sup>th</sup> 2006) foresees a Generation IV reactor in France to deal with radioactive waste management and minor actinides burning. In this framework French Atomic Energy Commission (CEA) has been charged with industrial partners to develop a fast reactor able to face this issue. The project has been called



ASTRID, which is the acronym of “Advanced Sodium Technological Reactor for Industrial Demonstration”.

ASTRID main goals are identified as<sup>6</sup>:

- Keep safety and security level at least to the same extent as current Generation III+ reactors;
- Specifically reducing the risk associated with the Sodium-water interaction in Steam Generators;
- Demonstrating the technological feasibility of sodium fast reactors to electrical energy production;
- Minor actinides and long life radioactive waste burning;
- Better use of uranium natural resources.

In order to meet these goals, some design guidelines have been identified<sup>6</sup>:

1. Improved core design to lower the probability of core meltdown and/or the energy release following during an accident scenario<sup>7, 8</sup>;
2. Better in-service and out-of-service inspection methods and instrumentation;
3. Civil structures have to account for mechanical integrity in case of internal or external (see aeroplane impact) hazards;
4. Three independent shutdown systems;
5. Innovative gas power conversion system.

In particular, an innovative gas power conversion system is of primary interest for the present work. Gas power conversion system has been studied at CEA from early 2000s<sup>9</sup>. Its main interest is due to practical elimination of the risk associated with the sodium-water interaction<sup>10, 11</sup>, since no steam generator is necessary anymore. Therefore the plant layout is shown in Figure 1.8 and in is composed by the primary sodium loop cooling the reactor core, a secondary sodium loop to mitigate the radioactive release in case of failure of the primary circuit and a tertiary gas loop ending in the turbine-generator group producing electrical power.

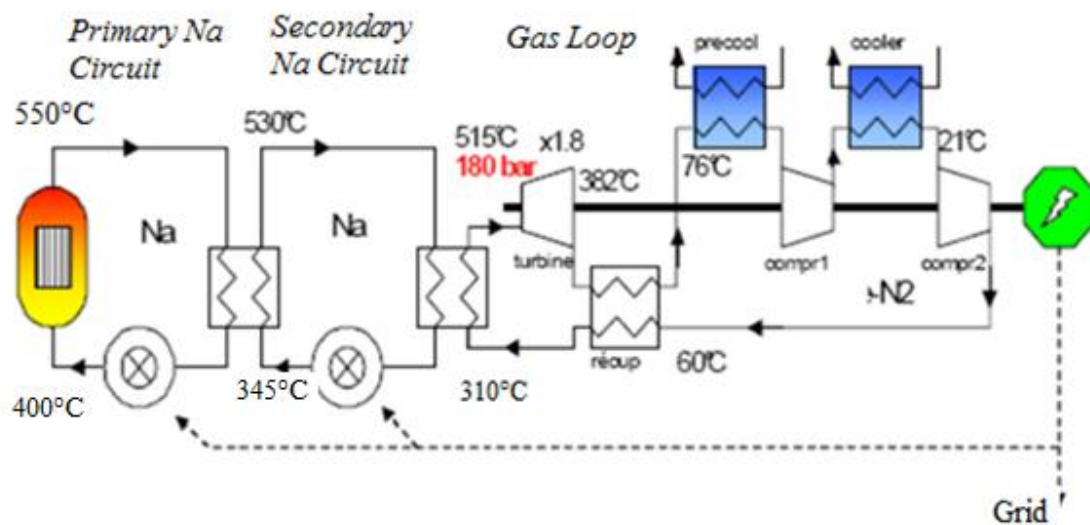


Figure 1.8 - Gas Power Conversion System (PCS) Layout

Preliminary investigation showed that the most suitable gas for power conversion was a mixture between Helium (He) and Nitrogen ( $N_2$ ), as shown in Figure 1.9. This is particularly true for high loop pressures, which are desired to increase the global cycle net efficiency.

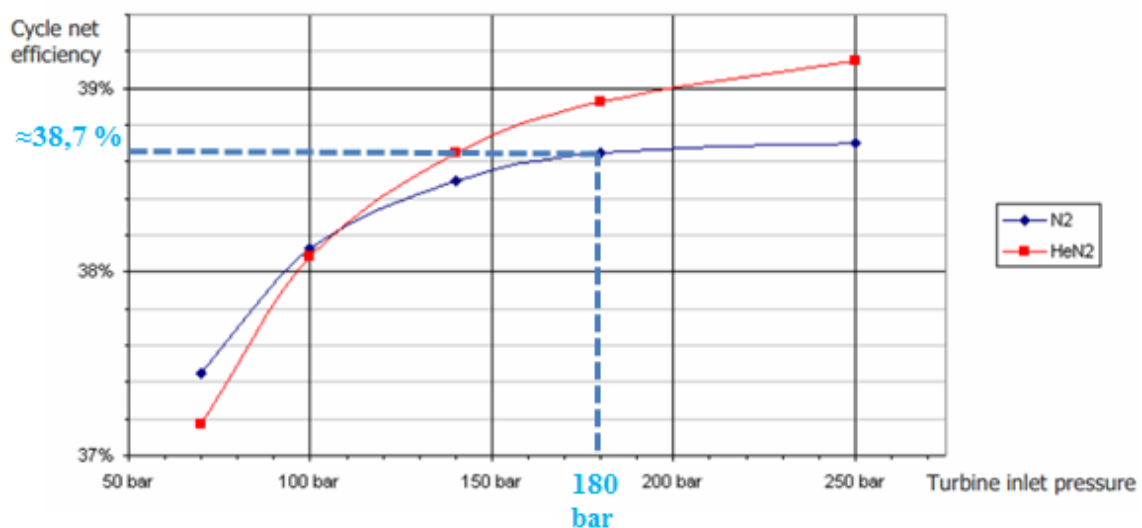


Figure 1.9 - Cycle net efficiency evaluation versus turbine inlet pressure for the gas PCS

Nevertheless, since helium-based turbine needed a strong R&D program compared to the nitrogen (i.e. air) based turbine due to the industrial experience with gas-fired fossil-fuelled power plants, nitrogen has been chosen as the reference option for the ASTRID project. In this sense, see that a cycle net efficiency of around 38.7% (37.3% taking into

account electrical power generator efficiency) is obtained, which is slightly lower than that obtained with a steam-water power conversion cycle due to the lack of boiling phenomena increasing the heat transfer. The selected operating pressure is 180 bar which represent the best trade-off between cycle efficiency and mechanical resistance that the tertiary loop component must withstand.

In this framework the most crucial component to be designed is the sodium-nitrogen heat exchanger. In fact it is responsible for the effective heat transfer from the secondary sodium to the gas that will eventually go through the turbines. It has been already shown<sup>9</sup> that its contribution to the gas circuit total pressure drop is of primary importance for the cycle efficiency: hence the design choice is to limit the sodium/gas heat exchanger pressure drop at 1 bar at maximum on the gas side. This is one of the most important design constraints to be respected.

Compact technologies are necessary for the present application because of the low heat transfer capacity of the nitrogen compared to that of boiling water. In this sense, the goal is to design a component being as compact as possible. Preliminary investigations done at CEA<sup>12</sup> showed that one technology is of primary interest due to its compactness: the Plate Stamped Heat Exchanger, which is potentially the most compact technology among those studies<sup>12</sup>. Therefore the present work starts studying the PSHE technology, to investigate its thermal-hydraulic behavior and to understand the physical phenomena providing the efficient heat transfer. The physical understanding will be used to determine the research pattern that will be followed in this PhD work aiming to increase the thermal-hydraulic performance of the compact sodium-gas heat exchanger. Note that, since the heat transfer performance of the heat exchanger (i.e. its heat transfer coefficient) is primary determined by the thermal-hydraulic behavior of the gas-side due to its higher thermal resistance, the present work will only focus on the gas (nitrogen) side of the heat exchanger itself.

#### **4. PHD THESIS OUTLOOK**

Given the design constraints described in Section 3, the PhD work will consist in:

- A bibliographic overview on the PSHE technology, to evaluate why it can provide superior heat transfer performance than the other solutions. The

bibliographical research will also investigate the numerical approach to study such components, in particular with regard to the computational domain and the turbulence modeling approach. A final innovative heat transfer geometry consisting in an innovative channel will be proposed to increase the heat transfer in the sodium-gas heat exchanger. This will be done in **Chapter 2**.

- A preliminary numerical model validation based on the conclusions of Chapter 2. Three different turbulence modeling approaches will be tested against basic validation test cases. This will be described in **Chapter 3**.
- An experimental facility description to acquire an experimental database that will be useful to actually validate the numerical model and to study the fluid flow inside the innovative channel. Some preliminary tests will be also described, to validate the database. This will be shown in **Chapter 4**.
- Final model validation and flow analysis with regard to mixing and swirling flow inside the innovative channel will be shown. Once the model is validated, a performance comparison among the existing technology and the innovative geometry will be provided, showing the gain obtained by the innovative solution. This will be done in **Chapter 5**.
- Conclusions and perspectives of the present work will be presented in **Chapter 6**.

# Chapitre 2: Echangeurs de chaleur à plaques embouties - (PSHE) Etude technique et bibliographique

Une étude bibliographique sur les échangeurs de chaleur compacts à plaques a été réalisée. Parmi les différents types d'échangeurs de chaleur compacts (à savoir les échangeurs de chaleur à circuit imprimé - PCHE, les échangeurs de chaleur plaques-ailettes-PFHE et les échangeurs de chaleur à tôles embouties -PSHE), une recherche bibliographique approfondie a été effectuée sur les PSHEs afin de mieux comprendre le comportement thermo-hydraulique de ces composants.

Les PSHEs consistent essentiellement en un certain nombre de plaques de différentes formes empilées.. Les plaques empilées se touchent dans de nombreux points de contact: cette configuration donne de la résistance mécanique en compression, améliore le transfert de chaleur et diminue le colmatage grâce à un haut niveau de turbulence. Les caractéristiques géométriques les plus importantes en ce qui concerne la géométrie des plaques PSHE type chevron ont été identifiées. L'identification précise de l'écoulement fluide pour un PSHE est très difficile parce qu'il n'existe pas de configuration bien identifiée entre les plaques en raison de l'absence de canaux bien définis.

Un vaste ensemble de corrélations pour le transfert de chaleur et la perte de charge a été présenté sur la base de considérations théoriques ou semi-empiriques. Une grande dispersion des données a été montrée, ce qui est probablement dû à la très large gamme de nombres de Reynolds et de paramètres géométriques des plaques pour chaque cas.

Pour mieux étudier ces effets géométriques, un aperçu de l'influence de la géométrie de la plaque sur l'échange thermique ainsi que sur le frottement a été présenté, ce qui montre que le facteur de forme ainsi que l'angle chevron sont les principaux paramètres d'intérêt pour le concepteur.

Différents paramètres géométriques définissant l'emboutissage de la plaque ont été étudiés pour vérifier leur effet sur les performance thermo-hydraulique..

Conjointement avec les mesures expérimentales, plusieurs études numériques ont été effectuées pour étudier l'écoulement de fluide à l'intérieur des plaques. Les résultats dépendent à la fois du domaine de calcul et du modèle adopté.

Enfin, des critères d'évaluation des performances ont été présentés, en essayant d'évaluer lequel est potentiellement le plus utile pour définir la compacité de différentes géométries. Cela sera d'une importance primordiale pour statuer sur l'atteinte de l'objectif de ce travail de thèse (l'amélioration du transfert de chaleur avec des contraintes sur la perte de charge dans l'échangeur de chaleur compact à plaques).

L'idée de base de ce travail est de qualifier un motif d'échange innovant où l'écoulement du fluide est le plus tridimensionnel possible, ce qui est censé augmenter l'échange thermique .

Un dernier volet de l'étude bibliographique concerne la modélisation. Une approche numérique de type RANS à bas nombre de Reynolds fournit théoriquement les informations les plus exactes sur l'écoulement du fluide. En ce sens, et en tenant compte également de la géométrie de canal, le modèle de turbulence le plus adapté semble être un modèle basé sur le taux spécifique de dissipation: en fait, il a été largement démontré que ce type de modèle fournit une meilleure description des écoulements à gradients de pression adverses sans avoir besoin de modifications spécifiques pour les faibles nombres de Reynolds à la paroi. En outre, il a été également montré que les modèles de référence basés sur  $\omega$  prennent mieux en compte les effets de compressibilité thermique (i.e. variations importantes des propriétés physiques dans la région près de paroi). Par conséquent, pour la présente application, l'approche de modélisation basée sur  $\omega$  sera adoptée.

Pour valider le modèle numérique, une base de données expérimentale est d'une importance primordiale. La littérature ne fournit pas vraiment des cas-tests semblables au motif d'échange innovant. Donc une base de données expérimentale sur la géométrie réelle est nécessaire.

# Chapter 2: Plate Stamped Heat Exchanger (PSHE) Technical Bibliographic Review

## 1. GENERAL OVERVIEW

### 1.1 PSHE DESCRIPTION

Plate-stamped heat exchangers basically consist in a number of single plates of various shape stacked to form a frame. In the most common case, the assembly is the one shown in Figure 2.1:

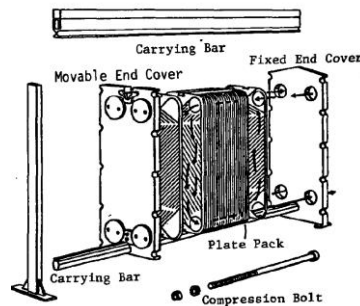


Figure 2.1- PSHE assembly<sup>13</sup>

The use of plates gives the designer many flexible alternatives depending on the specific needs<sup>14,15,16</sup>. In this sense, concentrate on the single plate to describe the component. Essentially one plate is a corrugated thin metal plate. Figure 2.2 shows some of them among the various proposed by the producers (more than sixty, according to Shah and Focke<sup>13</sup>):

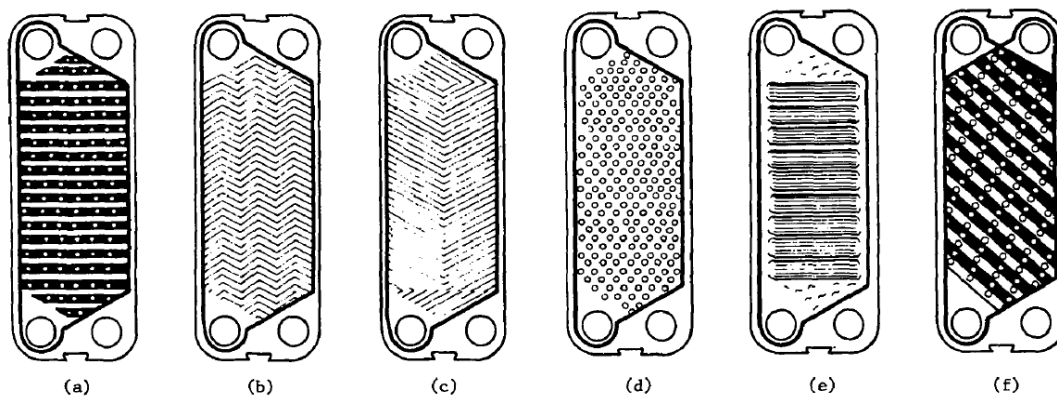


Figure 2.2 - Different types of plate: (a) Washboard, (b) Zig-zag, (c) Chevron/Herringbone, (d) Protrusions and depressions, (e) Washboard with secondary corrugations, (f) Oblique washboard<sup>13</sup>

The stacked plates touch themselves in many contact points: this configuration gives some mechanical compression resistance, enhances heat transfer and decreases fouling through an increased turbulence. A plate stacking cross-section is shown in Figure 2.3:

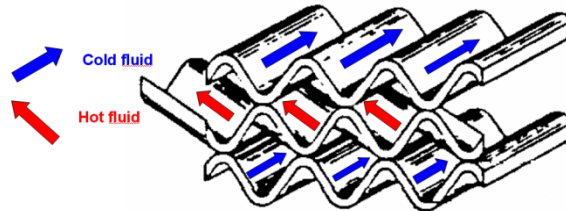


Figure 2.3 - PSHE fluid passages

Each plate has four ports, one for each corner, as Figure 2.4 shows:



Figure 2.4 - Two of the four plate ports <sup>13</sup>

Indeed only two of these ports provide the flow inlet and outlet, the other two being a passage for the secondary fluid to the next inter-plate passage. This is possible either by the use of gaskets or welding in the corner edges (black corners in Figure 2.4). Of course the latter present a better mechanical behaviour. The flow arrangement is shown in Figure 2.5:

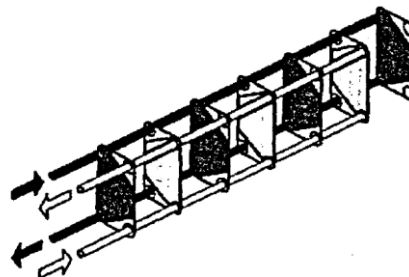


Figure 2.5 - PSHE flow scheme <sup>17</sup>



This modularity results in a number of heat transfer flow arrangements, which slightly differs with regard to the thermal performance. Figure 2.6 shows some of the possible flow arrangements:

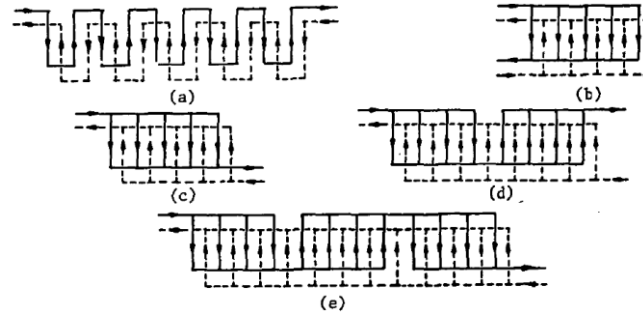


Figure 2.6 - Possible flow arrangement scheme

## 1.2 PLATE GEOMETRICAL CHARACTERISTICS

The aim of this section is to better describe a single plate to be able to understand the following sections.

Among all the existing types, we are going to concentrate our attention on the Chevron/Herringbone-type plate (Figure 2.2c), because of its major industrial importance and adoption. Basically, a chevron-type plate is shown more in detail in Figure 2. 7:

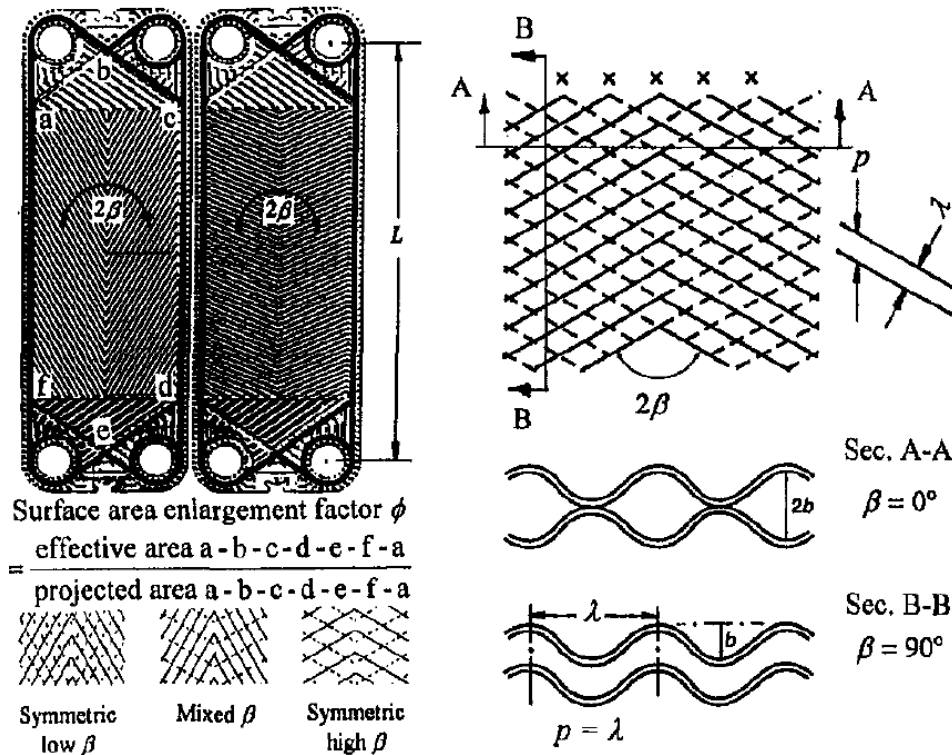
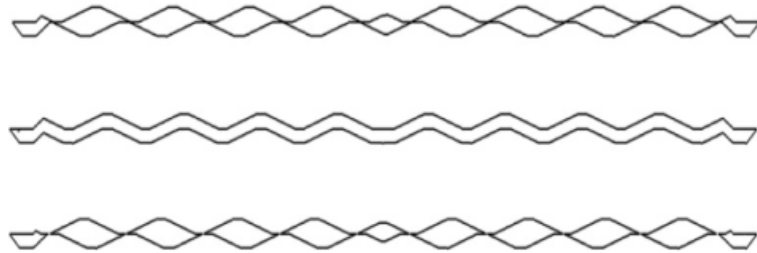


Figure 2. 7- Chevron-type plate <sup>18</sup>

Figure 2. 7 shows some interesting geometrical characteristics regarding the chevron plate geometry, in particular:

- the “chevron angle”  $\beta$ , or the angle between the corrugation and the main flow direction;
- the “area enlargement factor”  $\phi$ , or the ratio between the actual plate surface and the projected surface (which is calculated as the plate were a flat rectangular plate);
- the wavelength of surface corrugation  $\lambda$ , or the distance between two consecutive corrugation peaks;
- the corrugation depth  $b$ , or the amplitude of the single plate corrugation;
- the plate length, or the length between the inlet and outlet central points;
- the inverse plate configuration, both symmetric and mixed;
- the cross-sectional area of the hydraulic channel in two particular cases.

To give a picture of the hydraulic channel with a generic chevron angle, look at Figure 2.8, which shows a generic channel cross-section in various axial locations:



**Figure 2.8 - Hydraulic channel cross-section at different axial locations**<sup>19</sup>

Nevertheless authors do not agree each other with the given definition. In fact, some of them use different geometrical definitions which result in a strong formal impact on their final results. Hence, it is to carefully manage these parameters in order to have actual consistent comparisons.

In particular, Figure 2.9 shows two of the most common definitions for the chevron angle and the plate length:

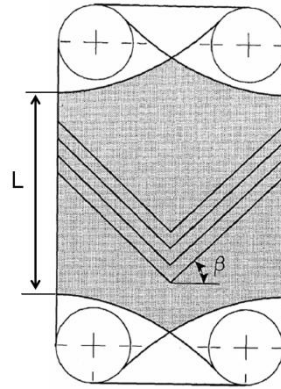


**Figure 2.9 - Alternative geometrical definitions** <sup>20</sup>

In particular, note that the chevron angle is the complementary angle to that previously defined and that the plate length actually is the length of the heat transfer active zone. With regard to the latest difference, note that this choice has likely been done to exclude from the consideration the inlet and outlet flow ports, which behaviour is completely different from that of the plate central zone.

Charre et al.<sup>21</sup> provide a number of parameters which have an influence on PSHE performance as high as eleven; they are listed as follows, even though some of them do not refer to a single plate:

1. Number of plates ;
2. Corrugation inclination angle in the central part ;
3. Angle in the distribution zone ;
4. Central part pitch ;
5. Pitch of distribution zone ;
6. Maximum height of the plate profile (distance between the top and the bottom of the profile, which is supposed to be sinusoidal);
7. Diameter of the collector ;
8. Width of the plate ;
9. Length of the chevron segment ;
10. Length of the central part zone ;
11. Length of the distribution zone.

All the previously listed parameters play a role in the global thermal-hydraulic performance of the heat exchanger; nevertheless it is often hard to really have such data since they are industrial property of the manufacturer.

### 1.3 HYDRAULIC DIAMETER DEFINITION

The aim of this section is to show the relationship between the two different definitions of the hydraulic diameter and its influence on other thermal-hydraulic variables.

Given the plate geometrical characteristics in Figure 2. 7, the theoretical definition of hydraulic diameter  $D_h$  is:

$$D_h = \frac{4Channel\_Section}{Wetted\_perimeter} = \frac{4bw}{2(b + \phi w)}$$

Being  $w$  the plate width. Now, since  $b \ll w$ , we obtain:

$$D_h = \frac{4bw}{2(\phi w)} = \frac{2b}{\phi}$$

Indeed some authors do not use this definition of hydraulic diameter. They use a simpler definition, sometimes defined as “equivalent diameter”  $D_e$ , where:

$$D_e = 2b$$

The advantages of such an approach (based on the equivalent diameter  $D_e$ ) are:

- Easily comparing the performance of a PSHE with those of two parallel plates;
- Utilizing the plate projected area in the heat transfer calculations, which is easier to use because it simply refers to the outer geometrical plate dimensions. Indeed the area enlargement factor  $\phi$  is not taken into account anymore (as in the  $D_h$  definition), therefore the plate projected area is to be used because it does not consider the area enlargement factor.

To convert a hydraulic diameter-defined correlation into an equivalent diameter-defined any correlation should use the following correction factors, as calculated in APPENDIX A:

- Multiply the Nusselt number correlation by  $\phi^{1-d}$  <sup>IV</sup>;
- Multiply the friction factor correlation by  $\phi^{1+b}$  <sup>V</sup>

#### 1.4 FINAL DEFINITION OF THE PARAMETERS OF INTEREST

In the end, it is worth to give a final definition of the parameters of interest for the following considerations. The choice is:

- With regard to the geometrical parameters, the definitions are those shown in Figure 2. 7:
  - the “chevron angle”  $\beta$ , or the angle between the corrugation and the main flow direction;
  - the “area enlargement factor”  $\phi$ , or the ratio between the actual plate surface and the projected surface (which is calculated as the plate were a flat rectangular plate);
  - the wavelength of surface corrugation  $\lambda$ , or the distance between two consecutive corrugation peaks;
  - the corrugation depth  $b$ , or the amplitude of the single plate corrugation;
- With regard to the hydraulic diameter, the definition will be that one we have previously defined as “equivalent diameter”:

$$D_e = 2b$$

Hence all the following sections will refer to this choice.

## 2. FLOW CHARACTERISTICS

### 2.1 FLOW PATTERN

Identifying the flow pattern in a plate is of primary importance to describe the fluid flow and to understand why physical phenomena occur. Moreover, as it will be shown, fluid flow description and heat transfer enhancement are strictly related: hence the aim

---

<sup>IV</sup>Note that the superscript « d » corresponds to the superscript of the Reynolds number in the heat transfer correlation

<sup>V</sup>Note that the superscript « b » corresponds to the superscript of the Reynolds number in the friction factor correlation

of the current section is to show what the flow pattern is for different plate arrangements.

In this sense, there are studies which aim is to provide a comprehensive description of this phenomenon. See Figure 2.10 to visualize the definitions of furrow and contact point: indeed two superposed plates (touching each other in several contact points), form a channel-like space for fluid flow, which is defined as a furrow.

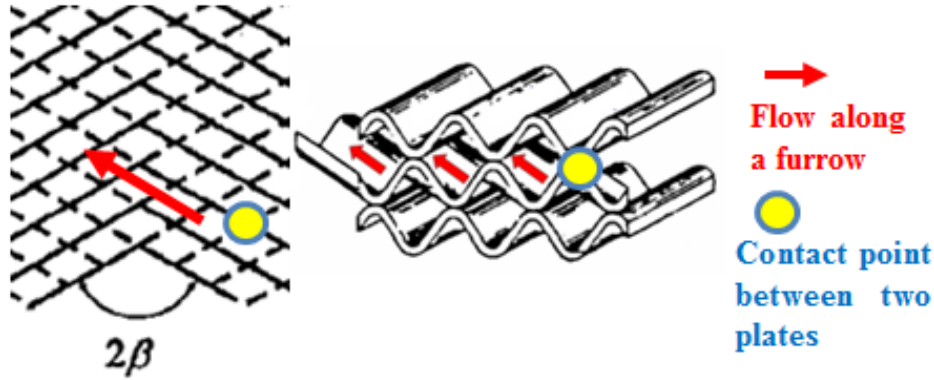


Figure 2.10 - Furrow and Contact Point visual definition

Focke et al.<sup>22</sup> and Focke and Knibbe<sup>23</sup> provide the following information for experiments done with an aqueous solution:

- $\beta = 45^\circ$ : the fluid pattern essentially follows the furrows.
- $\beta = 80^\circ$ : the fluid flows along a single furrow mainly but it is reflected at plate contact points. Hence the flow pattern is zig-zag (swirling) type.
- $\beta = 90^\circ$ : the two plates form a wavy wavy channel. Flow separation is observed at a Reynolds number as low as 20. Since the higher the Reynolds number, the higher the separated regions, the main flow becomes turbulent at Reynolds numbers slightly greater than 200.

These considerations are summarized in Figure 2.11 . Note that, for  $\beta = 90^\circ$ , the two superposed plates create a wavy channel, where the distinction between furrows and contact point is no longer applicable.

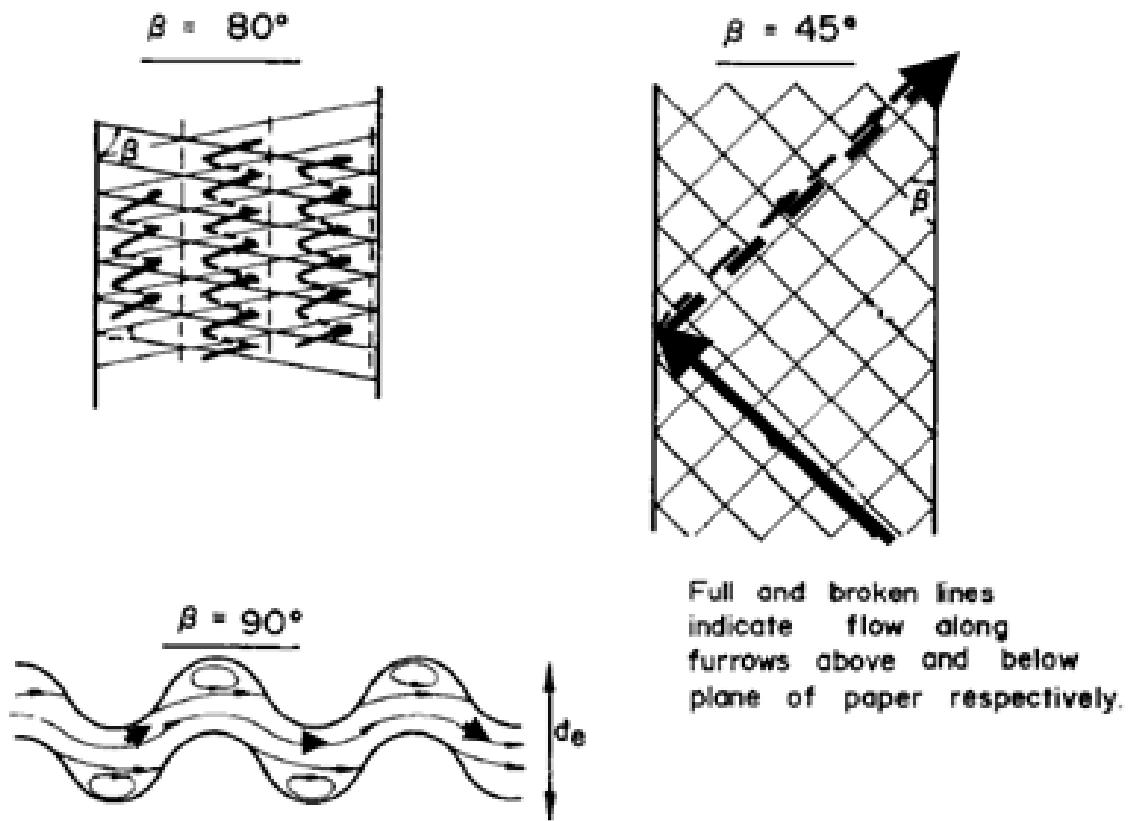


Figure 2.11 - Flow patterns depending on the chevron angle <sup>22</sup>

We can find very similar conclusions in Zhang and Tian<sup>24</sup>.

A possible explanation for this behaviour (see Focke and Knibbe<sup>23</sup>, Zhang and Tian<sup>24</sup>, and Gaiser and Kottke<sup>25</sup>) is that the different flow pattern is due to the increasing effect of a retarding force of the flow from the adjacent furrow (see Figure 2.12). In fact, for angles below  $\beta < 45^\circ$ , momentum in the furrow direction (the A1 component of the momentum F in Figure 2.12) is high enough not to be changed by the retarding flow coming from the adjacent furrow (the B1 component of the momentum F in Figure 2.12). On the other hand, for  $\beta > 45^\circ$ , the retarding effect (B2) is stronger due to the lower value of the momentum (A2) in the furrow direction.

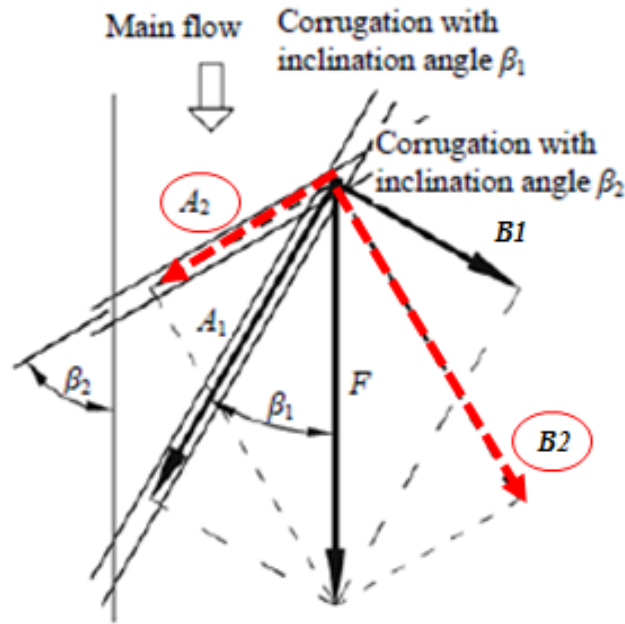


Figure 2.12 - Momentum influence on PSHE flow pattern

Further confirmations of this behaviour arrive from Gherasim et al.<sup>19</sup>, where the CFD simulation results for a plate with  $\beta = 60^\circ$  (Re=1565) are shown in Figure 2.13:

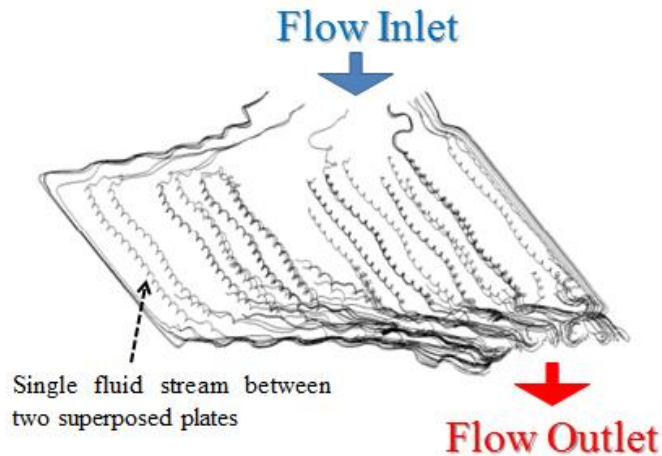


Figure 2.13 - Flow pattern from CFD simulation for  $\beta=60^\circ$  and Re=1565<sup>19</sup>

Again we see that for angles higher than  $45^\circ$ , the fluid flow is highly swirling, i.e. it changes direction every time it gets in contact with an opposite direction fluid stream. This means that the flow is really three-dimensional, since it continuously goes up and down in the corrugations of the upper and bottom plate respectively.

Even though the presented velocity component approach could be extended to velocity as high as desired (therefore also for very high Reynolds numbers the flow



pattern could be similar), this assumption must be extremely carefully managed and experimentally evaluated. In particular the effects of turbulence at very high Reynolds numbers in homogenizing the fluid flow have to be studied more deeply. In this sense, Gaiser and Kottke<sup>25</sup> show how the increased turbulence (somehow related to the fluid velocity) promotes the mass and the heat transfer, flattening the local difference of transfer coefficient along the plate.

To conclude this session we report some conclusions from Hessami<sup>26</sup>, on the fluid flow pattern with regard the Reynolds number. Indeed they give a good explanation on the highly mixed 3D flow created by a PSHE plate arrangement:

*“The use of “laminar” and “turbulent” flow in PHEs appears inappropriate, because flows even at very low Re numbers may not satisfy the strict definition of laminar flow [...]. The flow structure in PHEs is always random, erratic and fully mixed with cross-streamline movements, even at low values of Re. Therefore, it is perhaps more appropriate to refer to these flows as “low Re mixed flow” and “high Re mixed flow” instead of the conventional “laminar” and “turbulent” flows, respectively”.*

## **2.2 LOCAL THERMAL PERFORMANCE OF WAVY CHANNEL CORRUGATION**

The aim of this section is to investigate the local behaviour of the corrugations in terms of contribute to heat transfer and pressure drop. Note that there are only few studies on actual PSHE plates but much more on wavy (usually sinusoidal) channels. In fact these can be considered as particular PSHE with a chevron angle  $\beta=90^\circ$  (see Figure 2. 7).

It is worth to start showing the results of GRETh<sup>27</sup> workgroup about the flow pattern as a function of the Reynolds number in wavy channels Figure 2.14:






Re	FLOW VISUAL DESCRIPTION	FLOW CHARACTERISTICS
< 100		Uniform laminar flow. No recirculation zone detected.
100 ↓ 200		Flow divided in 2 zones: <ul style="list-style-type: none"> <li>Principal laminar flow in the stream centre;</li> <li>Stable recirculation zones in the bends with separation and reattachment points.</li> </ul>
200 ↓ 350		Flow divided in 2 zones: <ul style="list-style-type: none"> <li>Principal laminar flow in the stream centre;</li> <li>Unstable secondary motions in the bends: separation and Von Karman vortices are detected.</li> </ul>
200 ↓ 2000		Unstable turbulent flow: great vortices disrupt principal flow in some zones of the fluid stream, but they are neutralized by still flow in other zones of the fluid stream.
>2000		Turbulent flow divided in 2 zones (with unstable interface between): <ul style="list-style-type: none"> <li>Principal turbulent flow in the stream centre;</li> <li>Zones with low relative velocity and potentially recirculation</li> </ul>

Figure 2.14 - Different single wavy channel flow patterns as a function of Reynolds number <sup>27</sup>

It is interesting to note that the first turbulent characteristics already appear at very low Reynolds numbers (i.e. 200) due to the instabilities generated by continuous detachment and reattachment of the boundary layer within the bends. For Reynolds numbers greater than 2000 the flow is fully turbulent with a fluid core interfacing with low-velocity (i.e. recirculating or not) zones corresponding to the bends.

In this framework, Metwally and Manglik<sup>28</sup> provide the results of the heat flux distribution in a wavy channel for high-viscosity fluids ( $Pr = 35$ ). The influence of the recirculation zones is deeply analysed in Figure 2.15, where the local heat flux normalized to the mean heat flux is calculated on the bottom wall. The high heat transfer region is that with flow acceleration due to the onset and development of

recirculation zone in the opposite wall. Obviously the vice versa is for the high heat transfer region. Note that  $\gamma = 4b/\lambda$  represents the wall corrugation aspect ratio:

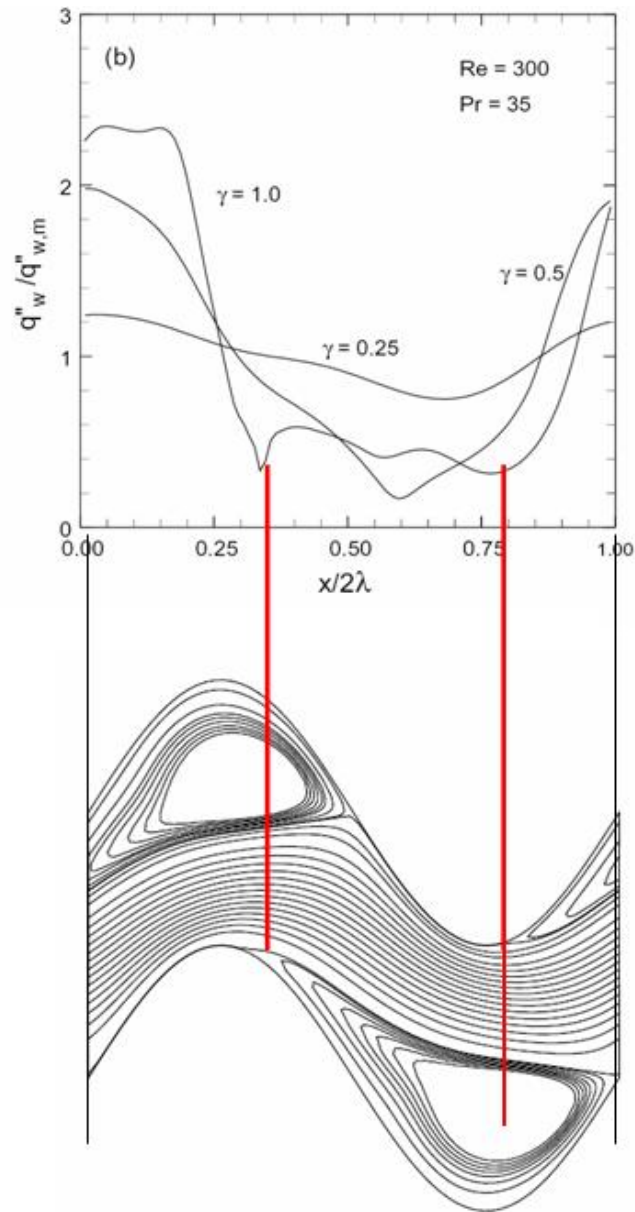


Figure 2.15 - Influence of recirculation zone on heat transfer <sup>28</sup>

Xin and Tao<sup>29</sup>(working fluid being air) provide also the shape of the local Nu number on the top wall, shown in Figure 2.16:

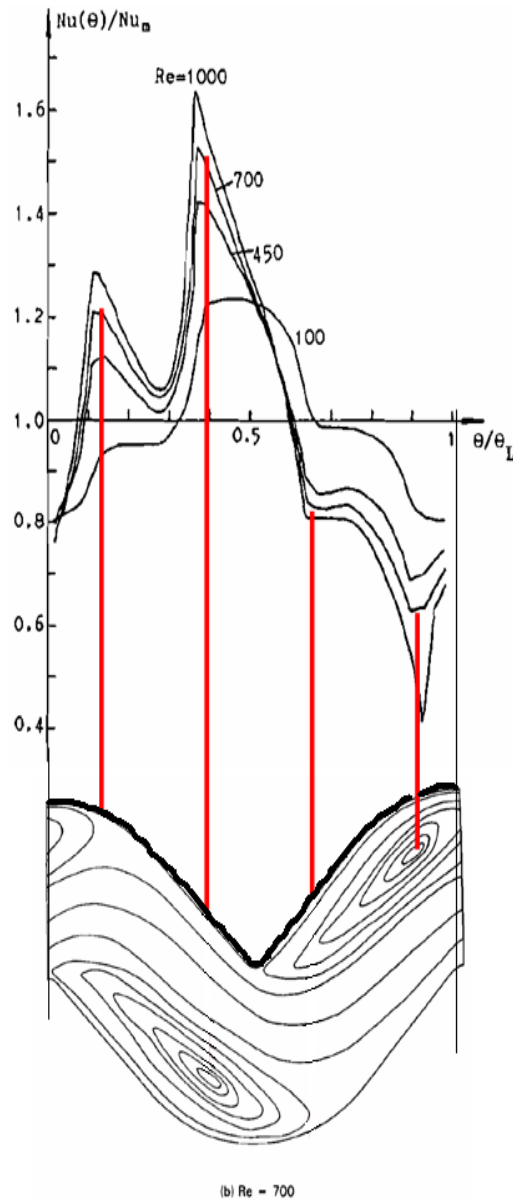


Figure 2.16 - Influence of recirculation zone on local Nusselt number<sup>29</sup>

Again, note the influence of the recirculation zone on the heat transfer. Local Nusselt number increase corresponds to the high-velocity region of the top wall (even if local decreases occur, there is no doubt that the higher heat transfer region is that with the higher velocity). On the other hand, where recirculation occurs, heat transfer is immediately degraded to lower values.

Also Oyakawa et al.<sup>30</sup> present interesting results about heat transfer and pressure drop in wavy channels shown in Figure 2.17, the working fluid being air:

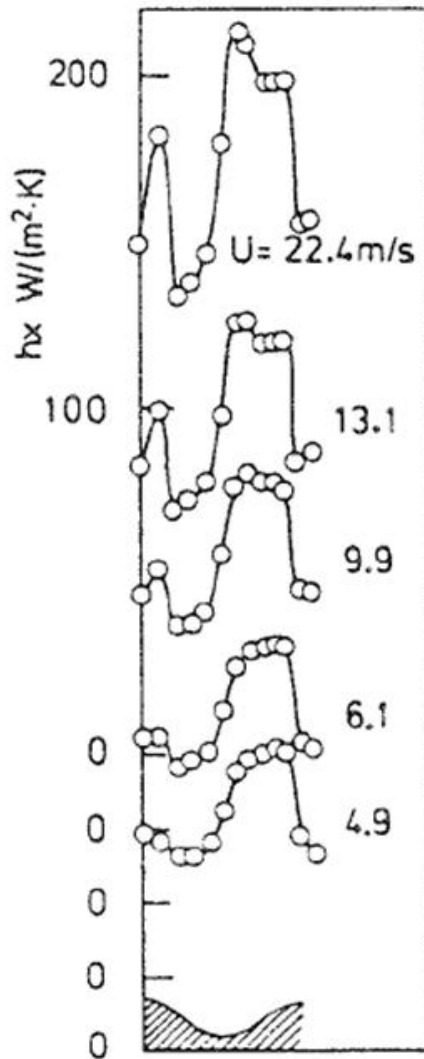


Figure 2.17 - Pressure drop and heat transfer coefficient local distribution<sup>30</sup>

Note that if there were a recirculation zone in the upstream part of the wave (as GRETh could suggest, see Figure 2.14), the behaviour shown could be easily explained. In fact, since no flow visualization is shown in the original reference of Oyakawa et al<sup>30</sup>, we can suppose that the geometry of the channel they investigated leads to flow separation (in the upstream part of the wave) and hence to a lower heat transfer coefficient. As soon as the flow reattaches, the heat transfer increases.

Gradeck et al.<sup>31</sup> (working fluid being liquid water) provide the information shown in Figure 2.18 about the heat transfer coefficient distribution over the sinusoidal shape of the plate:

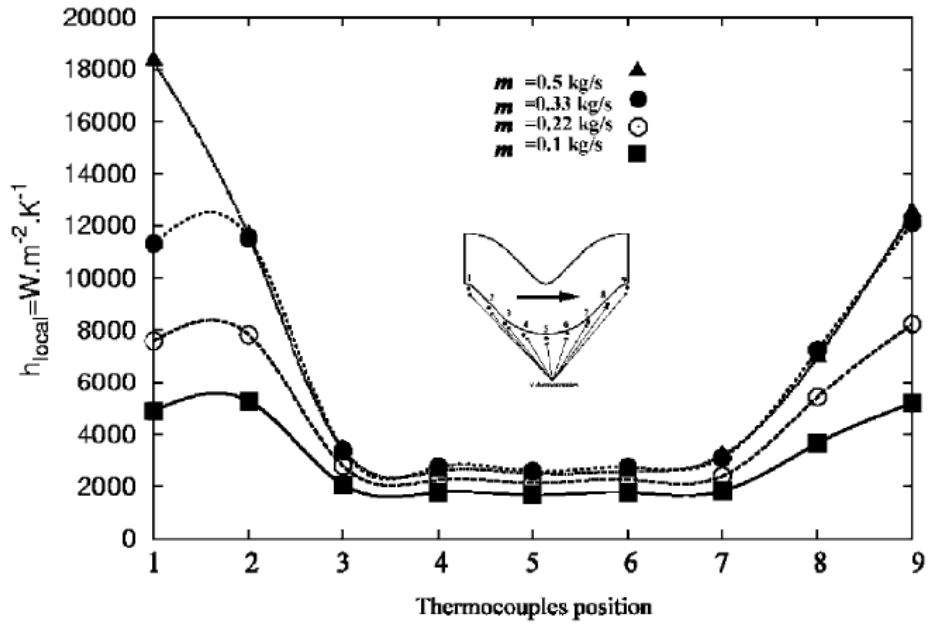


Figure 2.18 - Local heat transfer coefficient <sup>31</sup>

Even though there are small geometrical differences between these results and those of Oyakawa et al.<sup>30</sup>, the results appear to be qualitatively similar. The Reynolds numbers range about from 5600 to 23000 for a mass flow rate ranging from 0.1 kg/s to 0.5 kg/s. Hence, according to Figure 2.14, a separation bubble might be present in the central part of the bottom wall, explaining the decreased heat transfer. It could be pointed out that the recirculation bubble could not be perfectly symmetric with regard to the bottom wall central point, as the heat transfer coefficient suggests; anyway, since no direct information about flow separation is presented, we consider these data as in qualitative agreement with our hypothesis.

Thonon et al.<sup>32</sup> provide the results in Figure 2.19, which are qualitatively similar to those of reference<sup>30</sup> (note that the shape is inverse because the local Nusselt number is calculated on the top wall rather than in the bottom one):

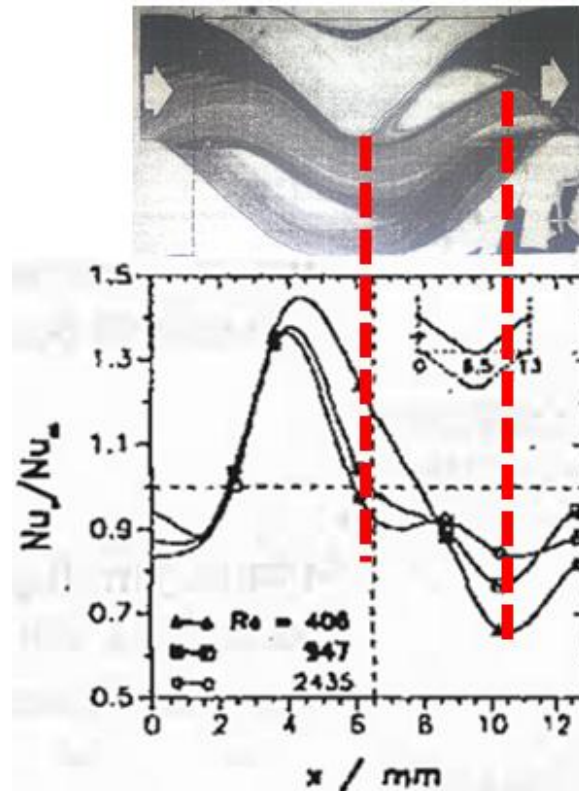


Figure 2.19 - Local Nusselt number 17

From all the references provided it seems that better performance is localized in the corrugation zones opposite to the recirculation zones (see for example Figure 2.19). This is confirmed by works of Oyakawa et al.<sup>30</sup>, Metwally and Manglik<sup>28</sup> and Xin and Tao<sup>29</sup> and Thonon et al.<sup>32</sup>. Indeed a localized flow acceleration can be noted there (due to the smallest cross section for the fluid flow) which directly influences the local heat transfer; of course the vice versa is for the zone of recirculation, in which the heat transfer is poorer. This seems to be the same phenomenon explaining the local heat transfer coefficient values in Gradeck et al.<sup>33</sup>, even though no recirculation zone is clearly shown in their work. However, since it is likely that a recirculation occurs in the central part of the studied bottom wall, we might conclude that it is the fluid acceleration that results in an enhanced heat transfer. This phenomenon would agree with the non-dimensional analysis, from which we can express the heat transfer (i.e. Nusselt number) as a function of the fluid velocity (i.e. the Reynolds Number). This seems to be true both on a global scale and on a local scale, as previous results showed. Results of Oyakawa et al.<sup>30</sup> may also confirm this trend if we suppose the recirculation occurs in the upstream part of the bend.

Anyway, since the geometries (hence the occurrence of recirculation) are different in presented works, we can say with Snyder et al.<sup>34</sup> that:

*“It seems clear from these separate investigations that different flow mechanisms may play starring roles in promoting heat transfer, depending crucially on operating regime and local details of the surface geometry.”*

In conclusion what can be inferred is that in wavy channels, recirculation zones indirectly enhance the heat transfer (i.e. creating local accelerating regions on the opposite wall). This means that such recirculation zones are desired for an enhancing heat transfer technology. Moreover, what is not necessarily described by investigations on wavy channel is that the three-dimensional flow (that we can observe for PSHEs) continuously attaches and detaches the flow thermal boundary layer, i.e. the high temperature region of the fluid. This is easily understandable considering that a wavy channel is a two-dimensional flow whereas a 3D flow inherently has one more direction for boundary layer attachment and detachment. Finally, this process does increase the heat transfer, being the hotter fluid somehow mixed with colder one, hence homogenising the global fluid temperature. This is very favourable and desirable for a technology aiming to increase thermal performance of a heat exchanger.

### **3. CORRELATIONS**

As previously exposed, thermal-hydraulic performances essentially depend on the geometrical characteristics of the plate. Nevertheless many of the available correlations do not take into account these dependences but only fit experimental or simulation data.

Indeed a few authors tried to theoretically investigate the problem in order to obtain generally applicable correlations: actually they have to introduce some semi-empirical factors to close the model: in this sense refer to them as semi-theoretical correlations.

The aim of this section is to provide a comparison of the existing correlations. We are going to explicitly show only a few correlations, both semi-theoretical and experimental. For the other ones, refer to the original references.



### 3.1 SEMI-THEORETICAL CORRELATIONS

One of the most famous works in this field is that of Martin<sup>35</sup>. The friction factor and Nusselt number are given by the following relations, based on the link between heat transfer and pressure drop. Note that the shown original correlations are based on the hydraulic diameter  $D_h$ .

$$\frac{1}{\sqrt{f}} = \frac{\cos\beta}{\sqrt{b \tan\beta + c \sin\beta + \xi_0(\text{Re})/\cos\beta}} + \frac{1 - \cos\beta}{\sqrt{\xi_1(\text{Re})}}$$

$$Nu = 0.122 \text{Pr}^{1/3} (\mu/\mu_w)^{1/6} [f \cdot \text{Re}^2 \sin(2\beta)]^{0.374}$$

The Fanning friction factor “ $f$ ” is calculated based on geometrical parameters. In particular, the reference length is the  $L$  of Figure 2. 7; moreover the angle  $\beta$  has a major influence in determining the plate pressure drop. The  $b$  and  $c$  coefficients also depend on the geometry. The  $\xi_0$  term represents the friction factor for a straight channel, whereas the  $\xi_1$  term represents the friction factor for a flow across a wavy channel between two parallel plates (i.e.  $\beta=90^\circ$ ). Note finally that the temperature gradient close to the wall is taken into account in the heat transfer correlation by the ratio between the bulk and the wall dynamic viscosity powered to 1/6.

Abu-Kadher<sup>36</sup> presents a semi-theoretical correlation for  $Nu$  very similar to Martin's, but with the numerical coefficients slightly different and depending on the plate geometry (plate type in Figure 2.2, high or low chevron angles).

Another interesting work is that of Dovic' et al.<sup>37</sup>, which presents the following correlations for the Nusselt number and the friction factor:

$$Nu = 0.15 \cdot \left( \frac{4f \text{Re}^2 d_e}{L \cdot \phi} \right)^{0.375} \text{Pr}^{1/3} (\mu/\mu_w)^{0.14}$$

$$f = \frac{C}{\text{Re}} + B$$

The B and C coefficients depend on plate geometrical parameters. Note that the parameters which have a major influence are the same as those in Martin<sup>35</sup>.

### 3.2 NON-THEORETICAL CORRELATIONS

Muley and Manglik<sup>18</sup> presented a correlation (based on their own experimental data), which is a function of the chevron angle and area enlargement factor as defined in Figure 2. 7:

$$\begin{aligned} Nu &= \left[ 0.2668 - 0.006967\beta + 7.244 \cdot 10^{-5} \beta^2 \right] \times \left[ 20.78 - 50.94\phi + 41.16\phi^2 - 10.51\phi^3 \right] \times \\ &\times \text{Re}^{(0.728 + 0.0543 \sin(\pi\beta/45 + 3.7))} \times \text{Pr}^{1/3} \times \left( \frac{\mu}{\mu_w} \right)^{0.14} \\ f &= \left[ 2.917 - 0.1277\beta + 2.016 \cdot 10^{-3} \beta^2 \right] \times \left[ 5.474 - 19.02\phi + 18.93\phi^2 - 5.341\phi^3 \right] \times \\ &\times \text{Re}^{-(0.2 + 0.0577 \sin(\pi\beta/45 + 2.1))} \end{aligned}$$

Lee et al.<sup>38</sup> modified the previous Nusselt number correlation, adding a term to take into account the dependence from the aspect ratio or the ratio AR between the plate length and the plate width:

$$\begin{aligned} Nu &= Nu_{\text{Muley, Manglik}} + f(AR) \\ \text{where } f(AR) &= 14.0002 - \frac{19.73}{AR} \end{aligned}$$

Finally the correlations of Charre et al.<sup>21</sup> are proposed in the following form:

$$\begin{aligned} Nu &= A(T_v, T_h) \text{Re}_p^{a(T_v, T_h)} \text{Pr}^{1/3} \left( \frac{\mu}{\mu_m} \right)^n \\ \frac{f}{2} &= B(t_v, t_h) \text{Re}_p^{b(t_v, t_h)} \end{aligned}$$

### 3.3 CORRELATIONS BACKGROUND

Having shown how the many geometrical parameters have a strong influence on the thermal-hydraulic performance of the heat exchanger, it is useful to show what are the main geometrical parameters for each work we are going to show.

Table 2.1 provides these and other pieces of information. Note that the label NA in the Table 2.1 means the value was not available, the label “/” means that the parameters are not taken into account in that reference while the label “?” means that the parameter is inferred from calculations based on some provided reference (i.e. Martin<sup>35</sup>) but not directly from the original work.

<u>Reference</u>	<u>Fluid</u>	$\phi$	$\lambda/b$	<u>De [mm]</u>
Savostin and Tikhonov <sup>39</sup> (1970)	Air/Water	NA	0.81-2.29	1.34 $\phi$ -2.18 $\phi$
Okada et al. <sup>40</sup> (1972)	Water	1.147- 1.412	2, 2.5, 3.75	8
Cooper <sup>41</sup> (1974)	Liquid	/	/	/
Rosenblad and Kullendorff <sup>42</sup> (1975)	Air	1.21	3.1	6.4
Marriott <sup>43</sup> (1977)	/	/	/	/
Price and Fattah <sup>44</sup> (1978)	Water or aqueous glycerol	1.18	Inconsistent definitions of given geometrical parameters values	
Tovazhnyanski et al. <sup>45</sup> (1980)	/	/	/	/
Focke et al. <sup>22</sup> (1985)	Nitrogen	1.464	2	10
Chisholm and Wanniarachchi <sup>46</sup> (1992)	/	/	/	/

Heavner et al. <sup>20</sup> (1993)	Water	confidential	confidential	confidential
Talik et al. <sup>47</sup> (1995)	Water	1.22	1.55	4.65
Wanniarachchi et al. <sup>48</sup> (1995)	Water	confidential	confidential	confidential
Martin <sup>35</sup> (1996)	/	/	/	/
GRETh <sup>27</sup> (1999)	/	/	2-3.33	/
Muley and Manglik <sup>18</sup> (1999)	Water	1.29	3.6	5.08
Lee et al. <sup>38</sup> (2000)	Water	1.29	NA	NA
Kanaris et al. <sup>49</sup> (2006)	Water	1.1 ?	NA	6.7 ?
Abu-Khader <sup>50</sup> (2007)	/	/	/	/
Dovic' et al. <sup>37</sup> (2009)	/	/	/	/
Khan et al. <sup>51</sup> (2010)	Water	1.117	2.84-3.68	4.35-7.04
Akturk et al. <sup>52</sup> (2011)	Water	1.304	2.41 ?	NA
Kapustenko et al. <sup>53</sup> (2011)	/	/	/	/
Gherasim et al. <sup>54</sup> (2011)	Water	1.17 ?	3.6	5

**Table 2.1 - Correlation preliminary information**

### 3.4 HEAT TRANSFER CORRELATION COMPARISON

It has been previously explained (chapter General Overview ) that different authors' correlations may vary not only in the fitting coefficients or in the correlation form, but also in the definition of the geometrical parameters. In this sense, it is useful to provide (in Table 2.2) an overview of this issue. Note that the difference between Dh and De is highlighted since it has a direct influence on the correlation coefficients (See Appendix A). On the other hand the angle  $\beta$  is that defined in Figure 2. 7.

<u>Reference</u>	<u>Defined heat transfer factor</u>	<u>Dh vs De</u>	<u>Origin</u>	<u>Comments</u>
Savostin and Tikhonov <sup>39</sup> (1970)	Nu	Dh	Experimental	$\psi = 2\beta$ $0^\circ < \beta < 33^\circ$ $200 < Re < 4000$
Okada et al. <sup>40</sup> (1972)	$Nu/Pr^{0.4}$	De	Experimental	$\beta = 30^\circ, 40^\circ, 60^\circ, 75^\circ$ $700 < Re < 25\ 000$
Maslov and Kovalenko <sup>55</sup> (1972)	$Nu/Pr^{1/3}$	De	Experimental	$\beta = 60^\circ$ $50 < Re < 20\ 000$
Cooper <sup>41</sup> (1974)	Nu	Dh	Manufacturer	/
Rosenblad and Kullendorff <sup>42</sup> (1975)	$j_D = \frac{Nu}{Pr^{1/3} Re}$	Dh	Experimental	$\beta = 60^\circ$ $50 < Re < 2000$
Marriott <sup>43</sup> (1977)	h	/	Manufacturer	$\beta = 32.5^\circ, 65^\circ, 32.5^\circ/65^\circ$
Tovazhnyanski et al. <sup>56</sup> (1980)	Nu	De	Experimental	$\beta = 30^\circ, 45^\circ, 60^\circ$ $2000 < Re < 25\ 000$
Focke et al. <sup>22</sup> (1985)	$j = \frac{Nu}{Pr^{1/2} Re}$	De	Experimental	$\beta = 30^\circ, 45^\circ, 60^\circ, 72^\circ, 80^\circ, 90^\circ$ $20 < Re < 42\ 000$
Chisholm and Wanniarachchi <sup>46</sup> (1992)	$j_{Nu} = \frac{Nu}{Pr^{0.4}}$	Dh	Semi-theoretical	$30^\circ \leq \beta \leq 80^\circ$ $1000 < Re < 40\ 000$

Heavner et al. <sup>20</sup> (1993)	$j_{Nu} = \frac{Nu}{Pr^{1/3} \left( \frac{\mu}{\mu_w} \right)^{0.17}}$	Dh	Experimental	$\beta=45^\circ/90^\circ, 23^\circ/90^\circ,$ $45^\circ/45^\circ, 23^\circ/45^\circ, 23^\circ/23^\circ$ $400 < Re < 10\,000$
Talik et al. <sup>47</sup> (1995)	Nu	De	Experimental	$\beta=60^\circ$ $10 < Re < 11\,460$
Wanniarachchi et al. <sup>48</sup> (1995)	$j_{Nu} = \frac{Nu}{Pr^{1/3} \left( \frac{\mu}{\mu_w} \right)^{0.17}}$	Dh	Experimental	Function of $\theta = 90^\circ - \beta$  Note that there is a misleading double definition of one parameter in the heat transfer coefficient.
Martin <sup>35</sup> (1996)	Nu	Dh	Semi-theoretical	/
GRETh <b>Errore. Il egnalibro non è definito.</b> (1999)	Nu	De	Experimental	$40 < Re < 20\,000$ Function of $\beta$ and $\lambda/b$
Muley and Manglik <sup>18</sup> (1999)	Nu	De	Experimental	Function of $\beta$ and $\Phi$  $Re > 1000$  $30^\circ < \beta < 60^\circ$  $1 < \phi < 1.5$
Lee et al. <sup>38</sup> (2000)	Nu	De	Experimental	$600 < Re < 3200$  Modified Muley-Manglik with a correction factor based on the aspect ratio $AR = L/W$
Kanaris et al. <sup>49</sup> (2006)	$Nu/Pr^{1/3}$	De	CFD	$\beta=60^\circ$  $500 < Re < 3500$

Abu-Khader <sup>50</sup> (2007)	Nu	Dh	Semi-theoretical	Modified Martin <sup>35,s</sup>
Dovic' et al. <sup>37</sup> (2009)	Nu/Pr <sup>1/3</sup>	Dh	Semi-theoretical	Modified Martin <sup>35,s</sup>
Khan et al. <sup>51</sup> (2010)	Nu	Dh	Experimental	$\beta=30^\circ, 60^\circ, 30^\circ/60^\circ$ $500 < Re < 2500$
Akturk et al. <sup>52</sup> (2011)	Nu	De for Re  Dh for Nu	Experimental	$\beta=60^\circ$ $450 < Re < 5250$
Kapustenko et al. <sup>53</sup> (2011)	Nu	De	Semi-theoretical	$100 < Re < 25\,000$ $14^\circ < \beta < 65^\circ$ $0.5 < b/\lambda < 1.5$ $1.14 < \Phi < 1.5$
Gherasim et al. <sup>54</sup> (2011)	Nu	De	Experimental	$\beta=60^\circ$ $400 < Re < 1400$

**Table 2.2 - Heat transfer correlation differences**

As one can see, authors often correlate the heat transfer coefficient according to a modified Dittus-Boelter-McAdams' correlation for straight ducts  $Nu = a \cdot Re^b Pr^\alpha$ , where the coefficient “a” and the superscripts “ $\alpha$ ” of the Prandtl number and even more “b” of the Reynolds number generally differ<sup>VI</sup>. Reference<sup>13</sup> suggests:

$$Nu = c_1 Re^{c_2} Pr^{c_3} \left( \frac{\mu}{\mu_w} \right)^n$$

With:

- $C1 = 0.15 - 0.40$
- $C2 = 0.65 - 0.85$

---

<sup>VI</sup>Remember the Dittus-Boelter-McAdams' correlation  $Nu = 0.022 \cdot Re^{0.8} Pr^{0.4}$

- $C3 = 0.30 - 0.45$
- $n = 0.05 - 0.20$

In particular references<sup>20,57</sup> note that the Reynolds number superscript “b” for PSHEs is generally lower than that in straight tubes (typically 0.8 in the Dittus-Boelter-McAdams’ correlation). They partially explain that this might be due to the stronger presence of “wake regions” or recirculation zones in PSHEs, which would not actively participate in the heat transfer. Shah and Focke<sup>13</sup> note that working on theoretical solution of the thermal entry region problem with developed velocity profiles the dependence of Nu from Pr is  $Nu \propto Pr^{1/3}$ . Nevertheless literature suggests that for fully developed turbulent flow in ducts of constant cross section that dependence should be  $Nu \propto Pr^{0.4}$ . Hence the authors suggest that the most appropriate value appears to be 0.4 but that 1/3 is recommended for conservatism. Note that Croce and D’Agaro<sup>58</sup> report that Pr superscript is actually a function of Re, with the value of 1/3 reached already at  $Re = 600$  (Figure 2.20). The trend is increasing as Reynolds number increases, suggesting that a higher superscript may be acceptable for higher Re numbers. Anyway no quantitative value is given; hence the specific case of study and intentions of authors will make the choice.

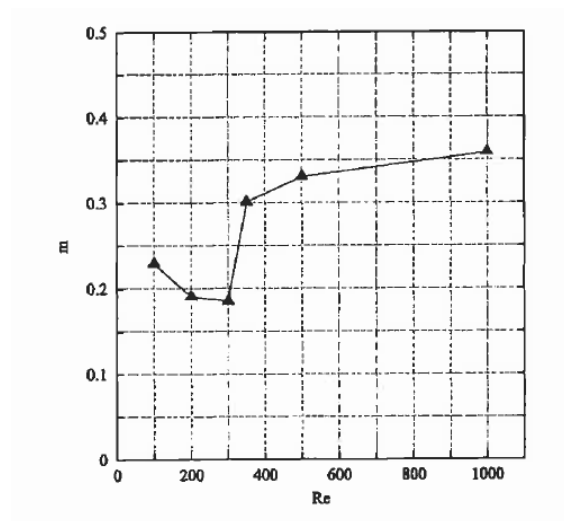


**Figure 2.20- Recommended value of the superscript of Prandtl number in the Nusselt number correlation<sup>58</sup>**

Figure 2.21 provides a comparison between many of the available correlations in the literature, done adjusting all the differences and referring to Section 1.4. In particular, note that only the correlations for  $\beta=60^\circ$  are presented, as an example.



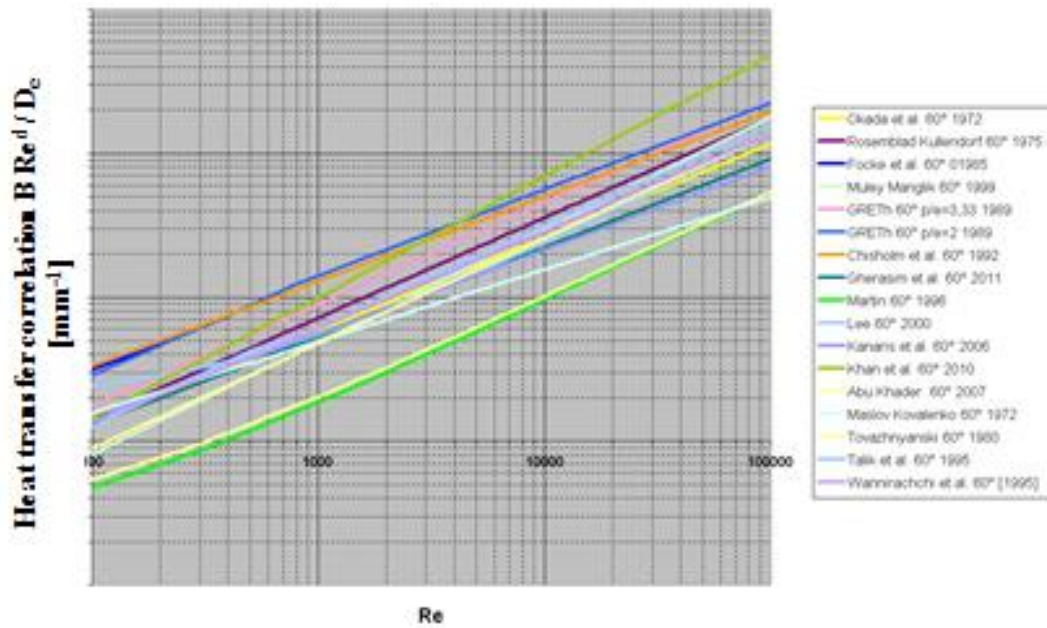


Figure 2.21 - Comparison of Nusselt number existing correlations for  $\beta=60^\circ$

### 3.5 FRICTION FACTOR CORRELATION COMPARISON

As already done for the heat transfer correlations, it is useful to provide (see Table 2.3) an overview of the different definitions of the plate geometrical parameters. Again note that the difference between  $D_h$  and  $D_e$  is highlighted since it has a direct influence on the correlation coefficients (See Appendix A). The angle  $\beta$  is that defined in Figure 2. 7. The label “/” means that the parameters are not taken into account in that reference, while the label “?” means that it was not possible to understand the actual definition of that parameter.

It is worth to highlight that for the friction factor correlations there is the issue of the definition of the reference plate length.

There are four major definitions:

1.  $L_p$ , as shown in Figure 2. 7, which is the distance between the two plate ports;
2.  $L$ , which is the plate heat transfer region length;
3.  $L_c$ , which is equal to  $L_p$  minus the port diameter;
4.  $A_{dev}/W$ , which is the ratio between the developed heat transfer area and the plate width.

Each of them is useful for different reasons: in particular  $L_p$  considers the influence of the distribution zone,  $L$  is purely referred to the thermal active zone,  $L_c$  is somehow

in the middle of the two previous definitions, the developed length takes into account the actual heat transfer surface.

Reference	Defined friction factor	Dh vs De	Origin	L- definit on	Comments
Savostin and Tikhonov <sup>39</sup> (1970)	$\xi = \frac{\Delta p}{\rho v^2 / 2g} \frac{D_h}{L}$	Dh	Experimental	L	0°<β<33° 200<Re<4000
Cooper <sup>41</sup> (1974)	$f = \frac{\Delta p \cdot \rho \cdot g}{2G^2} \frac{D_h}{L}$	Dh	Manufacturer	A <sub>dev</sub> /W	/
Marriott <sup>43</sup> (1977)	Δp	/	Manufacturer	/	β=32.5°, 65°, 32.5°/65°
Price and Fattah <sup>44</sup> (1978)	$f = \frac{\Delta p}{2\rho v^2} \frac{D_h}{L}$	Dh	Experimental	A <sub>dev</sub> /W	300<Re<3000
Tovazhnyanski et al. <sup>45</sup> (1980)	$f = \frac{2\Delta p}{\rho v^2} \frac{D_e}{L}$	De	Experimental	?	β=30°, 45°, 60° 2000<Re<25000
Focke et al. <sup>22</sup> (1985)	$f = \frac{2\Delta p}{\rho v^2} \frac{D_e}{L}$	De	Experimental	?	β=30°, 45°, 60°, 72°, 80°, 90° 90<Re<50 000
Chisholm and Wanniarachchi <sup>46</sup> (1992)	$f = \frac{\Delta p}{2\rho v^2} \frac{D_h}{N_p Z}$	Dh	Semi-theoretical	?	30°≤β≤80° 100<Re<40 000
Heavner et al. <sup>20</sup> (1993)	$f = \frac{\Delta p}{2\rho v^2} \frac{D_h}{L}$	Dh	Experimental	A <sub>dev</sub> /W	β=45°/90°, 23°/90°, 45°/45°, 23°/45°, 23°/23° 400<Re<10 000 Note that Chisholm and

<i>Continued</i>					Wanniarachchi <sup>46</sup> report that the f- correlations are inconsistent with the provided plots.
Talik et al. <sup>47</sup> (1995)	$\xi = \frac{2 \cdot \Delta p}{\rho v^2} \frac{D_h}{L_p}$	De	Experimental	?	$\beta=60^\circ$  10<Re<11 460
Wanniarachchi et al. <sup>48</sup> (1995)	$f = \frac{\Delta p \cdot \rho \cdot g_c}{2G^2} \frac{D_h}{L} \left( \frac{\mu}{\mu_w} \right)^{0.17}$	Dh	Experimental	A <sub>dev</sub> /W	Function of $\theta = 90^\circ - \beta$  g <sub>c</sub> =conversion factor ( = 1 in SI)
Martin <sup>35</sup> (1996)	$\xi = \frac{2 \cdot \Delta p}{\rho v^2} \frac{D_h}{L_p}$	Dh	Semi-theoretical	Lp	/
GRETh <sup>27</sup> (1999)	$f = \frac{\Delta p}{2\rho v^2} \frac{D_e}{L}$	De	Experimental	L	40<Re<20 000  Function of $\beta$ and $\lambda/b$
Muley and Manglik <sup>18</sup> (1999)	$f = \frac{\Delta p}{2(\dot{m}/N \cdot A_c)^2} \frac{D_e}{L_p}$	De	Experimental	Lp	Function of $\beta$ and $\Phi$  Re> 1000  30°< $\beta$ <60°  1< $\Phi$ <1.5
Kanaris et al. <sup>49</sup> (2006)	$f = \frac{\Delta p}{2\rho v^2} \frac{D_h}{L} ?$	De	CFD	A <sub>dev</sub> /W ?	$\beta=60^\circ$  700<Re<1700
Abu- Khader <sup>50</sup> (2007)	$\xi = \frac{2 \cdot \Delta p}{\rho v^2} \frac{D_h}{L_p}$	Dh	Semi-theoretical	Lc	Modified Martin <sup>35</sup> 's

Dovic' et al. <sup>37</sup> (2009)	$f = \frac{\Delta p}{2\rho v^2} \frac{D_h}{L_{long}}$	Dh	Semi-theoretical		Modified Martin <sup>35</sup> s;  $L_{long}$ is computed on base of the unitary cell
Akturk et al. <sup>52</sup> (2011)	$f = \frac{\Delta p \cdot \rho \cdot N_p}{2G^2} \frac{D_h}{L_p} \left( \frac{\mu}{\mu_w} \right)^{0.17}$	Dh	Experimental	Lp	$\beta=60^\circ$  $450 < Re < 5250$
Gherasim et al. <sup>54</sup> (2011)	$\xi = \frac{2 \cdot \Delta p}{\rho v^2} \frac{D_e}{L_c}$	De	Experimental	Lc	$\beta=60^\circ$

**Table 2.3 - Friction factor correlation differences**

As one can see, authors generally correlate friction factor and Reynolds number in an “Ergun-type” correlation in the form  $f=aRe^{-b}$ . Sometimes the correlation form is slightly different, see  $f=ARe^{-b}+c$ . References<sup>20,57</sup> affirm that when the f-correlation is in the first form, the superscript b ranges from 0 to 0.25; this is consistent with the literature: for very high chevron angles the superscript of the Pr can reach 0.0, while for angles as low as  $0^\circ$  the plate channel approaches a collection of vertical tubes, for which the known value of this coefficient in the literature is 0.2-0.25 in fully turbulent flow.

Nevertheless friction factor values from different correlations may vary significantly: Figure 2.22 shows the comparison (again done adjusting all the differences and referring to Section 1.4) of many existing friction factor correlations, all referred to the value given by the correlation from Muley and Manglik<sup>18</sup>. Indeed it is

worth to specify that the reference choice was to consider  $f = \frac{\Delta p}{2\rho v^2} \frac{D_h}{L_p}$ . Anyway, in

absence of an accurate description of the whole plate, some assumptions regarding the reference length have been done. In particular:

- $L_p = L_c$
- $L_p = A_{dev}/W$
- $f(L_p) = 1.05 f(L)$

See (Figure 2.22) that correlations may differ by more than an order of magnitude: this implies a very difficult choice of the reference option. Again we are going to arbitrarily extrapolate all the correlations from their reference range and to consider the case of  $\beta=60^\circ$  as an example.

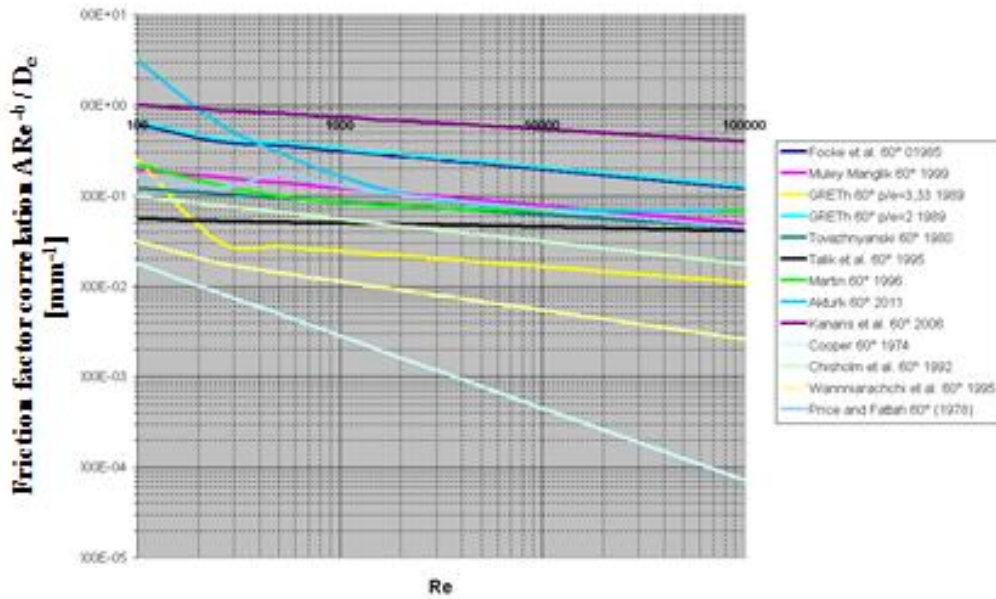


Figure 2.22 - Comparison of friction factor existing correlations for  $\beta=60^\circ$

#### 4. PARAMETERS OF INTEREST

The aim of this section is to provide an overview of the influence of the major parameters of interest for the thermal-hydraulic performance of the PSHEs. It has already been shown how performances are affected by many different factors (see Correlations).

##### 4.1 ASPECT RATIO ( $\lambda/b$ RATIO)

Gaiser and Kottke<sup>25</sup> studied the effects of wavelength and inclination angle on the homogeneity of local heat transfer coefficient in PSHE.

They found what Figure 2.23 shows, with regard to the influence of the corrugation characteristics on PSHE performance. Note that their  $\lambda/a$  ratio is actually equal to two times the  $\lambda/b$  ratio.

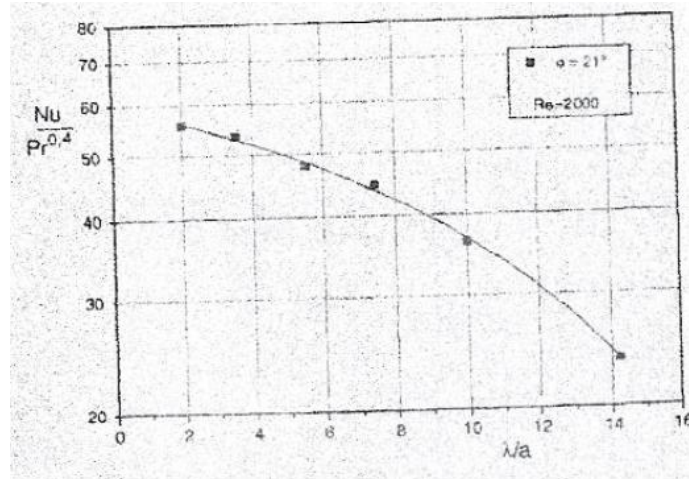


Figure 2.23 - Effect of aspect ratio on PSHE's thermal performance<sup>25</sup>

See that thermal performance decreases with the increasing of the  $\lambda/a$  ratio.

This behaviour can be easily explained by the flow physics: in fact, the higher the  $\lambda/b$  ratio, the more similar to a flat plate the single PSHE plate is. A flat plate has intrinsically worse heat transfer and lower pressure drops. With regard to Section 2.2, see that the heat transfer enhancement acts where local flow acceleration occurs: hence, for a quasi-flat plate it is likely that no great heat transfer increase will be detected as a result of the poor flow dynamics.

This trend is numerically confirmed by Blomerius and Mitra<sup>59</sup> (Figure 2.24), who studied the convective heat transfer and pressure drop in wavy ducts for air flows ( $Pr = 0.7$ ).

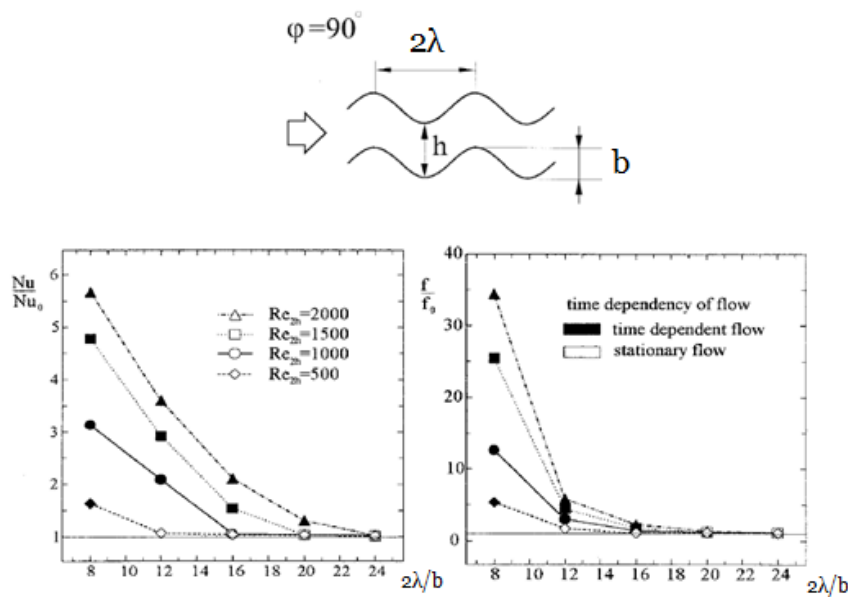


Figure 2.24- Effect of aspect ratio on thermal-hydraulic performance according to Blomerius and Mitra<sup>59</sup>

The “0” index refers to a flat plate situation: hence the higher the ratio  $b/a$ , the flatter the plate and the lower the heat transfer and the friction factor.

Analytically, one can see the influence of this factor in the definition of the  $\phi$  factor. Hence, in the correlations based on the equivalent diameter definition, consider the correction factors given in Appendix A: the higher the  $\phi$  factor the higher the Nusselt number. Martin<sup>35</sup> provides the following approximate equation for the  $\phi$  factor:

$$\phi \approx \frac{1}{6} \left( 1 + \sqrt{1 + X^2} + 4 \sqrt{1 + \frac{X^2}{2}} \right)$$

$$X = \frac{\pi}{\lambda/b}$$

The previous equation is plotted in Figure 2.25:

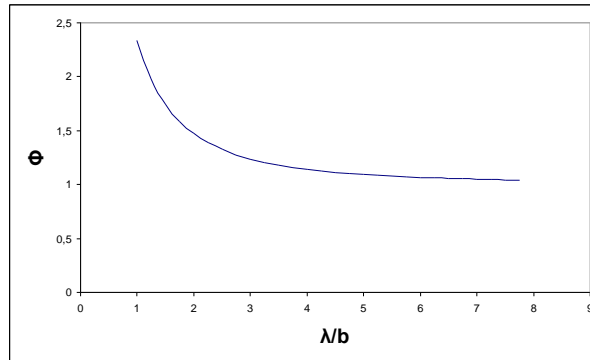


Figure 2.25 -  $\phi$  versus  $\lambda/b$  plot

Figure 2.25 shows that the lower the  $\lambda/b$  ratio the higher the  $\phi$  factor. Finally we can conclude that the higher the  $\lambda/b$  ratio the lower the Nusselt number and the lower the friction factor.

## 4.2 CHEVRON ANGLE $\beta$

Many authors presented their studies about the influence of the chevron angle  $\beta$  on the heat transfer and friction factor. To cite some of them, see references of Okada et al.<sup>40</sup>, Rosemblad and Kullendorff<sup>42</sup>, Gaiser and Kottke<sup>25</sup>, Heavner et al.<sup>20</sup>, Muley and Manglik<sup>18</sup> and Dovic et al.<sup>37</sup>.

Since results of these studies essentially agree with regard to the main conclusions, only the most popular paper on the influence of the corrugation angle on performance is presented: it is that of Focke et al.<sup>22</sup>, which provides the following results for the Colburn factor  $j = \frac{Nu}{Re Pr^{1/2}}$  and the Darcy friction factor (Figure 2.26 and Figure 2.27):

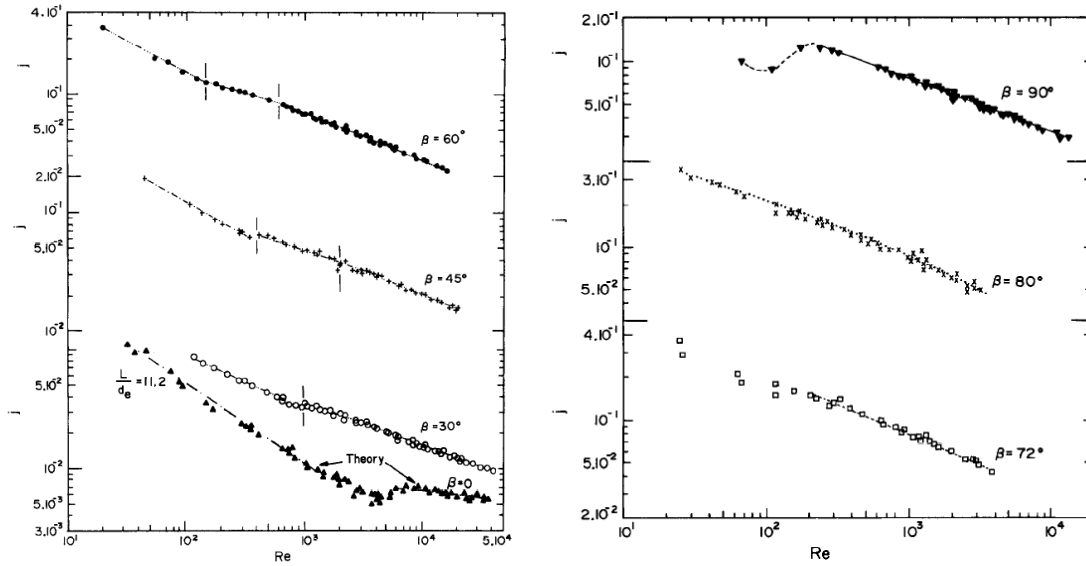


Figure 2.26 - Influence of  $\beta$  on heat transfer<sup>22</sup>

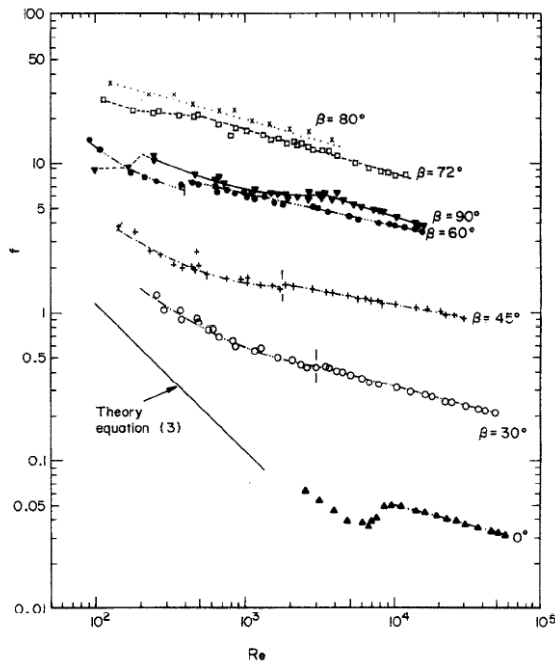


Figure 2.27 - Influence of  $\beta$  on friction factor<sup>22</sup>



Increasing  $\beta$  (at constant Reynolds number) from  $0^\circ$  to  $80^\circ$  leads to pressure drop increases of over 2.5 orders of magnitude, although heat transfer increases by a factor of only 4 to 10 times. Note that, while the heat transfer increases monotonically with the chevron angle  $\beta$ , this is not the case for the friction factor, which is lower at  $\beta=90^\circ$  than  $80^\circ$ . This is possibly explained by the fact that for  $\beta=90^\circ$  a wavy channel is formed, where no contact points and stream crossing occur. Indeed this are potentially the phenomena that provide such a high friction factor value for  $\beta=80^\circ$ . Anyway it is worth to say that there is no general agreement whether this local maximum friction factor value has to occur or not. However there is no doubt about the fact that an increased chevron angle  $\beta$  provides, in the general case, higher heat transfer and pressure drops.

#### 4.3 AREA ENLARGEMENT FACTOR

Muley and Manglik<sup>18</sup> highlight the influence of the area enlargement factor on the heat transfer, as Figure 2.28 shows:

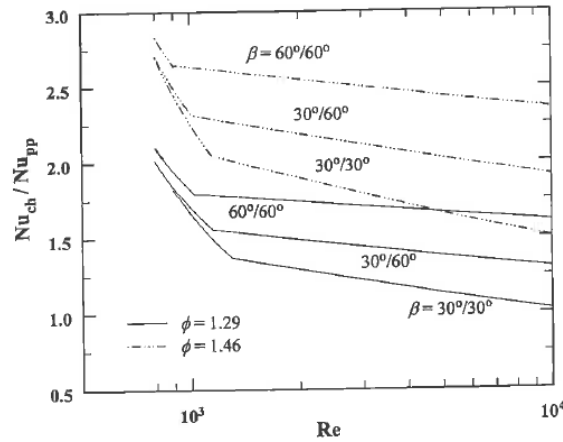


Figure 2.28 - Influence of the area enlargement factor  $\phi$  on heat transfer<sup>18</sup>

It is straightforward to understand that the larger the area enlargement factor  $\phi$ , the larger the heat transfer area (projected area being fixed). Hence the heat transfer is improved, but also pressure drop will be higher. However, note that the area enlargement factor is strictly related to the plate geometrical characteristics: hence it somehow includes all the effects typically due to these plate geometrical parameters.

## 5. OTHER CORRUGATION GEOMETRIES

The aim of this section is to provide an overview on other non-conventional plate geometries, which could potentially be of interest for their thermal-hydraulic performance.

Zhang<sup>60</sup> investigated cross-corrugated triangular channels (Figure 2.29) in transitional flow regime.

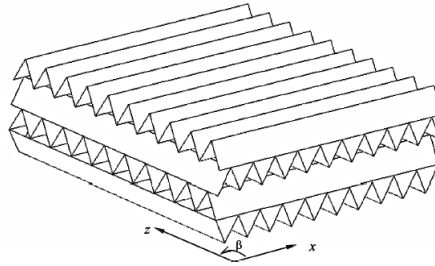


Figure 2.29 - Triangular wavy channels<sup>60</sup>

Their findings are that the friction factor for triangular shaped channels are lower than those for sinusoidal channels, while the Nu for the two configurations is similar, as Figure 2.30 shows:

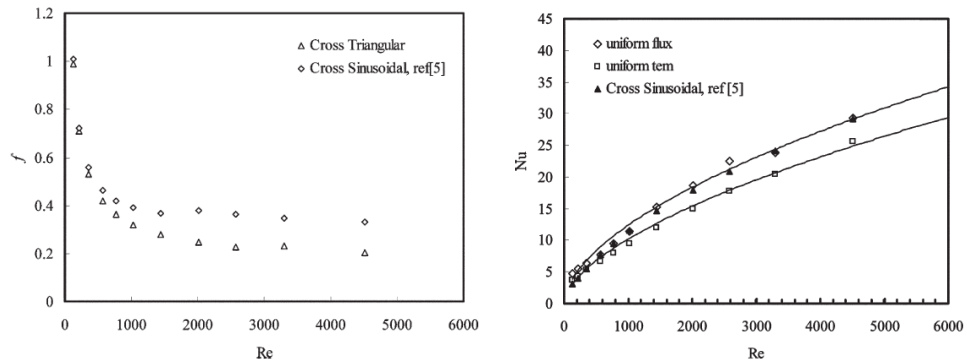


Figure 2.30 - Triangular channel performance<sup>60</sup>

A very interesting study on the potential alternative geometries was pursued by Zhang et al.<sup>61</sup>, who investigated the influence of corrugation profile on the thermal-hydraulic performance of cross-corrugated plates. The different geometries they studied are shown in Figure 2.31:

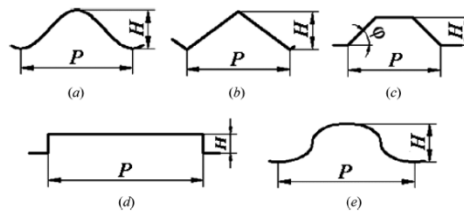


Figure 2.31 - Corrugation profiles<sup>61</sup>

They numerically simulated the different geometries (using air as working fluid), providing the results shown in Figure 2.32:

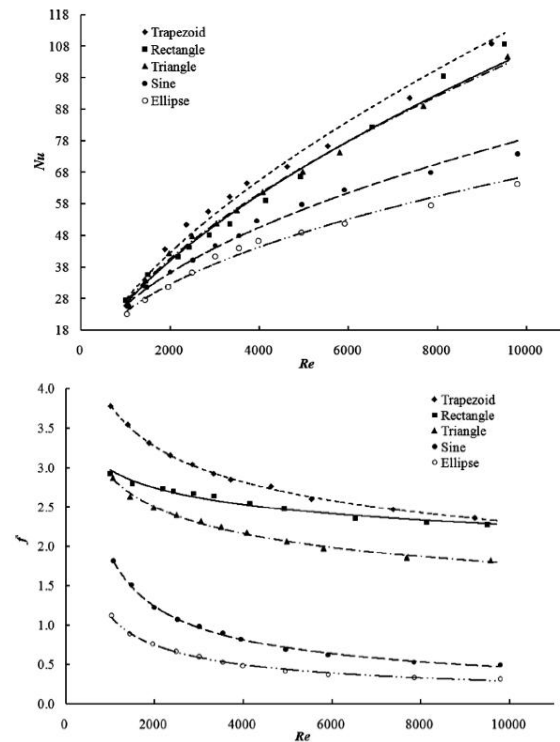


Figure 2.32 - Thermal-hydraulic performance of the different corrugation profiles<sup>61</sup>

Note that the trapezoidal geometry provides both the best heat transfer and the highest friction factor. So, even if the sinusoidal profile is the easiest profile to manufacture, indeed the trapezoidal channel can potentially be very interesting if the pressure drop constraint is not the most important one. The trapezoidal geometry is the one utilized by Gherasim et al.<sup>19</sup> since it is considered representative of their actual plate. There is a difference indeed between these results and those of Zhang<sup>60</sup>: the triangle shape corrugation presents higher friction factor than the sine shape (note the vice versa); the heat transfer is not so similar between the two profiles, as reported by Zhang<sup>60</sup>. Moreover there is a factor of 2 to 4 between the results of Zhang<sup>60</sup> and

Zhang<sup>61</sup> in terms of computed Nusselt number and friction factor. The explanation for this difference is not clear: the different turbulence models and computational domain used could have played an important role in this sense. See Section 6 for further discussion about this topic.

## 6. CFD MODEL

The aim of this section is to provide an overview on the computational simulation of the PSHEs. In particular we are not going to provide any theoretical and analytical description of the cited models. Our aim is to show the different choices made by different investigators as regards the adopted turbulence model and computational domain.

With regard to the latter, three main approaches have been identified:

- The Unitary Cell (UC) approach, shown in Figure 2.33:

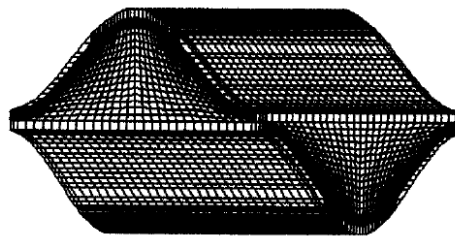
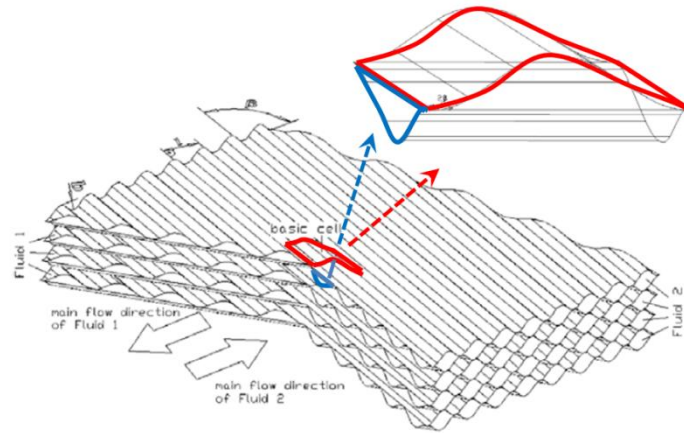


Figure 2.33 - Unitary cell approach

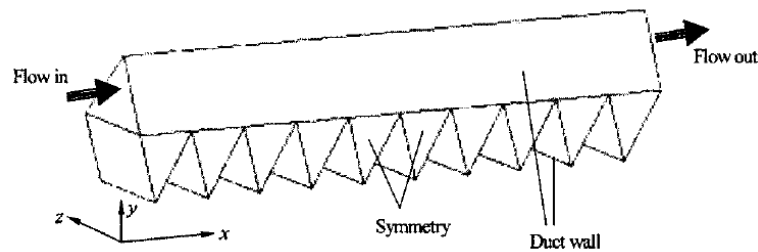
Essentially it takes into account the basic corrugation pattern to address conclusion to the whole plate. Indeed this procedure is very useful because of the relatively small computational time required. Also the UC can easily make use of the near-wall approach as well as more costly computational approaches such as LES. On the other hand it does not show plate global phenomena which can be not negligible to describe the plate thermal-hydraulic behaviour. At last note that the unitary cell approach generally needs periodic boundary conditions, which one should manage very carefully. Some authors used Dirichlet inlet and Neumann outlet boundary condition to avoid the periodic conditions. For the thermal boundary conditions, a constant heat flux or wall temperature can be easily imposed with an inlet temperature. Anyway it will be difficult to evaluate a posteriori the global temperature increase provided by the plate (which is an engineering parameter of primary importance) since the number of total UC in the

plate flow direction should be known. See that the UC volume is easily identified when looking at a PSHE plate stack (Figure 2.34):



**Figure 2.34 - Unit Cell domain definition with regard to a plate stack**

- The Single Channel (CH) approach, shown in Figure 2.35:



**Figure 2.35 - Single channel approach**

Essentially it takes into account a single hydraulic channel of the PSHE (or several unit cell in line), taking into account wider thermal-hydraulic effects. The computational time is actually higher as long as the near-wall approach is adopted. The periodic boundary conditions are not definitively avoided, since the CH still represents only a portion of the whole plate, but it is easily to handle with Dirichelet/Neumann boundary conditions. Thermal boundary conditions consist on an imposed wall heat flux of temperature and in an inlet/outlet temperature if periodic boundary conditions are avoided. Moreover it is to pay attention to the definition of hydraulic channel, since it is not a priori defined (See Section 2.1).

- The whole plate (PL) approach, shown in Figure 2.36:



**Figure 2.36 - Whole plate approach**

Essentially it models the whole plate not using any sub-domain. Of course this is the more realistic type of simulation; nevertheless its needed computational time can be extremely high and the wall-function approach is necessary. On the other hand the thermal-hydraulic boundary conditions can be as precise as desired.

Table 2.4 provides an overview of the various references on this topic.

<u>Reference</u>	<u>Domain</u>	<u>Turbulence Model</u> <u>Used/Suggested</u>	<u>Fluid</u>	<u>Corrug. Type</u>	<u>Re # range</u>	<u>Near-wall Treatment</u>
Ciofalo et al. <sup>62</sup> (1996)	UC	Smagorinsky-Lily LES Lam-Bremhorst Low Re k- $\epsilon$	Air	Sinusoidal	500-7000	Low-Re with damping function for the k- $\epsilon$ model  Smagorinsky-Lily subgrid model

Zhang <sup>60</sup> (2005)	CH	Launder-Reece-Rodi RSM in the whole Re range; Low Re k- $\omega$ in 2000-6000; Standard k- $\epsilon$ 6000-20000	Air	Triangular	2000-20000	High-Re with Wall functions
Kanaris et al. <sup>49</sup> (2005)	PL	SST k- $\omega$	Water	Trapezoidal	1500-2500	NA
Jain et al. <sup>63</sup> (2007)	PL	k- $\epsilon$ RNG	Water	Sinusoidal	400-1300	High Re with Wall Functions
Etemad and Sundén <sup>64</sup> (2007)	UC	High Re k- $\epsilon$ Low Re k- $\epsilon$ V2F Speziale-Sarkar-Gatski RSM	Air	Sinusoidal	4930	Depending on the model, even though y+ values are not always appropriate
Freund and Kabelac <sup>65</sup> (2010)	UC	SST k- $\omega$ BSL EARSM	Water	Sinusoidal	1060-3980	Low-Re with no damping functions
Han et al. <sup>66</sup> (2011)	CH	SST k- $\omega$	Water	Sinusoidal	250-2200	Low-Re with no damping functions
Gherasim et al. <sup>67</sup> (2011)	PL	Laminar for Re<400 Realizable k- $\epsilon$ NEWF for high Re	Water	Trapezoidal	50-3000	? (2.8 < y+ < 11.25)

Zhang and Che <sup>61</sup> (2011)	UC	Lam-Bremhorst Low Re k-ε	Air	Trapez. Rectang. Triang. Sinusoid. Ellipsoid.	1000- 10000	Low-Re with damping functions
Zhang and Che <sup>68</sup> (2011)	UC	Lam-Bremhorst Low Re k-ε k-ω SST	Air	Sinusoidal	1000- 10000	Low-Re for Lam- Bremhorst k-ε  Low-Re with no damping functions for the k-ω SST

**Table 2.4 - Turbulence Model Comparison**

Note that there is not a unique computational technique and moreover the answers regarding the best model to be used significantly change among the presented studies. The k-ε model (with all his variants, either High or Low Reynolds number formulation) is still widely employed, while the SST model is getting more and more popularity. Few authors use more complex models such as the Reynolds Stress models or the LES.

Now talking about the turbulence model comparison and the conclusions of such studies, generally we can see that the low-Re number formulation gives accurate results when used in a UC configuration; anyway, when employed, other RANS models (SST or Launder-Reece-Rodi RSM) act at least as well as the Low-Re k-ε model. Rarely used and only for UC configurations, LES gives rather good results, even though it is not always foreseen as the better model to be used. Indeed the few details provided in the references do not help in understanding if a proper LES mesh has been settled for those cases. As regards the CH configuration, results of Zhang<sup>60</sup> seem to be quite reasonable, since the RSM gives accurate results on the whole range of Reynolds number; by the way for lower Reynolds number the low-Re formulation of the k-ω model gives good results, since it can take into account viscous effects and turbulence damping in the near-wall region. When the Reynolds number is sufficiently high, the channel geometry



configuration can model macroscopic effects when viscous contribution becomes small: hence a High-Re k- $\epsilon$  model predicts the good trends. Note that the k- $\epsilon$  model has been developed as a High-Re model, therefore it is not surprising that it can work pretty well in situations where wall viscous effects are significantly smaller than the core-fluid region phenomena.

A similar conclusion can be deduced looking at the suggestions of Gherasim et al.<sup>67</sup> for a PL geometry: in this case the wall effects are so negligible that a simple High-Re k- $\epsilon$  model gives sufficiently accurate results. Note that, due to the complexity of the in-plate flow, a non-traditional wall function approach (i.e. the Non-Equilibrium Wall Functions - NEWF) are suggested, trying to better describe the wall effects than the Standard Wall Functions. In fact, the latter have been developed for a uniform pressure gradient flow, which is not the case for the flow inside a PSHE, where continuous boundary layer separation and reattachment occur, as clearly shown in Section 2.1. However, it should be pointed out that the plate mesh for PL geometries seems to be excessively coarse, especially in the work of Jain et al.<sup>69</sup>: the number of total cells in their study is around 880.000 for a plate of L=357 mm. For a similar plate length (L=352 mm), Kanaris et al.<sup>49</sup> use 2.6 million cells, which seem to be a more reasonable value, also considering the use of wall functions<sup>VII</sup>.

---

<sup>VII</sup>RANS modelling is actually the only doable way to model a whole plate. Consider that, for a Wall-modelled LES calculation of the whole plate (i.e. L=0.352 m, W=0.123 m (plate width) and 2b=0.024 m as in Kanaris et al.<sup>49</sup>), a total number of cells of about 35 billion would be necessary! In fact, for a reference  $Re_{De} = 50000$ ,  $Re_L = Re_{De} \cdot \frac{L}{De} = 50\,000 \cdot \frac{0.352}{0.024} = 733\,000$ . Choi and Moin (*"Grid-point requirements for large eddy simulation: Chapman's estimates revisited"*, Center for Turbulence Research - Annual Research Briefs 2011, pp.31-36) propose the following expression to determine the number of grid points for a wall-modelled LES calculation:

$$N = 54.7 \frac{L_z}{L_x} n_x n_y n_z Re_L^{2/7} \left[ \left( \frac{Re_L}{Re_{x_0}} \right)^{5/7} - 1 \right]$$

Where  $Re_{x_0}$  is the Reynolds number based on the boundary layer development length. If we assume  $x_0 \ll L$  and hence  $Re_{x_0} \ll Re_L$  we obtain:

$$N \approx 54.7 \frac{L_z}{L_x} n_x n_y n_z Re_L$$

According to Chapman (*"Computational aerodynamics development and outlook"*, AIAA J. 17 (12), 1293–1313, 1979), the cell dimension  $\Delta x \Delta y \Delta z$  should satisfy the following relations:

$$\Delta x = \frac{\delta}{n_x}, \Delta y = \frac{\delta}{n_y}, \Delta z = \frac{\delta}{n_z}$$

With  $n_x = 10$ ,  $n_y = 25$ ,  $n_z = 10$ . Hence we can find the already mention total number of cell of around 35 billion cells as:

$$N \approx 54.7 \frac{L_z}{L_x} n_x n_y n_z Re_L = 54.7 \cdot \frac{0.123}{0.352} \cdot 10 \cdot 25 \cdot 10 \cdot 733\,000 \approx 35 \text{ billion cells!}$$

Note that, despite the large spread of turbulence models, near wall treatments and domains, CFD is a very promising tool for studying the performances of PSHEs. See, for example how computations of Ciofalo et al.<sup>62</sup> do represent the good experimental trend of the friction coefficient as a function of the chevron angle (see Figure 2.37 compared to results in Section 4.2 - Chevron angle  $\beta$ ):

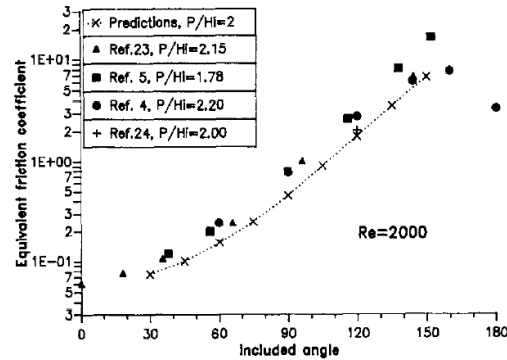


Figure 2.37 – Influence of  $\beta$  on Friction factor: CFD vs experimental results in Ciofalo et al.<sup>62</sup>

Moreover, a proper computation set up on a whole plate can give also useful global parameter trends, as shown in Figure 2.38 from calculations of Kanaris et al.<sup>49</sup>:

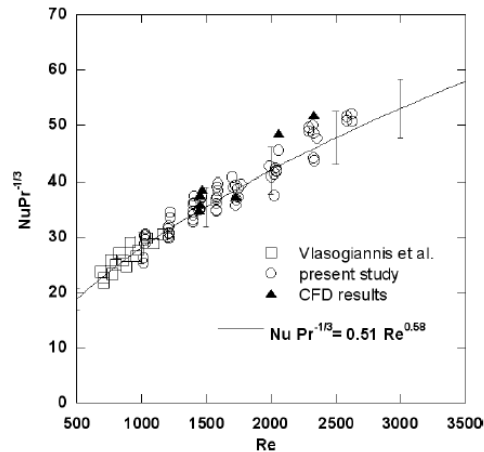


Figure 2.38 - CFD vs experimental results in Kanaris et al.<sup>49</sup>

In conclusion we can state that CFD is a very promising tool for flow analysis of PHSE, giving potentially good global parameter trends. On the other hand, it should be carefully used with regard to a more detailed local analysis of the fluid flow (as described in Section 2.2), since the computational results could potentially be misleading. In this sense, the larger the computational domain, the poorer the physical description is, since only major phenomena can be described.

## 7. ENGINEERING PERFORMANCE COMPARISON METHODS

Performance criteria are often of primary importance for engineering application since they make it possible to rapidly identify the best trends to eventually optimize the component. For heat exchanger applications, such parameters must take into account heat transfer and pressure drops, which are the key parameters of interest for a designer.

Stone<sup>70</sup> provides a very useful description of the various parameters proposed in the last years as performance criteria. Hereafter only the most used will be presented.

### 7.1 AREA GOODNESS FACTOR

The simplest but still very used parameter for heat transfer enhancement evaluation is the “Area Goodness Factor”. It is defined as the ratio between  $j$  and  $f$  values, where  $j$  is the Colburn Factor ( $j = StPr^{2/3} = \frac{Nu}{Re Pr^{1/3}}$ ) and  $f$  is typically the Fanning friction factor. The method consists in comparing the ratio  $j/f$  versus the Reynolds number. Obviously, a  $j/f$  value as high as possible is desired (for a given Reynolds number). In fact, the  $j/f$  value is inversely proportional to the total flow cross-section: hence, the higher the  $j/f$  value, the lower the total component cross-section. However one of the most evident deficiencies of this method is that in the Reynolds number there are several design options (i.e. the hydraulic diameter, the fluid velocity and hence the number of plates) that are not rigorously considered. Moreover the total volume of the component is not considered, because the total length (giving the actual pressure drop) is not taken into account: hence this parameter gives a very rough idea on the actual performance.

### 7.2 VOLUME GOODNESS FACTOR

Another method consists in comparing the heat transfer coefficient  $h_{std}$  versus the flow friction power per unit area  $E_{std}$ . These two parameters are defined as follows (note that the notation is the same as Stone<sup>70</sup>, Shan and London<sup>71</sup>):

$$h_{std} = \frac{k}{D_h} Nu$$
$$E_{std} = \frac{W \cdot \Delta p}{\rho A}$$

Where  $W$  is the volumetric flow rate and  $A$  is the heat transfer area. Again, one would want a  $h_{std}/E_{std}$  value as high as possible (for a given Reynolds number). This

would mean, for example, that for a given pressure drop and heat transfer coefficient the heat transfer area for the better geometry is higher. Note that there is a direct link between heat transfer area and volume of one side of a heat exchanger, i.e. through the generalized hydraulic diameter definition  $D_h = \frac{4V}{A}$  and hence  $A \propto \frac{V}{D_h}$ . A higher heat transfer area does not directly result in a smaller volume: a higher heat transfer surface could be given either by a smaller  $D_h$  for the same volume or by a higher volume, that is not desirable for compactness. Therefore even though the presence of the pumping power somehow makes this method more interesting than the Area Goodness factor, still their lacks are evident when dealing with the actual volume and compactness of the component.

### 7.3 PERFORMANCE PARAMETERS

Soland and al.<sup>72</sup> proposed methods consisting in comparing two performance parameters, defined as follows:

- Heat Transfer Performance Factor  $J = jRe$ ;
- Pumping power factor  $F = fRe^3$ .

This method prevents to depend anymore on the Reynolds number of the actual design application. In fact it will be shown that these two parameters are strictly related to heat transfer coefficient times the surface to volume ratio and to the pumping power per unit volume respectively. Nevertheless, it will also be shown that the method is still strictly valid for two applications with the same hydraulic diameter.

In fact, Soland and al.<sup>72</sup> propose another method, which is based on the comparison of the following parameters:

- Heat transfer coefficient times surface to volume ratio:

$$h_{std} \frac{A}{V} \approx \frac{k}{D_h} Nu \frac{D_h^2}{D_h^3} \approx \frac{k}{D_h} jRePr^{1/3} \frac{D_h^2}{D_h^3} \propto \frac{jRe}{D_h^2} \approx \frac{J}{D_h^2}$$

- Pumping power per unit volume:

$$\frac{W\Delta p}{\rho V} \approx \frac{S \cdot V \cdot 0.5 \cdot V^2 \cdot L \cdot f}{D_h \cdot D_h^3} \propto \frac{fRe^3}{D_h^4} \approx \frac{F}{D_h^4}$$

As already mentioned, this method prevents any problem due to the hydraulic diameter selection, because it is identical to the previous one if the  $D_h$  is the same for

the different geometries to compare. A priori, this method could be the best prediction regarding the comparison of different heat transfer geometries. Nevertheless see that the use of the approximation  $V = D_h^3$  does not correspond to the actual component geometry. In particular, it seems not to be correct the use of the hydraulic diameter for the main flow direction, which is the dimension influencing pressure drops. Hence the formulation of the volume of the component should be better modified to properly take into account geometry of the heat exchanger.

## 8. CONCLUSIONS

A technical bibliographic review on compact plate heat exchangers has been presented.

Among the various types of compact heat exchangers (i.e. the Printed Circuit Heat Exchangers - PCHE, the Plate-Fin Heat Exchangers-PFHE and the Plate Stamped Heat Exchangers-PSHE), an extensive bibliographic research has been done on the PSHEs in order to better understand the thermal-hydraulic behaviour of such components.

The Plate Stamped Heat Exchangers PSHEs basically consist in a number of single plates of various shape stacked to form a frame. Using plates let the designer have many flexible alternatives depending on the specific needs. The stacked plates touch themselves in many contact points: this configuration gives some mechanical compression resistance, enhances heat transfer and decreases fouling through an increased turbulence.

The most important geometrical characteristics regarding the PSHE chevron-type plate geometry have been identified (see Section 1), in particular:

- the “chevron angle”  $\beta$ , or the angle between the corrugation and the main flow direction;
- the “area enlargement factor  $\Phi$ , or the ratio between the actual plate surface and the projected surface (which is calculated as the plate were a flat rectangular plate);
- the wavelength of surface corrugation  $\lambda$ , or the distance between two consecutive corrugation peaks;
- the corrugation depth  $b$ , or the amplitude of the single plate corrugation;

- the plate length  $L$ , or the length between the inlet and outlet central points.

The identification of the fluid flow pattern for a PSHE is quite challenging since there is no a priori identified pattern between the plates due to the absence of single defined channels.

In this sense, there are studies the aim of which is providing a comprehensive description of this phenomenon. The following information is the most widely accepted (see Section 2.1):

- For  $\beta = 90^\circ$ : the fluid flows through a sinusoidal wavy channel. A flow separation is observed at a Reynolds number as low as 20. The main flow becomes turbulent at Reynolds numbers slightly greater than 200;
- For  $\beta = 45^\circ$ : the fluid pattern essentially follows the furrows, changing direction only at the plate edges. Such a pattern is also expected for  $\beta$  up to about  $60^\circ$ - $72^\circ$  ;
- For  $\beta = 80^\circ$ : the fluid flows along a single furrow mainly but it is reflected at plate contact points. Hence the flow pattern is zigzag type. Turbulence appears very early and the flow pattern seems to be still the same even in turbulent flow.

This behaviour is likely due to the increasing effect of a retarding force change due to the flow from the adjacent furrow. In fact, while for angles below  $\beta < 45^\circ$ , this interaction is positive because of the same direction components of the fluid velocities, for  $\beta > 45^\circ$ , the interaction becomes negative since the crossing streams have a negative velocity component which affects the flow. It is in this sense that this increasing retarding effect likely produces the flow pattern for higher angles.

Owing to the difficulties in determining the flow pattern inside the plates, experimental and simulations regarding the flow visualization in corrugated-wavy channels have been presented (Section 2.2). The experimental results, although of some interest, often do not refer to actual PSHE plates but to wavy channels, which do not completely represent the complexity of a PSHE hydraulic channel.

With regard to the experimental measurements, it seems that better heat transfer performances are localized in the corrugation zone opposite to the recirculation zone.

Indeed one can note a localized flow acceleration, which directly influences the local heat transfer; of course vice versa for the zone of recirculation in which the heat transfer is poorer. Moreover it has been underlined that a 3-dimensional flow such as that of a PSHE can enhance even more the heat transfer since there is no preferential direction for the fluid flow, since the boundary layer is continuously attached and detached in all directions. Pressure drops seem to be less sensitive to these flow characteristics, depending much more on wall friction due to possible larger wetted surfaces in wavy channels.

Then, a wide set of correlations for heat transfer and pressure drop has been presented (see Section 3 - Correlations) based on semi-theoretical considerations or experimental measurements. A large spread of data has been shown, which is likely due to the very large range of Reynolds numbers and plate geometrical parameters of every single case.

To better study these geometrical effects, an overview of the influence of plate geometry on heat transfer and pressure drops has been presented (see Section 4), showing that the aspect ratio as well as the chevron angle are major parameters of interest for the designer.

Also various plate corrugations have been studied, (see Section 5) to verify if some other corrugation presents better performances than the traditional ones (i.e. sinusoidal corrugations).

Together with the experimental measurements, several computational studies have been done to investigate the fluid flow inside the plates. Results depend both on the computational domain and on the adopted model (see Section 6).

With regard to the computational domain, three main approaches have been identified:

1. The Unitary Cell approach;
2. The Single Channel approach;
3. The whole plate approach.

It is clear that the best turbulence model depends on the aim of the simulation and on the computation capabilities of the available machines.

Finally, some engineering performance evaluation criteria have been presented, trying to assess which one is potentially more useful to evaluate the compactness of different geometries. This will be of primary importance to determine whether the final

goal of this PhD work (the heat transfer enhancement with pressure drop constraints in compact plate heat exchanger) is accomplished or not.

## **9. ADOPTED STRATEGY FOR THE PRESENT WORK**

### **9.1 INNOVATIVE GEOMETRY DESCRIPTION AND MOTIVATION**

The conclusion of the bibliographic review led us to understand that the complex 3-D flow of the PSHEs makes it possible to significantly increase the heat transfer performances of the component (see Section 2.2). On the other hand, the low mechanical resistance of this technology is often seen as too limiting for a wider industrial application for high-pressure flow such as that of a nuclear reactor loop. In fact, if PSHEs provide a relatively high heat transfer coefficient, on the other hand, they do not seem to be able to provide sufficiently good mechanical resistance to withstand working conditions (temperature and pressure) foreseen for ASTRID. Remember from Chapter 1 Section 3 that the secondary sodium loop is supposed to be pressurized only of a few bars while the tertiary nitrogen loop is supposed to reach up to 180 bar, with the nitrogen reaching temperatures as high as 530°C. PSHE cannot provide sufficient mechanical resistance due to the periphery welding (see Section 1.1)<sup>73, 74</sup>. Hence the plate stack acts “as an accordion”, with mechanical deformation not assuring the proper behavior during operations. This obviously means that a strong mechanical resistance has to be provided by the sodium/gas heat exchanger to meet the design goals in terms of performance and safety criteria. One of the PSHE vendors proposes his most performing heat exchanger reaching 40 bar and 350°C. In this sense it does exist a compact heat exchanger technology that can potentially stand this pressure difference: the Printed Circuit Heat Exchanger (PCHE) technology, using diffusion bonding as welding process. This results in a final unique block composed by all the plates welded together at molecular level. See Figure 2.39 to visualize a PCHE plate and stack.





Figure 2.39 - PCHE plate (on the left) and stack (on the right)

One of the vendors of the PCHE technology proposed the following performance chart shown in Figure 2.40:

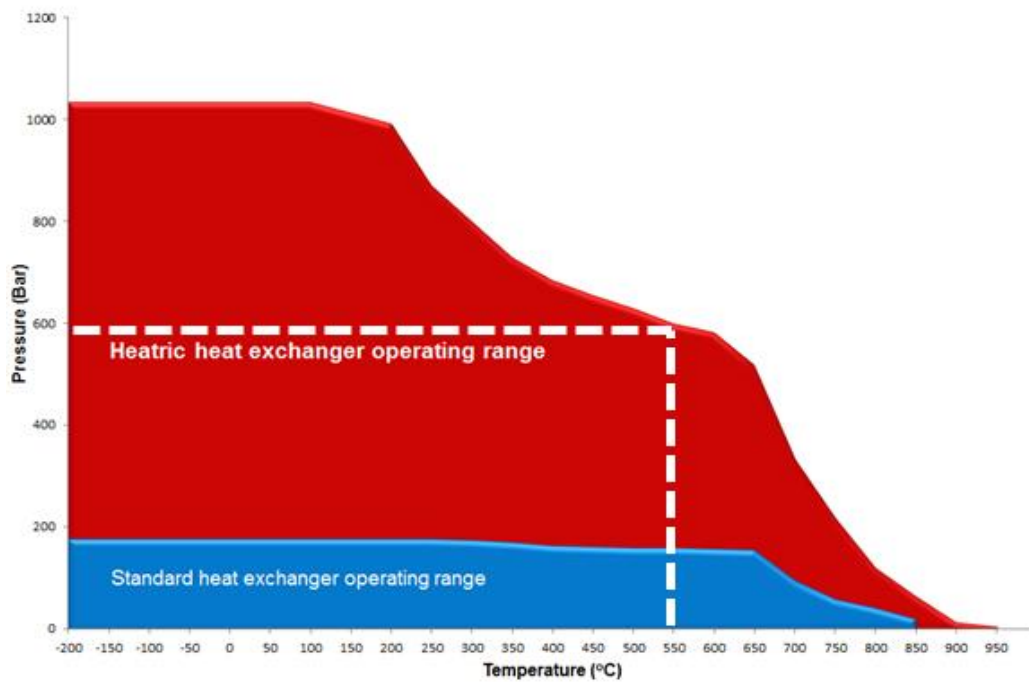
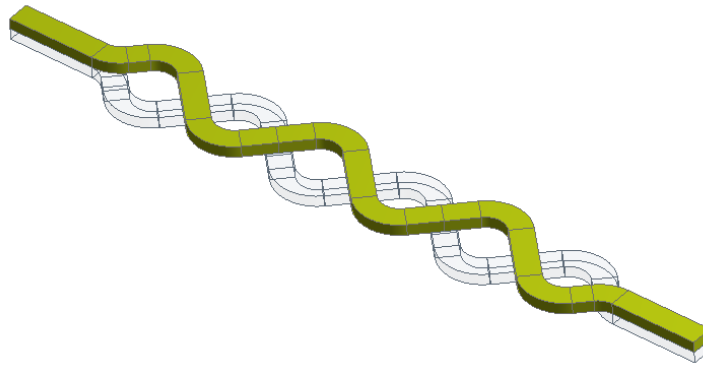


Figure 2.40 - PCHE performance chart<sup>75</sup>

See that with PCHE we can potentially operate at a maximum temperature of 550°C for an operating pressure of 600 bar (see also reference<sup>76</sup>). Even though the chart does not

assure a “nuclear quality” heat exchanger during its lifetime, its potential for the current application is not negligible.

The goal of the present work is to develop an innovative heat exchanger for ASTRID: this heat exchanger would provide a very good heat transfer (as PSHEs can do) having at the same time a good mechanical resistance (as PCHEs). Hence, in order to increase the heat transfer coefficient (and the global compactness) the basic idea of this work is to design a channel where the fluid flow is as much three-dimensional as possible.



**Figure 2.41 - Superposed channels identification**

In particular the channel can be thought as the result of the superposition of two single PCHE wavy channels in phase opposition (white and yellow in Figure 2.41), as Figure 2.42 shows. Note always in Figure 2.42 two of the possible fluid streams inside the channel (in green and orange) and compare them with the 3D fluid stream in a PSHE shown in Figure 2.11 and Figure 2.13)

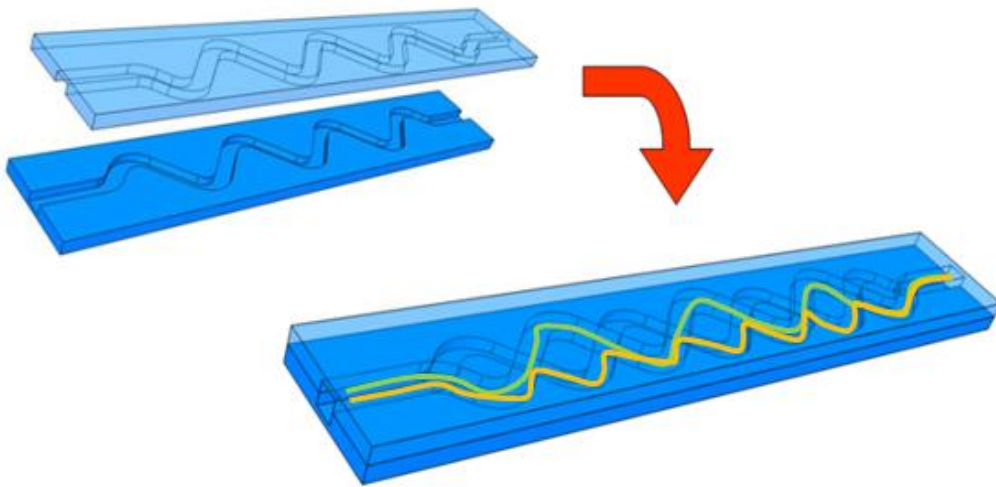


**Figure 2.42 - Innovative geometry concept**

Considering the PCHE plate showed in Figure 2.39, the actual fluid stream is composed by several wavy channels intersecting each other in several points, creating a fully 3D flow. An idea of the final configuration is shown in Figure 2.43.

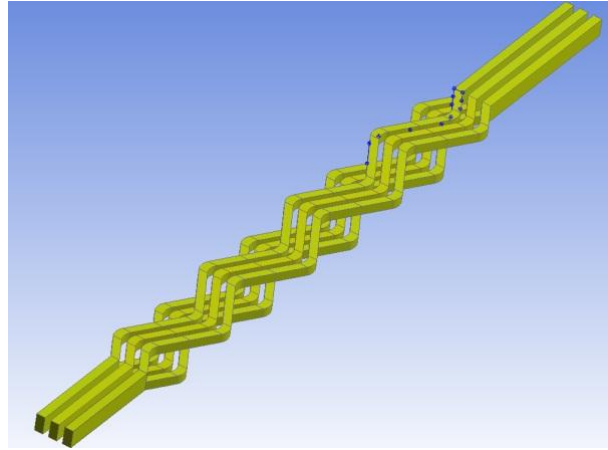


**Figure 2.43 - Example of the innovative fluid stream configuration (actual cross-section will be defined later)**

The innovative channel is composed by elementary geometrical elements, specifically bends, straight channels and mixing zones.

The bends are present in each of the two superposed wavy channels composing the innovative channels: Figure 2.44 identifies the upper channel and bottom channel bend:

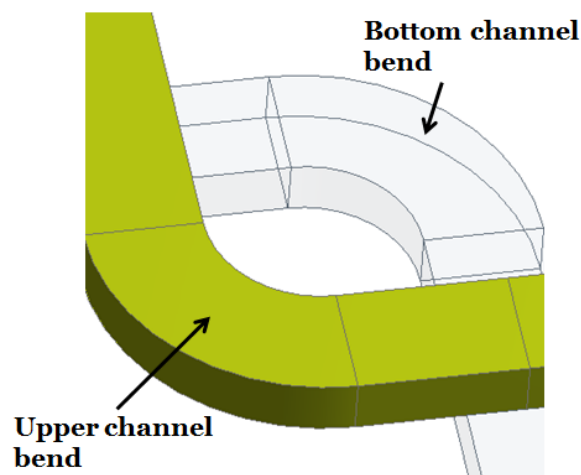
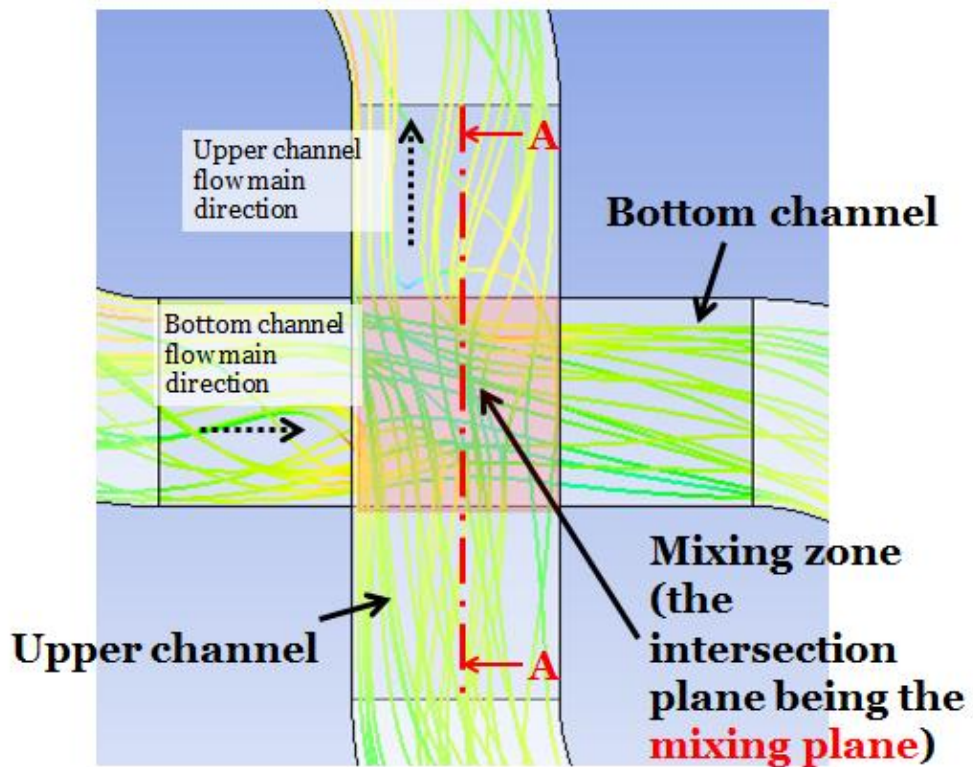


**Figure 2.44 - Bend definition for each pair of channel**

The mixing zone can be thought as the region corresponding to the intersection of the two superposed channels: they can communicate each other through an “open window” called mixing plane. Here mass, momentum and heat transfer are supposed to be strongly enhanced. See Figure 2.45 for visual explanation.



**A-A section**

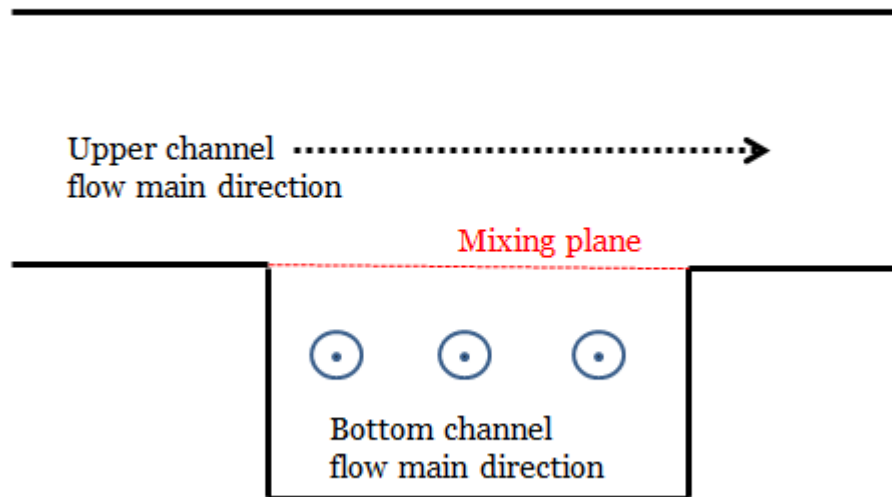


**Figure 2.45 - Mixing zone and mixing plane visualization**

The straight duct links the bends with the mixing zones.

See that mixing zones are supposed to create a strong fluid deformation, resulting in an important secondary motion (i.e. not only led by pressure gradient) in the bend flow. Moreover, since the bend flow itself creates secondary motion (typically Dean vortices),

the actual flow is supposed to be very three-dimensional with a continuous detachment and reattachment of the boundary layer. The complexity of the flow is thought to be responsible for the momentum and heat transfer enhancement, as demonstrated in Section 2.2. This phenomenological description is the objective of the numerical study and validation. It is worth noting that the innovative channel allows a large number of design options in terms of geometrical parameters: for example the designer has to set the half channel cross-section geometry, the proper angle  $\alpha$  with regard to the fluid principal direction (i.e. this corresponds to the chevron angle of a PSHE), the straight duct length  $L$  between two bends, the bend curvature radius  $R$ . While the choice of these three geometrical parameters can be done arbitrarily (and it will be shown in each section of the present work), the half channel cross-section geometry could potentially be of any shape. Anyway, previous studies at CEA<sup>77</sup> shows that the most performing cross-section geometry for a wavy (i.e. PCHE) channel is the squared cross-section. Given this results, an innovative channel should not exceed the PCHE total plate width (which is equal to the PCHE channel hydraulic diameter  $D_h$  plus the structural width  $\epsilon$  between channels), not to lose in compactness already at the concept stage. Therefore the reference half channel cross section for the innovative channel is rectangular, with the shorter side equals to half the longer side. In this way we obtain a final corresponding squared cross-section in the mixing zone, keeping the total plate width. See Figure 2.46 for explanation.

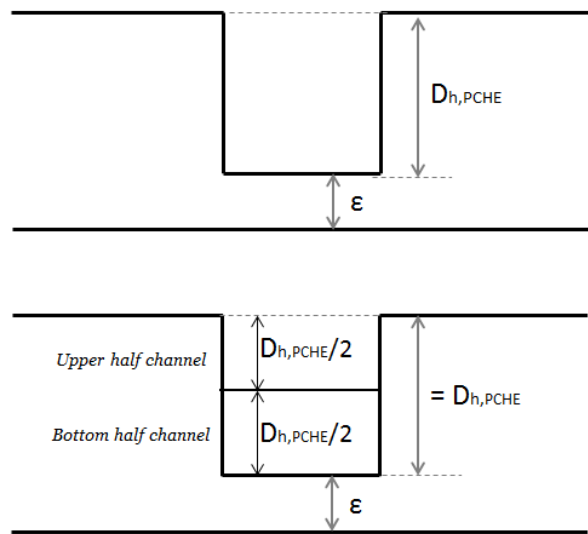


**Figure 2.46 - Innovative channel reference cross-section (bottom figure) compared to the reference PCHE reference cross-section (upper figure)**

See Figure 2.47 showing the geometrical description of the innovative channel:

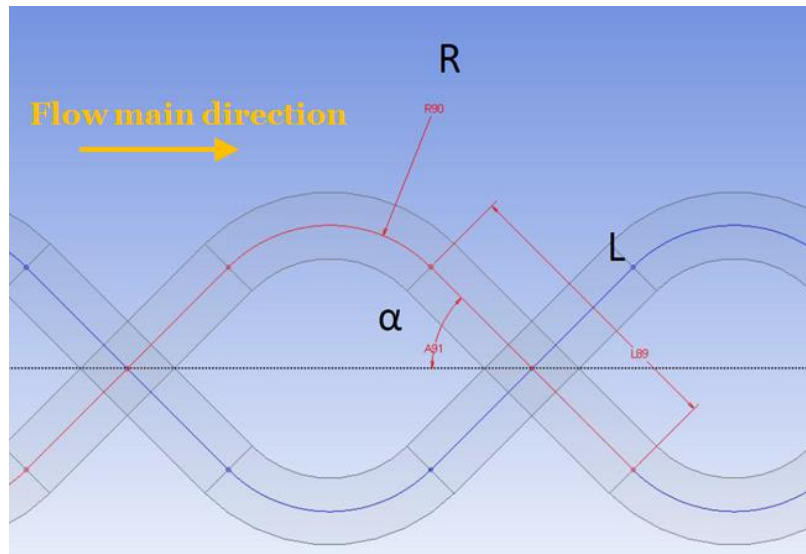


Figure 2.47 - Channel main geometrical parameters

The following sections describe the adopted approaches for the numerical and experimental validation.

## 9.2 NUMERICAL APPROACH

Numerical analysis is an industrial tool which is gaining more and more popularity thank to its capability to provide valuable information without the long and expensive time schedule of an experimental investigation. In this sense it is of primary importance to determine which model can give the most accurate results in terms of physical description of fluid flow.

Section 6 shows a general overview on the modelling approach, in particular on the studied domain and on the turbulence model.

As regards the computed domain, the full plate approach has to be discarded. In fact no precise physical flow description can be achieved, due to the very large domain requiring a coarse mesh to run calculations not too long in time. On the other hand, the Unity Cell approach could potentially be suitable because it allows for using fine local flow description. Nevertheless the boundary condition management is not always straightforward. In conclusion the channel approach seems to be a good compromise between physical description accuracy and computational time. Therefore the first calculations will be run for a single channel like the one show in Figure 2.41. Then, since it does not take into account the inter-channels mixing zones of Figure 2.43, a

wider calculation with a validated model will be run for a multiple channel configuration.

As regards the turbulence model (and remembering that deeper information and motivation will be given in Chapter 3), LES approach is discarded because the needed computational resources would be very costly; in fact, the final goal of our numerical analysis is to have an industrial model able to provide fast and accurate information enough. Hence Reynolds-Averaged Navier-Stokes (RANS) approach is selected. Conclusions of the bibliographic review show that a RANS low-Reynolds number approach (i.e. computation of the fluid flow all the way down to the wall) theoretically provides the most correct information about the fluid flow. In this sense, and considering also the channel geometry, the most adapted turbulence model seems to be a RANS model, specifically an  $\omega$ -based model: in fact it has been extensively shown<sup>78</sup> that this class of models provide better description of flow with adverse pressure gradients (as it could be imagined for the in-bend flow of the innovative channel) with no need of a specific low-Reynolds number modifications as for the  $\varepsilon$ -based models. Moreover it has been also shown in reference<sup>79</sup> that the  $\omega$ -based models better account for near-wall thermal compressibility, i.e. strong temperature gradients in the near wall region and for wall roughness. Therefore, for the present application, the  $\omega$ -based modelling approach will be adopted: Chapter 3 will deeply study the numerical model definition.

### **9.3 EXPERIMENTAL APPROACH**

To validate the numerical model and to prove the design basis for the innovative channel, an experimental database is of primary importance. Literature does not really provide test-cases similar to the innovative channel. In fact, some classical validation test-cases have been identified, but all of them lack in at least one important feature of the innovative channel flow. Chapter 3 will show the list of the identified test-cases with their similarities and differences with the current geometry of interest. Anyway, since no exact validation case is available in literature, an experimental database on the actual geometry is necessary. Measurements of velocities and Reynolds stresses will provide the information needed to a full investigation of the fluid flow phenomena and validation of the adopted numerical model. Chapter 4 will discuss in detail the experimental techniques and facilities employed to meet this fundamental goal.

# Chapitre 3: Définition du modèle numérique

Dans le Chapitre 2, les avantages du modèle RANS basé sur  $\omega$  pour simuler l'écoulement à l'intérieur du canal innovant sont expliqués. En effet, l'intérêt est basé sur le comportement de l'équation de transport de  $\omega$  dans la région de proche paroi. le modèle k- $\omega$ - standard est donc censé donner de meilleurs résultats dans la région de la couche limite, (même pour les écoulements à gradient de pression négatif), ne nécessitant pas de traitement spécifique proche de la paroi. Par conséquent, nous serions amenés à choisir entre un modèle k- $\omega$  à deux équations standard ou bien un modèle de transport des tensions de Reynolds plus sophistiqué. Dans le solveur disponible au laboratoire (ANSYS Fluent ®) il n'y a pas d'autre choix possible si l'on veut effectuer un calcul avec les équations de transport des contraintes de Reynolds basé sur une équation de transport en  $\omega$ . D'autre part, pour les modèles à deux équations on peut choisir entre le modèle k- $\omega$  standard et le modèle SST. Ce dernier gagne de plus en plus de popularité dans les applications industrielles en raison de ses améliorations potentielles par rapport au modèle k- $\omega$ - standard. En fait, l'un des inconvénients connus du modèle k- $\omega$  standard est sa dépendance vis-à-vis des valeurs loin de la paroi des variables transportées, ce qui peut détériorer la solution dans certains cas. En ce sens, un modèle k- $\epsilon$  est beaucoup plus stable que le k- $\omega$ , en fournissant des résultats très robustes, peu importe les valeurs loin de la paroi. Sur la base de ces considérations macroscopiques, le modèle SST associe un modèle k- $\epsilon$  standard dans la veine fluide avec un modèle k- $\omega$  standard dans la couche limite, en utilisant uniquement avantages des deux modèles originaux sans leurs inconvénients. En outre, il peut tenir compte de la relation de Bradshaw dans la couche limite et fournit une solution en limitant la production de l'énergie cinétique de la turbulence. Le choix final est d'utiliser le SST plutôt que le modèle k- $\omega$  standard en raison de ses propriétés bénéfiques potentielles pour résoudre les manques du modèle k- $\omega$  standard.

Le but de cette section est d'étudier le comportement de trois modèles de turbulence basés sur l'équation de transport de  $\omega$ , en utilisant trois approches de modélisation différentes: le modèle à viscosité turbulente isotrope (SST), le modèle Stress Omega de



transport du tenseur de Reynolds et un nouveau modèle à viscosité turbulente non-linéaire nommé ASST. Le modèle ASST, développé sur la base d'hypothèses théoriques, présente la caractéristique avantageuse d'être un modèle pleinement « réalisable », ce qui signifie que les caractéristiques turbulentes parasites et non-physiques sont évitées grâce à des considérations mathématiques et physiques. Le modèle a d'abord été développé pour fonctionner correctement dans la couche limite d'un écoulement cisailé, il a été mis en œuvre dans le solveur via des fonctions définies par l'utilisateur. Enfin, il a été validé par des données expérimentales, avec une comparaison au modèle SST et Stress Omega. Les trois modèles ont des performances identiques pour l'écoulement de canal droit (ayant essentiellement été développés pour un tel écoulement), ne différant que par la capacité à reproduire la turbulence anisotrope. Cela se traduit macroscopiquement par une reproduction correcte des tourbillons de coin dans un conduit droit à section de passage carrée et dans un coude à  $90^\circ$  des modèles ASST et Stress Omega. Des doutes vis-à-vis d'une application plus large du modèle Stress Omega naissent par des résultats inattendus sur les cas tests de la marche descendante et du faisceau de tubes: dans le premier, le modèle stress Omega prédit une longueur de rattachement plus courte que prévue (ce qui est en contradiction avec les résultats de son développeur); dans le second, le modèle Stress Omega échoue dans la région où la vitesse de déformation est élevée, fournissant une forte diminution de la contrainte de cisaillement de paroi par rapport aux mesures expérimentales. Ceci n'est pas cohérent avec sa capacité potentielle à produire des résultats précis pour des écoulements relativement simples. En ce sens, le modèle ASST peut fournir une alternative intéressante, donnant des résultats globaux qui sont au moins aussi bonnes que ceux du modèle Stress Omega. En outre, il conserve un temps de calcul très court, ce qui le positionne pour être un très bon outil industriel pour décrire potentiellement l'écoulement dans le canal innovant.

Aucun des cas tests indiqués ne représentent vraiment la complexité de l'écoulement du canal innovant, qui peut être considéré comme leur combinaison. Par conséquent, cette section identifie clairement la nécessité d'une base de données expérimentale pour l'écoulement dans le canal innovant pour valider le modèle numérique et la performance du motif. L'acquisition de cette base de données est l'objet du chapitre suivant.

# Chapter 3: Numerical Model Definition

## 1. INTRODUCTION

### 1.1 SECTION GOALS AND MOTIVATION

Chapter 2 Section 9.2 stated and explained the interest to use a RANS<sup>VIII</sup> $\omega$ -based model to simulate the flow inside the innovative channel. Indeed the interest is based on the  $\omega$ -transport equation behavior in the near-wall region. Hence we would be led to choose between a two-equation standard  $k$ - $\omega$ -model (i.e. that of Wilcox<sup>80</sup>) and a more sophisticated Reynolds stress transport model (i.e. Wilcox's Stress Omega model<sup>80</sup>). In the available solver (ANSYS Fluent ®) there is no other possible choice if one wants to perform a Reynolds stress transport calculation based on a  $\omega$ -transport equation. On the other hand, for the two equation models the possible choice is between the cited standard  $k$ - $\omega$ -model and the Shear Stress Transport (SST) model<sup>81</sup>. The latter has been gaining more and more popularity in industrial application in the last years due to its potential improvements with regard to the standard  $k$ - $\omega$ -model. In fact, one of the most known negative features of the standard  $k$ - $\omega$ -model is its dependence on the freestream values, which might deteriorate the solution for some cases. In this sense, the standard  $k$ - $\epsilon$  model<sup>82</sup> is much more stable than the  $k$ - $\omega$ -model, providing very robust results, no matter the freestream values. On the other hand, the standard  $k$ - $\omega$ -model is supposed to perform better in the boundary layer region, (even for adverse pressure gradient flows), not needing any specific near-wall treatment. Based on these macroscopic considerations, the SST model blends a standard  $k$ - $\epsilon$  model in the fluid bulk with a standard  $k$ - $\omega$ -model in the boundary layer, using only the positive features of the two original models. Moreover it can take into account the Bradshaw's relation in duct boundary layer and provides a pseudo-realizability condition by limiting the turbulence kinetic energy production. The final choice is to use the SST rather than the standard  $k$ - $\omega$ -model because of its potential beneficial features resolving the lacks of the standard  $k$ - $\omega$ -model. Therefore its mentioned characteristics will be discussed further in the next section.

---

<sup>VIII</sup>Remember that the RANS models uses the Reynolds decomposition of the velocity field i.e. the velocity  $U$  is decomposed as  $U = \bar{U} + u'$ , with  $\bar{U}$  being the average velocity and  $u'$  being the fluctuating velocity.

Anyway it is still necessary to perform a comparative analysis between models. In fact, due to its capability of transporting Reynolds stresses, the Stress Omega is supposed to provide the best overall results. On the other hand, all Reynolds stress transport models suffer a bit poor numerical stability, which (with the higher number of resolved transport equations) explains the success that two-equation models (especially the SST model) still have in industrial applications. In this sense, the approach provided by Non-Linear Eddy Viscosity Models (NLEVM), which try to take into account anisotropic effects by a nonlinear formulation of the Reynolds stress tensor, is very interesting. This results in a very good numerical behavior (the added terms are essentially velocity gradients, which do not increase the computational time so much) and in a potentially better fluid flow description. Obviously there is still the basic lack of the turbulence history, since the turbulence still responds instantaneously to velocity variations.

In the end the aim of this section is to compare the three approaches, trying to investigate their application. Hence a number of test-cases will be identified (based on similarities with the innovative channel flow) and the results of the SST model, the Stress-Omega model and of a new NLEVM will be shown, aiming to identify the best candidate to study the actual innovative channel flow.

## 1.2 SELECTION OF THE PRELIMINARY VALIDATION TEST-CASES

Turbulence model validation is a very wide area. Selection of test-cases is often done to demonstrate the applicability of a specific model to a specific test case. Nevertheless there are a few basic test cases which are fundamental to demonstrate the model consistency. For the current application validation test-cases have been identified trying to take into account both the classical turbulence model validation and verification and the application to the innovative channel. What is of interest for the current innovative channel application is the ability to reproduce the bend and mixing zone flow, where anisotropy and secondary motion are predominant. Table 3.1 shows the list of the chosen test cases, with a brief explanation of the reasons why they have been selected.

Test Case	Reference	Motivation
Channel Flow	Kim et al. (1987) <sup>83</sup> Laufer (1954) <sup>84</sup>	Classical validation test-case; Current application consists in a channel flow
Backward Facing Step	Driver and Seegmiller (1985) <sup>85</sup>	Classical validation test-case; Innovative channel flow jumps over a step when entering in the mixing zone.

<b>Developing Flow in a 90° bend</b>	Taylor et al. <sup>103</sup>	Innovative channel is composed by bends; The flow entering in the bends cannot be considered as fully developed due to the mixing zones.
<b>Secondary motion of the second type in a duct of square cross section</b>	Huser and Biringen (1993) <sup>86</sup>	Turbulence-driven anisotropy and secondary motion.
<b>Secondary Motion in Tight Lattice Rod Bundle</b>	Mantlik et al.(1976) <sup>87</sup>	Secondary motion.

**Table 3.1 - List of selected validation test cases**

## 2. TURBULENCE MODELS USED

### 2.1 THE SHEAR STRESS TRANSPORT (SST) MODEL

The Shear Stress Transport (SST) model has been proposed by Menter<sup>81</sup>.

The baseline of an isotropic model is the Boussinesq approximation, i.e.  $\rho \overline{u_i u_j} = \frac{2}{3} \rho k - \mu_t S_{ij}$ .

Transport equations of the turbulent variables (the turbulence kinetic energy  $k$  and the specific dissipation rate  $\omega$ ) for an incompressible flow are:

$$\begin{aligned} \frac{\partial}{\partial t}(\rho k) + \frac{\partial}{\partial x_j}(\rho k u_j) &= \frac{\partial}{\partial x_j} \left[ \left( \mu + \frac{\mu_t}{\sigma_k} \right) \frac{\partial k}{\partial x_j} \right] + \\ &+ \widetilde{G_k} - \rho \beta^* k \omega \quad (1) \end{aligned}$$

$$\begin{aligned} \frac{\partial}{\partial t}(\rho \omega) + \frac{\partial}{\partial x_j}(\rho \omega u_j) &= \frac{\partial}{\partial x_j} \left[ \left( \mu + \frac{\mu_t}{\sigma_\omega} \right) \frac{\partial \omega}{\partial x_j} \right] + \\ &+ G_\omega - \rho \beta \omega^2 + D_\omega \quad (2) \end{aligned}$$

The turbulent Prandtl numbers for  $k$  and  $\omega$  are expressed in the following way:

$$\sigma_k = \frac{1}{\frac{F_1}{\sigma_{k,1}} + \frac{(1-F_1)}{\sigma_{k,2}}} \quad (3) \quad \sigma_\omega = \frac{1}{\frac{F_1}{\sigma_{\omega,1}} + \frac{(1-F_1)}{\sigma_{\omega,2}}} \quad (4)$$

The function  $F_1$  is computed as:

$$F_1 = \tanh(\phi_1^4), \quad (5)$$

$$\phi_1 = \min \left[ \max \left( \frac{\sqrt{k}}{0.09\omega y}, \frac{500\mu}{\rho y^2 \omega} \right), \frac{4\rho k}{\sigma_{\omega,2} D_{\omega}^+ y^2} \right] \quad (6)$$

$$D_{\omega}^+ = \max \left[ 2\rho \frac{1}{\sigma_{\omega,2}} \frac{1}{\omega} \frac{\partial k}{\partial x_j} \frac{\partial \omega}{\partial x_j}, 10^{-10} \right] \quad (7)$$

The turbulence kinetic energy production term in the SST models has a limiter, which provides a pseudo-realizability as expressed by Durbin<sup>88</sup>. The limiter is defined as:

$$\widetilde{G_k} = \min(G_k, 10\rho\beta^*k\omega) \quad (8)$$

Where  $G_k$  is given by Eq.42.

The specific dissipation rate production is given by:

$$G_{\omega} = \frac{\rho\alpha}{\mu_t} \widetilde{G_k}, (23) \alpha = F_1\alpha_{\infty,1} + (1 - F_1)\alpha_{\infty,2}, (9)$$

$$\alpha_{\infty,1} = \frac{\beta_{i,1}}{\beta^*} - \frac{\kappa^2}{\sigma_{\omega,1}\sqrt{\beta^*}}, (10)$$

$$\alpha_{\infty,2} = \frac{\beta_{i,2}}{\beta^*} - \frac{\kappa^2}{\sigma_{\omega,2}\sqrt{\beta^*}} (11)$$

The coefficient  $\beta$  is expressed by:

$$\beta = F_1\beta_{i,1} + (1 - F_1)\beta_{i,2} \quad (12)$$

The Cross-Diffusion term  $D_{\omega}$  is expressed as follows:

$$D_{\omega} = 2(1 - F_1)\rho \frac{1}{\sigma_{\omega,2}} \frac{1}{\omega} \frac{\partial k}{\partial x_j} \frac{\partial \omega}{\partial x_j} \quad (13)$$

Finally the model is closed by the definition of the eddy viscosity:

$$\mu_t = \frac{\rho k}{\omega} \frac{1}{\max\left[1, \frac{S^* F_2}{a_1 \omega}\right]} \quad (14)$$

$$F_2 = \tanh(\phi_2^2), (15) \phi_2 = \max\left(\frac{2\sqrt{k}}{0.09\omega y}, \frac{500\mu}{\rho y^2 \omega}\right) \quad (16)$$

$S^*$  is the modulus of the strain rate tensor, i.e.

$$S^* = \left(\frac{1}{2} S_{ij} S_{ij}\right)^{1/2} \quad (17)$$

$$\text{Where } S_{ij} = \left(\frac{\partial U_i}{\partial x_j} + \frac{\partial U_j}{\partial x_i}\right).$$

The eddy viscosity formulation presents two terms: one is the standard High-Re eddy viscosity formulation, i.e.  $\mu_t = \frac{\rho k}{\omega}$ . The second one is based on Bradshaw's assumption in boundary layer, i.e.  $\tau = -\rho \overline{u'v'} = a_1 \rho k$ . Since the Reynolds stress in a boundary layer is:  $\tau = -\rho \overline{u'v'} = \mu_t S^*$  it results the Eq.14. Note that the modulus of the strain rate tensor has been chosen as the generalized velocity gradient. As the  $F_1$  function, the  $F_2$  function blends the High-Re and the boundary layer formulation of the eddy viscosity.

Finally, model constants are:

$$\sigma_{k,1} = 1.176, \sigma_{k,2} = 1.0, \sigma_{\omega,1} = 2.0, \sigma_{\omega,2} = 1.168, \beta^* = 0.09, a_1 = 0.31, \\ \beta_{i,1} = 0.075, \beta_{i,2} = 0.0828.$$

## 2.2 THE STRESS OMEGA REYNOLDS STRESS MODEL

The Stress Omega model<sup>80</sup>, it is based on Reynolds stress transport equations (18) and on the  $\omega$  transport equation (2) without the term  $D_\omega$ .

$$\frac{\partial}{\partial t} (\rho \overline{u_i' u_j'}) + \frac{\partial}{\partial x_k} (\rho u_k \overline{u_i' u_j'}) = \frac{\partial}{\partial x_k} \left[ \left( \mu + \frac{\mu_t}{\sigma_k} \right) \frac{\partial}{\partial x_k} (\overline{u_i' u_j'}) \right] + \\ - \rho \left( \overline{u_i' u_k} \frac{\partial u_j}{\partial x_k} + \overline{u_j' u_k} \frac{\partial u_i}{\partial x_k} \right) + \phi_{ij} + \varepsilon_{ij} \quad (18)$$

$$\text{Where } \varepsilon_{ij} = \frac{2}{3} \delta_{ij} \rho \beta^* k \omega$$

In particular the different pressure-strain formulation is modelled as the sum of the slow pressure-strain  $\phi_{ij,1}$  and a rapid pressure-strain term  $\phi_{ij,2}$ :

$$\phi_{ij} = \phi_{ij,1} + \phi_{ij,2} \quad (19)$$

Where:

$$\begin{aligned} \phi_{ij} = & -C_1 \rho \beta_{RSM}^* \omega \left[ \overline{u_i' u_j'} - \frac{2}{3} \delta_{ij} k \right] + \\ & -\hat{\alpha}_0 \left[ P_{ij} - \frac{1}{3} P_{kk} \delta_{ij} \right] - \hat{\beta}_0 \left[ D_{ij} - \frac{1}{3} D_{kk} \delta_{ij} \right] + \\ & -k \hat{\gamma}_0 \left[ S_{ij} - \frac{1}{3} S_{kk} \delta_{ij} \right] \end{aligned} \quad (20)$$

The Buoyancy and System Rotation Productions have always been neglected, since no system rotation has been identified and buoyancy is not supposed to play a major role since no high temperature gradients are identified for the test cases shown in Table 3.1.

## 2.3 THE ANISOTROPIC SHEAR STRESS TRANSPORT (ASST) MODEL

### 2.3.1 Model Background and Formulation

In the last decades Non-Linear Eddy Viscosity models received a great deal of attention due to their performance with regard to traditional Eddy Viscosity models and the minor extra computation cost necessary to produce accurate results. Table 3.2 shows some of the better-known NLEV models proposed:

Reference	Non-Linear approximation order	Underlying model
Speziale <sup>89</sup>	2 <sup>nd</sup>	k-ε / k-kl
Shih, Zhou, Lumley <sup>90</sup>	2 <sup>nd</sup>	k-ε
Craft, Launder, Suga <sup>91</sup>	3 <sup>rd</sup>	k- $\tilde{\epsilon}$
Hellsten and Laine <sup>92</sup>	3 <sup>rd</sup>	k-ε / k-ω BSL

<b>Wallin, Johansson<sup>93</sup></b>	3 <sup>rd</sup>	k-ε / k-ω
<b>Menter, Garbaruk, Egorov<sup>94</sup></b>	3 <sup>rd</sup>	k-ω BSL

**Table 3.2—Examples of non-linear eddy viscosity models**

All of them use a polynomial approximation to express the anisotropy tensor  $a_{ij} = \frac{\overline{u'_i u'_j}}{k} - \frac{2}{3} \delta_{ij}$  according to the Caley-Hamilton theorem. The main differences lie in the formulation of the closure coefficients (which are either constants or general functions of the non-dimensional deformation or rotation rate) and in the non-linear approximation order. In particular, Craft et al.<sup>91</sup> and Wallin and Johansson<sup>93</sup> showed that the third order terms are directly responsible for the correct description of rotating system effects.

Given the success they obtained in modeling complex flows, an innovative Anisotropic Shear Stress Transport (ASST) model is developed and implemented into the solver: it will be shown to produce very trustful results for a large variety of flow and applications. See that, since rotation effects are negligible for many channel flow industrial applications and for the innovative channel flow (still there are applications where they are of primary importance, i.e. turbomachinery), the present model presents a 2<sup>nd</sup> order approximation of the anisotropy tensor. The development of higher order terms would be necessary for future improvement of the model itself.

The underline of the Non-Linear Eddy Viscosity Model is to express the Reynolds Stress tensor  $\tau_{ij}$  in a nonlinear polynomial form:

$$\rho \tau_{ij} = \rho \overline{u'_i u'_j} = \rho k \left( a_{ij} + \frac{2}{3} \delta_{ij} \right) \quad (21)$$

As already mentioned, the anisotropy tensor  $a_{ij}$  and hence the Reynolds stress tensor  $\rho \overline{u'_i u'_j}$  can be expressed according to the Caley-Hamilton theorem. Following the approach of Shih et al.<sup>90</sup>, the normalized Reynolds stress tensor can be expressed as (up to second order terms):

$$\begin{aligned} \frac{\overline{u'_i u'_j}}{2k} = & \frac{1}{3} \delta_{ij} + \beta_0 \tau \left( U_{i,j} + U_{j,i} - \frac{2}{3} U_{i,i} \delta_{ij} \right) + \beta_1 \tau^2 \left( U_{i,k} U_{k,j} + U_{j,k} U_{k,i} - \frac{2}{3} U_{i,j} U_{j,i} \delta_{ij} \right) \\ & + \beta_2 \tau^2 \left( U_{i,k} U_{j,k} - \frac{1}{3} U_{i,j} U_{i,j} \delta_{ij} \right) + \beta_3 \tau^2 \left( U_{k,i} U_{k,j} - \frac{1}{3} U_{i,j} U_{i,j} \delta_{ij} \right) \quad (22) \end{aligned}$$



Where  $U_{i,j} = \frac{\partial U_i}{\partial x_j}$ ,  $\tau$  being the turbulent time scale, usually defined, for an  $\omega$ -based model, as  $\tau = \frac{1}{\beta^* \omega}$  and  $\beta^* = 0.09$ .

To properly account for Realizability, i.e. the mathematical and physical principle that imposes non-negative value of the principal Reynolds stresses  $\overline{u'_i u'_i}$ , we study model's behavior for basic flows. Consider a pure strain flow where the deformation rate tensor is as follows:

$$\begin{pmatrix} \frac{\partial U}{\partial x} & 0 & 0 \\ 0 & \frac{\partial V}{\partial y} & 0 \\ 0 & 0 & 0 \end{pmatrix} = \begin{pmatrix} U_{1,1} & 0 & 0 \\ 0 & U_{2,2} & 0 \\ 0 & 0 & 0 \end{pmatrix}$$

Because of continuity for incompressible flow, it results that  $U_{2,2} = -U_{1,1}$ . The  $\overline{u'_1 u'_1}$  normalized Reynolds stress is:

$$\frac{\overline{u'_1 u'_1}}{2k} = \frac{1}{3} + 2\beta_0 \tau U_{1,1} + \frac{1}{3} (2\beta_1 + \beta_2 + \beta_3) (\tau U_{1,1})^2 \quad (23)$$

Defining the non-dimensional strain rate  $S = \tau \left( \frac{1}{2} S_{ij} S_{ij} \right)^{1/2}$  write

$$\frac{\overline{u'_1 u'_1}}{2k} = \frac{1}{3} + \beta_0 S + \frac{1}{3} (2\beta_1 + \beta_2 + \beta_3) S^2 \quad (24)$$

To ensure positive values of the principal Reynolds stress, the following conditions must hold:

1.  $\frac{\overline{u'_1 u'_1}}{2k} > 0$  if  $0 < S < \infty$
2.  $\frac{\overline{u'_1 u'_1}}{2k} \rightarrow 0$  if  $S \rightarrow \infty$
3.  $\left( \frac{\overline{u'_1 u'_1}}{2k} \right)_{,S} \rightarrow 0$  if  $S \rightarrow \infty$

The can be satisfied in various way. Shit et al.<sup>90</sup> propose:

- $2\beta_0 = -\frac{2/3}{A_1 + S}$
- $2\beta_1 = \frac{C_{\tau 1}}{f(S)}$
- $2\beta_2 = \frac{C_{\tau 2}}{f(S)}$
- $2\beta_3 = \frac{C_{\tau 3}}{f(S)}$

In the easiest version,  $f(S)$  has a polynomial form of  $S$ , which order is higher than two. Shih et al.<sup>90</sup> propose:

$$f(S) = A_2 + S^3 \quad (25)$$

To ensure full realizability, the adjustable constants must satisfy the following relations:

- $A_1 > 0$ ;
- $A_2 > 0$ ;
- $2C_{\tau 1} + C_{\tau 2} + C_{\tau 3} > 0$ .

Shih et al.<sup>90</sup> affirm that the sale previous three conditions can be found also by applying realizability conditions on a three-dimensional pure strain rate tensor.

To find further realizability constraints consider a pure shear flow (i.e. fully developed channel flow) with a deformation rate tensor as follows:

$$\begin{pmatrix} 0 & \frac{\partial U}{\partial y} & 0 \\ 0 & 0 & 0 \\ 0 & 0 & 0 \end{pmatrix} = \begin{pmatrix} 0 & U_{1,2} & 0 \\ 0 & 0 & 0 \\ 0 & 0 & 0 \end{pmatrix}$$

In this case it results that:

$$\frac{\overline{u'_1 u'_1}}{2k} = \frac{1}{3} + \frac{S^2}{6(A_2 + S^3)} (2C_{\tau 2} - C_{\tau 3}) \quad (26)$$

$$\frac{\overline{u'_2 u'_2}}{2k} = \frac{1}{3} + \frac{S^2}{6(A_2 + S^3)} (2C_{\tau 3} - C_{\tau 2}) \quad (27)$$

$$\frac{\overline{u'_3 u'_3}}{2k} = \frac{1}{3} - \frac{S^2}{6(A_2 + S^3)} (C_{\tau 2} + C_{\tau 3}) \quad (28)$$

$$\frac{\overline{u'_1 u'_2}}{2k} = -\frac{S}{3(A_1 + S)} \quad (29 =$$

Since experiments show that  $\frac{\overline{u'_2 u'_2}}{2k} < \frac{1}{3} < \frac{\overline{u'_1 u'_1}}{2k}$ <sup>IX</sup>, following relation must hold:

$$C_{\tau 2} > 2C_{\tau 3}$$

Note that the adjustable coefficients have to be determined by tuning the model on test cases. In particular see that the  $\beta_0$  coefficient is somehow similar to the  $C_\mu$  coefficient of the eddy viscosity formulation if we couple the anisotropic formulation to a k- $\epsilon$  model:

$$C_\mu = -2\beta_0 = \frac{\frac{2}{3}}{A_1 + S} \quad (30)$$

---

<sup>IX</sup>For example, for a boundary layer it results that  $u':v':w'=4:2:3$ . Hence  $u'^2:v'^2:w'^2=16:4:9$  and  $u'^2/2k=16/29>1/3$ , while  $v'^2/2k=4/29<1/3$

First of all see that in the original High-Re versions of the model (that were coupled with a standard k- $\varepsilon$  model),  $C_\mu$  coefficient in the eddy viscosity definition was actually employed: for example in reference<sup>95</sup>:

$$C_\mu = \frac{2/3}{3.9 + S} \quad (31)$$

Where coefficient  $A_1 = 3.9$  is used to obtain  $C_\mu = 0.09$  for an equilibrium boundary layer, where  $S=3.5$ . For a  $\omega$ -based model the value of such a  $C_\mu$  coefficient is rather equal to one (since the  $\beta^* = C_\mu$  value is taken into account in the  $\omega$  definition): hence, to be consistent with the original model, the  $C_\mu$  formulation must be divided by  $\beta^{*X}$  to obtain:

$$C_\mu = \frac{7.4}{A_1 + S} \quad (32)$$

and an eddy viscosity formulation of the following type:

$$\mu_t = \rho C_\mu \frac{k}{\omega} \quad (33)$$

As it will be shown in next section, the value of the  $A_1$  coefficient has been raised a bit up to  $A_1 = \frac{110}{27} = 4.074$ .

It can be demonstrated that the Reynolds stress formulation in Eq.22 can be written in an equivalent way as (see Appendix B):

$$\begin{aligned} \rho \overline{u_i u_j} = & \frac{2}{3} \rho k \delta_{ij} - \mu_t S_{ij} + \rho C_1 k \tau^2 \left( S_{ik} S_{kj} - \frac{1}{3} \delta_{ij} S_{kl} S_{kl} \right) \\ & + \rho C_2 k \tau^2 \left( \Omega_{ik} \Omega_{kj} - \frac{1}{3} \delta_{ij} \Omega_{kl} \Omega_{kl} \right) + \rho C_3 k \tau^2 (\Omega_{ik} S_{kj} + \Omega_{jk} S_{ki}) \end{aligned} \quad (34)$$

Where  $S_{ij} = \left( \frac{\partial U_i}{\partial x_j} + \frac{\partial U_j}{\partial x_i} \right)$ ,  $\Omega_{ij} = \left( \frac{\partial U_i}{\partial x_j} - \frac{\partial U_j}{\partial x_i} \right)$  and

$$C_1 = \frac{C_{NL1}}{(C_{NL4} + C_{NL5} \cdot S^3)} \quad (35)$$

$$C_2 = \frac{C_{NL2}}{(C_{NL4} + C_{NL5} \cdot S^3)} \quad (36)$$

$$C_3 = \frac{C_{NL3}}{(C_{NL4} + C_{NL5} \cdot S^3)} \quad (37)$$

---

<sup>x</sup> Always remember that  $\omega = \frac{\varepsilon}{\beta^* k}$  and  $\frac{k}{\varepsilon} = \frac{1}{\beta^* \omega}$  hence there is always a factor equal to  $\beta^*$  between an  $\varepsilon$ -based and an  $\omega$ -based formulation.

Hence, hereafter, the choice is to use the second formulation, since it is easier to understand and to deal with.

It is worth noting that values of the unknown coefficients in Table 3.3, which have been found by tuning the model on a number of test cases:

Model coefficients	Shish et al. <sup>90</sup>	Baglietto et al. <sup>95</sup>
$C_{NL1}$	0.75	0.8
$C_{NL2}$	3.75	11
$C_{NL3}$	4.75	4.5
$C_{NL4}$	1000	1000
$C_{NL5}$	1.0	1.0

**Table 3.3 -- NLEVM closure coefficient in reference<sup>90</sup> and <sup>95</sup>**

As shown in Table 3.3, the major model improvement in reference<sup>95</sup> is the increased value of the  $C_{NL2}$  coefficient, which has been increased from a value of 3.75 to 11 to better represent the scale of the secondary motion. In fact, as reported by Baglietto et al., the  $C_{NL1}$  coefficient multiplies pure strain terms, which are responsible to restore flow isotropy. On the other hand, the  $C_{NL3}$  coefficient multiplies pure rotation terms, which do not act on originally isotropic turbulence. Hence, the  $C_{NL2}$  coefficient is the only one which is capable to take into account secondary flow anisotropies, where strain and rotation occur at the same time. We will discuss further about this in paragraph 3.5. For the present model, we will retain coefficients of reference<sup>95</sup>, as shown in Table 3.4:

Model Coefficients	Shish et al. <sup>90</sup>	Baglietto et al. <sup>95</sup>	ASST
$C_{NL1}$	0.75	0.8	0.8
$C_{NL2}$	3.75	11	11
$C_{NL3}$	4.75	4.5	4.5
$C_{NL4}$	1000	1000	1000
$C_{NL5}$	1.0	1.0	1.0

**Table 3.4 - NLEVM closure coefficient in present ASST model**

Anyway it is interesting to retain the Bradshaw's assumption related limitations of the original SST model, since it is supposed to provide very good results for adverse pressure gradient flows. Remember that the Bradshaw's assumption states that in boundary layers there is a linear relation between the principal turbulent shear stress and the turbulent kinetic energy, i.e.  $\tau = -\rho \overline{u'v'} = a_1 \rho k$  for a flat plate channel flow. It is

worth noting however that for a NLEVM there is a difference in the formulation of the Reynolds Stress, i.e. it depends on the quadratic velocity gradient:

$$\tau = -\rho \overline{u'v'} \propto \mu_t S^* - \rho C_1 k S^{*2} - \rho C_2 k S^{*2} - \rho C_3 k S^{*2} \quad (38)$$

Where the modulus of the strain rate tensor  $S^* = \left(\frac{1}{2} S_{ij} S_{ij}\right)^{1/2}$  is chosen again as the generalized velocity gradient, as in Menter et al.<sup>81</sup>. Hence, a formally correct geometry independent eddy viscosity formulation should be:

$$\mu_t = \frac{\rho(a_1 k + C_1 k S^{*2} + C_2 k S^{*2} + C_3 k S^{*2})}{S^*} = \frac{\rho B}{S^*} \quad (39)$$

The introduced correction is supposed to correctly take into account the constant ratio of the principal turbulent Reynolds stress to the turbulent kinetic energy in important range of boundary layer flows<sup>96</sup>. In fact there is no modification of the Bradshaw relation in simple shear flows by the second order terms:

$$\begin{aligned} \frac{\tau}{\rho} &= a_1 k = \nu_t \frac{\partial U}{\partial y} - \beta_1 (S_{xx} S_{xy} + S_{xy} S_{yy} + S_{xz} S_{zy}) + \\ &- \beta_2 (O_{xx} S_{xy} + O_{xy} S_{yy} + O_{xz} S_{zy} + O_{xy} S_{xx} + O_{yy} S_{yx} + O_{yz} S_{zx}) + \\ &- \beta_3 (O_{xx} O_{yx} + O_{xy} O_{yy} + O_{xz} O_{yz}) = \nu_t \frac{\partial U}{\partial y} \quad (40) \end{aligned}$$

Second order terms do not act, since all other terms but  $S_{xy} = \frac{\partial U}{\partial y}$  are equal to zero.

However, this is not the case for complex geometries, where non-zero values of the second order velocity gradients cannot be a priori excluded. Therefore the generalized formulation given by Eq.39 provides the right first and second velocity gradient scale thanks to the use of the modulus of the strain rate tensor.

Given the previous considerations, the proposed eddy viscosity formulation taking into account the realizability condition (i.e. strain-dependent eddy viscosity in the High-Re region) and the Bradshaw relation in boundary layers is:

$$\mu_t = \frac{\rho B}{\max\left[\frac{B\omega}{C_\mu k}, F_2 S^*\right]} \quad (41)$$

Where the  $F_2$  function is the same as the SST model.

The model is closed through the  $k$  and  $\omega$  transport equations:

$$\frac{\partial}{\partial t}(\rho k) + \frac{\partial}{\partial x_j}(\rho k u_j) = \frac{\partial}{\partial x_j} \left[ \left( \mu + \frac{\mu_t}{\sigma_k} \right) \frac{\partial k}{\partial x_j} \right] + \widetilde{G}_k - \rho \beta^* k \omega \quad (1)$$

$$\frac{\partial}{\partial t}(\rho \omega) + \frac{\partial}{\partial x_j}(\rho \omega u_j) = \frac{\partial}{\partial x_j} \left[ \left( \mu + \frac{\mu_t}{\sigma_\omega} \right) \frac{\partial \omega}{\partial x_j} \right] + G_\omega - \rho \beta \omega^2 + D_\omega \quad (2)$$

Finally, to be consistent with the NLEV formulation, the turbulence kinetic energy production term can be expressed in the proper form:

$$G_k = -\rho \overline{u_i u_j} \frac{\partial U_i}{\partial x_j} \quad (42)$$

Note that, due to the realizability condition given by the eddy viscosity modification and the model coefficient expressions, no turbulence kinetic energy production limiter is needed.

Finally the specific dissipation rate is expressed in the original form i.e.

$$G_\omega = \frac{\rho \alpha}{\mu_t} G_k \quad (43)$$

The other parameters not mentioned so far maintains the same definition as the original SST model formulation. Closure constants are:

$$\begin{aligned} \sigma_{k,1} &= 1.176, & \sigma_{k,2} &= 1.0, & \sigma_{\omega,1} &= 2.0, & \sigma_{\omega,2} &= 1.168, \\ \beta^* &= 0.09, & \alpha_1 &= 0.31, & \beta_{i,1} &= 0.075, & \beta_{i,2} &= 0.0828 \end{aligned}$$

### 2.3.2 Logarithmic layer model analysis

To justify the fact that no SST model closure coefficient has been changed in the ASST formulation, we will show that the latter does not impact on the logarithmic layer of the law of the wall. Remember that the only coefficient Menter changed from the original k- $\omega$  is the  $\sigma_{k,1}$  coefficient in order to recover the correct behavior for a flat plate boundary layer. Remember that original k and  $\omega$  equations are satisfied in the logarithmic region by the following solutions (see Wilcox<sup>80</sup>):

$$u = \frac{u_\tau}{\kappa} \ln \left[ \frac{u_\tau y}{\nu} \right] + C \quad (44)$$

$$k = \frac{u_\tau^2}{\sqrt{\beta^*}} \quad (45)$$

$$\omega = \frac{u_\tau}{(\sqrt{\beta^*} \kappa y)} \quad (46)$$

Where  $C$  is a constant and  $\kappa$  is the von Karman constant.

It is worth studying the eddy viscosity solution first, since it has been modified by the new ASST formulation with respect to the original SST formulation. In fact, as already mentioned, in the original SST model, the eddy viscosity solution in the log-layer is<sup>XI</sup>:

$$v_t = \min\left(\frac{a_1 k}{S^*}, \frac{k}{\omega}\right) \quad (47)$$

Since  $S^* = \frac{\partial U}{\partial y} = \frac{u_\tau}{\kappa y}$  for simple shear flow log-layer, write:

$$v_t = \min\left(a_1 \frac{u_\tau^2 \kappa y}{\sqrt{\beta^*} u_\tau}, \frac{u_\tau^2 \sqrt{\beta^*} \kappa y}{\sqrt{\beta^*} u_\tau}\right) = \min\left(\frac{a_1}{\sqrt{\beta^*}} u_\tau \kappa y, u_\tau \kappa y\right) \quad (48)$$

The value  $\frac{a_1}{\sqrt{\beta^*}} = 1.03$  let us affirm that it is the formulation based on the high-Re version of the eddy viscosity solution is used in a shear flow log-layer. For the ASST model the  $C_\mu$  modification has to been taken into account:

$$v_t = \min\left(\frac{a_1 k}{S^*}, C_\mu \frac{k}{\omega}\right) = \min\left(\frac{a_1 k}{S^*}, \frac{7.4}{A_1 + S} \frac{k}{\omega}\right) \quad (49)$$

See that the secondary order terms in the Bradshaw's assumption has not been modified, since it has already been demonstrated how they act only on complex geometry flows. Hence:

$$\begin{aligned} v_t &= \min\left(a_1 \frac{u_\tau^2 \kappa y}{\sqrt{\beta^*} u_\tau}, \frac{7.4}{A_1 + \frac{1}{\beta^*} \frac{\sqrt{\beta^*} \kappa y}{u_\tau} \frac{u_\tau}{\kappa y}} \frac{u_\tau^2 \sqrt{\beta^*} \kappa y}{\sqrt{\beta^*} u_\tau}\right) = \\ &= \min\left(\frac{a_1}{\sqrt{\beta^*}} u_\tau \kappa y, \frac{7.4}{A_1 + \frac{1}{0.3}} u_\tau \kappa y\right) \quad (50) \end{aligned}$$

To keep the same behavior as the original SST model, it must be:

---

<sup>XI</sup> The hypothesis  $F_2=1$  has been made, since we are inside the boundary layer.

$$\frac{7.4}{A_1 + \frac{1}{0.3}} u_\tau \kappa y = u_\tau \kappa y \rightarrow \frac{7.4}{A_1 + \frac{1}{0.3}} = 1 \rightarrow A_1 = \frac{110}{27} \quad (51)$$

Hence we have the final ASST eddy viscosity solution in a logarithmic layer:

$$= \min(1.0\bar{3}u_\tau \kappa y, u_\tau \kappa y) \quad (52)$$

Therefore we can conclude that the anisotropic formulation has been tuned not to change SST model behavior with regard to eddy viscosity formulation in the log-layer. By the way, see how the difference between the value of the  $A_1$  coefficient in the Baglietto et al.<sup>95</sup> and in the present version is around 4.5%. However, this difference is supposed to play a fairly important role, since it restores the correct SST boundary layer behavior for the ASST formulation.

In the logarithmic layer of a simple shear flow the momentum,  $k$  and  $\omega$  equations reduce respectively to:

$$0 = \frac{\partial}{\partial y} \left[ v_t \frac{\partial U}{\partial y} \right] \quad (53)$$

$$0 = v_t \left[ \frac{\partial U}{\partial y} \right]^2 - \beta^* \omega k + \frac{1}{\sigma_{k,2}} \frac{\partial}{\partial y} \left[ v_t \frac{\partial k}{\partial y} \right] \quad (54)$$

$$0 = \alpha \left[ \frac{\partial U}{\partial y} \right]^2 - \beta \omega^2 + \frac{1}{\sigma_{\omega,2}} \frac{\partial}{\partial y} \left[ v_t \frac{\partial \omega}{\partial y} \right] \quad (55)$$

Which are the same formulations as the standard SST model and where the solutions given by (39) to (41) are still valid. To demonstrate that Equations (53) to (55) are the log-layer equations for the ASST model as well, note that the eddy viscosity solutions does not change, as already demonstrated. Moreover, only the turbulence kinetic energy production term (and hence the specific eddy dissipation production term) have been modified in the  $k$  and  $\omega$  transport equations with regard to those of the SST model. Hence, if there was a difference, it would be in such two terms. Indeed the second order terms never appear, since in the simple shear flow only one principal velocity component  $U$  is present and only gradients along the  $y$  direction (normal to velocity) are



allowed. Therefore, in the logarithmic layer the turbulent kinetic energy production terms is:

$$\begin{aligned} \frac{G_k}{\rho} = & -\overline{u_i u_j} \frac{\partial U_i}{\partial x_j} = -\overline{uv} \frac{\partial U}{\partial y} = - \left[ -\nu_t \frac{\partial U}{\partial y} + \beta_1 (S_{xx} S_{xy} + S_{xy} S_{yy} + S_{xz} S_{zy}) + \right. \\ & + \beta_2 (O_{xx} S_{xy} + O_{xy} S_{yy} + O_{xz} S_{zy} + O_{xy} S_{xx} + O_{yy} S_{yx} + O_{yz} S_{zx}) + \\ & \left. + \beta_3 (O_{xx} O_{yx} + O_{xy} O_{yy} + O_{xz} O_{yz}) \right] \frac{\partial U}{\partial y} = \nu_t \left[ \frac{\partial U}{\partial y} \right]^2 \quad (56) \end{aligned}$$

Again, second order terms do not appear in the final formulation, since all other terms but  $S_{xy} = \frac{\partial U}{\partial y}$  are equal to zero.

If the  $G_k$  term does not change, so it does the  $G_\omega$ , since the two are related by multiplying coefficient. Hence it is easily verified that no added term is present and that the ASST acts exactly like the SST model in the logarithmic boundary layer. This is consistent with the fact that the non-linear terms are not supposed to influence the flow main characteristics for simple shear flow cases, but only to act on flow anisotropy. This will be further shown in the next section, where the analysis of a channel flow boundary layer is presented.

## 2.4 THERMAL MODELLING APPROACH

Aiming to build a solid numerical model to study the innovative channel thermal-hydraulic performance, the thermal modelling approach has to be faced. In fact, if the pure aerodynamic model can already improve the flow thermal description, still there is the problem of how to model the turbulent heat flux for a complex flow.

In this context, the simplest modelling approach is to use a Simple Gradient Diffusion Hypothesis (SGDH) model. It consists of modelling the turbulent heat flux  $\overline{u'_i \theta'}$  with the same approach as the linear eddy viscosity models, i.e. with a formal dependence on the temperature gradient.

$$\overline{u'_i \theta'} = - \frac{\nu_t}{\sigma_t} \frac{\partial \Theta}{\partial x_i} \quad (57)$$

The temperature  $T$  is decomposed as for the Reynolds decomposition  $T = \Theta + \theta'$ , with  $\Theta$  being the average temperature and  $\theta'$  being the fluctuating temperature. The  $\sigma_t$  is the

turbulent Prandtl number<sup>XII</sup>, which is assumed to be constant and equal to 0.85 in the fluid bulk. In the near-wall region (laminar and logarithmic layer) its value is a bit higher (around 1.1<sup>97</sup>).

A finer modelling strategy uses the Generalized Gradient Diffusion Hypothesis (GGDH) proposed by Daly and Harlow<sup>98</sup>. They propose the following expression to evaluate turbulent scalar fluxes:

$$\overline{u'_i \theta'} = -C \frac{1}{\beta^* \omega} \overline{u'_i u'_j} \frac{\partial \Theta}{\partial x_j} \quad (58)$$

Where C is a constant usually equal to 0.15.

The used solver ANSYS Fluent ® only provides a default SSGH model for the turbulent heat flux evaluation. Still the GGDH model can be implemented into the solver through User Defined Functions. See that this approach could potentially be beneficial for the Stress Omega model and for the ASST model, since they are supposed to provide better results in terms of Reynolds stresses  $\overline{u'_i u'_j}$ . However, since the use of such a GGDH model resulted to be numerically unstable even for the simplest test cases (remember the goal to build a solid industrial numerical model), we will use the available SGDH model with  $\sigma_t = 0.85$  already implemented into the solver. It could be stated that the SGDH model is a too simple model to be used in a complex flow such as that of the innovative channel. Nevertheless a constant turbulent Prandtl number can give some good results for near-wall heat transfer, which is a major phenomenon occurring in the innovative channel. On the other hand, the choice of a proper turbulence model, aiming to improve the aerodynamic model, can be seen as a mean to increase the computational accuracy of the global heat transfer.

### 3. MODEL VERIFICATION AND VALIDATION

#### 3.1 CHANNEL FLOW

##### 3.1.1 Motivation

The test case of fully developed channel flow has been studied extensively to increase the understanding of the mechanics of wall-bounded turbulent flows. Its geometric

---

<sup>XII</sup> The name follows the similarity between the viscous and turbulent heat flux formulation, with the total heat flux being  $\varphi_k = \left[ \left( \frac{\nu}{Pr} + \frac{\nu_t}{\sigma_t} \right) \frac{\partial \Theta}{\partial x_k} \right]$

simplicity is attractive for theoretical investigations of complex turbulence interactions near a wall. It is of interest for the present application since it is the simplest test case of channel flow.

### 3.1.2 Test Configuration

The flow geometry and the coordinate system are shown in Figure 3.1.

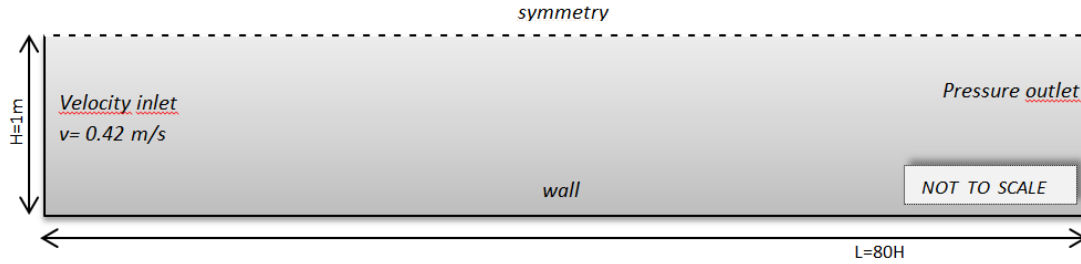


**Figure 3.1- Channel Flow Geometry**

In order to obtain a fully developed flow the height  $H$  and body length  $L$  of the plate is chosen respectively  $H = 1m$  and  $L = 80 H$ . Flat plate's geometry is symmetric about the middle plane. The inlet boundary condition is taken as a velocity inlet and the outlet boundary condition as a pressure outlet. The inlet velocity is set based on the desired flow Reynolds number. In particular several Reynolds numbers, corresponding to different database, have been used to demonstrate the model's applicability on different flow conditions and turbulence levels. Table 3.5 shows the used database and corresponding Reynolds numbers:

Database	Reynolds Number
Laufer <sup>84</sup>	14 000
Kim et al. <sup>83</sup>	5 600

**Table 3.5 - Channel flow reference flow conditions**

### 3.1.3 Numerical discretization

All calculations are run adopting the *second-order upwind discretization scheme* for transport equations. The discretized equations are solved in a segregated manner with the *Semi-Implicit Method for Pressure-Linked Equations* (SIMPLE) algorithm.

Furthermore gradients are evaluated using the *Least Squares Cell-Based* evaluation and the pressure is discretized with the *Standard* discretization scheme. Convergence criteria are based on a value of  $10^{-5}$  (absolute residuals) for all transported variables.

### 3.1.4 Mesh convergence evaluation

To determine a mesh-independent model, calculations have been run using three increasingly refined meshes. Figure 3.2 provides an example of the channel flow mesh:

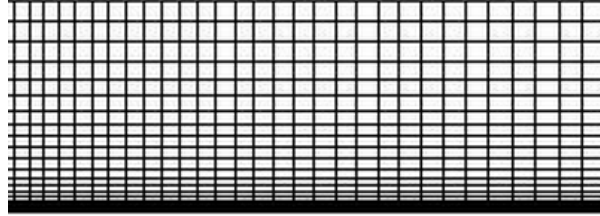


Figure 3.2 - Channel Flow Mesh

These different configurations give following values of  $y^+$  (Table 3.6):

<i>Coarse Grid (Mesh A)</i>	$y^+ = 2.242$
<i>Fine Grid (Mesh B)</i>	$y^+ = 1.487$
<i>Refined Grid (Mesh C)</i>	$y^+ = 0.743$

Table 3.6 - Channel flow used grids

To establish mesh convergence, the average wall shear stress  $\tau_w$  is evaluated: Table 3.7 shows the results:

$Y^+$	<i>Mesh A</i>	<i>Mesh B</i>	<i>Mesh C</i>
$\tau_w$	$5.790e^{-04} Pa$	$5.801e^{-04} Pa$	$5.864e^{-04} Pa$

Table 3.7 - Channel flow grid convergence evaluation

The comparison shows that there is almost no difference between the two finer grids (difference of 0.2% between the fine and refined grids). Therefore we will adopt the finest calculation grid to capture the finest turbulence phenomena occurring.

### 3.1.5 Results

In this section we will show several velocity and Reynolds Stress profiles to compare and verify the correct implementation of the three turbulence models described in Section 2.

#### 3.1.5.1 Law of the Wall

The law of the wall is one of the most famous empirically-determined relationships in turbulent flow near solid boundaries. Measurements show that, for both internal and

external flows, the streamwise velocity in the flow near the wall varies logarithmically with distance from the surface.

The form of this law, valid for flows at high Reynolds numbers under constant favorable pressure gradient and far enough from the wall for viscous effects to be negligible ( $y^+ > 30$ ), is the mean velocity profile normalized in variables given by:

$$u^+ = \frac{1}{k} \ln y^+ + C \quad (59)$$

where  $u^+ = \frac{u}{u_\tau}$  and  $y^+ = \frac{y u_\tau}{\nu}$  where  $u_\tau = \frac{\tau_w}{\rho}$ .

$u$  is the mean velocity,  $y$  is the distance from the wall,  $\nu$  is kinematic viscosity and  $u_\tau$  is the friction velocity defined from the wall shear stress  $\tau_w$ . The Von Karman constant,  $k$ , and the additive constant  $C$  is widely thought to be universal constants. From experiments, the Von Kármán constant is found to be  $k \approx 0.41$  and  $C \approx 5.5$  for a smooth wall. Due to the functional form of the law of the wall, this region is also called the *logarithmic sublayer*.

Near the wall, where turbulent fluctuations are strongly suppressed due to the requirement that all fluctuations be zero at the wall, the flow is controlled by viscous effects and the variation of  $u^+$  to  $y^+$  is approximately 1:1.

$$u^+ = y^+ \quad (60)$$

This region, approximately located when  $y^+ < 5$ , is also known as *viscous sublayer*.

In the transition region ( $5 < y^+ < 30$ ), viscous turbulent momentum transport are of comparable magnitude. The transition region, where there isn't an applicable law for variation of  $u^+$  to  $y^+$ , is also known as the *buffer or transition zone*.

So computational results based on the previously described turbulence models have been compared with the law of the wall. Results are obtained considering velocity at  $x = 75H$  location, where the flow can be considered as fully developed.

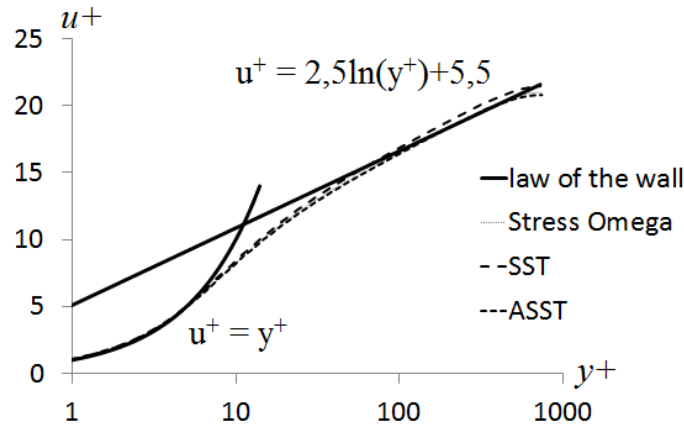


Figure 3.3 - Channel Flow law of the wall verification

Figure 3.3 shows that all models, the SST as well as the ASST and the RSM, produce very similar good predictions.

#### 3.1.5.2 Turbulence Kinetic Energy

Turbulent kinetic energy is also compared with the DNS data assembled by Kim et al.<sup>83</sup>.

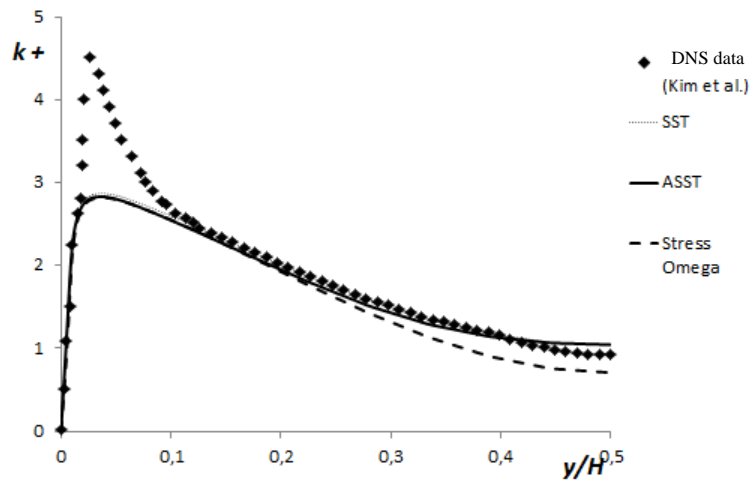


Figure 3.4 - Non-dimensional turbulence kinetic energy distribution for Re=14000 (Kim et al.)

Figure 3.4 shows that all models fail to capture the peak in non-dimensional turbulent kinetic energy  $k^+ = \frac{k}{u_\tau^2}$  due to the form of the  $k-\omega$  model used in the near-wall region, particularly due to the absence of low-Reynolds formulations in the viscous sublayer. This would allow to better capture the pick, as shown by Wilcox<sup>80</sup>. Anyway the three models correctly predict the trend in the logarithmic region as well as in the outer

region. Similar information and conclusions can be acquired looking at the three fluctuating velocity components showed in Figure 3.5:

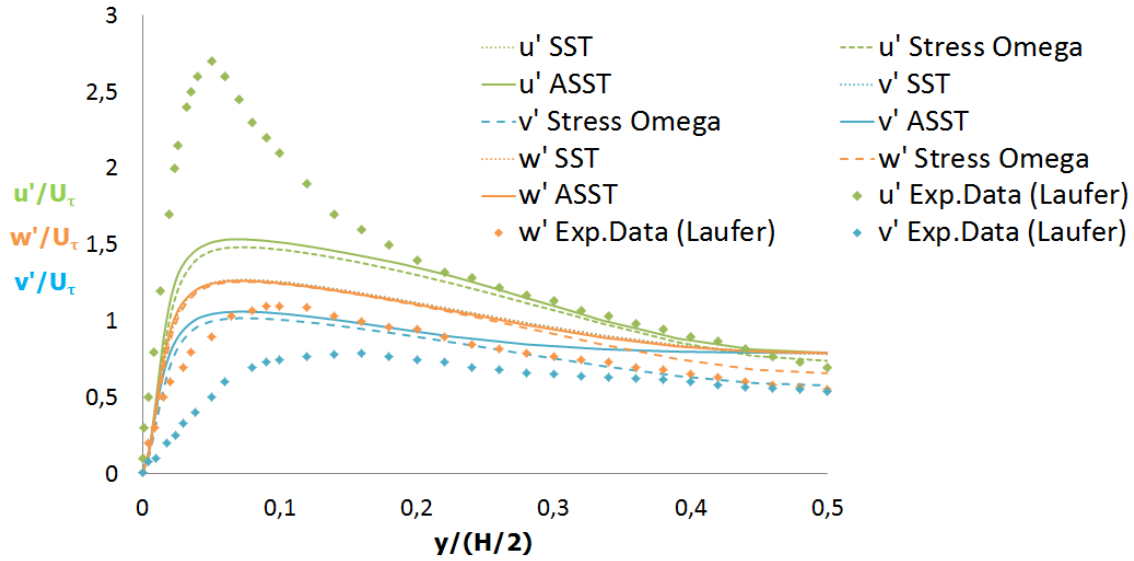


Figure 3.5 - Fluctuating velocity components compared with experimental data of Laufer for  $Re = 14\,000$

See that the SST model predicts identical fluctuating velocities, i.e. equal to  $\frac{2}{3}k$ . This is consistent with the SST isotropic formulation. This is not the case for the ASST model which slightly improves the description, giving three different values of the fluctuating velocities. In any case this anisotropic description is much more evident in the near wall region, since in the channel center the three ASST computed fluctuating velocity components converge to the same value. In this sense the Stress Omega model provide superior results even in the channel center, where the three components are still quantitatively different.

### 3.1.5.3 Reynolds Stress

Computational results based on the previously described turbulence models have been compared with the DNS data available (Kim et al.<sup>83</sup>).

Figure 3.6 shown that Shear Reynolds Stress  $\frac{uv}{u_\tau^2}$ , in plane channel flow at  $Re = 5600$  is very well predicted by all these turbulent models. This Reynolds stress is of primary importance in channel flow since it is often the most important in terms of magnitude, justifying the macroscopic phenomena occurring in such a flow. Therefore it is not surprising to see such results, since turbulence models are usually tuned to be able to reproduce the turbulent shear stress.

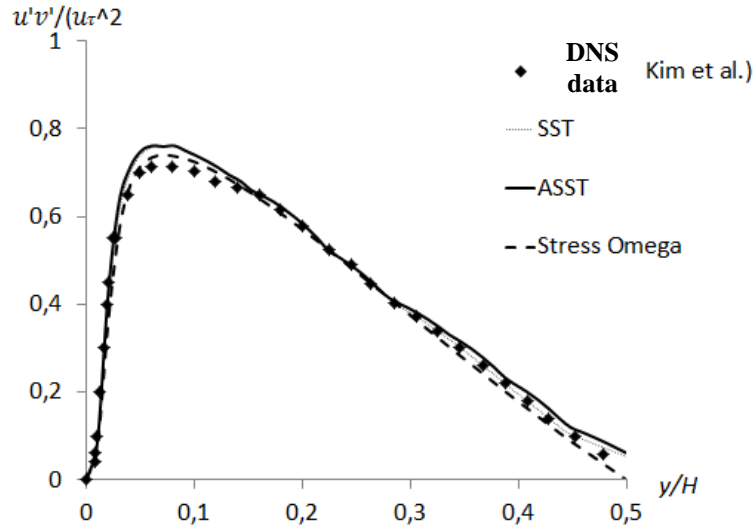


Figure 3.6 - Channel flow mixed Reynolds stress distribution for Re=5600 (Kim et al.)

#### 3.1.5.4 Flow anisotropy

In Figure 3.7 the normal Reynolds stress difference  $\tau_{yy} - \tau_{xx} = \overline{v'^2} - \overline{u'^2}$ , predicted by the nonlinear model (ASST), the SST model and the Stress Omega RSM model, is compared with the experimental data of Laufer<sup>84</sup>:

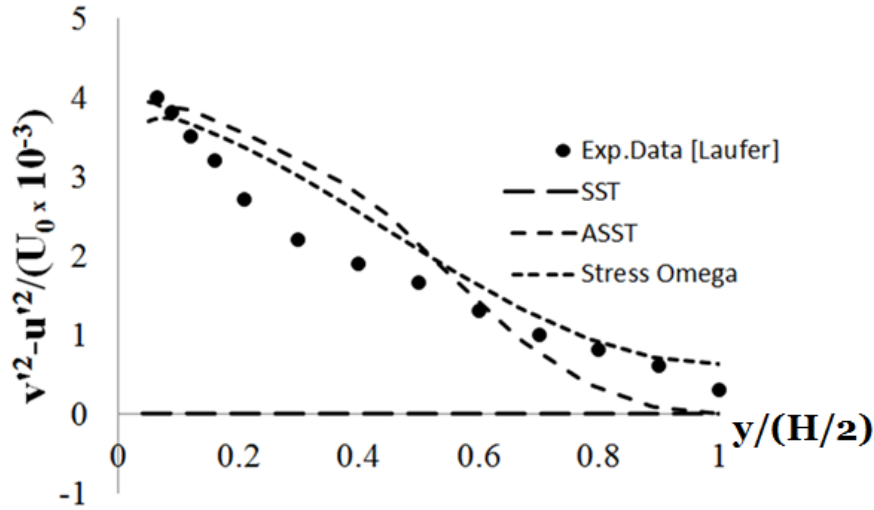


Figure 3.7 - Channel Flow anisotropy distribution at Re = 14 000 (Laufer<sup>84</sup>)

The difference between the experimental data and the linear model predictions is entirely related to the effects of anisotropy. The new proposed model reformulates the non-linear terms coefficients, adjusting them on the macroscopic physical phenomena they are responsible for, i.e. secondary flow. To verify this behavior, see how the normal Reynolds stresses are calculation by the ASST model, remembering that only the  $S_{xy} = \frac{\partial U}{\partial y}$  strain component is present in simple shear flow:



$$\overline{u'^2} = \frac{2}{3}k + C_1 \frac{k}{\omega^2} \left( \frac{1}{3} \cdot S_{xy}^2 \right) + C_2 \frac{k}{\omega^2} (2 \cdot O_{xy} S_{yx}) + C_3 \frac{k}{\omega^2} \left( \frac{1}{3} \cdot O_{xy}^2 \right) \quad (61)$$

On the other hand, the standard SST model predicts that  $\tau_{yy} - \tau_{xx} = 0$  since no effect of the only velocity gradient  $\partial U / \partial y$  is present on the principal Reynolds stresses.

Stress Omega model is also used in this comparison, because, as we can see in the figure, it offers a greater potential for predicting the anisotropic phenomena. This is of primary importance for the prediction of more complex flows, since the parameter shown in Figure 3.7 is considered to be responsible to the prediction of the reattachment length downstream a backward facing step<sup>99</sup> (see following Section 3.2) as well as the secondary motion of the second type in curved ducts of circular cross-section<sup>100</sup>.

### 3.1.6 Conclusions

The analysis of the channel flow shows that the formulated ASST model correctly represents the basic turbulent characteristics of a turbulent flow. In particular, it has been shown that the anisotropic formulation does not act in the logarithmic sublayer (as already motivated), giving the correct law-of-the-wall shape. Moreover, it has already been shown that the model reproduces the velocity fluctuations better than the SST model (but always slightly worse than the Stress Omega model), taking into account the lack of a low-Re formulation to reproduce the near wall turbulence kinetic energy peak. Finally, it has been demonstrated that the anisotropic formulation can reproduce flow anisotropies even in a simple shear flow: in this sense ASST results are very similar to those of the Stress Omega model, but are also much better than those of SST model. This is very promising for the application to complex flows, where anisotropy is supposed to play a major role.

## 3.2 BACKWARD FACING STEP

### 3.2.1 Motivation

Turbulent flow past a backward facing step is often used as a test case for improvement of numerical schemes and turbulence model. Indeed reattachment of separated turbulent shear layers in the presence of adverse pressure gradients occurs in many flows of interest and the geometry of this test case offers one of the least complex separating and reattaching flows (fixed location of separation), facilitating a study of the reattachment process by itself.

Particularly the *reattachment length* is a commonly used parameter to determine the ability of a turbulence model to correctly simulate the flow over backward facing step. A key measure of the computational accuracy of any numerical model is the prediction of the reattachment point. This parameter can be determined, for example, as the distance from the step to the position on the wall, at the bottom of the channel, at which *wall shear stress* is equal to zero.

Therefore the wall shear stress and pressure distributions, Velocities and Reynolds stresses measured by a laser Doppler velocimetry system in the experiment of Driver and Seegmiller<sup>85</sup> will be compared with the results obtained with the three turbulent models of Section 2.

### 3.2.2 Test configuration

Backward facing step consists of a sudden expansion in a duct. The present test configuration is that of the experiment of Driver and Seegmiller<sup>85</sup>. In order to better understand the flow configuration See Figure 3.8:

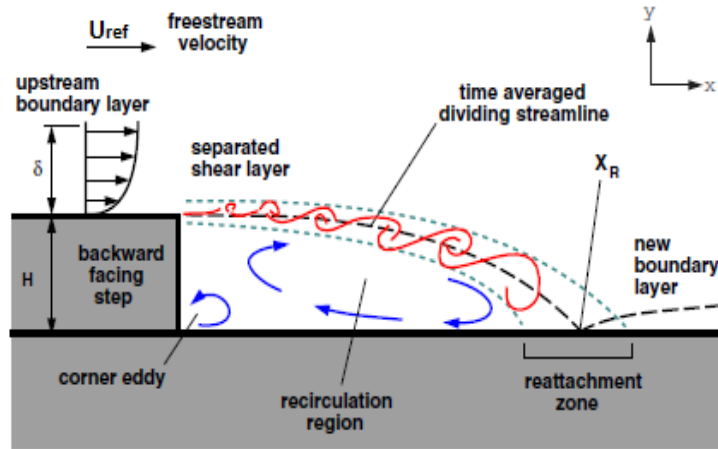


Figure 3.8 - Concept of Backward Facing Step

The most interesting region is located immediately downstream the step and it is confined downstream of the reattachment point. It is characterized by the presence of primary vortex circulation and secondary vortex located in bottom corner of the step.

The inlet boundary condition is taken as a uniform velocity profile and the outlet boundary condition as a pressure outlet. An inlet length upstream the step of around

120H is used to obtain a fully developed flow approaching the step<sup>xiii</sup>. Calculations were performed at a freestream velocity of 44.2 m/s and at atmospheric pressure and temperature. These conditions correspond to a freestream Mach number of 0.128 at a location 4 step-height upstream of the step ( $X/H = -4$ ).

### 3.2.3 Numerical Discretization

The solver is the Pressure-based one and the Coupled pressure-velocity algorithm with pseudo-transient option is used. Gradients are evaluated through the Least Square Cell Based method with SST model and the Green-Gauss Node Based using ASST and Stress Omega model. Finally the Second Order Upwind Scheme is used for the spatial discretization of momentum, turbulent kinetic energy, turbulent dissipation rate and the Reynolds Stresses equations of the stress Omega model. Convergence criteria are based on a value of  $10^{-5}$  (absolute residuals) for all transported variables.

### 3.2.4 Mesh convergence evaluation

Three different meshing configurations have been preliminarily studied in order to evaluate the influence of mesh size on the solution. The three structured mesh configurations (hereafter named as A, B, C) differ on the  $y^+$  value of the first cell near the wall. The  $y^+$  average values, on the wall downstream of the step, are 1.972, 1.126 and 0.3855 for configuration A, B and C respectively. Meshing convergence has been evaluated by comparing the average values of Wall Shear Stress  $\tau_w$  on wall downstream of the step for each mesh configuration (Table 3.8):

Mesh ID	$y^+ = 1.972$ <i>mesh A</i>	$y^+ = 1.126$ <i>mesh B</i>	$y^+ = 0.3855$ <i>mesh C</i>
$\tau_w$	1.963 Pa	1.945 Pa	1.942 Pa

**Table 3.8 - Backward Facing Step grid convergence evaluation**

The comparison of the wall shear stress values in Table 3.8 shows that the difference between the results of B and C configurations is less than 0.2%. This difference is considered as acceptable for the present analysis. Hence the final choice is to use Configuration B, which gives a good balance between calculation results and total number of mesh nodes. The final mesh of configuration B is shown in Figure 3.9:

---

<sup>xiii</sup>Driver and Seegmiller used an inlet length around 800H, which has been reduced in the present model to reduce the number of mesh elements.

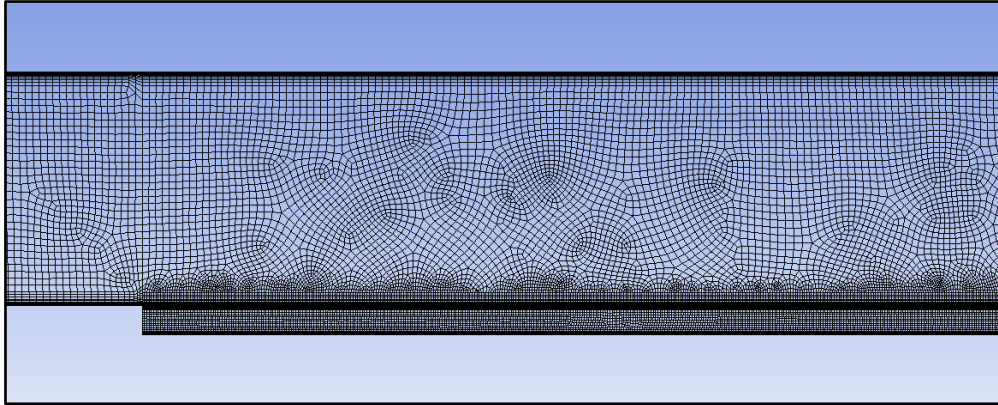


**Figure 3.9 - Backward Facing Step mesh B**

### 3.2.5 Results

#### 3.2.5.1 Step upstream conditions at $X/H = -4$

Streamwise velocity and Reynolds stress measurements are shown in Figure 3.10 and Figure 3.11 and they are compared with computed profiles obtained using the three different turbulent models of Section 2.

All results show a correct prediction of streamwise velocity and turbulent Reynolds stress.

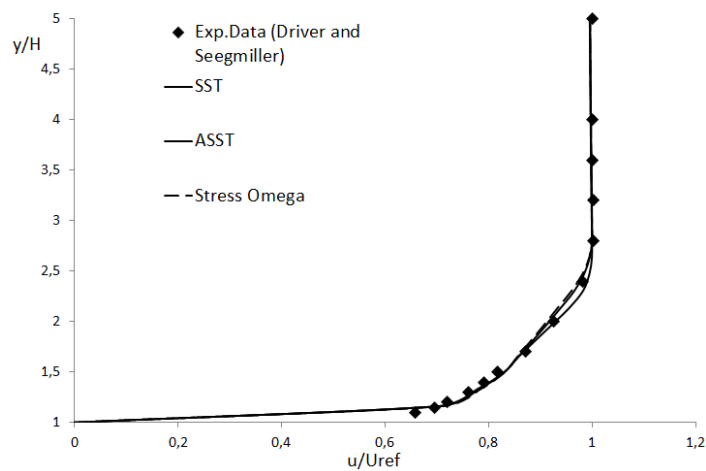


**Figure 3.10 - Backward Facing Step velocity upstream the step at  $X/H = -4$**

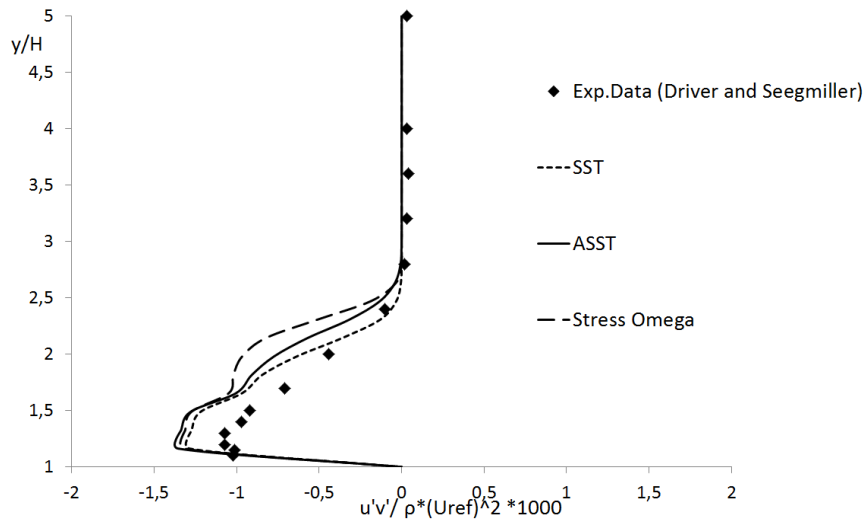


**Figure 3.11 - Backward Facing Step mixed Reynolds Stress upstream the step at X/H = -4**

#### 3.2.5.2 Step downstream pressure coefficient

When dealing with a backward facing step it is interesting to study the distribution of wall static pressure.

$$C_p = \frac{P_w - P_{ref}}{\frac{1}{2}\rho v_{ref}^2} \quad (48)$$

where  $P_{ref}$  is pressure value at about  $x/H = -4$  location upstream the step. Note that the zero X coordinate corresponds to the beginning of the wall downstream the step. Figure 3.12 shows the results:

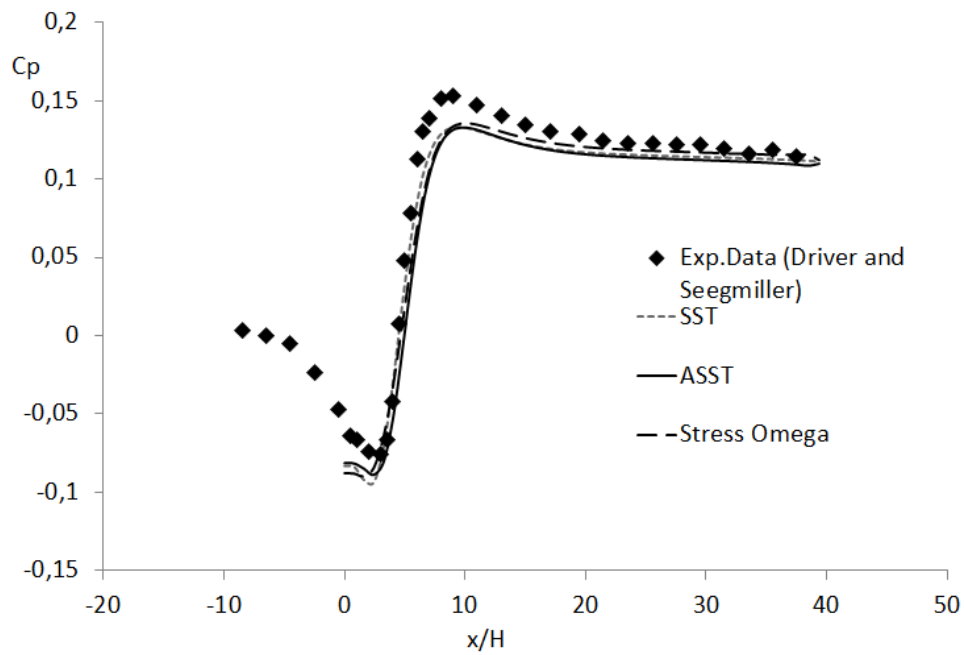


**Figure 3.12 - Backward Facing Step pressure coefficient distribution downstream the step**

As shown in Figure 3.12, the recirculation zone is obviously characterized by an adverse pressure gradient before the reattachment point. We clearly see that looking at the velocity profiles downstream the step (Figure 3.13) at four different location,  $X/H=1, 4, 6$  and  $10$  respectively. The  $Y/H = 0$  plane corresponds to the channel wall downstream the step. The adverse pressure gradient is still acting on the principal velocity at  $X/H = 6$ . Then we see that the velocity field tends to restore to a zero-pressure gradient flow, even if this situation is not yet achieved at  $X/H = 10$ . Indeed the  $C_p$  distribution rather suggests that a negative pressure gradient only occurs at  $X/H > 10$ . However note that the three models generally provide very good results, even if the Stress Omega model gives spurious boundary layer descriptions, especially from  $x/H=4$ . In fact, the boundary layer velocity seems to be underestimated, which is somehow surprising for a model which is supposed to properly account for flow anisotropies. We will see how this feature impacts the other model's predictions.

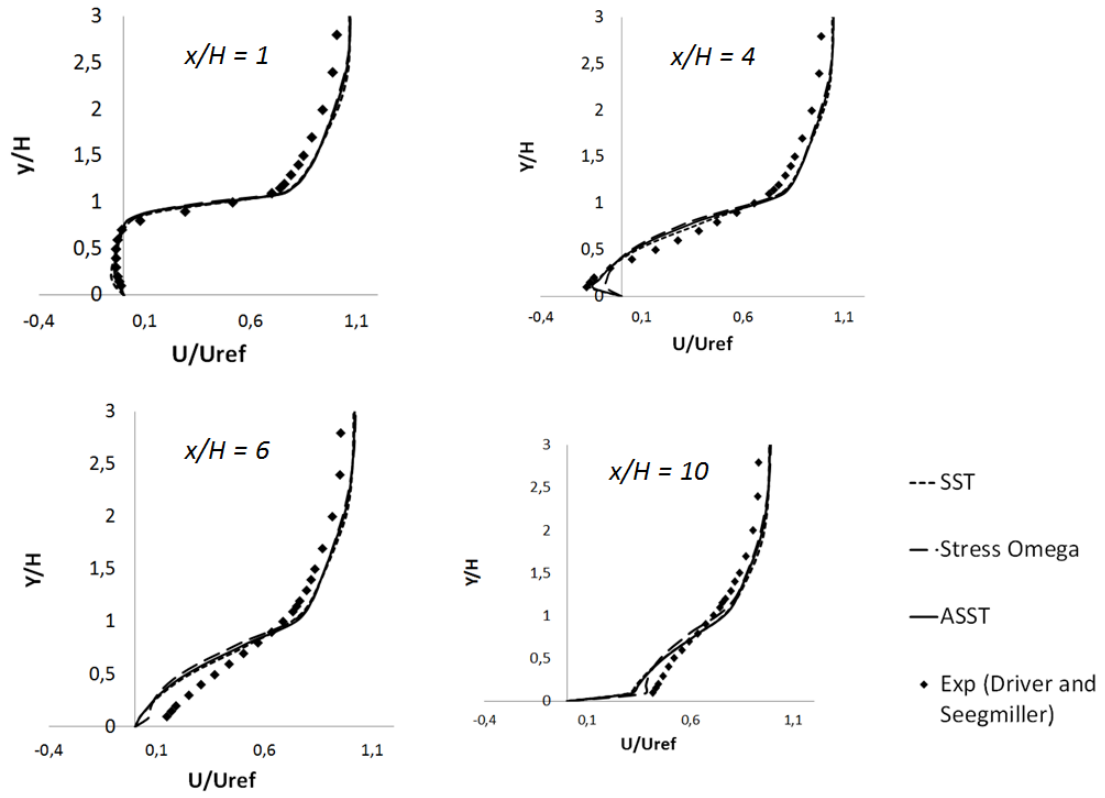


**Figure 3.13 - Velocity profiles downstream the step**

### 3.2.5.3 Step downstream skin friction coefficient and reattachment length

As already mentioned, the most interesting comparison is done considering the value of the reattachment length  $X_R$ . In order to estimate this length it is possible investigate the trend of skin-friction distribution along the wall downstream of the step.

$$C_f = \frac{\tau_w}{\frac{1}{2} \rho v_{ref}^2} \quad (49)$$

where  $v_{ref} = 44.2 \frac{m}{s}$  is velocity at  $x/H = -4$  location upstream the step. Results are shown in Figure 3.14:

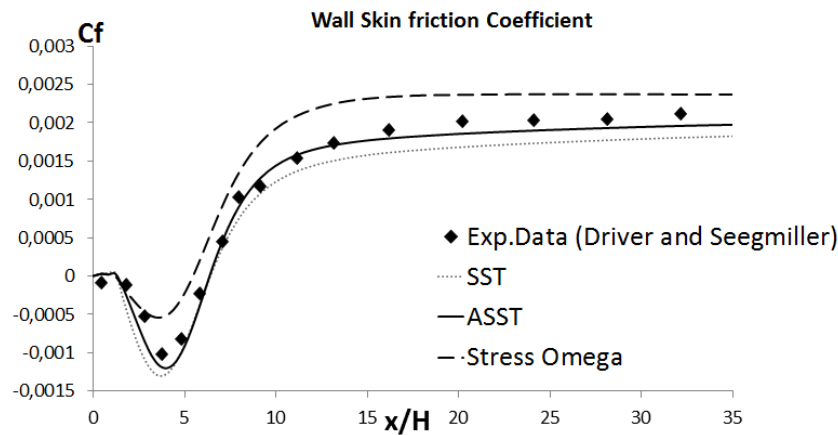


**Figure 3.14 - Backward Facing Step skin friction coefficient downstream the step**

The experimental reattachment length value is  $X_R = 6.26 \pm 0.10$ . the value is consistent with the observed velocity field downstream the step (i.e. adverse pressure gradient still acting at  $X/H=6$ ). Going further in the analysis, the reattachment length is determined by finding the zero streamwise wall shear stress location. Results are shown in Table 3.9:

Model	RSM-Stress Omega	ASST	SST	Data Exp
$X_R$	5.44	6.37	6.40	$6.26 \pm 0.10$

**Table 3.9 - Backward Facing Step calculated reattachment lengths**

Table 3.9 shows the comparison of the reattachment length estimated by different turbulence models with that of experiment. It can be noted that SST and ASST models slightly overpredict the value of  $X_R$ , although predictions by ASST model show quite good agreement with the experimental data. This may be due to the ability of the ASST model to predict the anisotropic behaviour of the principal Reynolds Stresses for the Channel Flow case (see Section 3.1), as suggested by S.Thangam and C. G. Speziale<sup>99</sup>. Note that Menter<sup>101</sup> affirms that the SST computed reattachment length for the current case is around 6.5, which is fairly close to the found value of 6.40. The RSM Stress Omega model substantially underpredicts the reattachment point, despite its capability to predict anisotropic phenomena.

This result shows an unusual behaviour of traditional  $\omega$ - based stress-transport and two-equations model that generally, as demonstrated by Wilcox<sup>80</sup>, predict a reattachment length slightly longer than experimental (whereas the  $\varepsilon$ -based stress-transport and two equations model are generally supposed to underpredict  $X_R$ ).



Considering that the RSM- Stress Omega model used in this validation study is different from the one proposed in Wilcox<sup>80</sup>, it would be interesting to verify the correct model implementation in to the solver.

#### 3.2.5.4 Heat transfer downstream the Backward Facing Step

The unexpected behavior of the Stress Omega model has been observed even studying the heat transfer downstream the backward facing Step. Here data of normalized Stanton number ( $St = \frac{Nu}{Re_H Pr}$ ) have been plotted against the non-dimensional distance after the step shifted by the reattachment length. For the thermal model used, all three calculations have been done using a Simple Gradient Diffusion Hypothesis (SGDH) approach, with a classical Turbulent Prandtl number equal to 0.85. See Figure 3. 13 showing the results compared to experimental data of Vogel and Eaton<sup>102</sup>.

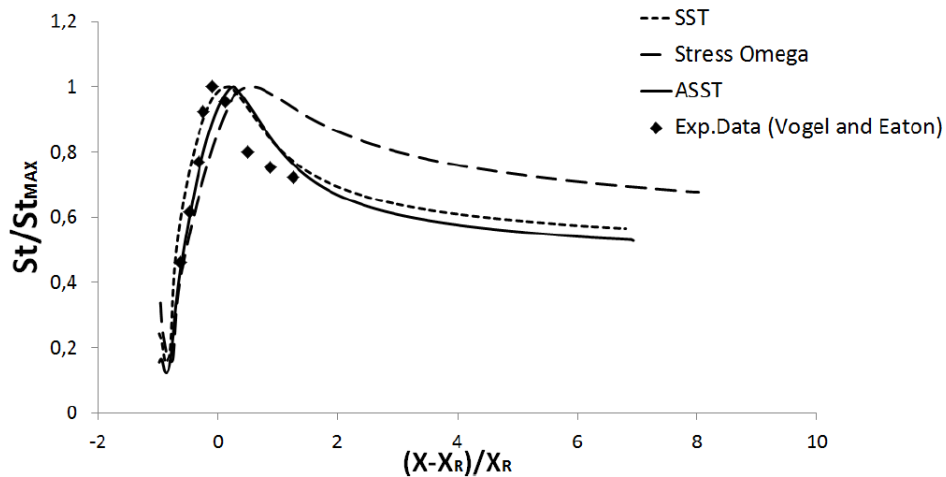


Figure 3.15 - Normalized Stanton number downstream a backward facing step

Both the SST and the ASST model predicts a good trend of the heat transfer downstream the step. Indeed it is worth noting the fact that none of the model correctly predicts the peak location, which is around 0.1 normalized  $X_R$  upstream the reattachment point. Even the SST and ASST models, which provide a good description of the ongoing heat transfer, predict the maximum occurring downstream the reattachment point (0.003 and 0.08 normalized reattachment length respectively). Anyway it is definitely the Stress Omega model which provides the worse results. If the maximum normalized Stanton number location is not very different from those given by the other two models, the global heat transfer trend is largely overpredicted downstream the reattachment point. Indeed the SGDH modeling is quite unfavorable for a Stress

Model application, since the potential better description of the Reynolds Stresses could be usefully used with a more sophisticated General Gradient Diffusion Hypothesis (GGDH), which is not an available option in ANSYS Fluent ®.

### **3.2.6 Conclusions**

The present analysis of backward facing step flow case shows that each of three turbulent models does a good qualitative job of predicting the flow, moreover the ASST model shows a good improvement over the other models. In fact it provides the best reattachment length in a pure aerodynamic calculation and very good description of the heat transfer downstream the step, when modelled. The SST model also provides valuable results both for reattachment length and heat transfer. On the other hand, unexpected behaviour of the Stress Omega model has been detected both for the reattachment length and the heat transfer. This somehow questions the applicability of such a model in more complex flows. Anyway it can be concluded that also this validation test case assures the correct formulation and applicability of the ASST model.

## **3.3 TURBULENT DEVELOPING FLOW IN A 90° BEND**

### **3.3.1 Motivation**

Fluid flow in a bend is a baseline flow studied for several applications in applied sciences. Configurations of interest are, for instance, centrifugal pumps, heat exchanger tube-side and industrial pipelines. It is of particular interest for the present application since the in-bend flow coming from mixing zones cannot be considered as fully developed flow: therefore it is interesting to verify the model capabilities to correctly describe this flow configuration.

A characteristic which distinguishes such flows from those in straight ducts is the generation of streamwise vorticity, or "secondary motion," within the duct, resulting in a pressure loss, the spatial redistribution of streamwise velocity and increased heat transfer at the duct wall.

Hence, the aim of this work is to numerically investigate the turbulent flow inside a 90 degree bend of squared cross-section, and determine the appropriate turbulence modelling level required to describe this flow.

### **3.3.2 Test Configuration**

The present work will study the bend geometry proposed by Taylor and al.<sup>103</sup> (Figure 3.16):



profile in the inlet section but not changing the paper base idea of developing flow into a bend. The original 50 D exit length has been retained.

Using the described geometry, three different meshing configurations have been preliminarily studied in order to evaluate the influence of mesh size on the solution. The three structured mesh configurations (hereafter named as A, B, C) differ by a factor of around 2 on the mesh size in the first layer thickness (Table 3.10):

Mesh Configuration	Y+
A	0.27
B	0.15
C	0.12

Table 3.10 - 90° bend used grids

The  $y^+$  average values are 0.27 and 0.14 and 0.12 for configuration A, B and C whereas the maximum  $y^+$  are 0.78, 0.40 and 0.21 respectively.

An example of the final mesh for the B configuration in the inlet channel cross-section is shown in Figure 3.17:

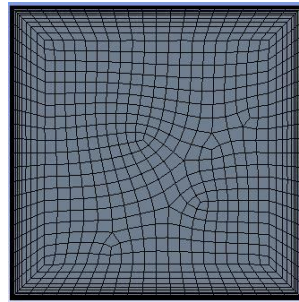


Figure 3.17 - 90° bend mesh example

Meshing convergence has been evaluated by comparing wall average wall shear stress.

The mesh convergence evaluation is shown in Table 3.11:

Mesh Configuration	$\tau_w$ [Pa]
A	2.61
B	2.70
C	2.72

Table 3.11 - 90° bend mesh convergence evaluation

The comparison of the wall shear stress values shows a good agreement for the B and C configurations (difference in the wall shear stress less than 1%). The final choice is to use Configuration B, which gives a good balance between calculation results and total number of mesh nodes.

### 3.3.5 Results

The comparison has been done on the values of the non-dimensional principal velocity  $U/V_c$ , the non-dimensional radial velocity  $V/V_c$  ( $V_c$  being the average velocity) and the non-dimensional Reynolds stress  $-u'v'/V_c^2$ . These values will be shown in two different lines of a cross-section: the line AA, defined as the line with  $r^*=0.5$  and  $0 < z^* < 1$  and the line BB defined as  $0 < r^* < 1$  and  $z^*=0$ . See Figure 3.18 for explanation. See that the BB line covers only half cross-section due to symmetry considerations.

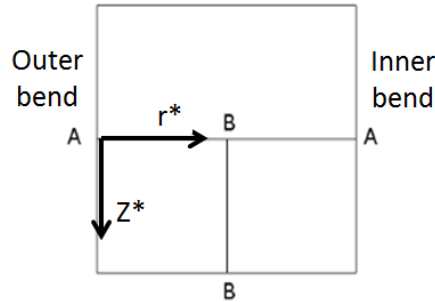


Figure 3.18 - 90° bend studied profiles

#### 3.3.5.1 Inlet principal and radial velocity and mixed Reynolds Stress profiles in the AA line

Results of the principal and radial velocity as well as of the mixed Reynolds Stress are shown in Figure 3.19, Figure 3.20 and Figure 3.21:

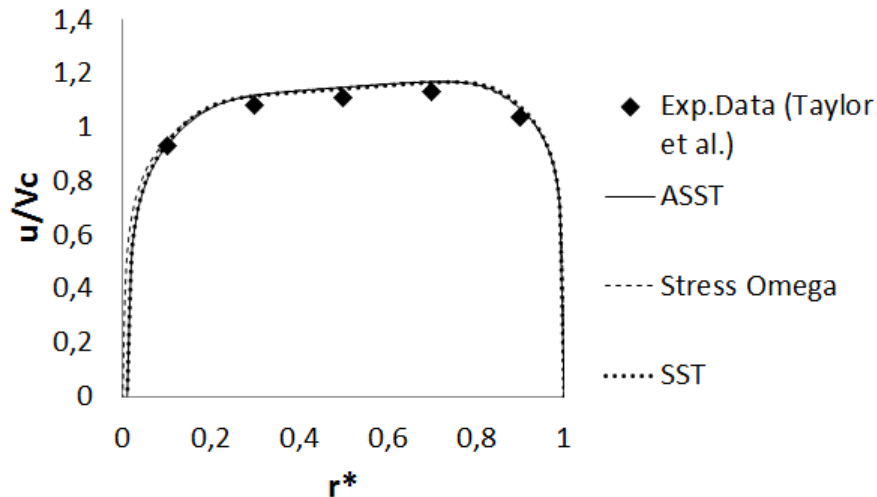
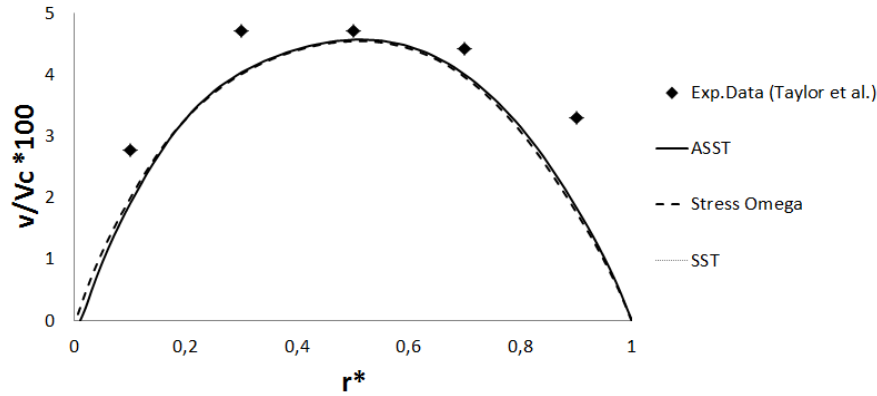
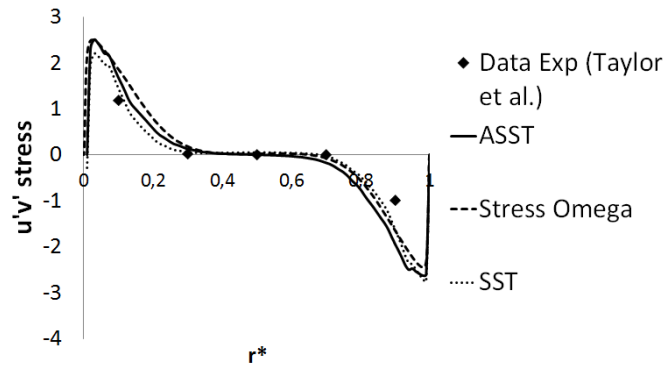


Figure 3.19 - AA line inlet section principal velocity distribution



**Figure 3.20 - AA line inlet section radial velocity distribution**



**Figure 3.21 - AA line inlet principal mixed Reynolds stress distribution**

See that there is no major difference in the description of the inlet conditions in line AA. Indeed we can clearly identify a non-symmetric principal velocity profile (due to the bend effect) and a non-zero radial velocity towards the inner bend. Anyway note that this velocity represents few per cents of the principal velocity. The mixed Reynolds stress is well predicted by the three models as a result of the changed inlet length, which has been determined to provide the correct flow inlet conditions.

#### 3.3.5.2 Outlet principal and radial velocity and mixed Reynolds Stress profiles in the AA line

Results of the principal and radial velocity as well as of the mixed Reynolds Stress are shown in Figure 3.22, Figure 3.23 and Figure 3.24:

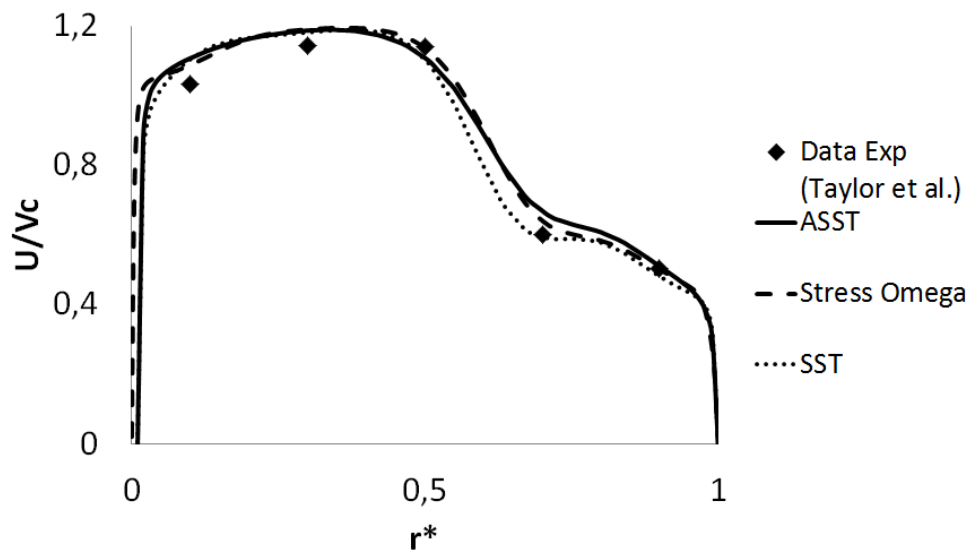


Figure 3.22 - AA line outlet section principal velocity distribution

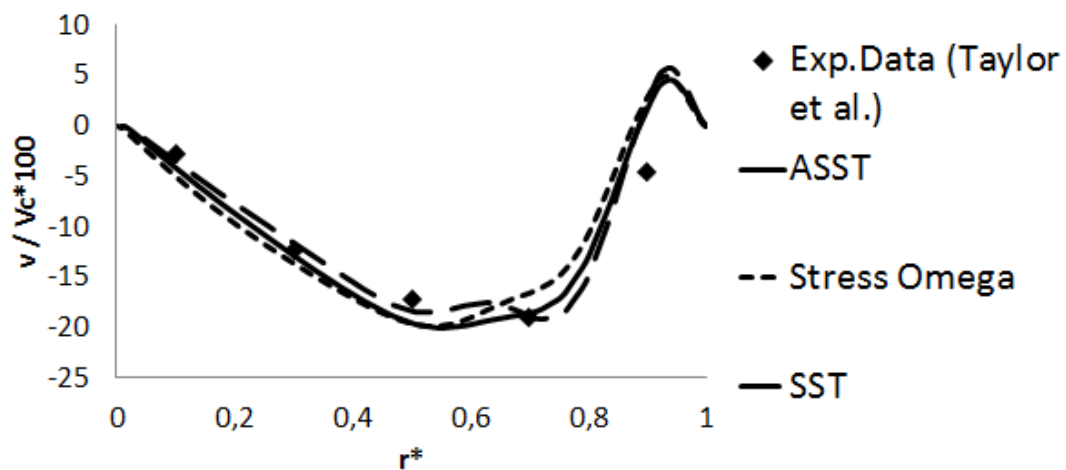


Figure 3.23 - AA line outlet section radial velocity distribution

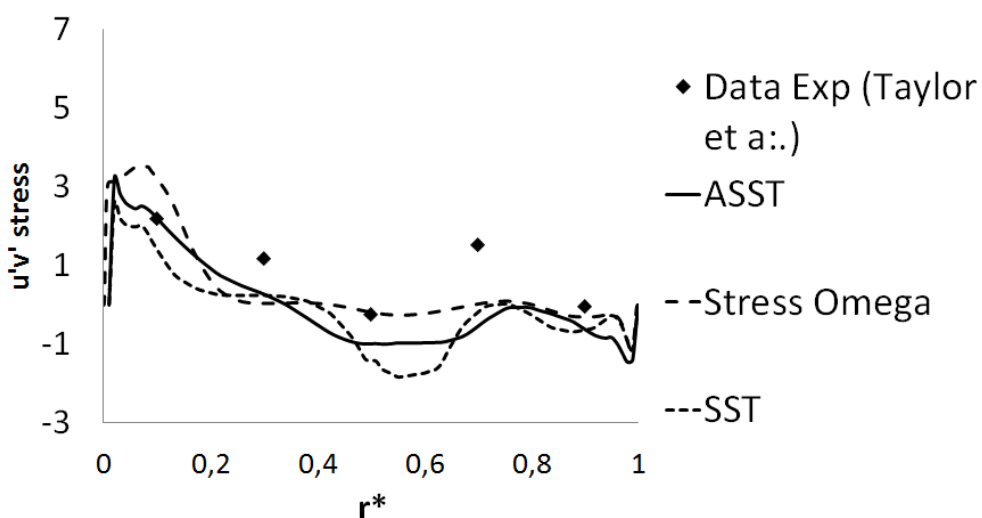


Figure 3.24 - AA line outlet section mixed Reynolds stress distribution

See again that there is no major difference in the description of the outlet velocity profiles in line AA. Note the clear non-symmetric principal velocity profile, where the radial pressure gradient acts pushing higher momentum fluid flow towards the outer bend. This is verified looking at the radial velocity, going towards the inner bend. Indeed if in the inlet profile the ratio between radial and principal velocity was about few per cents, now this ratio is around 20% at maximum. The mixed Reynolds stress is not well predicted by any of the three models: in particular the SST model predicts a spurious local minimum at  $Z^* \approx 0.55$ , whereas the ASST and the Stress Model somehow do a better job. In this sense it is worth noting the difference between the SST and the ASST models, with the latter giving results very close to those of the Stress Omega model thank to the anisotropic formulation.

### 3.3.5.3 Inlet principal and radial velocity and mixed Reynolds Stress profiles in the BB line

Results of the principal and radial velocity as well as of the mixed Reynolds Stress are shown in Figure 3.25, Figure 3.26 and Figure 3.27:

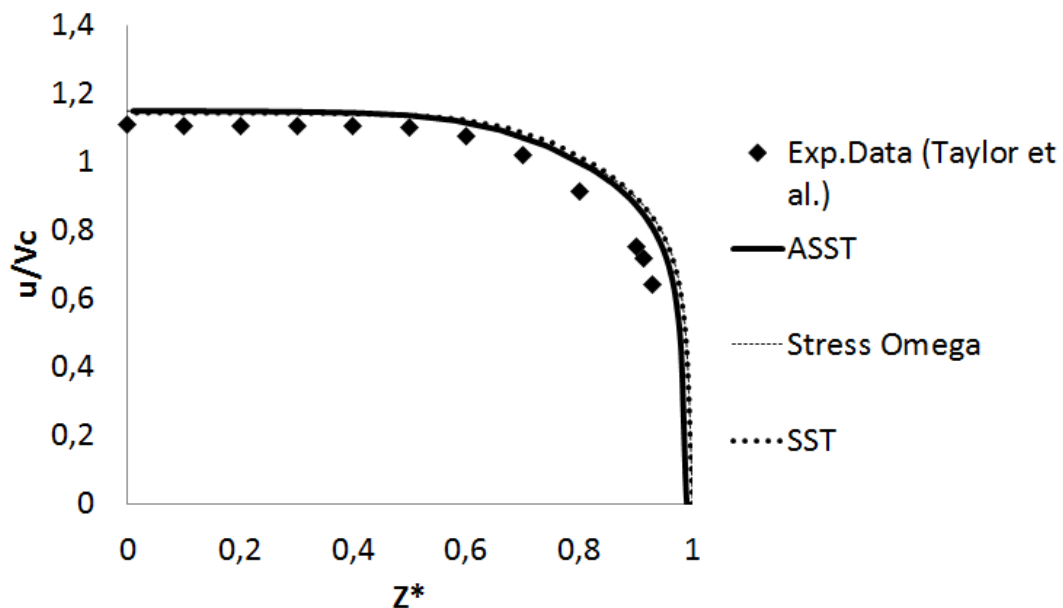


Figure 3.25 - BB line inlet section principal velocity distribution



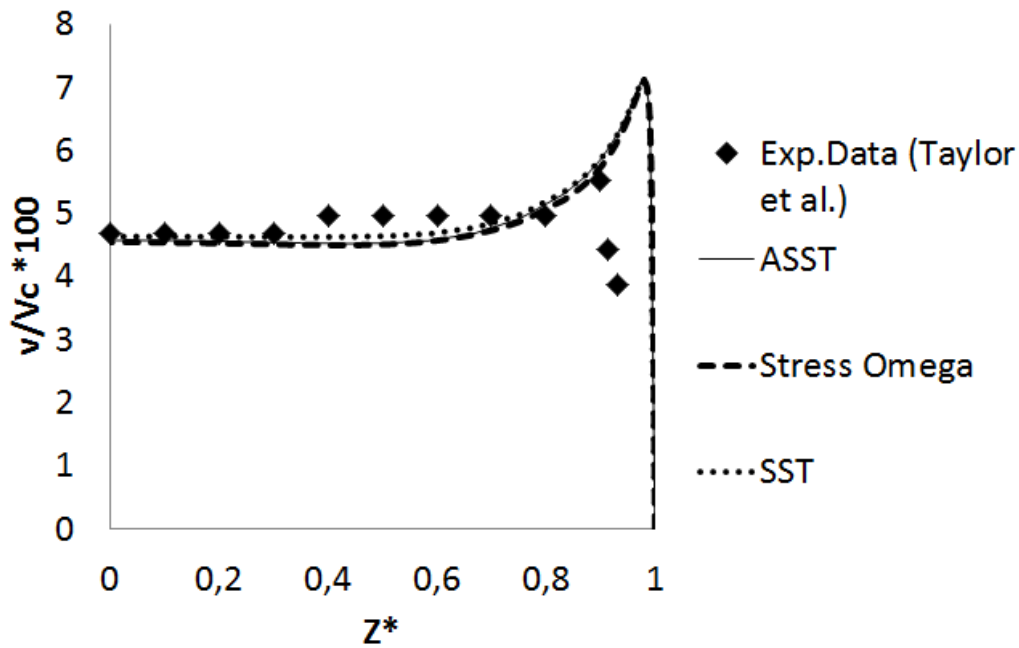


Figure 3.26 - BB line inlet radial velocity distribution

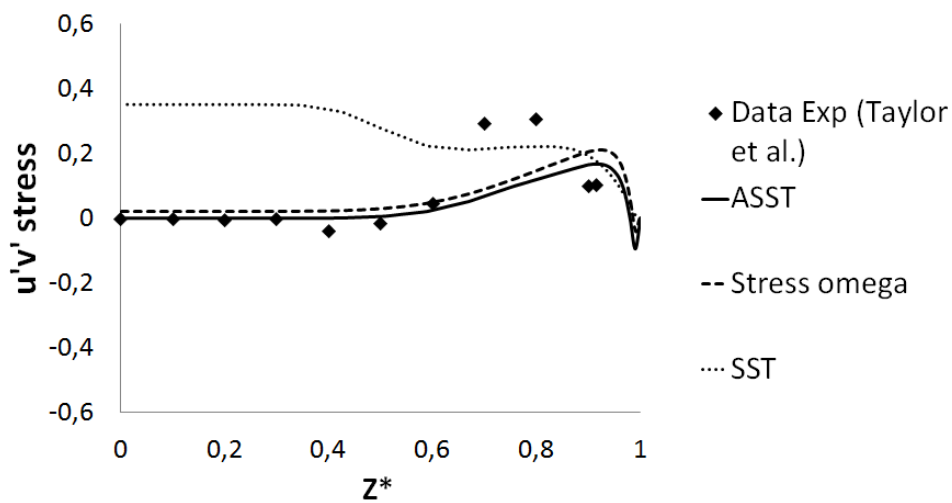


Figure 3.27 - BB line inlet Reynolds Stress distribution

See that, as in the inlet AA line, there is no major difference in the description of the inlet velocities in line BB. Still, if the main velocity seems to approach a fully developed velocity profile, this is not the case for the radial velocity. Again the radial velocity is towards the inner bend and it represents few per cents of the principal velocity. However, all the three models predict a false maximum very close to the wall. This might be to the lack of a low-Re formulation in the models (see Figure 3.4), providing an incorrect turbulence damping near the wall, resulting in a thinner computed boundary layer. The mixed Reynolds stress is well predicted by ASST and

the Stress Omega model, whereas the SST fails in providing the correct value in the fluid bulk (Figure 3.27). A possible explanation can be found looking at the Reynolds stress formulation for the SST model, i.e.:

$$\overline{uv} = -\nu_t \left( \frac{\partial u}{\partial r^*} + \frac{\partial v}{\partial x} \right) \quad (62)$$

The  $\frac{\partial u}{\partial r^*}$  gradient can be detected in Figure 3.19. Remember that, strictly speaking, the the  $r^*=0.5$  point of Figure 3.19 and the  $Z^*=0$  of Figure 3.27 are actually coincident. Hence, it is likely that the non-zero velocity gradient in Figure 3.19 is responsible for the non-zero Reynolds stress in Figure 3.27. Obviously, the ASST model can prevent this issue by the anisotropic formulation given by the positive squared term tensor  $A_{r^*x}$ :

$$\overline{uv} = -\nu_t \left( \frac{\partial u}{\partial r^*} + \frac{\partial v}{\partial x} \right) + A_{r^*x} \quad (63)$$

The Stress-Omega model gives, as expected, the most accurate results for the mixed Reynolds stress profile. However the differences with the ASST model are hardly detectable.

#### 3.3.5.4 Outlet principal and radial velocity and mixed Reynolds Stress profiles in the BB line

Results of the principal and radial velocity as well as of the mixed Reynolds Stress are shown in Figure 3.28, Figure 3.29 and Figure 3.30:

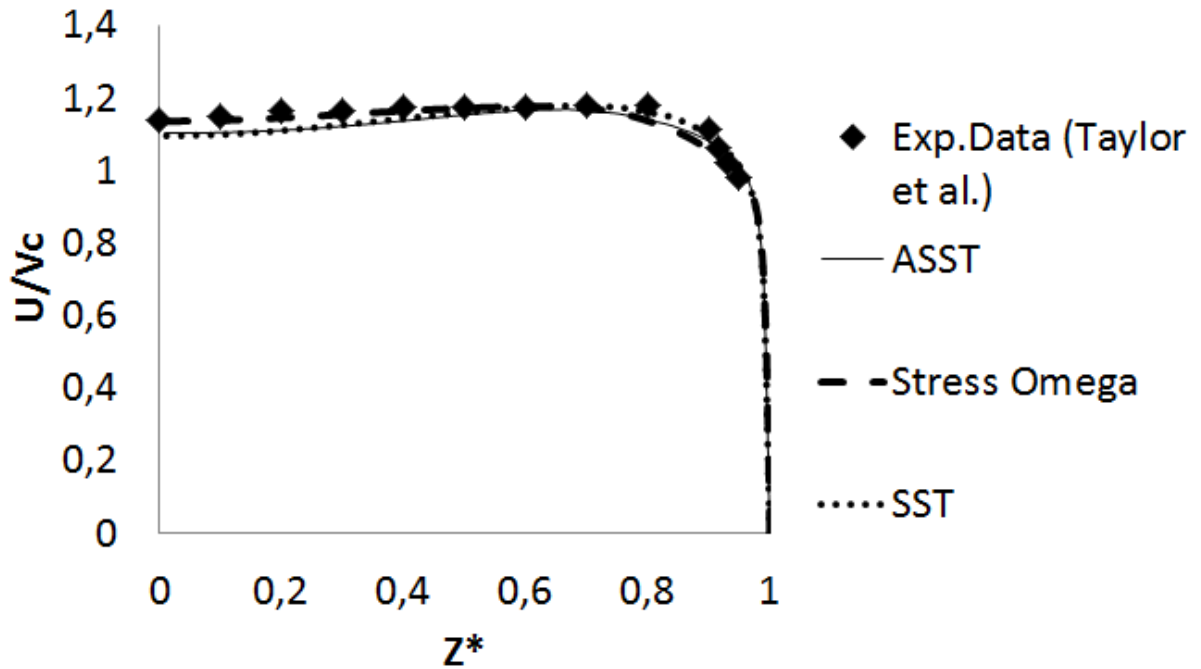


Figure 3.28 - BB line outlet principal velocity distribution

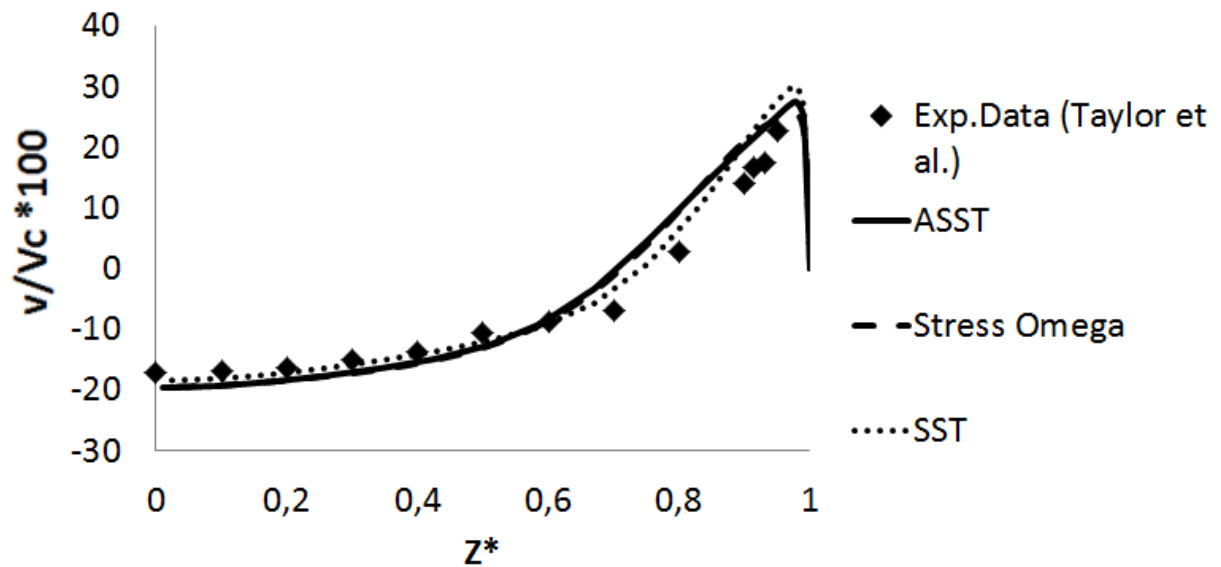


Figure 3.29 - BB line outlet radial velocity distribution

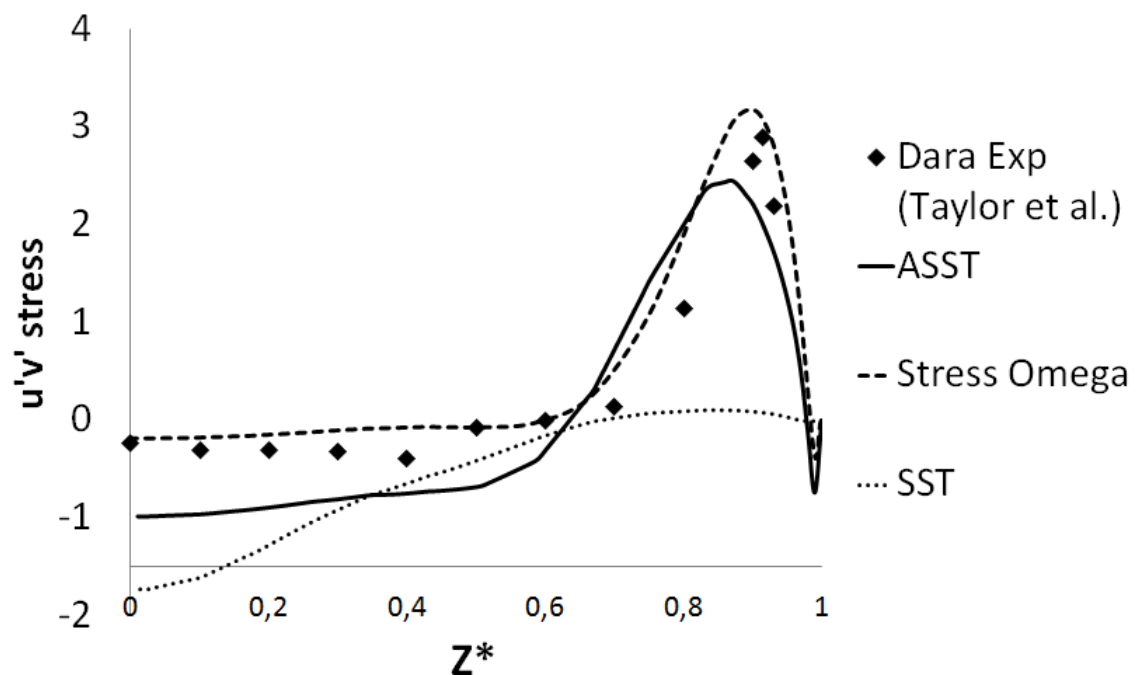


Figure 3.30 - BB line outlet mixed Reynolds stress distribution

Once again, as in the inlet AA line, velocity profiles are very well predicted by the three models in outlet line BB. The main velocity  $U$  is slightly deformed by the bend effects and again the radial velocity around 20-30% per cents of the principal velocity. It is clear how the flow is swirling by the radial velocity profile: this is due to the onset of Dean Vortices<sup>105</sup> in curved ducts. Anyway there is no surprise in noting that the mixed Reynolds stress is poorly predicted by SST model: on the other hand see again that the

ASST model provides correct trends. Moreover, the fact that the ASST results lies between the poor results of the SST model and the valuable results of the Stress Omega model seems to confirm the qualitative explanation given for the inlet BB line. Indeed see again how the non-zero principal velocity gradient at  $r^*=0.5$  in Figure 3.22 can explain the wrong prediction of the SST model and at the same time the better prediction of the ASST model due to the second order terms capturing the actual anisotropy occurring in the fluid bulk and not detectable by the simple velocity analysis.

### **3.3.6 Conclusions**

The illustrated 90° bend represents a very hard task to be accomplished for turbulence models. The fact that the flow entering the channel is not fully developed makes it harder to describe turbulence phenomena which are dominated both by the curvature adverse pressure gradient and bend-induced anisotropy. The three models under examinations show quite a good behavior in performing velocity predictions, where no major difference is detectable. Nevertheless when we look at the turbulent stresses we see that isotropic eddy viscosity models fail: this is particularly clear for the Reynolds stress along BB line, where the flow anisotropy induces a bad SST model prediction even at flow inlet. The Stress Omega model can give a very good overall flow description due to its inherent capability to take into account flow distortions. Anyway the ASST model as well resulted to be very valuable, practically showing no difference from those of the Stress Omega model. In this sense it is worth noting the dramatic improvement given by the anisotropic formulation.

## **3.4 TURBULENCE-DRIVEN SECONDARY MOTION IN STRAIGHT-DUCT OF SQUARE CROSS-SECTION**

### **3.4.1 Motivation**

Straight channel flow has been already investigated in Section 3.1. However the straight duct of squared cross-section is a test-case of primary importance due to the onset of corner vortices that are particularly hard to predict. The corner vortices consist in eight vortices at the four corners of the square cross-section: they are known to be secondary motion of the second type (turbulence driven), since no pressure gradient imbalance can justify their onset as for the Dean Vortices already seen in Section 3.3. See the corner vortices in Figure 3.31.

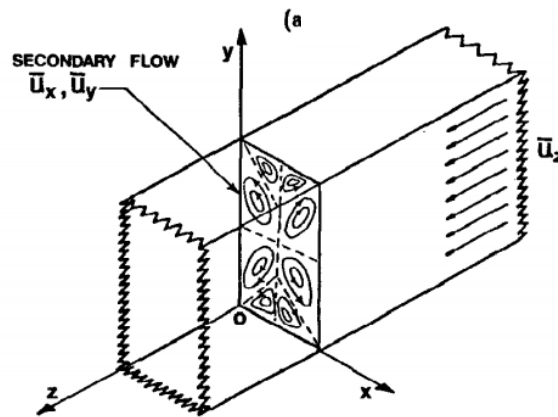


Figure 3.31 - Corner vortices as shown by Speziale<sup>89</sup>

Since isotropic eddy viscosity models are not supposed to predict any corner vortex<sup>89</sup>, the interest of the present investigation is to determine the behaviour of the Stress-Omega model (which should provide the best overall results due to its capability to transport the Reynolds stresses) and the ASST model (which should be able to provide some anisotropy, see Figure 3.7). The results will be very interesting since the poor behaviour of isotropic eddy viscosity models can be easily extended to more complex flows, arising doubts on the final applicability of such models in such cases.

#### 3.4.2 Test configuration

Test configuration is shown in Figure 3.32: only a quarter of the total cross-section has been simulated: hence symmetry conditions have been imposed on the two sides to take into account the rest of the cross-section. Periodic boundary conditions have been imposed on the streamwise faces in order to consider a fully developed flow. The working fluid is air at atmospheric pressure and temperature.

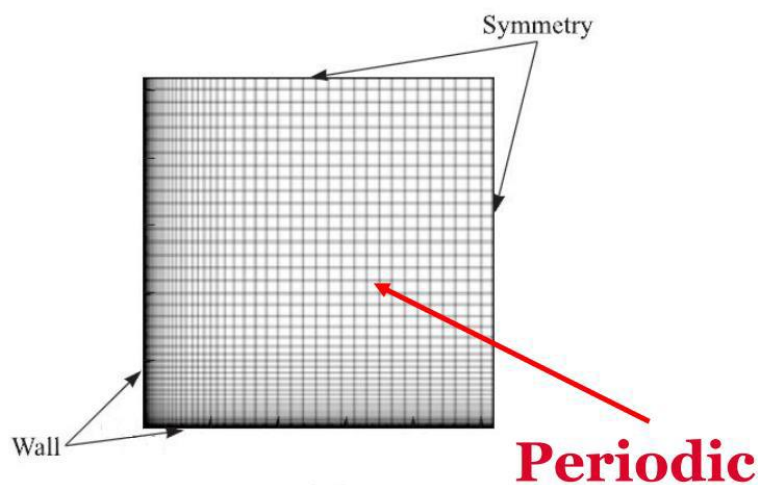


Figure 3.32 - Straight duct of squared cross-section configuration

### 3.4.3 Numerical discretization

The solver is the Pressure-based one and the SIMPLE pressure-velocity algorithm with pseudo-transient option is used. Gradients are evaluated through the Least Square Cell Based method. Finally the Second Order Upwind Scheme is used for the spatial discretization of momentum, turbulent kinetic energy, turbulent dissipation rate and the Reynolds Stresses equations of the RSM model. Convergence criteria are based on a value of  $10^{-5}$  (absolute residuals) for all transported variables.

### 3.4.4 Mesh convergence evaluation

Three meshes differing by around two in the  $y^+$  value have been used to test grid convergence; results of this study are shown in Table 3.12:

Mesh ID	$Y^+$	$\tau_w$
A	0.81	4.82 mPa
B	0.35	4.73 mPa
C	0.13	4.71 mPa

**Table 3.12 - Straight duct of squared cross-section grid independence evaluation**

Note that there is practically no difference between mesh B and C. Therefore mesh C is chosen, such a finest mesh not considering a major problem with regard to computational time.

### 3.4.5 Results

Results of the analysis are shown in Figure 3.33, where the comparison between the vertical velocities  $V$  (with respect to the mean velocity  $U_0$ ) is plotted. The difference between the SST and the ASST models is dramatic: as expected, the isotropic SST model cannot account for flow anisotropies resulting in the corner vortices, giving a vertical velocity identically equal to 0. On the other hand, the anisotropic formulation of the ASST model provides results that approach those of the Stress Omega model, which is the only one that correctly takes into account anisotropy and turbulence history. In this sense, the Stress Omega model provides the best approximation of the velocity maximum value, even though the profile is somehow smoother than expected. ASST model provides a lower maximum value but seems to reproduce better the global trend.

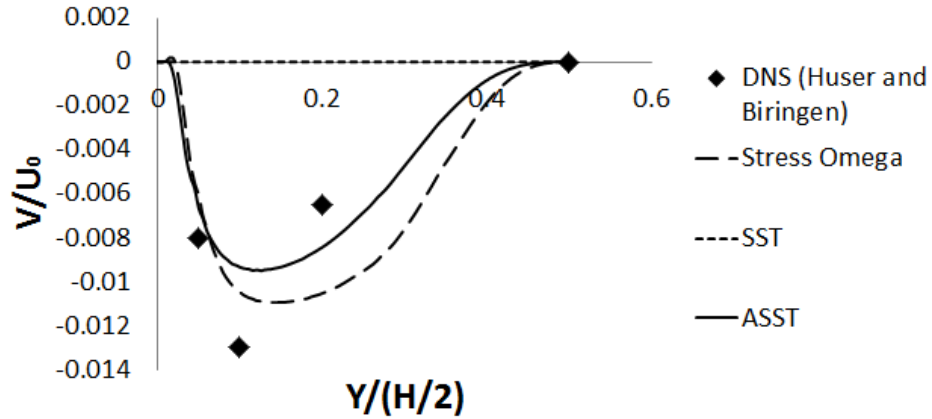


Figure 3.33 - Vertical velocity for a straight duct of squared cross-section

### 3.4.6 Conclusions

The potential of a non-linear eddy viscosity formulation is clearly shown: this can dramatically increase model's capability to correctly compute very complex flows.

## 3.5 SECONDARY MOTION IN TIGHT LATTICE ROD BUNDLE

### 3.5.1 Motivation

Fluid flow inside rod bundles is of interest in many engineering applications such as steam generator shell side or nuclear fuel assemblies. Secondary motion in tight lattice rod bundle is one of the phenomena occurring and it is responsible for the high transversal mixing and turbulence. The model capability to accurately predict this secondary motion is of primary importance to apply the model to more complex flows, where secondary motion is of the same order of magnitude as the primary flow. Since it is thought that secondary motion is very important in the innovative channel, it is worth studying the model capability in the present test case to verify whether the secondary motion is well predicted or not.

### 3.5.2 Test configuration

The geometry of triangular lattice is shown in Figure 3.34. See that this geometry is composed of six elementary modules (in grey), which are connected by symmetry conditions. Hence the chosen geometry is the one in dark grey in Figure 3.34 to minimize the geometry extension and maximize the meshing size. The geometry is that of measurements of Mantlik et al.<sup>87</sup>.

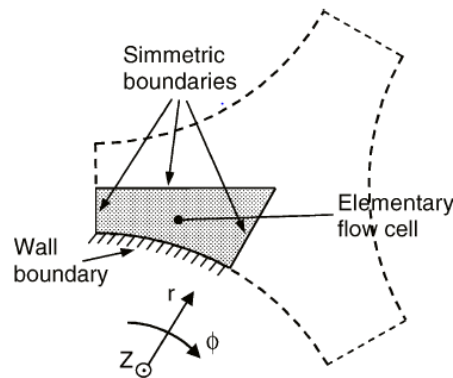


**Figure 3.34 - Tight lattice rod bundle test configuration<sup>87</sup>**

### 3.5.3 Numerical discretization

The solver is the Pressure-based one and the SIMPLE pressure-velocity algorithm with pseudo-transient option is used. Gradients are evaluated through the Least Square Cell Based method. Finally the Second Order Upwind Scheme is used for the spatial discretization of momentum, turbulent kinetic energy, turbulent dissipation rate and the Reynolds Stresses equations of the RSM model. Convergence criteria are based on a value of  $10^{-5}$  (absolute residuals) for all transported variables.

### 3.5.4 Mesh convergence evaluation

Three different grids have been used to verify the mesh convergence. They are show in Table 3.13 and differ by a factor of around two in the  $y^+$  value.

Mesh ID	$Y^+$	$T_w$
A	1.53	0.845 Pa
B	0.92	0.823 Pa
C	0.56	0.819 Pa

**Table 3.13 - Rod bundle grid convergence evaluation**

Again, since no major difference is detected between mesh B and C the final mesh is configuration C, since no greatly increased computational time is needed to calculate the finest mesh. Mesh C is shown in Figure 3.35.



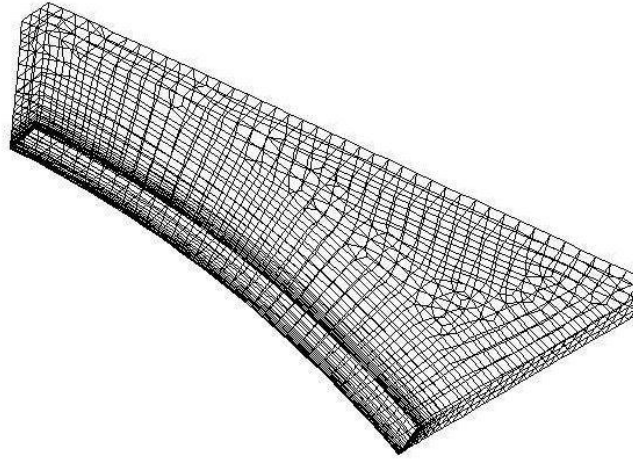


Figure 3.35 - Tight lattice rod bundle final mesh

### 3.5.5 Results

Secondary motion plays a primary role in this flow configuration. It is clearly visible when looking at the wall shear stress distribution shown in Figure 3.36. In fact, the isotropic SST model predicts a monotonically increase of the wall shear stress with the angular position, which is in contrast with the experimental measurements. Again see that the anisotropic formulation dramatically improves the prediction for the ASST model that correctly reproduces the trend both qualitatively and quantitatively. Baglietto et al.<sup>95</sup> affirm that the improvement is due to the  $C_{NL2}$  coefficient (see Eq.25), whose value has been increased with regard to the original one proposed by Shih et al.<sup>90</sup>. In this sense, it is worth showing the shown wall shear stress is equal to  $\tau_w = \mu \frac{\partial W}{\partial y}$ , where  $W$  is the velocity component tangential to the wall and  $y$  is the direction normal to the wall. Therefore it is clear that the anisotropic formulation better captures the secondary flow field, resulting in the proper velocity scale all along the wall. It has also to be noted that the isotropic formulation of the SST model results in a quasi-symmetric wall shear stress distribution, since the model cannot capture the correct scale of secondary motion. In this sense, it has already shown by Baglietto et al. that the original value of the  $C_{NL2}$  coefficient did not result in a major improvement. Moreover, it could not represent the non-monotonic shape of the wall shear stress distribution, where seems to be one of the hardest result to obtain. In this sense, the new  $C_{NL2}$  coefficient equal to eleven does produce better results<sup>XIV</sup>. Indeed it is worth noting the very strange behaviour of the

<sup>XIV</sup> Note that the present test case is the principal case used by Baglietto et al. to motivate the increased  $C_{NL2}$  coefficient value.

Stress Omega model, which correctly reproduces the low-angle region but completely fails to predict the region where  $\phi \approx 30^\circ$ , which is typically the region where the wall shear stress decreases due to adverse pressure gradient and secondary motion effects.

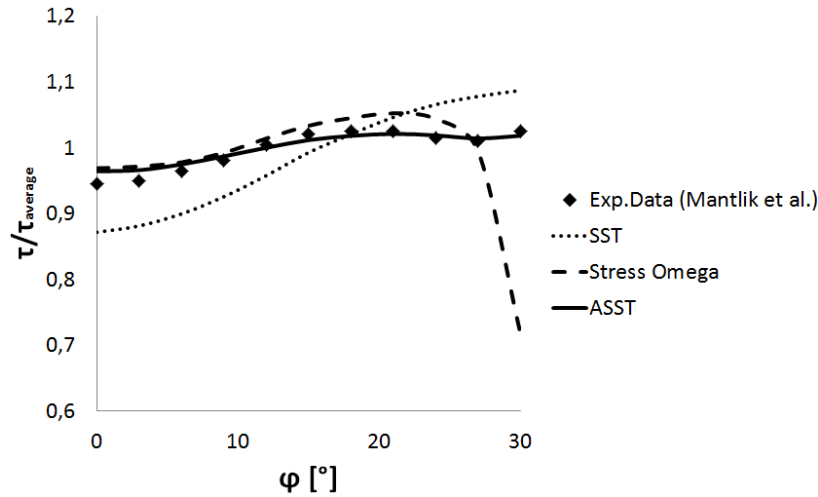


Figure 3.36 - Non-dimensional wall shear stress versus angular position

### 3.5.6 Conclusions

Results show again how the ASST model is a valuable model to predict complex flows where anisotropy and secondary motions play a major role. In this case, it results to be the best model, due to the SST model inability to reproduce the correct trend of the wall shear stress in tight bundles and to the Stress Omega model poor performance in the high strain region (high angular position). The major improvement is due to the increased value of the  $C_{NL2}$  coefficient, which is responsible for the scale of secondary motions. ASST model's performance results even more valuable taking into account the minor added computational time needed with respect to the SST model, which is always far shorter than that needed to perform a full Stress Omega calculation.

## 4. CONCLUSIONS

The aim of this section was to preliminarily investigate the behavior of three  $\omega$ -transport equation based turbulence models, responding to three different modeling approaches: isotropic eddy viscosity SST model, Reynolds Stress Transport Stress Omega model and a new non-linear eddy viscosity ASST model. The ASST model has been developed based on theoretical assumptions and it presents the beneficial feature to be a fully realizable model, which means that spurious and non-physical turbulent characteristics are avoided thanks to mathematical and physical considerations. The model has been first tuned to work correctly in the log-layer of a shear flow, then it has

been implemented into the solver via User Defined Functions. Finally it has been validated against experimental data, together with the SST and the Stress Omega models. The three models have identical performances for straight channel flow (basically having been developed for such a flow), differing only in the ability to reproduce turbulence driven anisotropies. This macroscopically results in a good behavior of the ASST and Stress Omega model to reproduce corner vortices in a straight duct a squared cross-section and turbulence characteristics in a 90° bend. Anyway the confidence towards a broader applicability of the Stress Omega model is questioned by two unexpected results found in the Backward Facing Step and Tight Lattice Rod Bundle cases: in the former, the Stress Omega predicts a shorter reattachment length than expected (which is in contrast with its developer's guideline); in the latter, the Stress Omega model fails in the high strain rate region, providing a dramatic decrease of the wall shear stress compared to experimental measurements. This is in contrast with its potential ability to provide very truthful results for such relatively simple flows. In this sense, it seems that the ASST model can provide a valuable alternative, giving global results that are at least as good as those of the Stress Omega model. Moreover, it keeps a very shorter computational time than the Stress Omega model, resulting to be a very good option for the desired industrial tool to potentially describe the innovative channel flow. See however that none of the shown test cases really represents the complexity of the innovative channel flow, which can be considered as a sum of all these test cases. Therefore this section clearly identifies the need of an experimental database for the innovative channel flow to validate the numerical model and the channel performance. The acquisition of this database is the object of the following Chapter.

As a final comment, it had been stated that non-linear eddy viscosity models result in a low additional computational effort compared to linear eddy viscosity models. In this sense, see that, for the case discussed in Section 3.1 – Channel flow, the computational time for the three tested models is about 2 minutes for the SST and ASST model (the difference was hardly detectable) and around 4.5 minutes for the Stress Omega model. This computational times are based on a 30 000 element meshing and have been evaluated on a single processor Intel Xenon E5440 machine at 2.83 GHz and 24 Gb RAM.

# Chapitre 4: Acquisition de la base de données expérimentales

Les chapitres 2 et 3 ont souligné le besoin d'une base de données expérimentale pour valider le modèle numérique et pour étudier l'écoulement dans le canal innovant. Dans le cas d'un canal pour un échangeur de chaleur, les besoins de validation concernent à la fois la description purement aérauliques et la description thermique. Pour la partie aéraulique deux bancs d'essai de vélocimétrie laser ont été mis en place : un banc de vélocimétrie laser à franges (LDV) et un banc de vélocimétrie laser par images de particules (PIV).

La campagne de LDV a permis d'acquérir une très grande base de données sur les vitesses d'écoulement et sur les fluctuations de vitesse dans plusieurs régions du motif innovant. Ces données sont très utiles pour la validation du modèle numérique, car ils permettent un accès géographique aussi bien dans le fluide que dans la couche limite. Par contre d'un point de vue physique, la vitesse verticale dans les profils orthogonaux à la zone de mélange, responsable du mélange, n'a pas pu être mesurée. Cette information peut être néanmoins retrouvée par la modélisation, une fois cette dernière validée. Les données acquises confirment l'hypothèse de conception en termes de développement de l'écoulement (qui est réalisé après quatre coudes) et la symétrie de l'écoulement, qui ont été démontrés. Par contre la campagne expérimentale LDV ne permet pas d'avoir une vue d'ensemble de l'écoulement du canal, qui est difficile de déduire des données acquises sur les profils locaux. Pour cela, la campagne PIV, moins précise en proche paroi, a permis l'acquisition de ces champs globaux sur le plan de mesure.

La base de données PIV a été acquise avec un nombre d'images par mesure trop faible pour la convergence statistique de chaque mesure en raison de contraintes de temps. Cependant, la convergence statistique non-parfaite a été prise en compte dans l'évaluation des incertitudes, en permettant une analyse correcte des données acquises. Ces données permettront de vérifier le comportement du modèle numérique tout en révélant les caractéristiques globales d'écoulement qui n'ont pas été observées au cours de la campagne LDV et qui seront discutées dans le Chapitre 5. La vérification du développement et de la symétrie de l'écoulement est importante pour valider l'hypothèse de conception. En ce qui concerne la validation thermique, un banc d'essai VHEGAS a

été conçu et mis en place pour mesurer le coefficient d'échange global du motif innovant. Deux essais ont été menés avec des densités de flux de chaleur différentes, pour analyser les effets potentiels de compressibilité thermique.

# Chapter 4: Experimental database acquisition

## 1. LASER DOPPLER VELOCIMETRY MEASUREMENTS

### 1.1 LASER DOPPLER VELOCIMETRY TECHNIQUE DESCRIPTION

Laser Doppler Velocimetry (LDV) represents one of the most used velocimetry techniques. It is widely used today both in the research and in the industrial sectors.

For our purposes, a 2 component LDV has been evaluated as a suitable measurement technique, taking into account technical and practical constraints in terms of timing, planning, cost and capability to properly show the boundary layers. The description of the LDV technique will be briefly exposed first and then the experimental facility will be described in the next section.

As most of the laser velocimetry techniques, it uses micro-scale particles to feed the fluid flow. These particles diffuse light when they go through a laser light. Therefore feeding particles are injected into the fluid flow in order to be detected by the acquisition system. The feeding particles must be sufficiently small to make the hypothesis that they flow with the the same fluid velocity i.e.

$$V_{fluidflow} = V_{feedingparticles}$$

In LDV, two laser beams are generated by a beam separator. Then they cross each other into the fluid flow with a characteristic angle  $\beta$ . The crossing zone is called measurement volume. See Figure 4.1 for explanation:

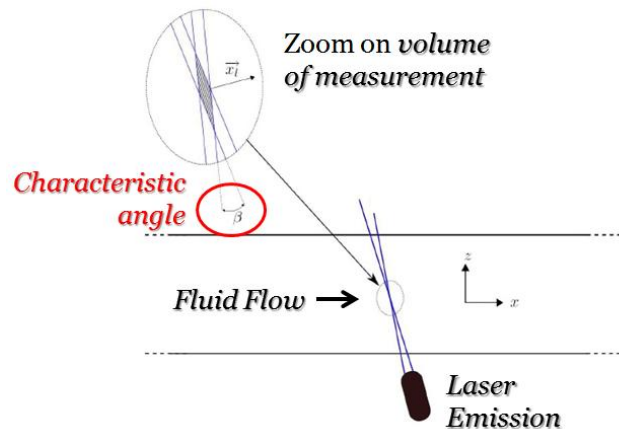


Figure 4.1 - LDV technique principle

Particles passing through the volume of measurement are detected and their velocity can be measured as described hereafter.

In fact once the angle  $\beta$  is measured during the calibration process, the inter-fringe distance is calculated:

$$i = \frac{\lambda}{2 \sin(\beta/2)}$$

The particles going through the fringes spark, creating a light signal like the one shown in Figure 4.2. A photomultiplier can acquire that signal and transfer it to a digital receiver. This latter measures the frequency “f”, giving the value of the actual velocity component orthogonal to the fringes by:

$$V = i \cdot f$$

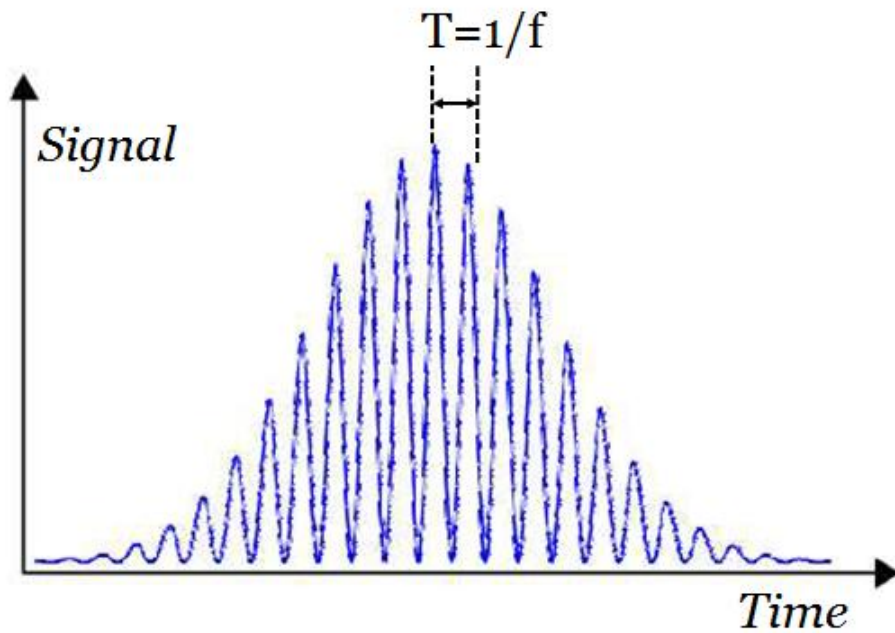


**Figure 4.2 - Light signal of a single measurement**

Indeed, to be able to see the difference between two particle with equal velocity module but in opposite directions, a Bragg frequency (B) shifting is used. In this way fringes move in the opposite direction than measured velocity component. Finally the actual velocity can be expressed as:

$$V = i \cdot (f + B)$$

## 1.2 EXPERIMENTAL FACILITY AND CALIBRATION

### 1.2.1 Experimental facility description

First of all the test section is presented. To simulate the innovative channel fluid flow, only a pair of superposing wavy channels is used, to form a single channel (like the one shown in Figure 4.3)<sup>xv</sup>.

Preliminary calculations showed that the inlet straight length does not really change the complete flow development, which seems to be reached after four bends. Hence, we decided to use a six bend channel to measure a fully developed flow in the last bend and mixing zone. The LDV technique needs two optical accesses (for laser emission and reception) to the test section (see Figure 4.2), which are typically on parallel planes. Hence two optical quality glass windows are put in the measurement test section. In the other parts of the test section aluminum is used as structural material whereas PMMA is used to constantly visualize the state of the wall (i.e. if there were DEHS spots, see Section 1.2.1). The channel is designed in terms of Reynolds similarity (inlet hydraulic diameter of 60mm, corresponding to an inlet Reynolds number of 47 600) with actual heat exchanger conditions, to provide trustful results to the aerodynamic validation. The two half channels have a rectangular cross-section of 60mm x 30mm. Measurements are done with air at atmospheric pressure and temperature.

The test section is shown in Figure 4.3 and Figure 4.4, while its geometrical characteristics are shown in Table 4.1:

---

<sup>xv</sup> Therefore we will hereafter use the term « bend » to indicate both the pair of opposite bends representing portion of the channel between two mixing zones and the single bend where measurements are done (see Section 1.3).



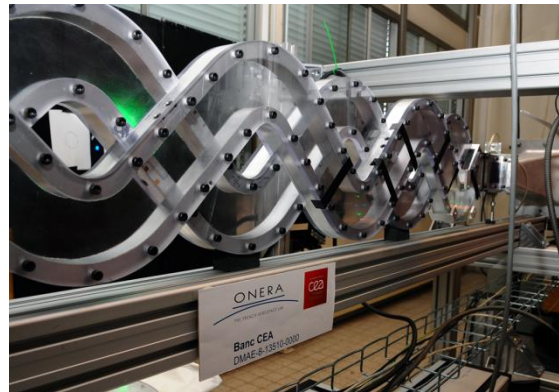


**Figure 4.3 - Global view of the LDV test section**

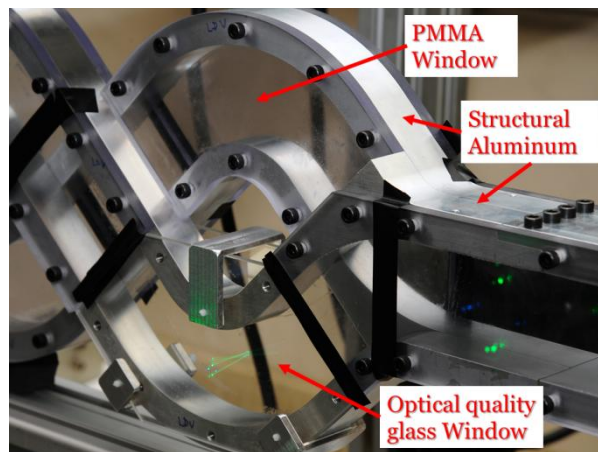


**Figure 4.4 - LDV test section material description**

LDV channel geometry	
Angle	45°
Straight distance between bends	173.9 mm
Bend radius of curvature	86 mm
Total channel height	60 mm

**Table 4.1 - LDV channel geometrical characteristics**

The experimental facility scheme is shown in Figure 4.5:

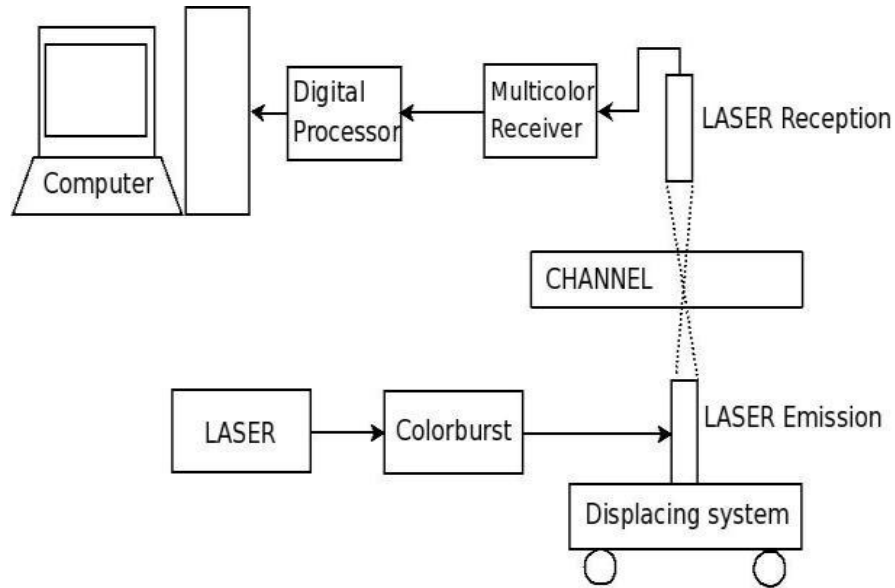


**Figure 4.5 -General scheme of the LDV experimental facility**

Since a 2-components LDV system is foreseen, a laser which can provide two pair of colors must be used.

The used laser is a Spectra Physics Stabilit  2017 Argon Laser, coupled to a TSI Colorburst Multicolor Beam Separator Model 9201 (the both shown in Figure 4.6) to split the two pair (blue and green) of beams and to provide the Bragg frequency shifting (10 MHz).

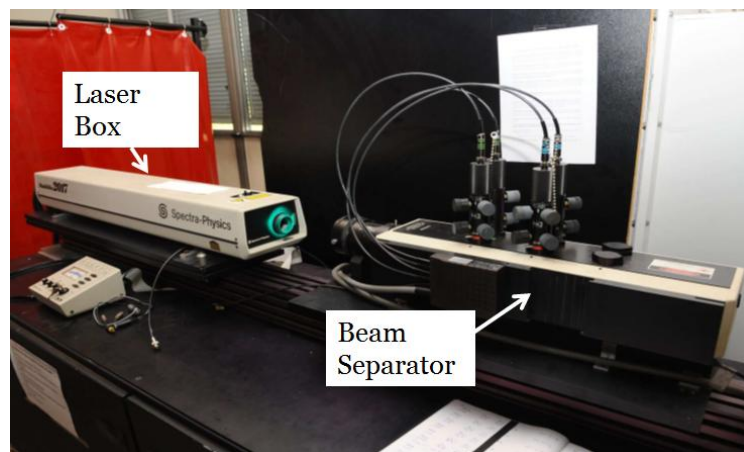


**Figure 4.6 - LDV Laser generator**

The laser power during the experimental tests is around 1 W. The laser emission (which creates the measurements volume by intersecting two beams per color) is

shown in Figure 4.7, whereas the laser reception is shown in Figure 4.8, together with the ISEL displacing system:

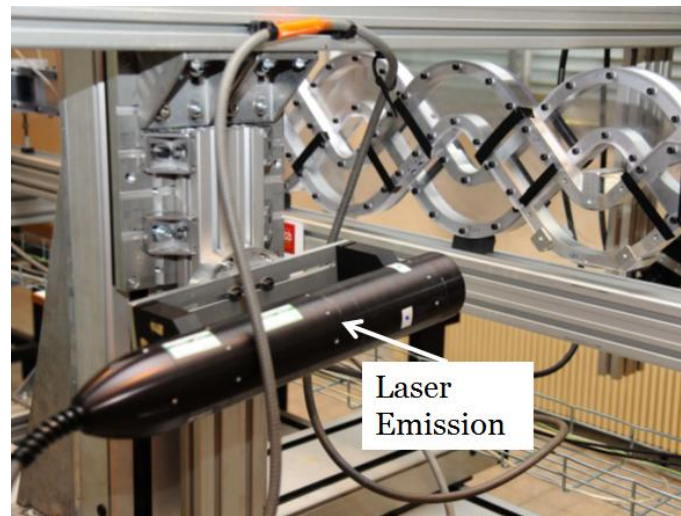


**Figure 4.7 - LDV Laser emission**

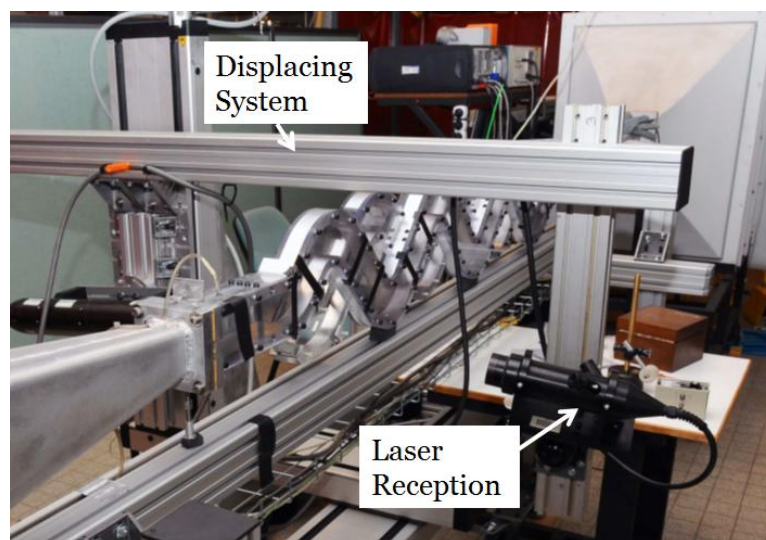


**Figure 4.8 - LDV displacing system and laser reception**

The volume of measurement is shown in Figure 4.9. See in particular the intersection of the two pairs of green and blue laser beams.

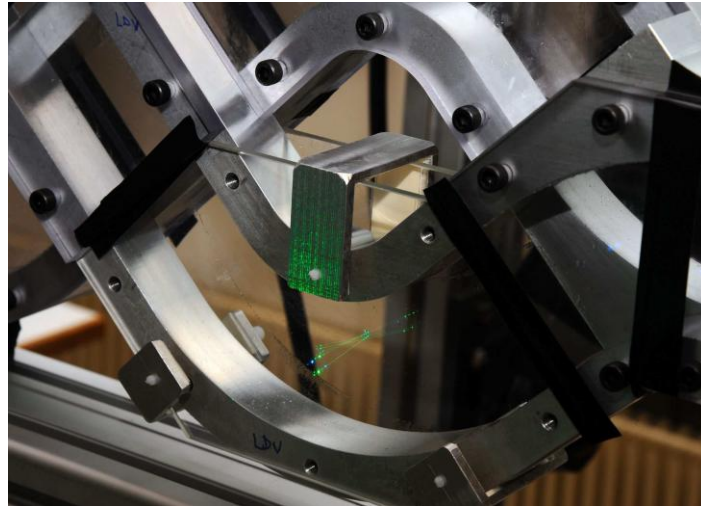


**Figure 4.9 - LDV volume of measurement (on laser beams crossing point)**

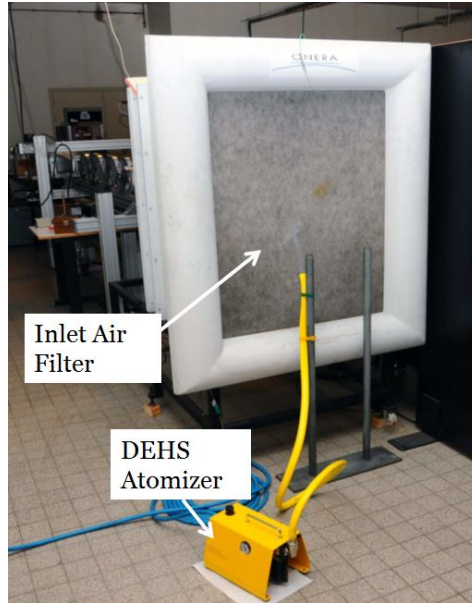
The acquisition chain is shown in Figure 4.10: it consists on a TSI Colorlink Plus Multicolor Receiver Model 9230 (converting light reception to electrical signal for each color) and a TSI FSA4000 Multibit Digital Processor (to provide digital data to the post-processing computer).



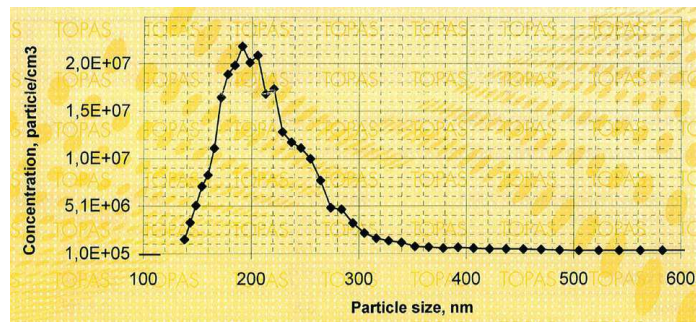
**Figure 4.10 - LDV acquisition chain**

The visualization particles are Di-Ethyl-Hexyl-Sebacat (DEHS) droplets. Droplets are created by a “TOPAS ATM 210” atomizer (Figure 4.11), fed by pressurized air. The droplet size map is shown in Figure 4.12:





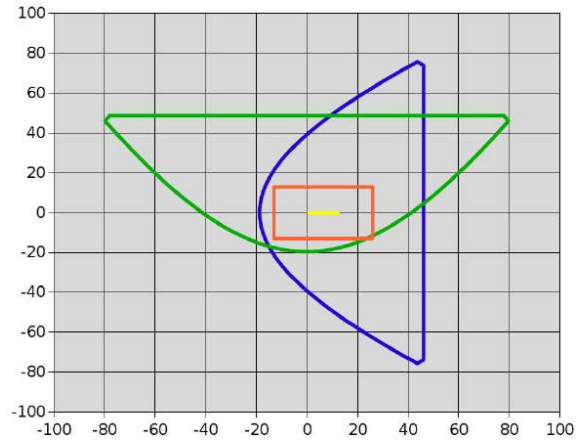
**Figure 4.11 -LDV feeding system**



**Figure 4.12 - DEHS droplet size map**

### 1.2.2 Calibration and testing

First of all the measurable domain has been set up. Figure 4.13 shows two domains characterized by a green and a blue line respectively. They represent the measurable domain by the pair of green and blue laser beams. To be able to measure at the same time (i.e. by the mean of the detection of same particle) the two velocity components, the actual measurable domain must lie in the intersection area. Orange line limited domain is the final measurable domain, lying in the area that can be measured both by the green and the blue pair of laser beams. Hence in every point of the orange rectangle two velocity components can be measured by the detection of only one particle.



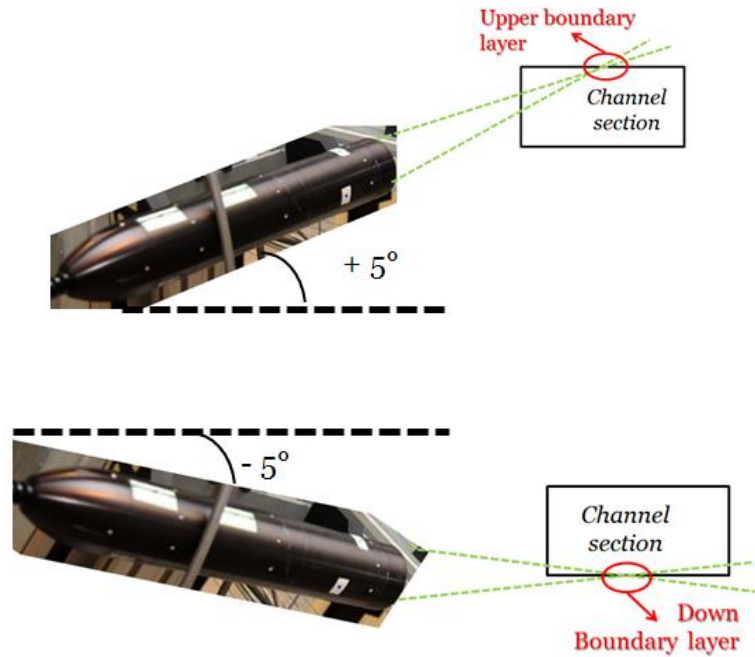
**Figure 4.13 - LDV laser beam measurement domain**

Table 4.2 shows the principal parameters of the laser beams used during the test campaign.

<b>Data/Color</b>	<b>Green</b>	<b>Blue</b>
Wavelength $[nm]$	514.5	488.0
Beam Diameter $[\mu m]$	90.42	85.76
Beam intersection major dimension $[mm]$	1.32	1.25
Fringe Spacing $[\mu m]$	3.70	3.52
Bragg Frequency $[MHz]$	10	10

**Table 4.2 - Laser Beams major parameters**

In order to measure both the upper and the bottom boundary layer, the laser emission and reception had to be changed in inclination with respect to the horizontal reference. See Figure 4.14 for visual explanation (note that only green laser beams are shown for sake of simplicity).



**Figure 4.14 - Laser emission double configuration (upwards and downwards) respectively**

Moreover, since the laser displacement system was not long enough to allow the measurements of the entry conditions, another modification of the system had to be done. For each laser emission setup, a new calibration is necessary to measure the actual angle of each beam with respect to an absolute system of coordinates (i.e. the room). This angle will allow calculating the correct correlation matrix to obtain the actual velocities. To calibrate the LDV system a Theodolite Wild T2002 was used (Figure 4.15).



**Figure 4.15 - Theodolite used for laser calibration**

Calibration results are correlation matrices to correctly calculate the measured velocity component. An example of the calibration results is shown in Appendix C.

The Data post processing has been done with the ASSA code, which has been developed at ONERA (References <sup>106</sup>, <sup>107</sup>). Using the calibrations matrices the code is able to provide actual measured velocities as well as Reynolds stresses and several other statistical parameters to be potentially used in data analysis.

### 1.2.3 Flow stability visualization and control

Test conditions have been continuously acquired during the LDV campaign. This allows an accurate description of the ongoing measurements with regard to the following numerical modeling. In particular, room turbine temperature, turbine rotation frequency, channel pressure drop and flow mean velocity could be *in continuo* visualized and stored. All the test instrumentation is connected to a National Instrument (NI) acquisition system, which consisted of:

- Acquisition card PCI-6052E;
- Box type SCXI-1000
- 1 module type SCXI-1102 associated with 1 rack TC-2095: 4x32 thermocouples
- 1 module type SCXI-1125 associated with 1 connection box SCXI-1328 with 8 /current inputs for: air room temperature, turbine rotation frequency, turbine pressure and channel inlet/outlet pressure difference.

Control station is shown in Figure 4.16:

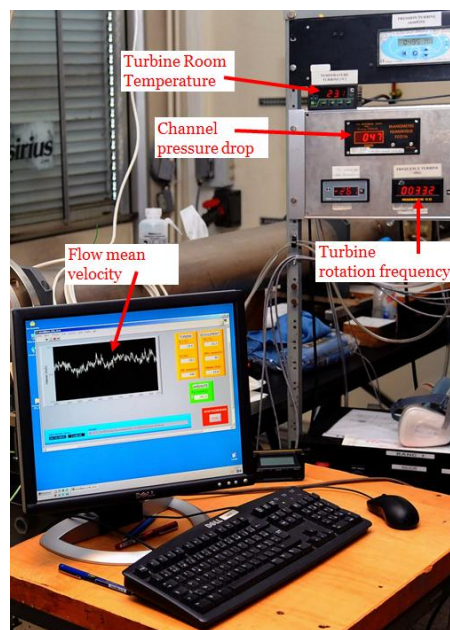


Figure 4.16 - Flow control station



The acquisition software is programmed under LABVIEW, specifically set in order to show and save visualized test conditions. In particular, data are stored every second all over the campaign.

The shown parameters are measured by the following means:

- An INSTROMET turbine for the volumetric flow rate associated with a frequency meter FC22;
- Probe type PT100 for the air temperature, associated with a monitor SFERE DIGINORM 105;
- FURNESS Model 318 manometer for the turbine pressure.
- FURNESS FC016 for the channel pressure drop.

To check the flow stability, an example (for turbine room air temperature in blue and flow mean velocity in red) is given in Figure 4.17:

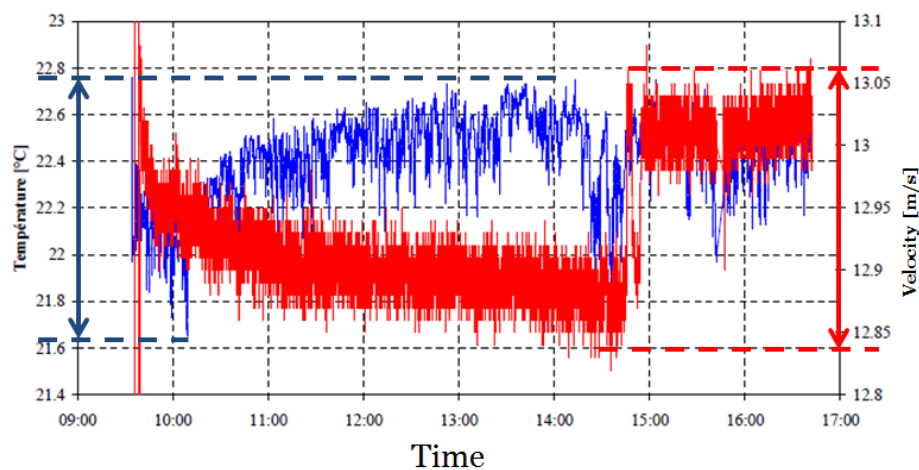


**Figure 4.17 - Flow velocity control over a day**

See that during a typical day the flow mean velocity tends to decrease of about 1.2% in 5 hours with regard to the reference value of 13 m/s. A manual adjustment is necessary in order to reset the velocity to a proper value. During the experimental measurements we assure that the velocity oscillations did not vary more than  $\pm 0.8\%$

(i.e.  $\pm 0.1$  m/s) all over the campaign. Anyway the flow test clearly shows that the flow is stable and the no macroscopic oscillatory phenomenon is detectable. Therefore the LDV averages do make sense for the subsequent analysis.

On the other hand, temperature oscillations varied no more than  $1.2^{\circ}\text{C}$  during that day. In general we can assure that temperature did not vary significantly during the experimental campaign. Hence air properties will be always considered constant at atmospheric pressure and temperature (specifically  $T_{atm} = 23^{\circ}\text{C}$  and  $p_{atm} = 101325 \text{ Pa}$ ).

### **1.3 EXPERIMENTAL CAMPAIGN DESCRIPTION**

#### **1.3.1 Experimental measurement program definition**

The experimental campaign has been defined in the following way: first of all, critical zones of interest have been identified, to be able to have a good overview of the fluid flow with regard to the numerical validation. Hence the inlet section (Figure 4.19), the last mixing zone as well as the last bend (Figure 4.20) are chosen as reference regions to investigate channel flow. Moreover, to verify flow development (hence the design hypothesis) the fourth and fifth bends are studied as well. Since measuring a whole cross-sections was impossible with regard to the set time schedule, only a few profiles on different cross-sections have been identified to be studied. In particular the strategy has been to always measure the two centerlines along plane main axis (i.e. Y and Z for all the planes but the mixing plane where X and Z axis are used). Moreover, two equally spaced profiles which are parallel to the main ones are used, in order to gather as much information as possible and considering that investigating the whole plane was unrealistic.

Prior to describe the experimental campaign it is worth showing the general test section system of coordinates in Figure 4.18.

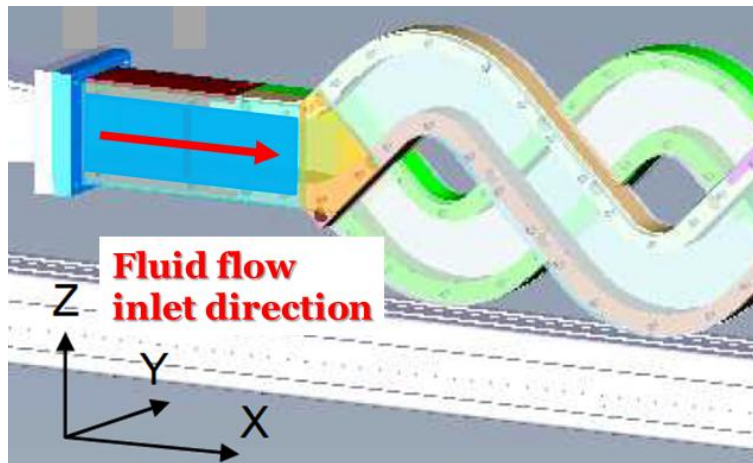


**Figure 4.18 - System of coordinates for LDV measurements**

The X, Y and Z axis are the global (i.e. room) system of coordinates: However it can be more practical to refer to local systems of coordinates, i.e.  $X^*$ ,  $Y^*$  and  $Z^*$ . In fact it is sometimes useful to compare different profiles lying in different planes (having the same geometrical shape but generally different global coordinates) using a local system of coordinates. Hence we will adopt the following local systems of coordinates, shown in Table 4.3, when considered as useful (note the  $X^*$  coordinate is never mentioned, since almost useless for data analysis):

Inlet Section	Bend	Mixing Zone
$0 < Y^* < 1$ for $0 < Y < 60$ mm $0 < Z^* < 1$ for $0 < Z < 60$ mm	$0 < Y^* < 1$ for $0 < Y < 30$ mm (Y being, in each measured cross section, the direction shown in Figure 4.18) with $Y^*=0$ being the wall having the same global Y coordinates as the mixing plane.. $0 < Z^* < 1$ for $0 < Z < 60$ mm (Z being, in each measured cross section, the direction shown in Figure 4.18)	$-1 < Y^* < 1$ for $0 < Y < 60$ mm (Y being, in each measured cross section, the direction shown in Figure 4.18), with $Y^*=0$ being the point lying on the mixing plane. $0 < Z^* < 1$ for $0 < Z < 60$ mm, with $Z^*=0.5$ being the point lying on the mixing zone middle plane normal to the mixing plane.

**Table 4.3 - LDV local systems of coordinates description**

See in Figure 4.19 to Figure 4.22 the visual explanation of the measured planes and system of coordinates.

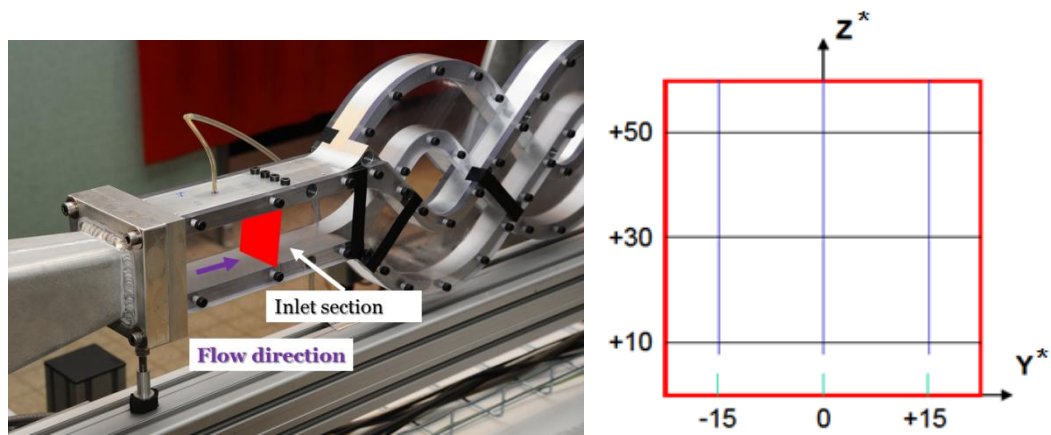


Figure 4.19 - Inlet section measured profiles

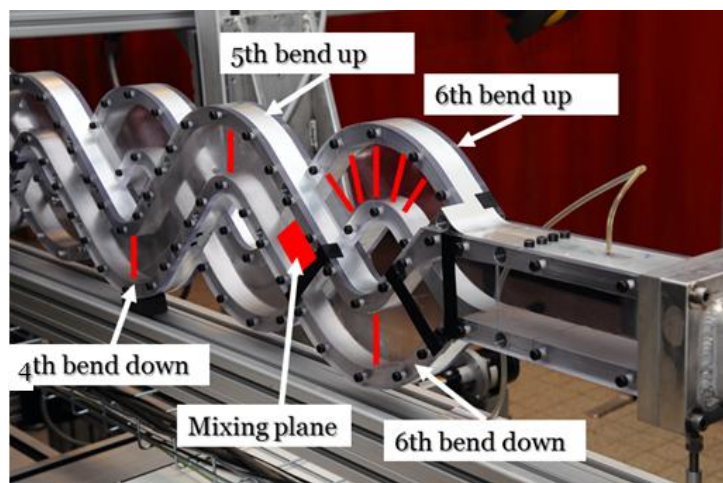
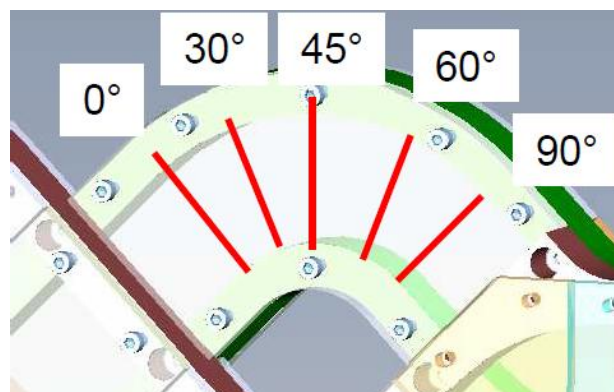


Figure 4.20 - Bend and mixing zone experimental campaign description



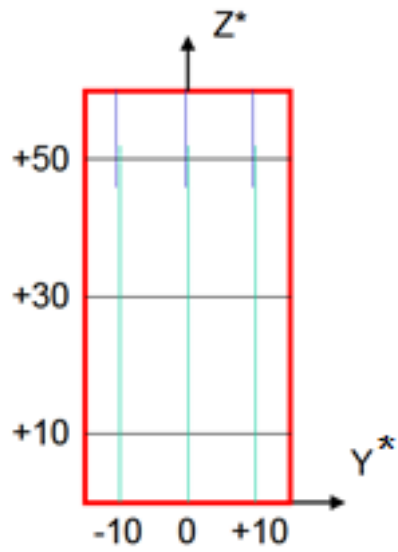


Figure 4.21 - Measurements of the In-bend flow

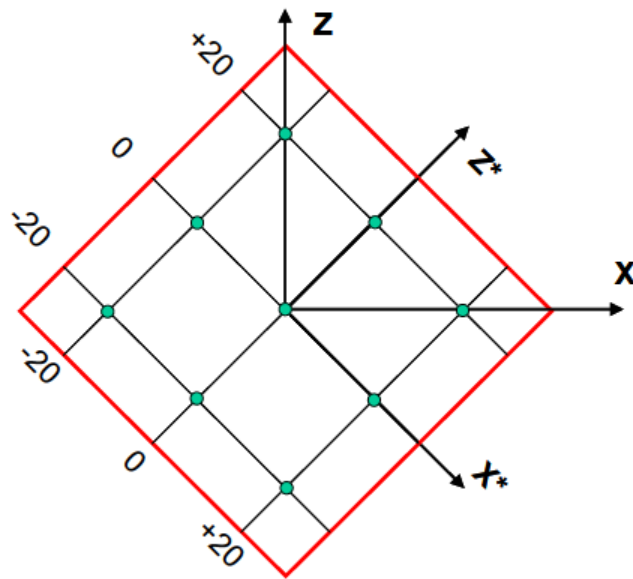


Figure 4.22 - Measurements in the mixing zone

Once defined the local systems of coordinates, it is worth showing the experimental campaign description in Table 4.4.

Inlet Section	Bend	Mixing Zone
<p>One cross-section</p> <ul style="list-style-type: none"> <li>• Three Z profiles</li> <li>• Three Y Profiles</li> </ul> <p>Two laser emission inclinations:</p> <ul style="list-style-type: none"> <li>• <math>+5^\circ</math> for <math>7.6 \text{ mm} &lt; Z &lt; 60\text{mm}</math></li> <li>• <math>-5^\circ</math> for <math>0 \text{ mm} &lt; Z &lt; 2.6 \text{ mm}</math></li> </ul>	<p><u>6<sup>th</sup> bend up</u>: Five plans (corresponding to five angles i.e. <math>0^\circ</math>, <math>30^\circ</math>, <math>45^\circ</math>, <math>60^\circ</math>, <math>90^\circ</math>)</p> <ul style="list-style-type: none"> <li>• Three Z* profiles</li> <li>• Three Y Profiles</li> </ul> <p>4<sup>th</sup> bend up, 5<sup>th</sup> bend down and 6<sup>th</sup> bend down: One plan (corresponding to <math>45^\circ</math>)</p> <ul style="list-style-type: none"> <li>• Three Z* profiles</li> <li>• Three Y Profiles</li> </ul> <p>Two laser emission inclinations:</p> <ul style="list-style-type: none"> <li>• <math>+5^\circ</math> for <math>45 \text{ mm} &lt; Z &lt; 60\text{mm}</math></li> <li>• <math>-5^\circ</math> for <math>0 \text{ mm} &lt; Z &lt; 52 \text{ m}</math></li> </ul>	<p>One mixing plane (contact plane between the two superposed channels, <math>Y^*=0</math>)</p> <ul style="list-style-type: none"> <li>• Three Z* profiles</li> <li>• Three X* Profiles</li> </ul> <p>Nine profiles along Y (green point on Figure 4.22)</p> <p>Two laser emission inclinations:</p> <ul style="list-style-type: none"> <li>• <math>-5^\circ</math> All the measurements</li> <li>• <math>+5^\circ</math> to complete the mixing plane profiles for <math>X^* &lt; -14 \text{ mm}</math> and <math>Z^* &lt; -14 \text{ mm}</math></li> </ul>

**Table 4.4 -Experimental campaign description**

The definition of each profile meshing has been done in order to optimize the number of points of acquisition. The final decision is to have forty points along every Z\* profile (the total profile length is 60 mm) and thirty points along every Y profile (the total profile length being 30 mm). The density of the points of measurement is higher in the boundary layer region (to be able to get the maximum information in that region) and lower in the flow bulk region. Section 1.4 will visually clarify this point.

Before showing the measurements it is worth noting that a 5 mm zone in the inlet section has not been measured. This appears strange since a standard method has been employed for the definition of the points to be measured. In this sense, the “black” zone could be due either to an error in the profile definition when measurements have

been done or to a low-feeding zone that made it impossible to measure any velocity. For sake of clarity, the following adopted profile identification strategy will be adopted: for the bends, the Y-direction profiles are named as “z##”, where z is chosen because it is the coordinate that differs from one profile to another. ## is a number representing the z coordinate expressed in millimeters. For example, z30 is the Y-direction profile at the middle of the section shown in Figure 4.21. The same, but opposite, notation is used for the Z-direction profiles named “y##”.

For the mixing zone, it is more complicated to fix a unique notation strategy. Hence, for the moment, no assumption is done. Hence the used notation will be detailed in each specific section.

### 1.3.2 Preliminary tests: Measurement statistical convergence

Before starting the actual test campaign, a preliminary study has been done in order to establish the measurement statistical convergence. In fact, feeding particles seen by the volume of measurement need to be sufficient to make a correct statistics to determine (i.e. measure) their properties.

In particular, a test has been done acquiring data of a pre-fixed number of feeding particles (200 000) and then verifying whether measurements are converged and eventually for which number of acquisition.

Since it was unrealistic to carry out such analysis on the whole fluid channel (due to time schedule), the analysis has been done in bend in the intersection point of line  $Y=0$  and  $Z=+30$  in Figure 4.21 and in the central point of the mixing plane (i.e.  $X=0$ ,  $Z=0$  in Figure 4.22). Since results are the same with regard to the number of acquired particles, only results of the in-bend test will be shown. Note in Figure 4.23 that the two measured velocity components reach a statistical convergence with around 50 000 acquired particles. In fact, see the shown dashed lines corresponding to a range of  $\pm 0.3\%$  of the reference velocity (around 0.04 m/s) and note how the mean and fluctuating velocities always lies in this range for the converged situation. This means that after 50 000 acquired particles, the average value of the two velocity components does not practically change anymore. On the other hand this is not the case for fluctuating components: see in Figure 4.24 that a converged value is reached only after 100 000 acquired particles.

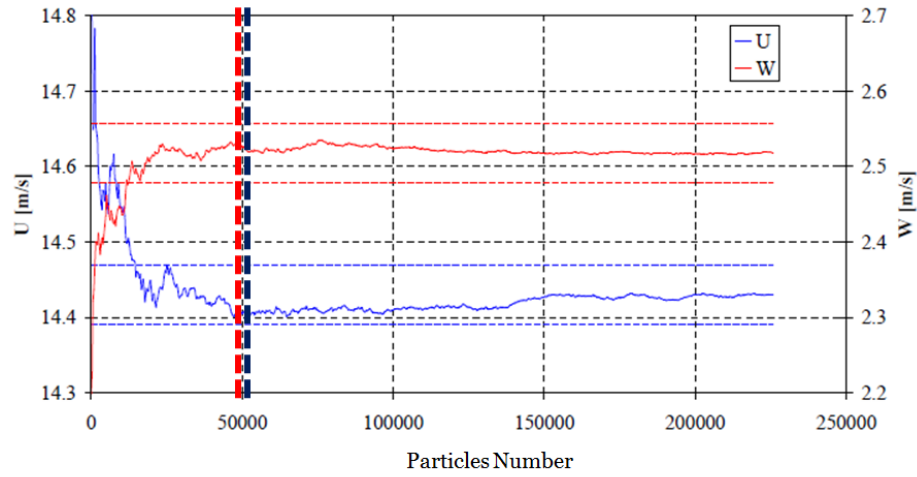


Figure 4.23 - Principal Velocity U convergence tests

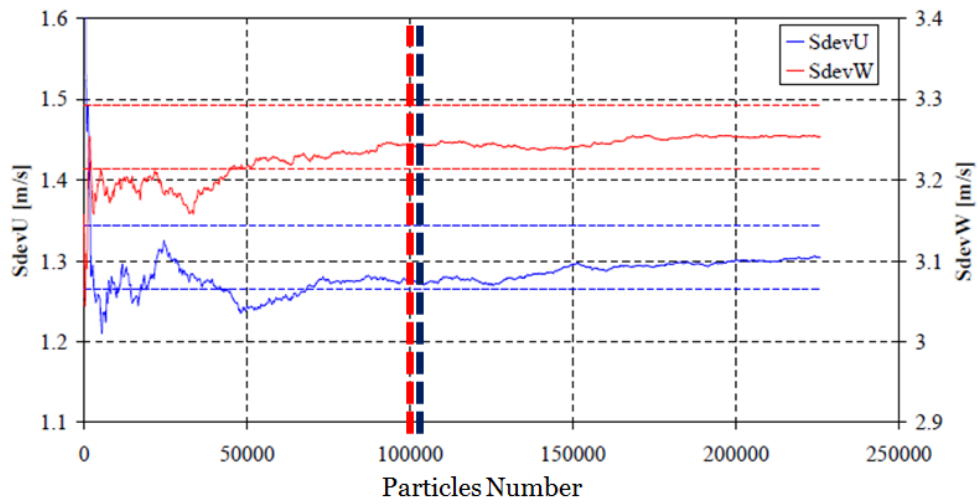


Figure 4.24 - Principal root-mean-square of the U velocity ( $u'$ ) convergence tests

This test led us to set a final number of acquired particles equal to 120 000, in order to have a margin for particularly hard convergence non-tested zones. Moreover, a 80 seconds time-out is selected in order to avoid too long acquisitions in low seeded regions. In fact, a usual acquisition in sufficiently high population regions lasts around 20 to 30 seconds.

### 1.3.3 Experimental uncertainty evaluation

Three types of uncertainties have been identified during the experimental campaign, specifically the uncertainty due to the data acquisition system, the uncertainty due to environmental conditions and the uncertainty due to the measurement volume position. Regarding the data acquisition system uncertainty, the



global system calibration gave a velocity standard deviation value never greater than 0.25% of the measured velocity. Moreover, a bootstrap statistical treatment implanted in the ASSA code has been used to quantify the resampling-related standard deviation. The two mentioned standard deviations are then summed up to have the acquisition system total standard deviation. In order to evaluate the experimental uncertainties in our measurements, two specific tests have been made: first, to be able to quantify the influence of external parameters such as low frequency velocity fluctuations, optical quality of the test section all over the measurements, in-day temperature variations etc. we performed a repeatability test consisting in repeating several times (i.e. around 400 times for the in bend flow and around 200 times for the mixing zone flow) the measurement at the same position. Once collected this data, the uncertainty in all statistical results has been calculated as the standard deviation of the sample with regard to the test mean value. Finally, to evaluate the uncertainty due to the measurement volume position, measurements have been done in the vertices of a cube centered in the reference point having the vertices at  $\pm 0.2$  mm from the center along the three axes X, Y, Z. See Figure 4.25 for visualization:

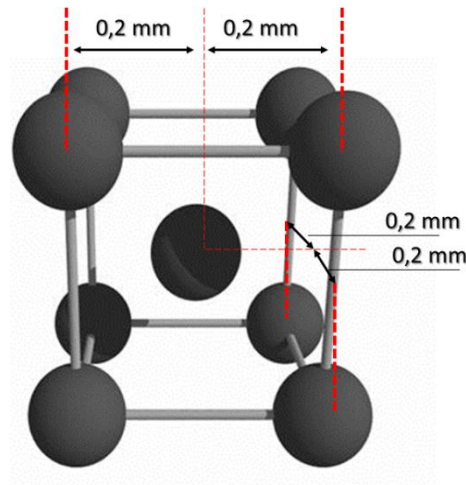


Figure 4.25 - Position uncertainty visual explanation

The final velocity uncertainty is calculated adding the three individual variances, defined as  $3\sigma$  where  $\sigma$  is the combined standard deviation determined by adding the variances of each source of uncertainty.

The final uncertainty analysis is shown in Table 4.5 to Table 4.8. Note that the evaluation is strictly valid only for the points where the repeatability and the position uncertainty tests have been performed (in fact, the measured values are also presented); nevertheless it gives a good evaluation of the global uncertainties for the actual flow.

	$\sigma$ System Chain	$\sigma$ Repeatability	$\sigma$ Position	Average U $\pm$ Total 3 $\sigma$ Uncertainty
Inlet Section	<b>0.032 m/s</b>	<b>0.015 m/s</b>	<b>0.012 m/s</b>	<b>13.18<math>\pm</math>0.11 m/s</b>
In-bend	<b>0.1 m/s</b>	<b>0.025 m/s</b>	<b>0.014 m/s</b>	<b>14.02<math>\pm</math>0.31 m/s</b>
In- mixing zone	<b>0.03 m/s</b>	<b>0.05 m/s</b>	<b>0.07 m/s</b>	<b>4.62<math>\pm</math>0.27 m/s</b>

**Table 4.5 - Velocity U Uncertainty Analysis**

	$\sigma$ System Chain	$\sigma$ Repeatability	$\sigma$ Position	Total 3 $\sigma$ Uncertainty
Inlet Section	<b>0.001 m/s</b>	<b>0.003 m/s</b>	<b>0.009 m/s</b>	<b>-0.03<math>\pm</math>0.03 m/s</b>
In-bend	<b>0.02 m/s</b>	<b>0.045 m/s</b>	<b>0.014 m/s</b>	<b>1.41<math>\pm</math>0.15 m/s</b>
In- mixing zone	<b>0.03 m/s</b>	<b>0.05 m/s</b>	<b>0.07 m/s</b>	<b>4.75<math>\pm</math>0.27 m/s</b>

**Table 4.6 - Velocity W Uncertainty Analysis**

	$\sigma$ System Chain	$\sigma$ Repeatability	$\sigma$ Position	Total 3 $\sigma$ Uncertainty
Inlet Section	<b>0.015m /s</b>	<b>0.003m/s</b>	<b>0.003m/ s</b>	<b>0.13<math>\pm</math>0.05 m/s</b>
In-bend	<b>0.01m/ s</b>	<b>0.013m/s</b>	<b>0.018 m/s</b>	<b>2.23<math>\pm</math>0.07 m/s</b>
In- mixing zone	<b>0.03m/ s</b>	<b>0.03m/s</b>	<b>0.03m/s</b>	<b>3.69<math>\pm</math>0.16 m/s</b>

**Table 4.7–u' Reynolds Stress Uncertainty Analysis**

	$\sigma$ System Chain	$\sigma$ Repeatability	$\sigma$ Position	Total $3\sigma$ Uncertainty
Inlet Section	<b>0.002m/s</b>	<b>0.006m/s</b>	<b>0.007 m/s</b>	<b>0.104±0.028 m/s</b>
In- bend	<b>0.02m/s</b>	<b>0.014m/s</b>	<b>0.018 m/s</b>	<b>2.93±0.09m /s</b>
In- mixing zone	<b>0.02m/s</b>	<b>0.04 m/s</b>	<b>0.024 m/s</b>	<b>3.82±0.15m /s</b>

Table 4.8–w' Reynolds Stress Uncertainty Analysis

Note that the position uncertainties are quite high and are responsible for a large part of the total uncertainty: indeed these high values are due to the high velocity gradients (hence the large amount of turbulence) in the fluid flow.

If the found uncertainties can be directly used to compare an actual measurement with an expected theoretical value, it is worth seeing how to use them when dealing with the comparison of two different measurements.

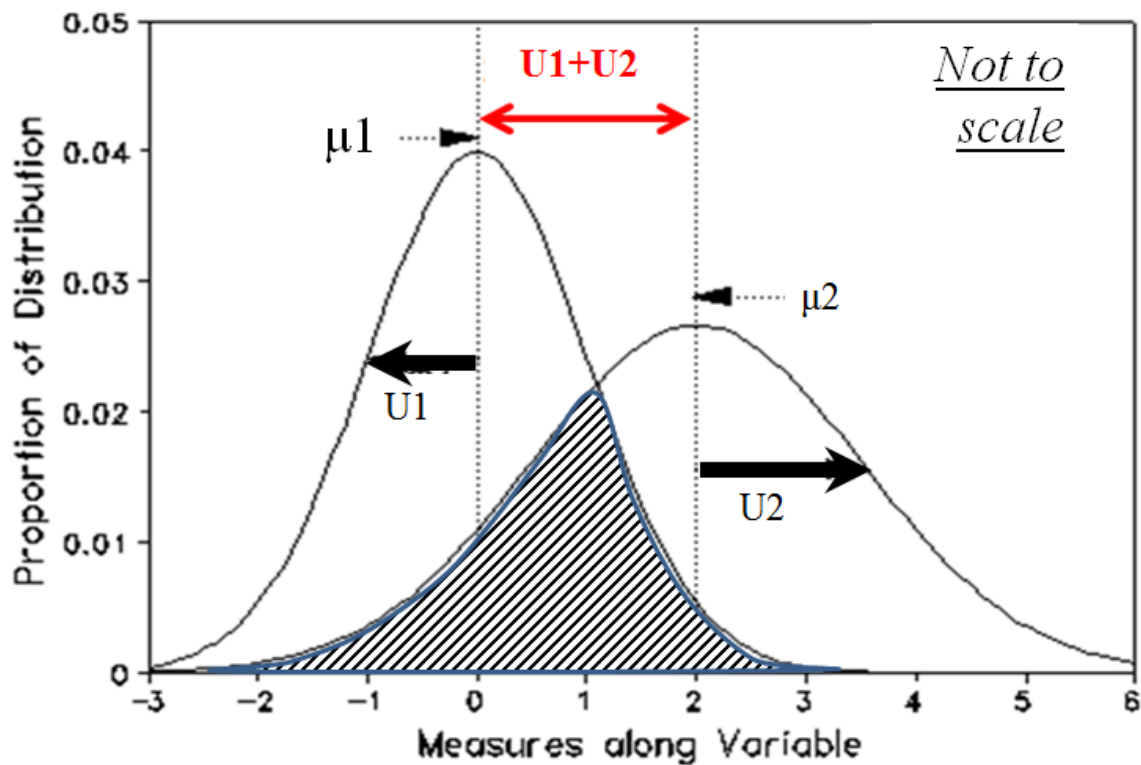


Figure 4.26 - Coincidence criterion with regard to experimental uncertainties

Given two measurements  $\mu_1$  and  $\mu_2$  distributed along two normal probability density functions, characterized by two uncertainties  $U_1$  and  $U_2$ , we can define:

$$U_1 = 3\sigma_1$$

$$U_2 = 3\sigma_2$$

Where  $\sigma_1$  and  $\sigma_2$  are the measurement standard deviations. The criterion to determine whether the profiles correctly match is the following (Figure 4.26):

$$|\mu_1 - \mu_2| < 2 \cdot (U_1 + U_2)$$

Corresponding to the dashed common region in Figure 4.26.

Finally, once described the uncertainty evaluation and utilization, preliminary measurements and analysis can be shown.

## **1.4 LDV EXPERIMENTAL MEASUREMENTS**

### **1.4.1 Flow Inlet Conditions**

First of all flow inlet conditions are studied, in order to verify the flow field that is going to influence the following measurements. Note that no asymmetry can be previewed at this stage. Hence a proper symmetric flow field is expected. Moreover no secondary velocity is expected, consistently with the experimental setup having a converged section before the channel inlet, which is supposed to provide an almost constant uniform velocity profile. It is worth noting that the measurements are not made in the inlet section, where there should be the uniform velocity field. Hence, a certain boundary layer should be present. Nevertheless, the secondary velocity is no longer expected, the flow supposed to be highly one-dimensional.

These measurements gave actual problems regarding their acquisition. In fact, as this section is very close to the inlet section, the injected DEHS particles did not have a sufficient degree of mixing to provide good quality populations (hence statistical relevance) to the measurements. See for example (Figure 4.27) the population for “y-15” axis set of measurements:

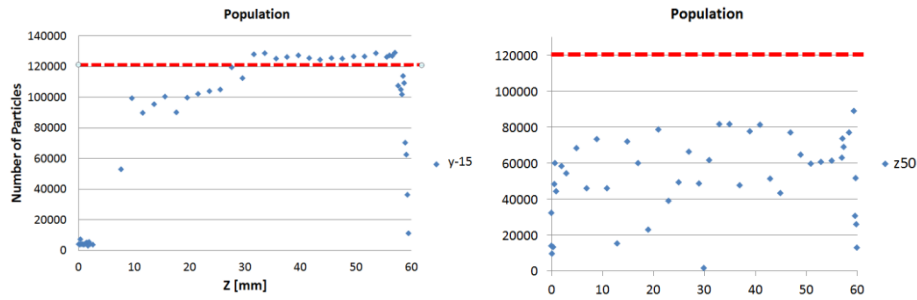


Figure 4.27 -Inlet section feeding particle population for y-15 and z50 profiles

See that, even in the core region, particles were not as many as 120000, which is the threshold set to have fully converged measurements (see section 1.3.2). Hence, while this is not supposed to result in bad velocity measurements (because of their faster statistical convergence), it might provide biased values for the velocity fluctuations.

Figure 4.28 and Figure 4.29 show the experimental measurements in the three Z axis of Figure 4.19.

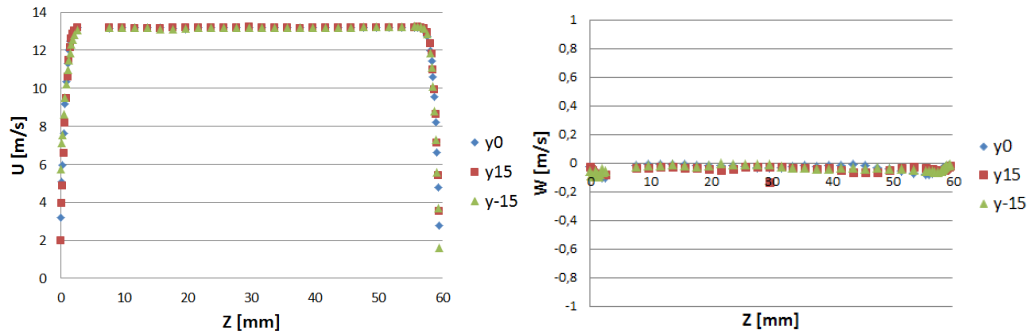


Figure 4.28 - Inlet Section Measured Velocity profiles along Z direction

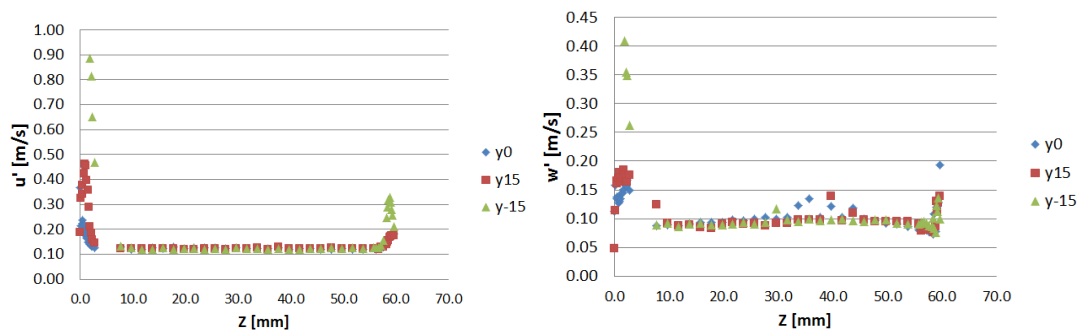
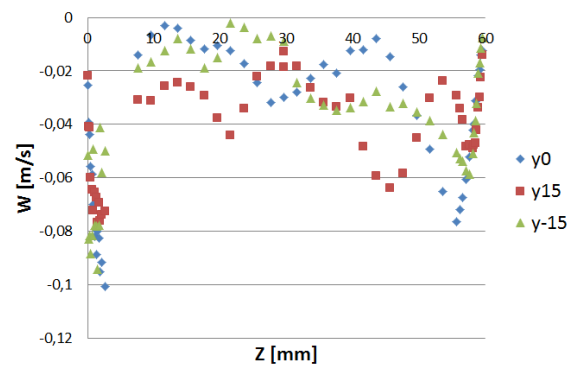


Figure 4.29 - Inlet Section Measured velocity fluctuations along Z direction

The principal velocity  $U$  has a good flow distribution along the section: the velocity profiles agree each other very well. See also that the secondary velocity  $W$  is almost negligible compared to  $U$  velocity, as expected for a one-dimensional flow. As regards the velocity fluctuations, note a pretty good distribution of the  $u'$  velocity, with a

constant value in the flow core region (i.e. corresponding to the shown 1% turbulence intensity of the inlet flow) and a very rapid increase in the boundary layer (i.e. high velocity gradient) region. The  $w'$  velocity acts similarly but higher data dispersion is noted: this is likely due to the very low acquired particles in this section, which can provide locally inconsistent measurement. Differences are located in the boundary layer, where particle population is relatively low, but also in the flow core. The experimental uncertainty cannot explain the differences, which are to be explained by low feeding in those regions as well. Indeed it is worth looking closer the  $W$  velocity measurements. It is negligible with regard to principal velocity  $U$ . Nevertheless,  $W$  velocity values do not seem to be identically equal to zero but they seem to have a negative (i.e. downwards) value. The experimental uncertainty shown in Table 4.6 can partially explain these values, since most of the biased values are within the experimental uncertainty. Locations where velocities seem to be out of the uncertainty range are again the zones nearer to the walls. It could be stated that this behavior could potentially result in a slightly unbalance of the fluid flow towards the half channel identified by 4<sup>th</sup> bend down, 5<sup>th</sup> bend up and 6<sup>th</sup> bend down. See Figure 4.30 for visual demonstration. Even though it is not likely that such unbalance (if present) affects the fluid flow symmetry after five mixing zones (which major effect is to homogenize the flow in the two channels), we will verify this hypothesis in next section where flow development is studied.



**Figure 4.30 - Measured  $W$  Velocity on a proper visual scale**

Figure 4.31 and Figure 4.32 show the experimental measurements in the three  $Y$  profiles of Figure 4.19:

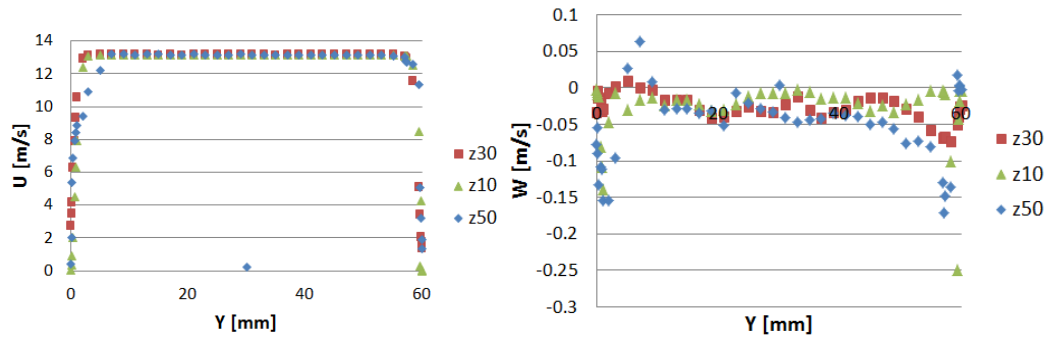


Figure 4.31 - Inlet Section Measured Velocity profiles along Y direction

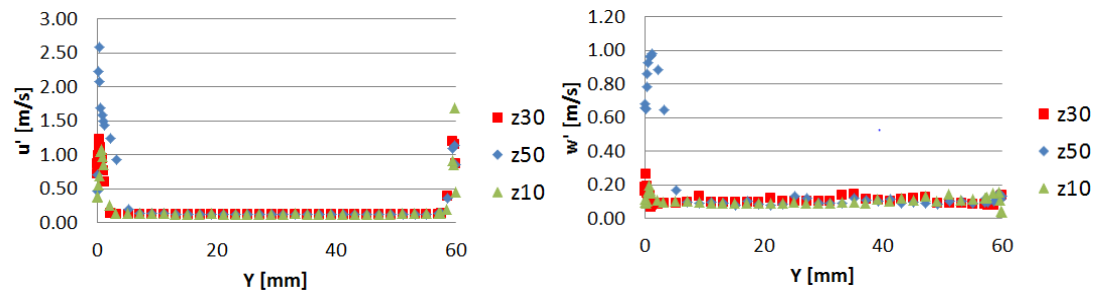


Figure 4.32 - Inlet Section Measured velocity fluctuations along Y direction

Considerations are practically the same as previous measurements, with the additional uncertainty due to the even lower population that give untruthful results especially for “z50” profile for  $Y \approx 5$ , where even U velocity boundary layer does not seem to correctly match the other velocity profiles. Indeed the population is as low as 40000, which is even lower than the 120000 particles that are supposed to give statistically fully converged measurements (Figure 4.23). W velocity is negligible with regard to principal velocity U but its values do not seem to be identically equal to zero, rather having a negative (i.e. downwards) value. By the way, taking into account experimental uncertainties in Table 4.6, the shown bias can be easily explained. The negative W velocity is more important in the boundary layer, suggesting that, if the experimental uncertainty was insufficient to explain those values, onset of corner vortices (coming from the air inlet) could provide the answer to the measured values. However previous data showed no evidence about the presence of corner vortices: hence, it is difficult to provide a unique motivation for the found negative values.

## 1.4.2 Flow Development

The experimental mockup has been designed in order to have a developed flow at the end of the fluid channel: as already stated, preliminary calculations showed that fully developed flow is achieved after four bends. Since experimental measurements have been done in the last mixing zone and bend, it is of primary interest to investigate if this hypothesis is actually verified. Hence we will present measurements in 4<sup>th</sup>, 5<sup>th</sup> and 6<sup>th</sup> bend to study flow development. Note that, since 4<sup>th</sup> and 5<sup>th</sup> bends are in the same half channel, 6<sup>th</sup> bend down is used to study flow development (Figure 4.20).

Only profiles “y0” and “z”30” of Figure 4.21 are analyzed. Figure 4.33 shows the comparison:

### 1.4.2.1 Comparison in “y0” profile

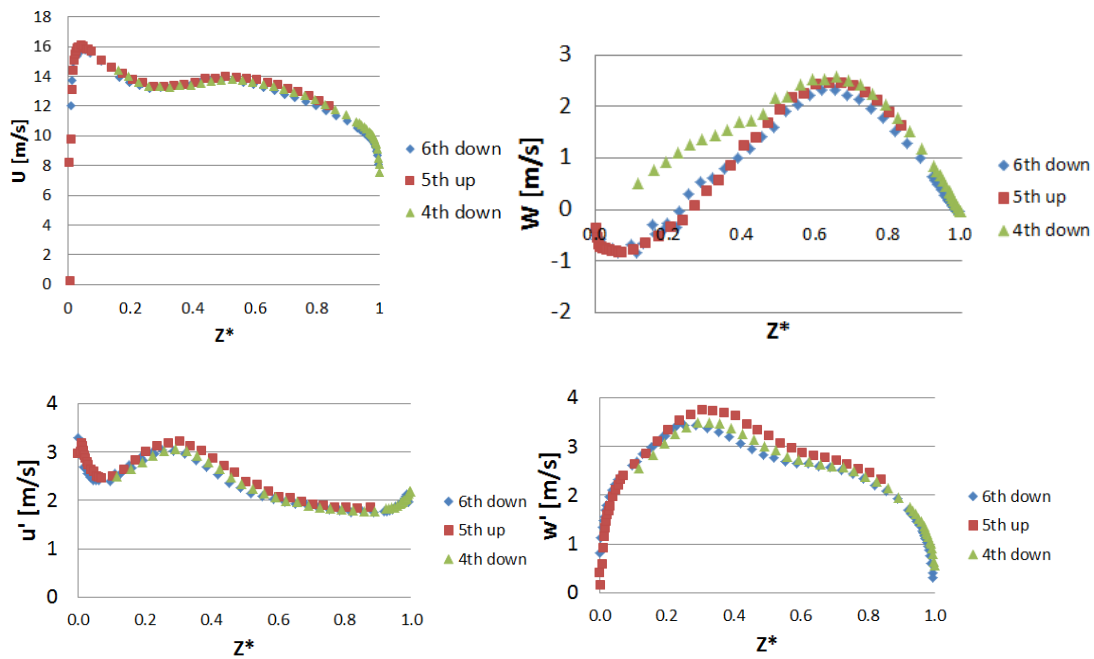


Figure 4.33 - U and W Velocities and velocity fluctuations profiles on the y0 line with regard to flow development

It is important to compare the experimental measurements taking into account the experimental uncertainties shown in Table 4.5 to Table 4.8. See that there is a very good agreement between the measurements in the last three bends for the  $U$  velocity components. This is not exactly the case for  $W$  velocity component, where the profile in the 4<sup>th</sup> bend does not seem to match the other profiles. Nevertheless, this difference does not lie in the velocity fluctuations. In fact a good agreement between 4<sup>th</sup> and 6<sup>th</sup> bend profiles can be observed in  $u'$  and  $w'$  velocities.



Remember that the shown uncertainties are strictly valid only in the measured point, e.g.  $Y^*=0.5$  and  $Z^*=0.5$ . This means that the uncertainties, although helpful for the comprehension of the measurements, do not give the global picture. However we will try to explain the experimental measurements by the experimental uncertainties all along the measured profiles. The  $U$  velocity agreement is always within the experimental uncertainty, which is not the case for the  $W$  profiles, where higher differences than the uncertainties are detectable in  $Z^*<0.3$  for the 4<sup>th</sup> bend. We find similar results in the  $u'$  and  $w'$  profiles, where higher differences are located at  $Z^*\approx 0.3$ . However, giving the very good trend agreement and having no actual uncertainty on that specific point, we consider that all the profiles match within the experimental uncertainties. In particular, as regards the  $W$  velocity profiles, we can affirm that the good correspondence between 5<sup>th</sup> bend and 6<sup>th</sup> bend suggests that the small difference in  $Z^*<0.3$  for the 4<sup>th</sup> bend is likely due to a non-detected incorrect profile definition during the experimental acquisition.

#### 1.4.2.2 Comparison in “z30” profile

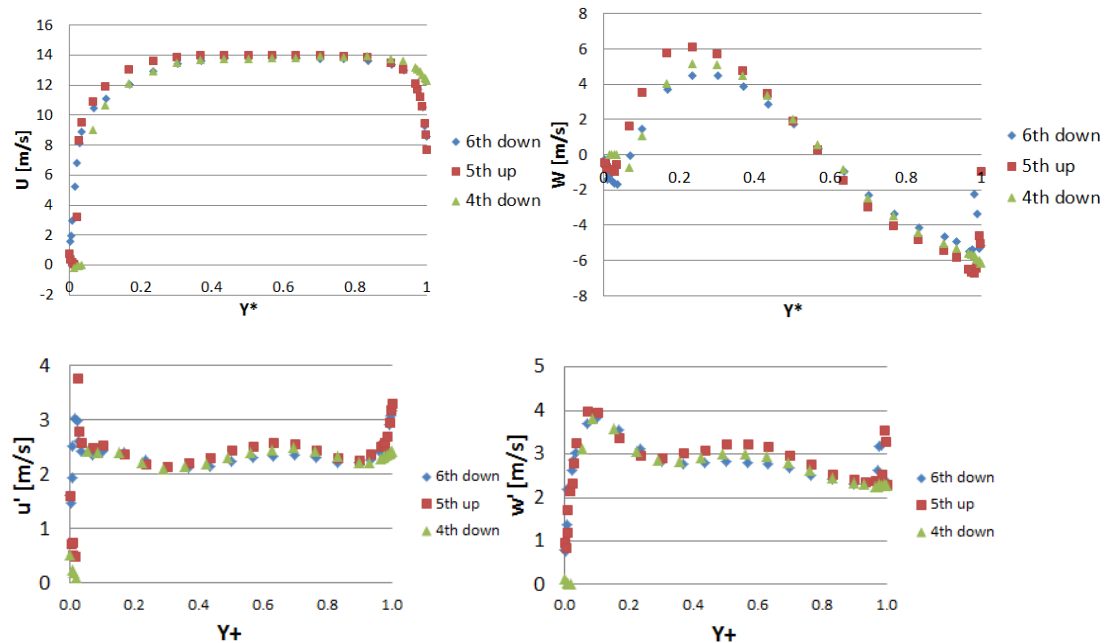


**Figure 4.34 -  $U$  and  $W$  Velocities and velocity fluctuations profiles on the z30 line with regard to flow development**

Similar considerations as comparison for “y0” profiles can be done for “z30” profiles (Figure 4.34). The profiles matching is even better than the “y0” case and this is not surprising since the “y0” profiles are more subjected to pressure-driven effects that are not so important for the present case. Nevertheless a larger difference in 5<sup>th</sup> bend

W velocity profile is detectable for  $Y^* \approx 0.2$ . The reason for this difference is not clear: the only thing to be said is the already mentioned lack of experimental uncertainty evaluation other than in the  $Y^*=0.5$   $Z^*=0.5$  point.. Anyway this does not change the global agreement which seems to confirm that the fluid flow is already fully developed from the 4<sup>th</sup> bend, as confirmed by the measurements in 4<sup>th</sup> and 6<sup>th</sup> bend.

#### 1.4.2.3 Conclusions

Measurements and uncertainty evaluations suggest that the fluid flow seems to be effectively fully developed after 4 bends, as it was proposed in the preliminary test design. The most evident discrepancies are so localized that are not considered as determinant for the final conclusion on fluid development.

### 1.4.3 Flow Symmetry

After having studied the flow development inside the innovative channel, it is interesting to study the flow symmetry not to have an unbalanced flow that could result in a bad mixing (hence decreasing the channel heat transfer efficiency). The flow symmetry is studied in the last (i.e. 6<sup>th</sup>) bend and shown in Figure 4.35. The comparison strategy is the same as Section 1.4.2 - Flow Development, with “y0” and “z30” profiles taken into account.

#### 1.4.3.1 Comparison in “y0” profile

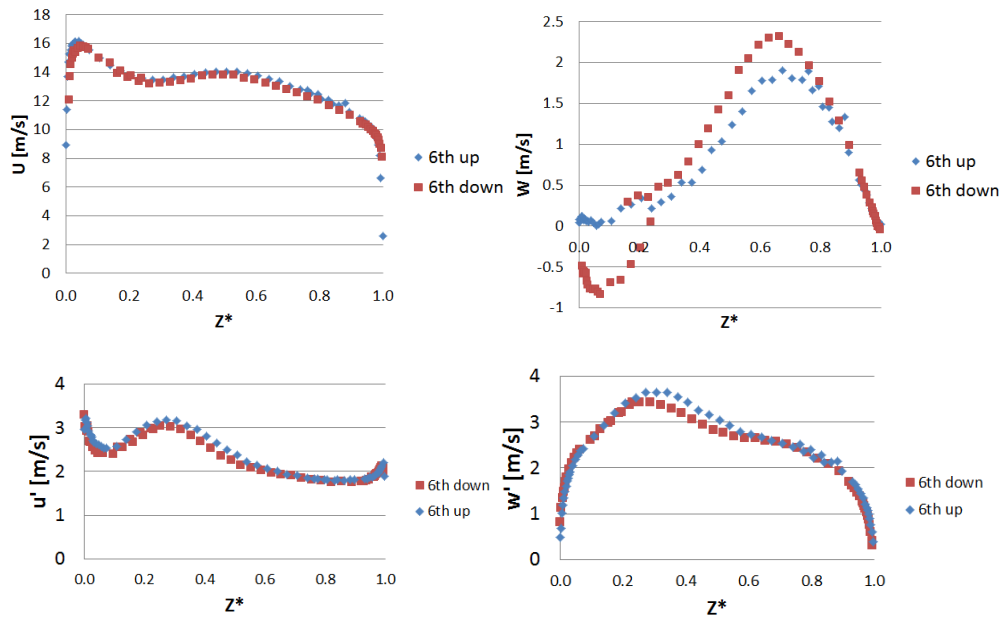
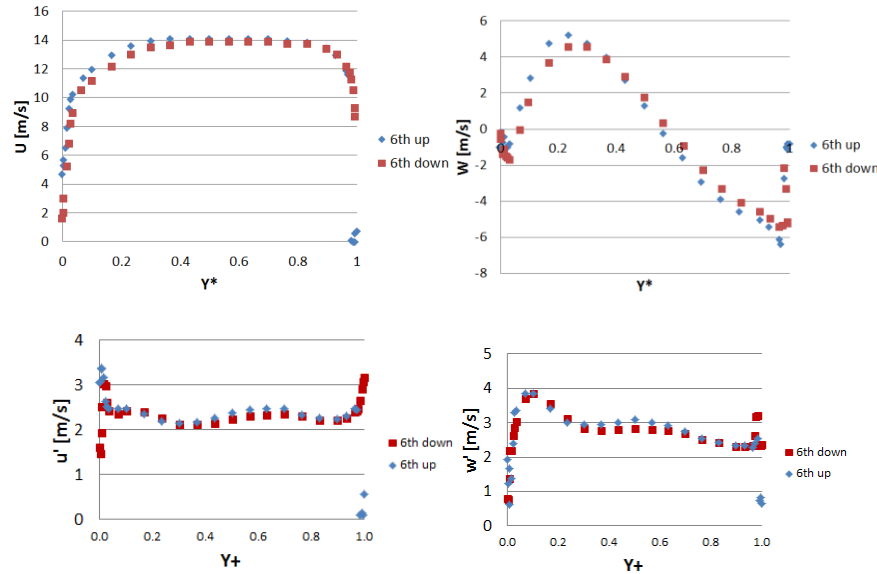


Figure 4.35 - U and W Velocities and velocity fluctuations profiles on the y0 line with regard to flow symmetry

First of all immediately note the disagreement in W profiles. In fact, even if the experimental uncertainties partially explain the differences, indeed discrepancies are detectable all along the profile, suggesting that something else must be explained. Stated that calculations shown in Chapter 5 will eventually help in understanding where the actual profile lies, it seems that the 6<sup>th</sup> bend down profile can be considered as the reference one (as demonstrated by the previous analysis). Hence, a possible explanation for the 6th bend up W profile could be a non-detected leakage in the inner wall ( $Y^*=0$ ), with the flow going towards the wall (i.e. the negative value) going out from the channel. This would explain the zero-velocity at  $Y^*=0$  and the global lower velocity value in the other position. However it is to be noted that the U profile as well as the velocity fluctuation would not be affected by the leakage, which is somehow difficult to explain. See that for the other shown profiles, considerations in Section 1.4.2 are perfectly applicable, with the difference in  $Z^* \approx 0.3$  for  $u'$  and  $w'$  velocities. Moreover the 6<sup>th</sup> bend up profiles are closer to those of 5 bend up, somehow confirming the conclusions about flow development and symmetry<sup>XVI</sup>.

#### 1.4.3.2 Comparison in “z30” profile



**Figure 4.36 - U and W Velocities and velocity fluctuations profiles on the z30 line with regard to flow symmetry**

<sup>XVI</sup>As a final comment about flow symmetry, it could be said that, since the two upper bends have similar trends, a gravity effect could be playing a role in bottom bends, explaining the differences. Anyway, calculating the flow Richardson number (representing the potential energy over the kinetic energy):

$Ri = \frac{gh}{U^2}$ , where  $g$  is the gravity acceleration,  $h$  is the vertical length scale and  $U$  is the principal velocity. For our purpose,  $h \approx 130$  mm and  $U = 13$  m/s. Hence  $Ri = 0.0075 \ll 1$  and hence gravity effects can be neglected.

Figure 4.36 shows the flow symmetry analysis in the z30 profile. Again measurements and considerations are similar as those of Section 1.4.2, with the difference in the velocity fluctuations being less important and therefore more easily explained by the experimental uncertainty.

#### 1.4.3.3 Conclusions

Measurements and uncertainty evaluations show that the fluid flow is symmetric in the two half-channels, as it could be hypothesized in a preliminary analysis with no data available. The most evident discrepancies are the same as those detected in studying the flow development and that are not considered as determinant for the final conclusion on fluid symmetry.

### 1.5 CONCLUSIONS ON THE LDV MEASUREMENTS

The LDV campaign allowed us acquiring a very large database on flow velocities and velocity fluctuations in several regions of the innovative channel. These data are very useful for the numerical model validation, since they give a full representation of the fine phenomena occurring in the fluid flow bulk as well as in the boundary layer. The acquired data confirm the design hypothesis in terms of flow development (which is achieved after four bends) and flow symmetry, which has been pretty well demonstrated. See that one very interesting measurement is missing, i.e. the vertical velocity in the profiles orthogonal to the mixing zone: indeed this velocity is responsible for the mixing. Nevertheless once the numerical model is validated, this information can be easily obtained from there. What would also miss in this LDV experimental campaign is a global overview of the channel flow, which is difficult to infer from data acquired on local profiles. Nevertheless this lack can be fulfilled by the other experimental campaign discussed in the next section.

## 2. PARTICLE IMAGE VELOCIMETRY MEASUREMENTS

### 2.1 PARTICLE IMAGE VELOCIMETRY TECHNIQUE DESCRIPTION

Particle Image Velocimetry (PIV) represents another widely used velocimetry technique both in the research and in the industrial sectors.

For our purposes, two-component (2C) PIV has been evaluated as a suitable measurement technique, taking into account technical and practical constraints in

terms of timing, planning, cost and capability to properly show eventual separation zones. First a brief description of the PIV technique will be shown, then the experimental facility will be described.

As LDV technique, PIV uses micro-scale particles to feed the fluid flow. The principle of particle sparkling when lightened is the same as LDV, as well as the hypothesis that they flow with the same fluid velocity i.e.

$$V_{fluidflow} = V_{feedingparticles}$$

In 2C PIV, a laser sheet is fired out a double pulse laser towards the measurement zone, to light up a plane. See Figure 4.37 for explanation:

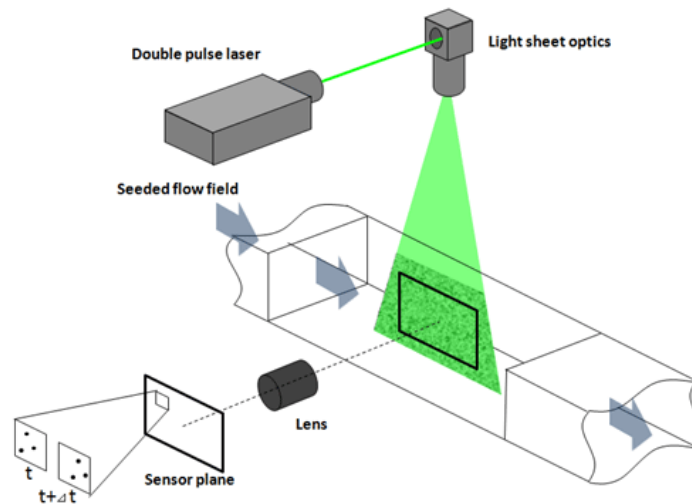


**Figure 4.37 - PIV technique principles**

Particles passing through the plane of measurement are detected and their velocity can be measured as described hereafter.

A high-frequency camera which is in phase with the laser pulsation is placed at 90° with respect to the laser sheet (i.e. just in front of the laser sheet) to take pictures of the lightened particles. In this sense, see the difference from PIV and LDV, since the former needs two optical accesses (for the laser and the camera) in two different planes whereas for the latter, if the back-diffusion acquisition is not used, the two optical access are parallel (compare Figure 4.1 and Figure 4.37). The camera typically takes two or more pictures to be compared in order to measure the velocity field. This

can be done by dividing the captured domain in smaller sub-domains (i.e. analysis windows), where a given number of particles can be detected (see Figure 4.38).

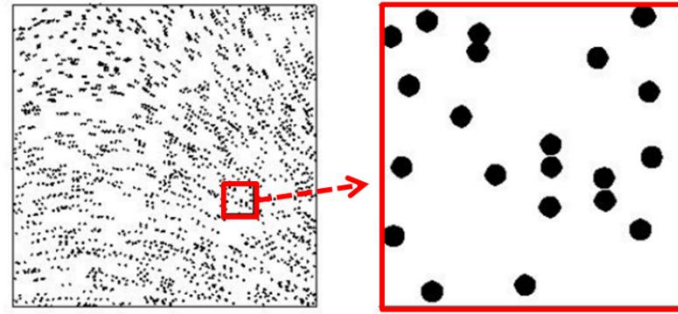


**Figure 4.38 - Example of PIV pixel division**

With the hypothesis that these particles (typically 5 to 20) in a sub-window move with the same velocity at time  $t$ , we can look for the same sub-window at time  $t+\Delta t$  in all directions around the original one. Normally a 16 to 24 pixel zone is used as interrogation domain. Using the cross-correlation method, the most likely sub-window at time  $t+\Delta t$  is determined. The displacement in sub-windows per unit time ( $\Delta t$  between two frames) is provided and the geometrical calibration will give the actual velocity value. Note that, since the correlation is searched all around the original pixel, the velocity direction is directly available once the maximum correlation is found. Figure 4.39 shows an example of the cross-correlation procedure, where the maximum value of the cross-correlation (i.e. the most likely velocity) is given by the local maximum of the right figure:

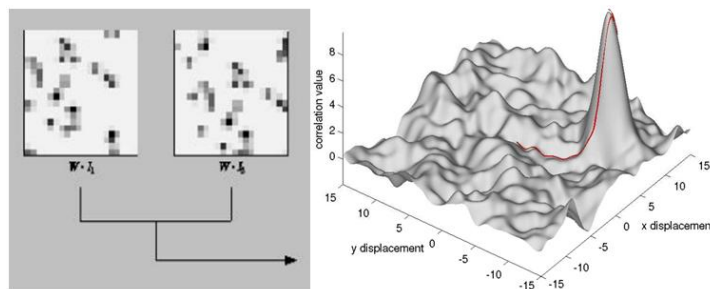


**Figure 4.39 - Example of PIV pixel cross-correlation**

## 2.2 EXPERIMENTAL FACILITY AND CALIBRATION

### 2.2.1 Experimental facility description

First of all the test section is presented. Again, only a pair of superposing wavy channels is used, to form a single channel (like the one shown in Figure 2.41). Its geometrical characteristics are shown in Table 4.9:

PIV channel geometry	
Angle	<b>45°</b>
Straight distance between bends	<b>114.6 mm</b>
Bend radius of curvature	<b>57.3 mm</b>
Total channel height	<b>40 mm</b>

**Table 4.9 - PIV channel geometrical characteristics**

Based on the already mentioned calculations on the developing flow, we decided to use a seven bend channel to measure a fully developed flow in the last bend and mixing zone. Since the PIV system needs two optical accesses to the test section (see Figure 4.37), an entire optical quality PMMA test section has been designed and assembled (see Figure 4.40).



**Figure 4.40 - PIV experimental PMMA mockup**

The test section is composed by four demountable plates (some of them shown in Appendix D), to be able to clean them if any spot is detected. The channel is designed with an inlet hydraulic diameter of 40 mm, corresponding to an inlet Reynolds number of 12 000. These are not the same conditions as the LDV tests (see Section 1). Nevertheless available material only allowed obtaining such flow rate, which is still fully turbulent and therefore useful for our study. The two half channels have a rectangular cross-section of 40mm x 20mm. Measurements are done with air at atmospheric pressure and temperature (i.e.  $p=1$  bar and  $T = 20^{\circ}\text{C}$ ).

The test section is globally shown in Figure 4.41:

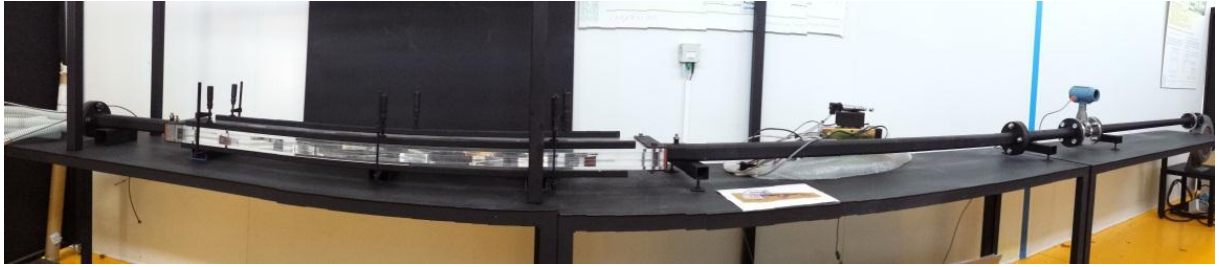


**Figure 4.41 - Global view of the PIV test section**

The used laser is a double cavity 2x200 mJ pulsed QUANTEC EverGreen 200 YAG Laser, (shown in Figure 4.42), providing a 532 nm (green) light sheet. Its pulse frequency is between 0 and 15 Hz.



**Figure 4.42 -PIV Laser generator**

The camera was a PowerView™ Plus 4MP camera, with a frame-straddling time up to 200 ns.

The laser power during the experimental tests changed in order to optimize the acquisition in each position. The laser emission is shown in Figure 4.43, together with the ISEL displacing system (moving the laser emission) and the Camera (which position has been adjusted for each measurement):



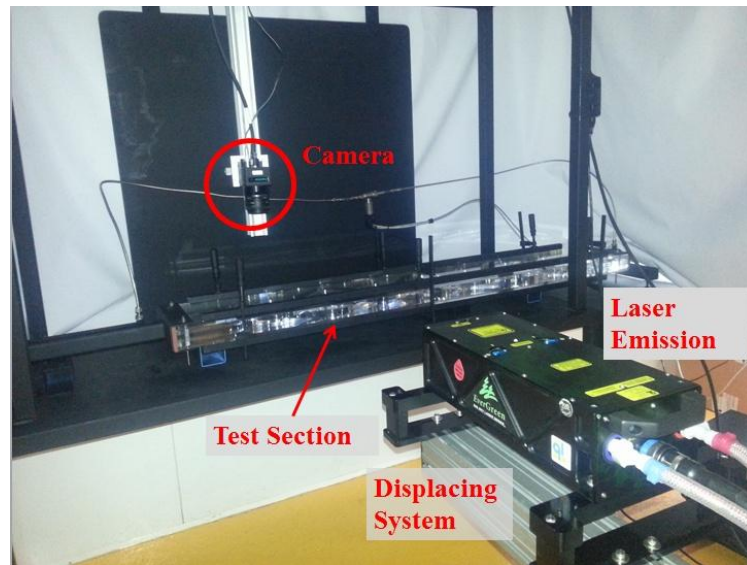


Figure 4.43 - PIV laser and camera configuration

The visualization particles are olive oil droplets. Droplets are created by a “TSI Oil Droplet Generator 9307” atomizer (Figure 4.44), feed by pressurized air. The average olive oil droplet size map is typically  $1\ \mu\text{m}$ .



Figure 4.44 - PIV feeding system

Data acquisition, pre and post-processing is done thank to the “TSI Insight 4G” software. Figure 4.45 shows a post-processed capture. A Nyquist grid is used, together with a Fast Fourier Transformation correlation scheme and a Gaussian-type peak engine.

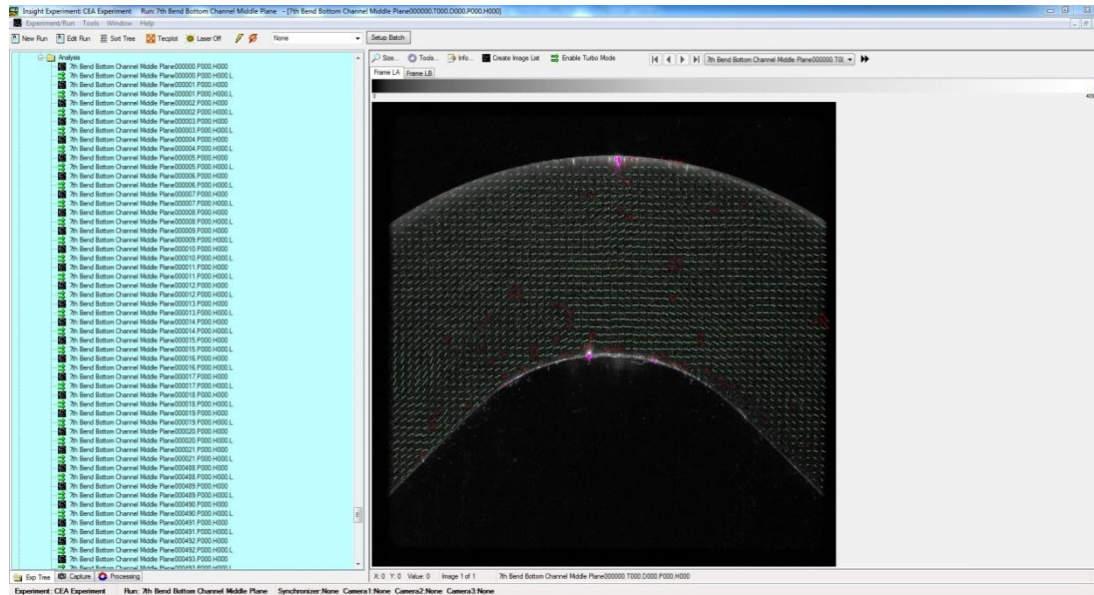


Figure 4.45 - Insight 4G software

## 2.2.2 Calibration and testing

Calibration has been done in two different but equivalent ways, to double-check the two methods. The first one is to define a line corresponding to the known channel width, to correlate the number of pixels in the line with its actual geometrical length. In this sense, INSIGHT4G allows to select a line in a picture and to specify its known length. See the white line in Figure 4.46 for explanation.

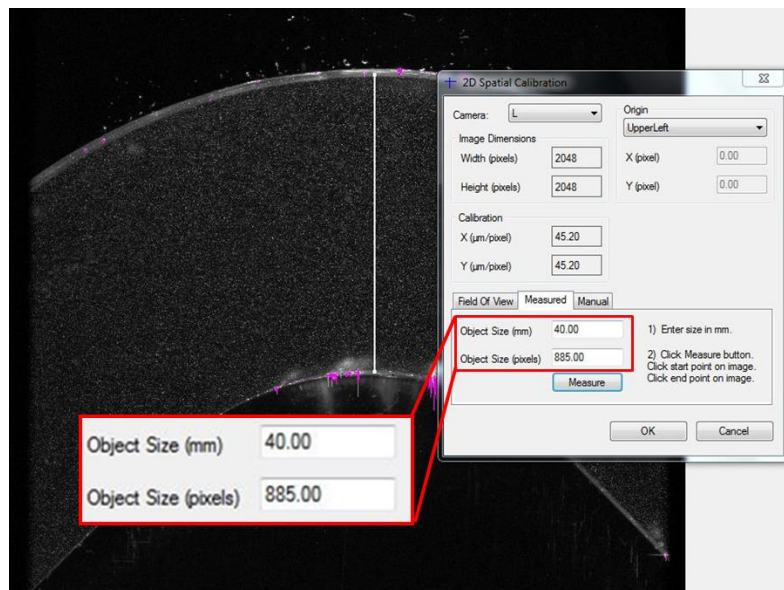


Figure 4.46 - PIV calibration first method

Similarly, the second method consists in taking a picture of known-size object in the fluid stream. This allows to check both the focus of the image and to calibrate the measurements. Several coins have been used for this kind of calibration. Again, see the white line in Figure 4.47 that shows the calibration done in the INSIGHT4G software.

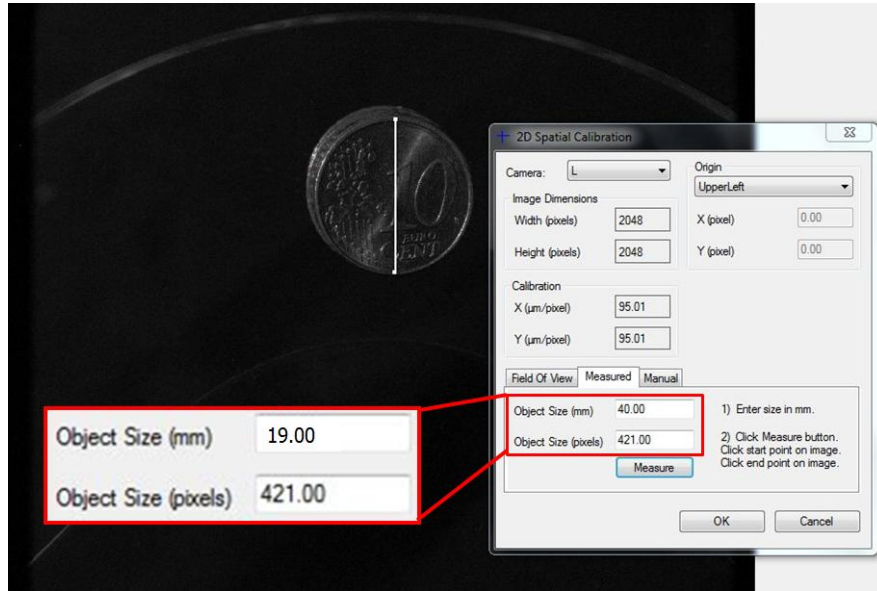


Figure 4.47 - PIV calibration second method

The interest of using the two methods lies in the potential different uncertainty when dealing with different geometries. In other words, it could be stated that the smaller the checked geometry, the higher the uncertainty in defining the number of sub-windows in a known length. In fact, given two measurements  $M_1 \pm U_1$  and  $M_2 \pm U_2$ , the geometrical calibrations provides the known length  $L$ . Hence, consider the calibration factor  $\frac{M_1}{L_1} = \frac{M_2}{L_2}$ . It clearly results that, if  $U_1 \approx U_2$  (i.e. 1 pixel) the final calibrated uncertainty  $\left(\frac{\pm U_1}{L_1}, \frac{\pm U_2}{L_2}\right)$  is higher if  $L$  is lower, i.e. if the known dimension is shorter. Anyway the two procedures showed no detectable differences in the average results: hence, the standard calibration has been done by defining the known channel width, which resulted to be the greater geometry (therefore the potentially lower uncertainty) as well as a more practical way to post-process the measurements.

## 2.3 EXPERIMENTAL CAMPAIGN DESCRIPTION

### 2.3.1 Experimental measurement program definition

The experimental campaign has been defined in a similar way as the LDV one: in particular, the inlet section, the last mixing zone as well as the last bend are chosen as reference regions to investigate channel flow. Moreover, to verify flow development (hence the design hypothesis) the fifth and sixth bend are studied as well.

Note that the test section system of coordinates is shown in Figure 4.48.

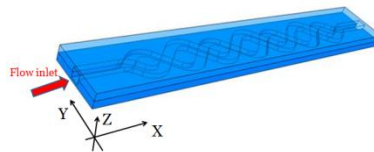


Figure 4.48 - System of coordinates for PIV measurements

It is worth mentioning immediately that the mixing plane could not be measured, since it corresponds to the physical interface between two plates (see Appendix E). Hence, it could not be properly illuminated by the laser sheet, diffraction phenomena being predominant. The used notation is provided in Table 4.10. Figure 4.49, Figure 4.50 and Figure 4.51 show then the planes that have been studied.

Inlet Section	Bend	Mixing Zone
The planes are named as a function of their distance in millimeters from the bottom plane, defined as the $Z=0$ plane ( $Z=40$ mm being the top plane). As an example, see Bottom plane + 16 mm.	For each half channel, the middle plane (i.e. the $Z=20$ mm for the bottom half channel and the $Z=30$ of the top half channel) are used as reference. Hence, the notation is a function of the distance from these middle-planes for each channel (i.e. top channel middle-plane + 4 millimeters).	Same as bend

Table 4.10 - PIV measured plane used notation

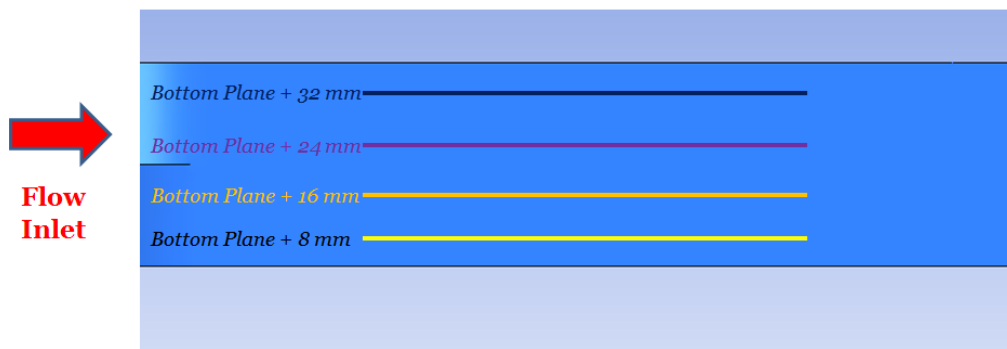


Figure 4.49 - Inlet section measured planes

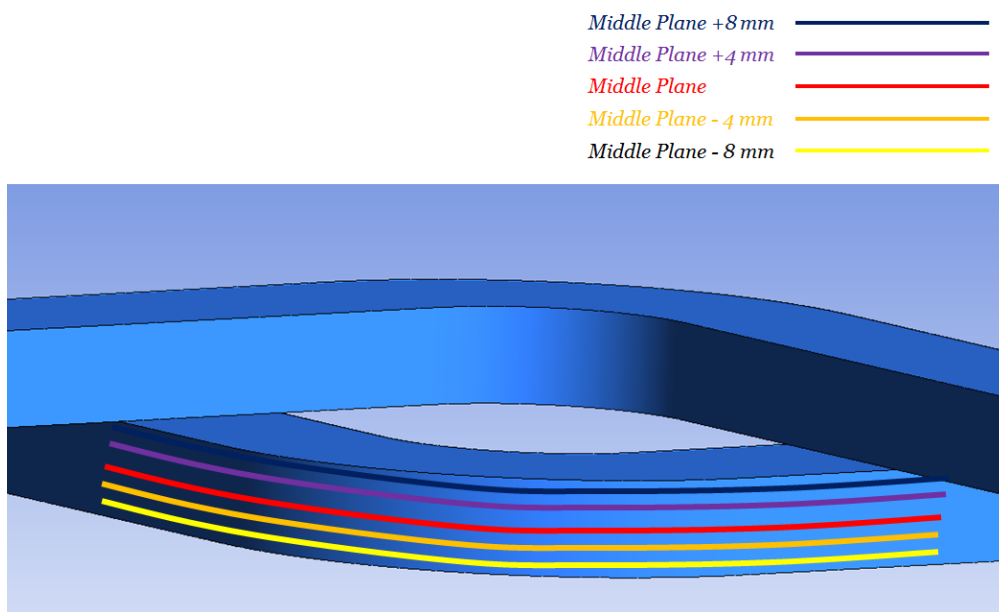


Figure 4.50 - Measurements of the In-bend flow

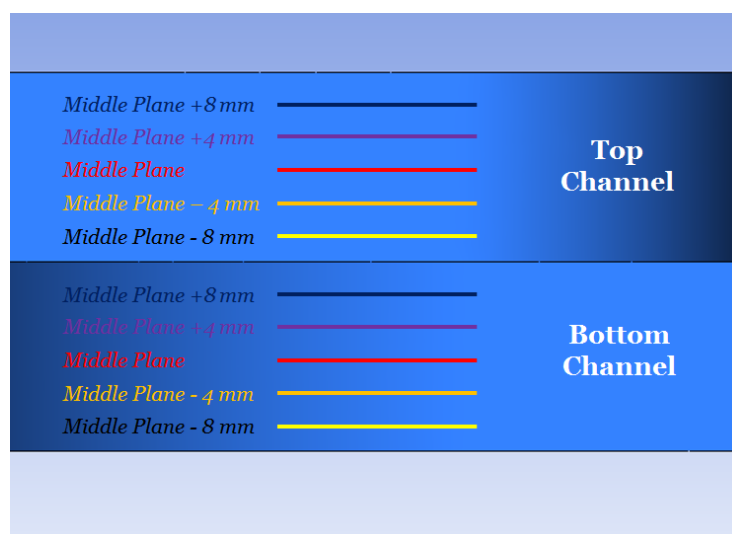


Figure 4.51 - Measurements in the mixing zone

	Bend	Mixing Zone
Four planes: Bottom Plane +8 mm Bottom Plane +16 mm Bottom Plane +24 mm Bottom Plane +32 mm	<u>6<sup>th</sup> bend up</u> : Five planes (middle plane, middle plane $\pm$ 4 mm and middle plane $\pm$ 8 mm) <u>6<sup>th</sup> bend down</u> : One planes (middle plane 5 <sup>th</sup> bend up, 6 <sup>th</sup> bend down/ One plane (middle plane)	Ten planes: 5 planes in the top channel (middle plane, middle plane $\pm$ 4 mm and middle plane $\pm$ 8 mm) 5 planes in the bottom channel (middle plane, middle plane $\pm$ 4 mm and middle plane $\pm$ 8 mm)

Table 4.11 - Experimental campaign description

### 2.3.2 Measurements statistical convergence and experimental uncertainty evaluation

As for the LDV technique, a preliminary analysis of the statistical convergence of the single measurement is necessary. What is ought to be verified is the number of images to be captured, in order to obtain fully converged values of the measured variables. Two tests with 200 and 250 images each had been run, to determine the final number of image for each measurements of the experimental campaign. The test was done only in the seventh bend, top channel middle-plane, since it was unrealistic to do it in the whole channel. Figure 4.52 shows the convergence comparison between the 200 and 250 image cases for the average velocity field.



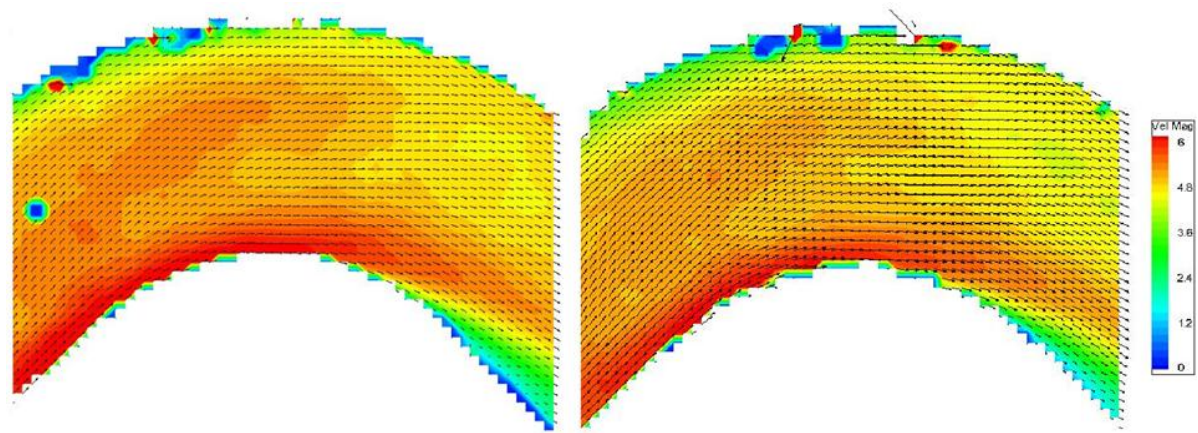


Figure 4.52 - PIV number of images convergence test of velocity field

See that there seems to be no real difference between the results of the 200 and 250 image tests for the present analysis. Therefore the final choice has been to use 250 images for the following analysis, to prevent potential issues due to the fact that the convergence evaluation could not be done all over the channel. However, when dealing with data post-processing (hence after having run the experimental campaign with the reference 250 images per measurement), it has been possible to carry out this test with a higher number of images, coming from the repeatability uncertainty analysis evaluation shown hereafter. Hence, we used up to 1000 pictures to verify the first measurement statistical convergence evaluation. In particular the average velocity field differences<sup>XVII</sup> have been plotted for the following cases: 250 vs 500 pictures, 500 to 750 pictures and 750 to 1000 pictures. Results are shown in Figure 4.53.

<sup>XVII</sup>This means that, for each sub-window, the velocity difference is calculated. If the sub-domain distribution is not exactly the same, interpolations are done.

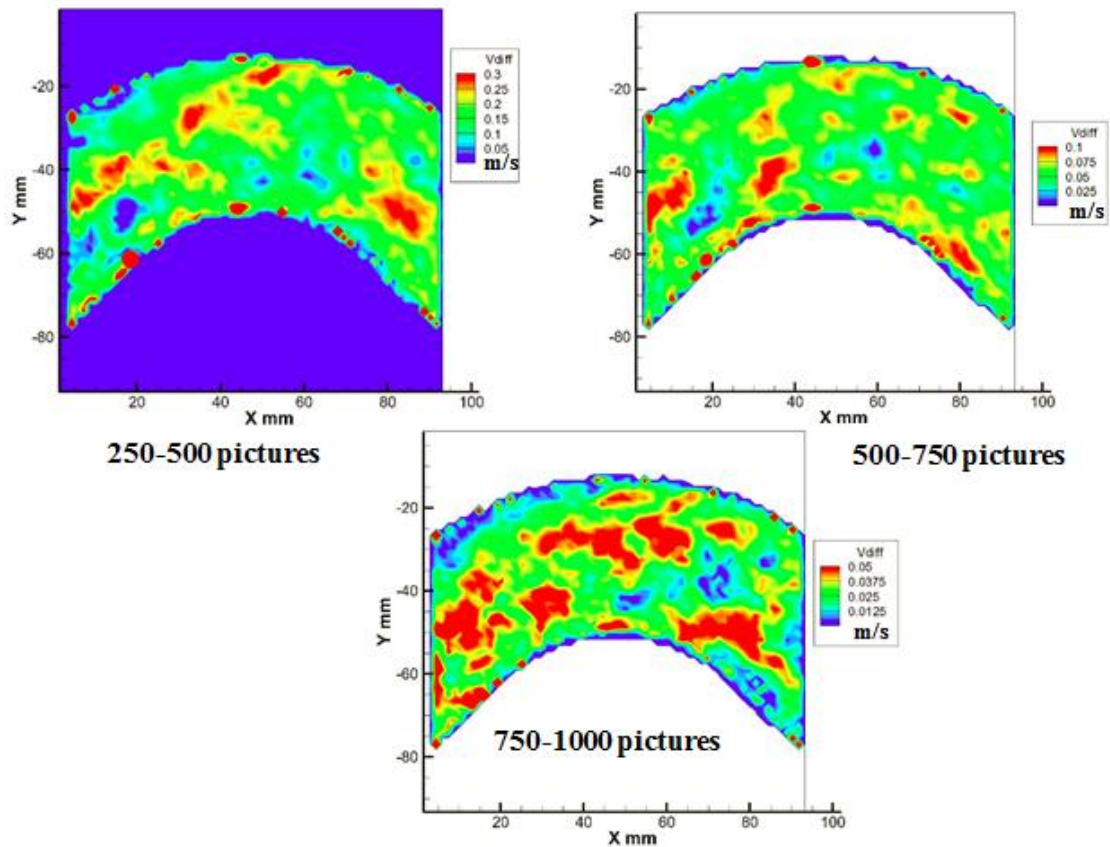


Figure 4.53 - PIV accurate measurement statistical convergence evaluation

If there is no particular zone where the differences are concentrated, it is clear, as expected, that the differences decrease as the number of picture increases. In particular, the maximum difference is about 0.3 m/s for the 250-500 pictures case, 0.1 m/s for the 500-750 pictures case and only 0.05 m/s for the 750-1000 pictures case. Therefore the choice that had been made of only 250 pictures per single measurement is clearly not sufficient to have fully converged measurements. Indeed it would have been worth capturing 750 to 1000 pictures per measurements to have statistically converged measurements<sup>XVIII</sup>. On the other hand, this would not have let us acquire a sufficiently wide database. In the end, due to the low number of pictures per measurement, high experimental uncertainties are expected.

<sup>XVIII</sup> This high needed number of pictures per measurements is likely due to the unstable behavior of the inlet fan (whose noise was clear during the measurements), creating a widely fluctuating flow, where fluctuations were created both by turbulence and by inlet fan vibrations.



To evaluate the experimental uncertainty, the same approach of Section 1.3.3 has been used. Indeed it is slightly more complicated to adopt such a method for a PIV measurement, because data are not available for a single and easily identified point but rather on a whole plane. Moreover, due to timing constraints, the uncertainty tests have been done only in the seventh bend top channel middle plane. The approximation is therefore to apply this uncertainty in the whole channel, and particularly in the mixing zone. However, Section 1.3.3 showed that no major difference has been detected between the uncertainties in the bends and mixing zones in the LDV measurements campaign. Hence, a slightly higher uncertainty in the mixing zone could be expected for the PIV campaign as well. We will take this into consideration for the following analysis.

Anyway, three types of uncertainty are identified: the uncertainty due to the data acquisition, the uncertainty due to environmental conditions and the uncertainty due to the measurement plane position. Regarding the data acquisition, the uncertainty has been evaluated based on the maximum local difference between the acquired 250 picture field and the reconstructed 1000 picture field, arbitrarily taken as a reference fully converged measurement. The standard deviation has been then calculated as the maximum difference was distributed on uniform probability density function. To evaluate the environmental uncertainty (repeatability), five identical measurements in the seventh bend top channel middle-plane have been done. The measurement standard deviation is obtained based on the maximum local difference among the five measurements as if they were distributed along a uniform probability density function. Finally, to evaluate the position uncertainty, measurements at  $\pm 1$  mm with regard to the seventh bend top channel middle plane have been done. This distance takes into account the uncertainty of the displacing system position and the laser sheet width, which has been estimate to be around 1 mm. Again, the standard deviation is calculated as previously described, as a uniform probability density function. The final uncertainty is calculated as the  $3\sigma$  total uncertainty, where  $\sigma$  is the uniform probability density function standard deviation. Hence, the proposed strategy for uncertainty evaluation covers all the possible sources of uncertainty. Results are provided in Table 4.12. Note that no average value is provided, since the uncertainty are calculated as

the maximum local uncertainty on an entire field, not referred to any specific average value.

	Data acquisition Uncertainty	Environmental conditions Uncertainty	Position Uncertainty	Total $3\sigma$ Uncertainty
Velocity Magnitude	0.17 m/s	0.12 m/s	0.24 m/s	0.80 m/s
u' Magnitude	0.07 m/s	0.09m/s	0. 09 m/s	0.38m/s
v' Magnitude Uncertainty	0.07 m/s	0. 09 m/s	0. 09 m/s	0.38m/s

**Table 4.12 - PIV experimental uncertainty evaluation**

Position uncertainty is still very high as for the LDV campaign. Here the environmental conditions are important to the same extent; anyway this is easily explained by the fact that the uncertainty evaluation procedure is different, as already explained: for LDV that has been done in a single point of measurements, whereas for PIV the local maximum difference has been used as the basis to calculate the total uncertainty. This means that the relative importance of position uncertainty and environmental conditions changes as a function of the local point of measurements (i.e. of the local flow conditions, gradients, etc.).

## **2.4 PIV EXPERIMENTAL MEASUREMENTS**

### **2.4.1 Flow Inlet Conditions**

First of all the flow inlet conditions are studied. Again no asymmetry is expected, since the inlet flow comes from several straight tubes. By the way, the flow is not almost uniform in the inlet section because of the same reason. Hence we expect to have clear turbulent developed flow profiles. Figure 4.54 shows the velocity profiles in the four measured planes:

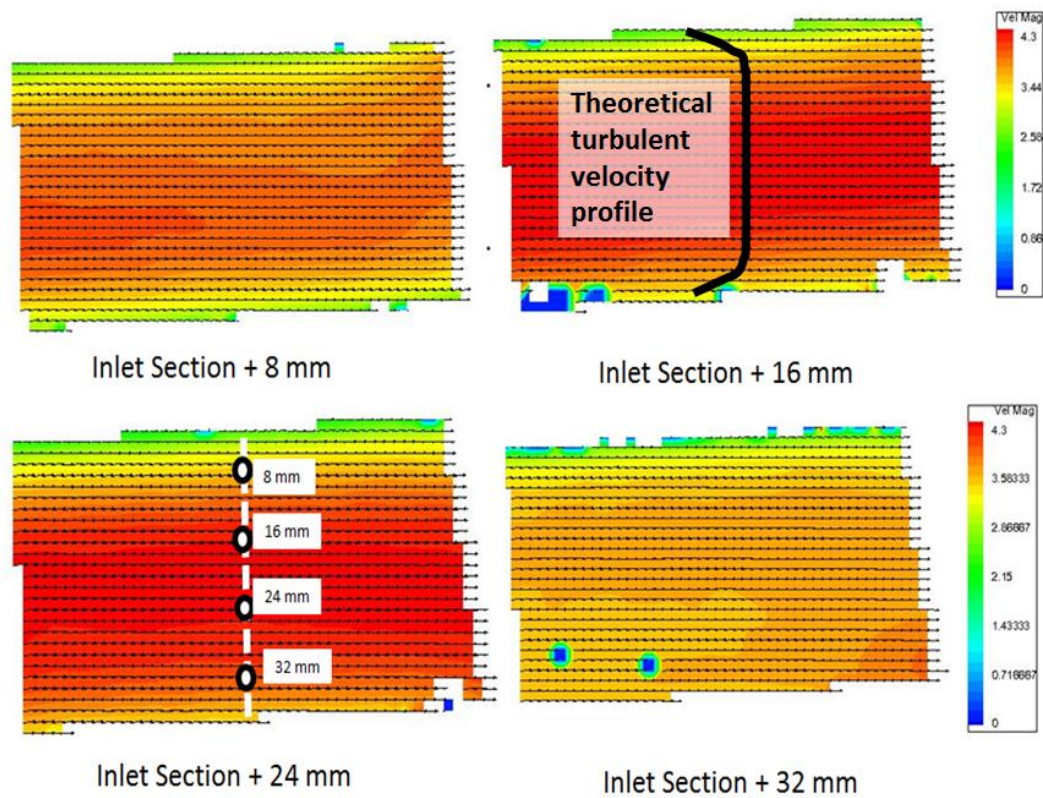


**Figure 4.54 - Inlet Flow Velocity field distribution**

Note that, as expected, the flow is practically fully developed. Moreover, see from Figure 4.54 that the lower velocity magnitude in the +8 mm and + 32 mm planes corresponds to the fact that those planes lie inside the boundary layer. To better describe the inlet velocity distribution, see the theoretical turbulent velocity profile that has been added in black line to the figure, to be compared to the experimental measurement.

As regards the velocity fluctuation evaluation, see the  $u'$  velocity distribution in Figure 4.55

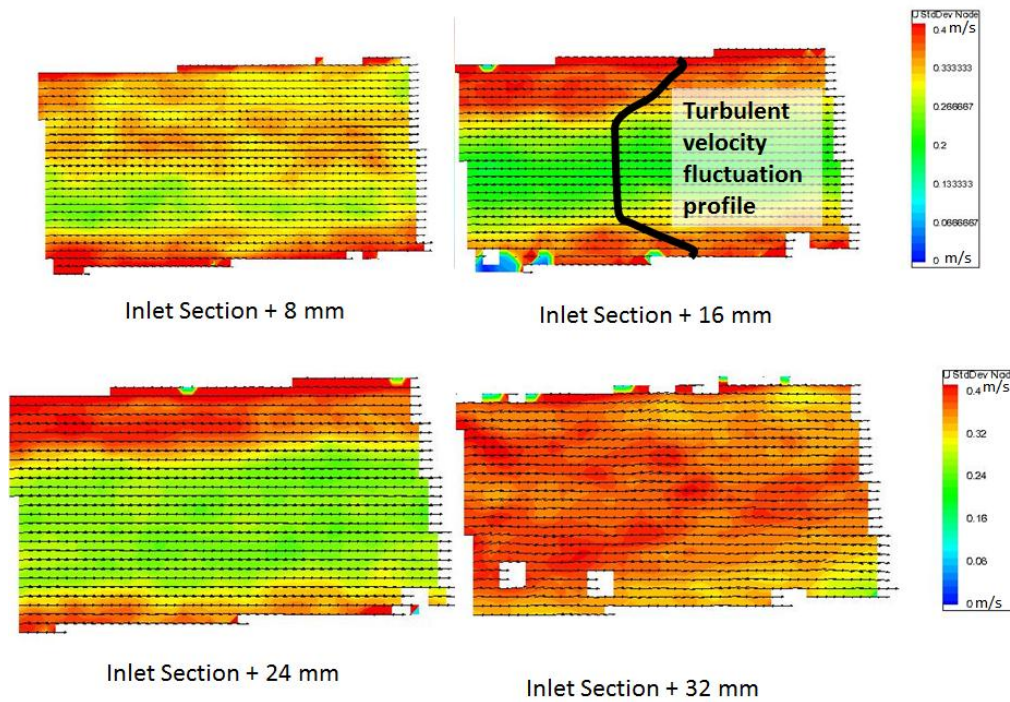


**Figure 4.55 - Inlet Flow  $u'$  velocity fluctuation field distribution**

The shown  $u'$  fields correspond to that shown in Figure 3.5 for the half straight channel (see the added turbulent velocity fluctuation profile in black line). This confirms the assumption of a fully developed inlet flow. The values in Plane + 32 mm seem to be slightly higher than the others. Nevertheless the other planes results, plane “+32 mm” distribution shape itself as well as the high total uncertainty are sufficiently clear to let us affirm that the inlet flow is a fully developed turbulent channel flow. In this sense, it is very important to verify if the different inlet flow between LDV and PIV measurements results in a different flow distribution inside the channel. The presence of the mixing zones let us say that qualitative differences are not expected. Moreover, since the Reynolds number is different, it would be difficult to split the effect of the different Reynolds number and the different inlet flow. We will discuss this aspect deeply we dealing with the flow analysis in Chapter 5.

#### **2.4.2 Flow Development**

As previously mentioned, the mockup has been designed to have a fully developed flow at the end of the channel. Section 1.4.2 already showed that after four bends the flow can be consider as fully developed. Here, the PIV mockup has seven bends, i.e. one more than the LDV mockup. Measurements have been done in 5<sup>th</sup>, 6<sup>th</sup> and 7<sup>th</sup>

bends middle-planes, which should present the same results within the experimental uncertainty. Figure 4.56 and Figure 4.57 show the absolute values of the differences between 5<sup>th</sup> vs 6<sup>th</sup> bend, 5<sup>th</sup> vs 7<sup>th</sup> bend and 6<sup>th</sup> vs 7<sup>th</sup> bend in terms of velocity and velocity fluctuation field. See that the maximum value of the scale is twice the experimental uncertainty given in Table 4.12, according to the approach previously described:

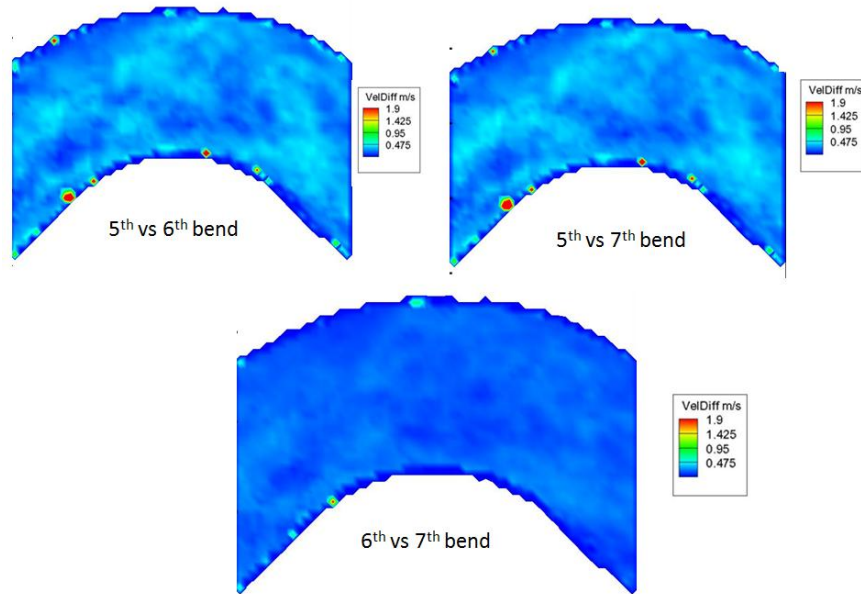


Figure 4.56 - PIV Flow development evaluation: velocity field

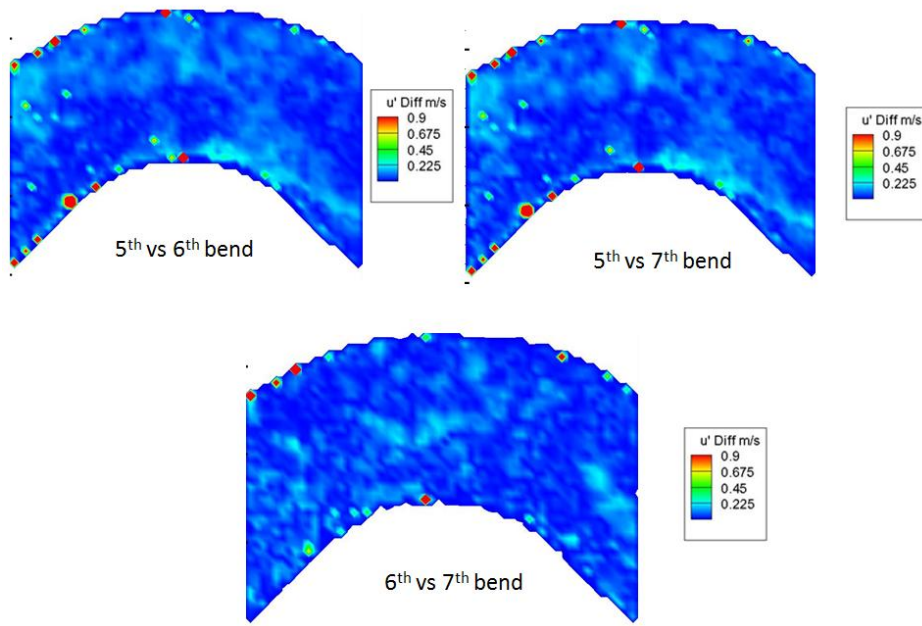


Figure 4.57 - PIV Flow development evaluation:  $u'$  velocity fluctuation



See that there are several spots in the velocity field comparison where the differences seem to be higher than the experimental uncertainty, especially in the  $u'$  velocity fluctuation fields. However, since the spots are essentially located in the boundary layer, there is little surprise in seeing these results. In fact, the boundary layer is traditionally a hard-to-be-measured region for the PIV technique; moreover, laser light saturation can occur, potentially giving untruthful results. Therefore, seen the general very good agreement of the velocity fluctuation fields, we can conclude that, as already shown in Section 1.4.2, fluid flow is fully developed after 5 bends. Therefore, the choice to actually do the measurements in the 7<sup>th</sup> bend is motivated by the need to verify the flow characteristics with no influence given by the inlet flow conditions.

### 2.4.3 Flow Symmetry

As for the LDV campaign, the fluid flow for the PIV experiment is supposed to be symmetric in the two superposed channel due to the effect of the mixing zone (in effect this zone would provide a high mixing between the two superposed channel flow, resulting in a symmetric flow if gravity effects or flow imbalances are avoided, as in the present case). To verify it, measurements in the 7<sup>th</sup> bend top channel and 7<sup>th</sup> bend bottom channel middle-plane are showed. The results are expected to be identical within the experimental uncertainty. Figure 4.58 and Figure 4.59 show the comparison in terms of terms of maximum local velocity and velocity fluctuation field differences. See again that the maximum value of the scale is twice the experimental uncertainty given in Table 4.12:

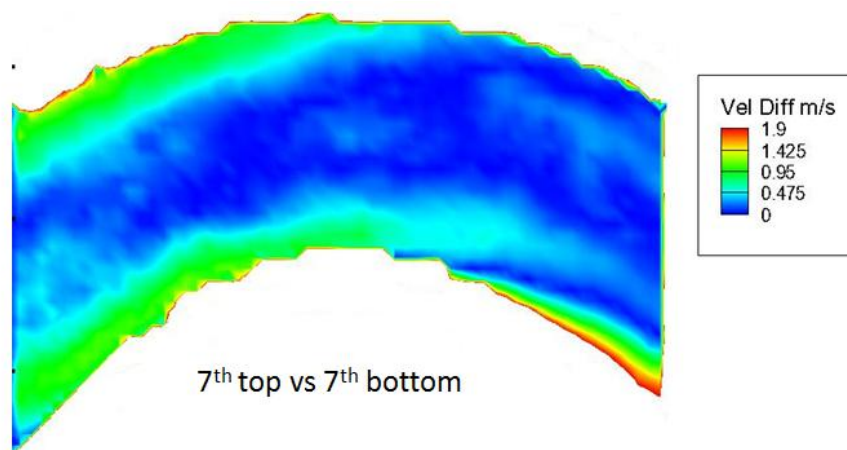
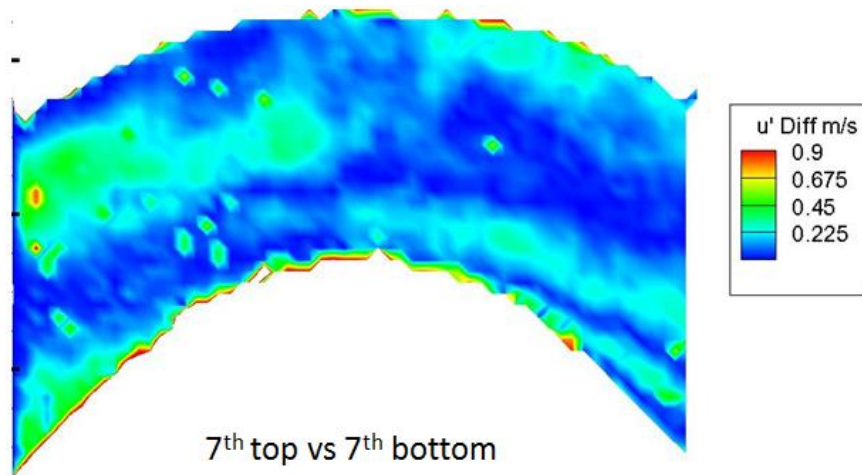


Figure 4.58 - PIV Flow symmetry evaluation: velocity field



**Figure 4.59 - PIV Flow symmetry evaluation:  $u'$  velocity fluctuation field**

See again that the measured fields are very similar and that differences lie within the uncertainty range. The same thing is for the velocity fluctuations, which are well within the uncertainty range. The maximum differences are present in the boundary layer regions, as expected. Therefore we can conclude that the fluid flow is symmetric in the two channels, which will help us in studying the fluid flow, since only one channel can be studied to show flow characteristics.

## **2.5 CONCLUSIONS ON THE PIV MEASUREMENTS**

Preliminary results and analysis of the PIV database shows that a very useful set of data has been acquired. This PIV database has been acquired using a too low number of pictures per measurement due to timing constraints. However, the non-perfect statistical convergence has been taken into account in the uncertainty evaluation, allowing for a correct analysis of the acquired data. These data will allow checking the numerical model behavior as well as revealing global flow characteristics that have not been observed during the LDV campaign and that will be discussed in Chapter 5. The verification of flow development and symmetry is of primary importance to validate the design hypothesis as well as the reference regions of measurements to be compared with the numerical model. See again that no information on the velocity component normal to the mixing plane is available, since it was far easier to design the whole facility for the current configuration. As previously mentioned, this information will be provided by the numerical model once it is validated against the present experimental database. Finally, to give a further double-check to the PIV with regard to LDV measurements, compare the velocity profiles named  $45^\circ y_0$  in the LDV campaign, which lies on the

bend middle plane for PIV measurements. The profiles show the non-dimensional principal velocity  $U$  (with respect to the channel average velocity) as a function of the non-dimensional channel width  $Z^*$  (see Table 4.3). Results are shown in Figure 4.60:

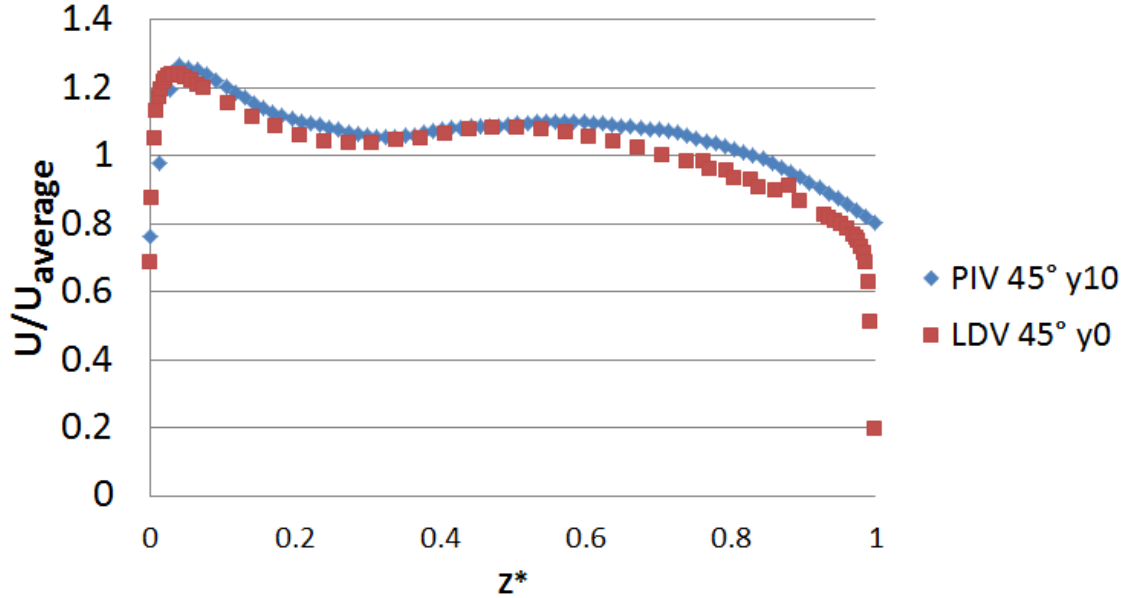


Figure 4.60 - LDV/PIV measurements double-check

The two velocity profiles are almost identical, which is very important to check the consistency of the two experimental campaigns. Remember that, since the Reynolds numbers are different, no exact consistency could be expected. However it is important to verify that the two campaigns provide a similar flow behavior, which is of primary importance for the innovative channel flow analysis done in Chapter 5.

### 3. “VHEGAS” THERMAL VALIDATION EXPERIMENTAL TEST-SECTION

#### 3.1 EXPERIMENTAL TEST SECTION MOTIVATION AND DESCRIPTION

Thermal validation of the illustrated numerical model is fundamental when dealing with thermal component such heat exchangers. Since the final goal of this work is to obtain trustful heat transfer and pressure drop correlations, the thermal study is necessary to complete the full numerical validation, having done the pure aerodynamic validation thanks to LDV and PIV experimental database.

Hence the idea is to indirectly measure the global heat transfer coefficient (i.e. Nusselt number) of a heated channel by inlet and outlet temperature measurements, as shown hereafter. The global heat transfer coefficient is defined as:

$$h = \frac{\phi}{(\bar{T}_{wall} - \bar{T}_{bulk})},$$



where  $\phi$  is an average heat flux,  $\bar{T}_{wall}$  is an average wall temperature and  $\bar{T}_{bulk}$  is an average fluid temperature. Therefore, the Validation of Heat Exchange in GAS “VHEGAS” test-section of Figure 4.61 has been designed in order to obtain these three quantities.



**Figure 4.61 - VHEGAS test section**

The aluminum experimental mockup (Figure 4.62) presents the geometrical characteristics shown in Table 4.13.



**Figure 4.62 - VHEGAS innovative channel mockup**

VHEGAS channel geometry	
Angle	<b>20°</b>
Straight distance between bends	<b>46.7 mm</b>
Bend radius of curvature	<b>20 mm</b>
Total channel height	<b>10 mm</b>

**Table 4.13 - VHEGAS channel geometrical description**

The geometry is not to scale to LDV and PIV mockups, since it has been identified the necessity to use different geometries for an actual validation and after the optimization process (see Chapter 5). As in Figure 2.42, the mockup is composed by two wavy channels of 5 mm height and 10 mm width, superposed in phase opposition. Eleven bends are used to obtain a thermally fully developed flow. Several holes are present on the mockup's surface for "1 mm - type K" thermo-couple installation (see a detail in Figure 4.63):

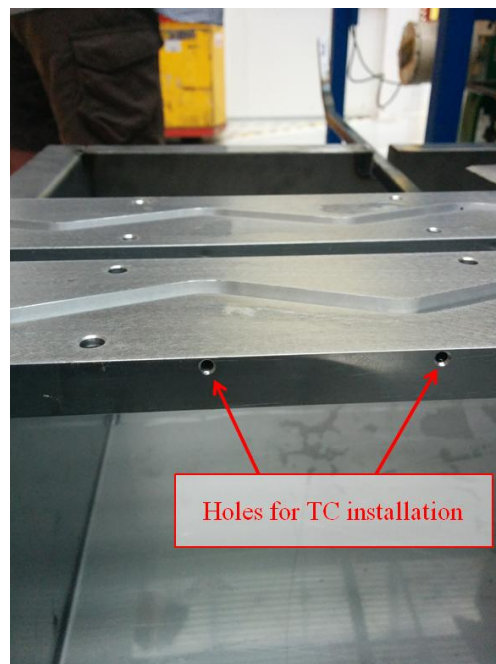


**Figure 4.63 - Holes for TCs position**

Twenty-two TCs have been installed, both to measure the inlet/outlet fluid temperature and the wall temperature. A scheme of the installed TCs is shown in Figure 4.64.

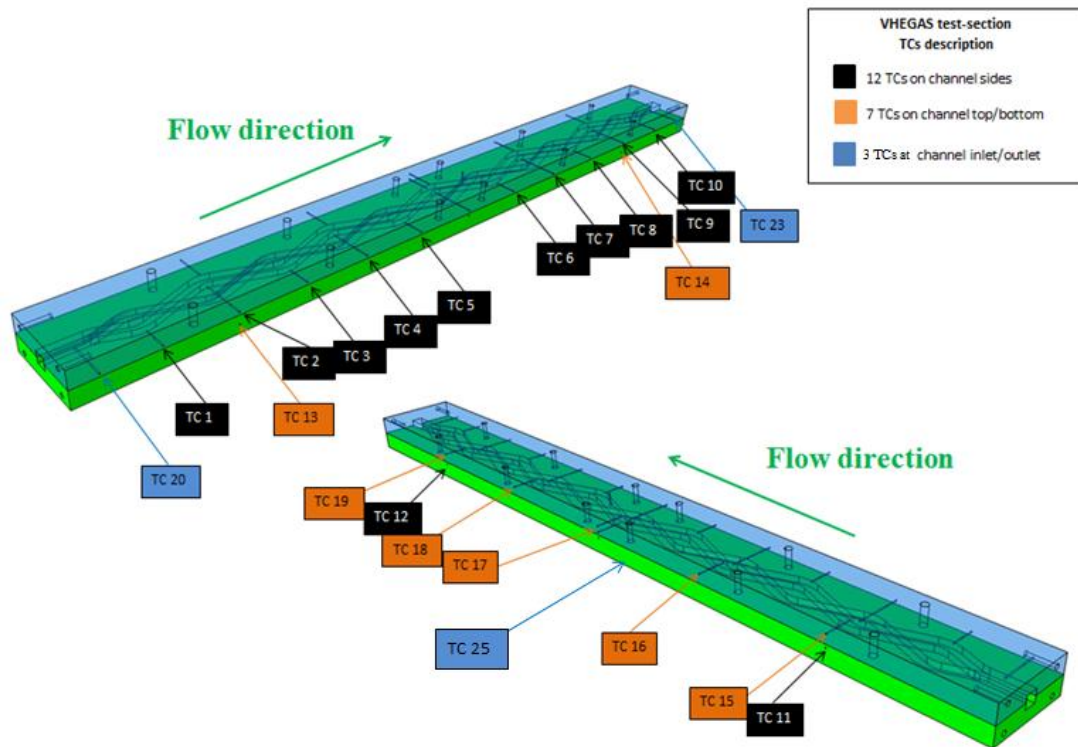


Figure 4.64 - VHEGAS TCs description

The channel side and channel top/bottom TCs are located at 1 mm distance from the channel wall. This has been done to approximate the actual local wall temperature by the measured local temperature. See in the next section that this hypothesis does not result in large errors. The inlet/outlet TCs are located at channel cross-section center. In this way we can calculate the  $\bar{T}_{wall}$  as the average temperature given by the side and top/bottom channel TCs, whereas  $\bar{T}_{bulk}$  is the fluid flow average temperature. The mockup is heated up by two heating plates as those shown in Figure 4.65, which are placed on the top and bottom surface of the mockup. Note that the two side walls are adiabatic, the mockup being placed into the insulating box, as shown hereafter.

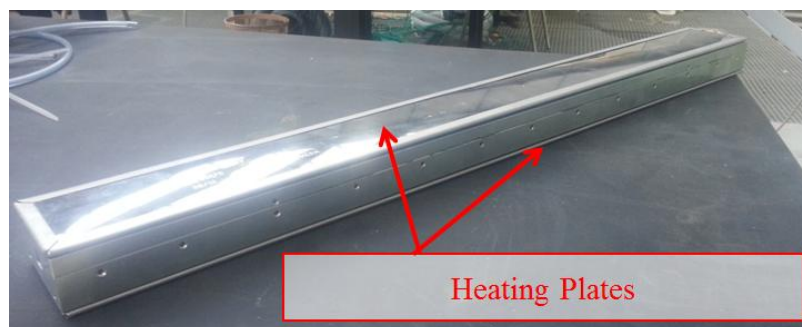


Figure 4.65 - VHEGAS heating plates

The heating plates provide a maximum thermal power of 1500W. Injected thermal power is controlled by a current-controller system as the one shown in Figure 4.66.



**Figure 4.66 - VHEGAS heating plates control system**

See that the mockup is placed inside a thermal insulation box shown in Figure 4.67, which contains mineral wool. The mockup is placed right in the middle of the insulating box. The mineral wool is then  $\pm 300$  mm thick with respect to the mockup along each of three Cartesian axes given by the box's edges.

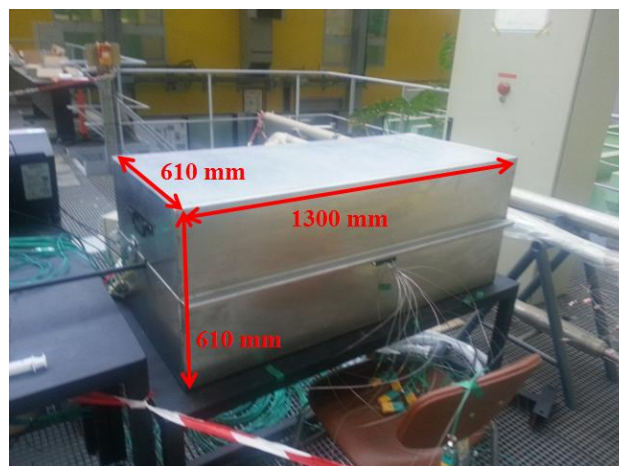


**Figure 4.67 - VHEGAS insulating box**



The flow inlet is given by 7-bar pressurized air underexpanded to atmospheric temperature and pressure. A pressure regulator is present to obtain a more stable flow rate. However, it has not been possible to fully control the flow rate, since the pressurized air came from a shared source: hence, unexpected variation could occur at any time. A Serv Instrumentation Vortex flow-meter type 8800 is used to measure volumetric flow rate upstream the mockup (Figure 4.68).



**Figure 4.68 - VEGAS flowmeter**

The known flow rate allows for calculation of the thermal power absorbed by the fluid flow, which is calculated as:

$$P_{th} = \rho Q c_p (T_{outlet} - T_{inlet})$$

Where  $\rho$  is the fluid density at atmospheric pressure and temperature (since the flowmeter is upstream the thermal mockup),  $c_p$  is the specific heat at atmospheric pressure and  $\bar{T}_{bulk}$  and  $Q$  is the measured volumetric flow rate. See that this procedure is independent from the actual thermal power provided by the heating plates, which is somewhere lost by test section thermal losses. This thermal power is transferred to the fluid flow by the wall heat flux that can be estimated as:

$$\phi = \frac{P_{th}}{S}$$

S being the channel wetted surface equal to  $0.039 \text{ m}^2$ . The wetted surface value is known thanks to CAD tools.

Hence all the three terms needed for calculating the global heat transfer coefficient are available and can be used for the model validation. The acquisition system (shown in Figure 4.69) is composed by a computer with VASCO software, which can be tuned as regard data acquisition frequency and data live follow-up.



**Figure 4.69 - VHEGAS acquisition system**

With these means, flow stability is studied by monitoring flow rate, inlet and outlet temperatures by 1 Hz frequency acquisition over several hours time. Once the flow is considered as stable, measurements are done by 10 Hz frequency acquisition over five minutes i.e. to finally have 3000 data points. This number is considered as sufficient to statistically analyze the experimental results.

### **3.2 EXPERIMENTAL CAMPAIGN DESCRIPTION**

Two different experimental campaigns have been carried out, to study two different flow conditions:

- A “high heat flux” case, heating up the mockup up to the maximum allowable temperature for the heating plates (i.e.  $200^{\circ}\text{C}$ ). This test is done to have a temperature as high as possible, compared to the  $350\text{-}530^{\circ}\text{C}$  operating temperature range foreseen for ASTRID heat exchanger. On the other hand, this test results in high flow temperature gradients, as it will be shown. Hence, near-wall thermal compressibility (which is neglected in the present numerical model, as mentioned in Chapter 3) could play an important role.

- A “low heat flux” case, heating up the mockup to a lower value than the previous case (i.e. 80°C). This case, even if less interesting with respect to ASTRID conditions, allows for practically neglecting near-wall thermal compressibility, which could potentially result in more accurate numerical results compared to the experiment.

### 3.3 FLOW STABILITY VISUALIZATION AND CONTROL

As for the LDV and PIV experimental campaigns, flow stability is first checked to verify if a steady-state assumption can be made. In particular, for a thermal experiment, both flow rate and temperatures must be checked. Results of the “high heat flux” case are shown in Figure 4.70 and Figure 4.71, where each shown variables is acquired with a frequency of 1 Hz:

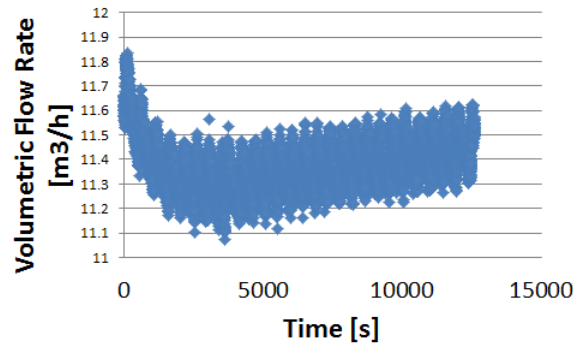


Figure 4.70 - "High heat flux case" flow stability

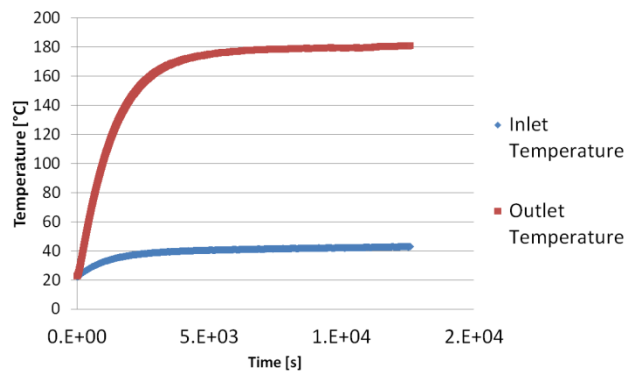


Figure 4.71 - "High heat flux" case thermal transient evaluation

See that, after an initial decrease of the flow rate, there is an almost constant increase of  $0.06 \text{ (m}^3\text{/h)/h}$ . This means a maximum increase of 0.5% with respect to the minimum measured value. Moreover, once the flow rate is practically stable (i.e. after 10 000 s), the maximum difference with regard to the mean value of  $11.45 \text{ m}^3\text{/h}$  is  $0.15 \text{ m}^3\text{/h}$ , which is around 1.5% of the mean value. These conditions are considered as

fine to assume a purely aerodynamic steady-state flow. By the way, as regards the temperature convergence evaluation, see that the flow tends to a fully steady-state conditions. The measurements have been done once all temperatures did not vary of more than 0.3°C/h (i.e. a variation of the outlet/inlet temperature difference of less than 0.7%/h with regard to its mean value). Finally, to quantify the evolution of the thermal transient, the thermal power absorbed by the aluminum mockup at time “t” has been plotted. This thermal power is defined as (neglecting the inertia of the insulation):

$$P_{alu}(t) = m_{alu} c_{p,alu} \frac{(\overline{T_{wall}}(t) - \overline{T_{wall}}(t - \Delta t))}{\Delta t}$$

Where  $m_{alu}$  is the mockup’s mass equal to 1,7 kg,  $c_{p,alu}$  is the aluminum specific heat at  $\overline{T_{wall}}$  and  $\Delta t = 1s$  (i.e. corresponding to the measurement frequency of 1 Hz). The analysis has been done for  $t > 6000s$  ( $\approx 50\%$  of the total measurement time), where the temperature field seems to be stable (see Figure 4.71). However, due to the time-derivative of the wall temperature, high fluctuations of the  $P_{alu}(t)$  are observed. Hence, trying to smooth these fluctuations, a simple moving-average (SMA) filter is applied, i.e.

$$P_{alu}(t)_{SMA} = \frac{1}{\tau} \sum_{i=1}^{\tau} P_{alu}(t - i)$$

Where  $\Delta t$  is a defined time interval. Since no a priori information on this  $\tau$  is available, a trial-and-error study has been done trying to minimize the observed fluctuations. Results are shown in Figure 4.72 in terms of mean value and standard deviation of  $P_{alu}(t)_{SMA}$ , with  $t > 6000 s$  as a function of  $\tau$ .

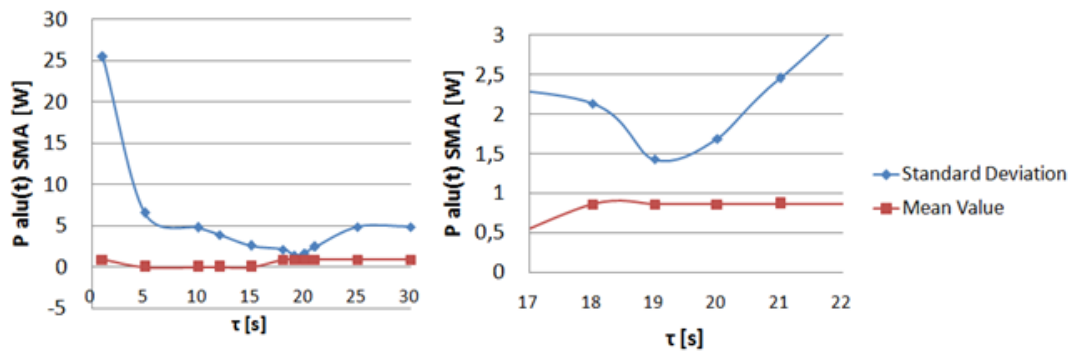


Figure 4.72–“High Heat Flux” case evaluation of thermal transient by mockup thermal power absorption



See that, even when the fluctuations are less important, the standard deviation is always higher than the mean value. This means that the thermal power absorbed by the mockup is practically zero, the fluctuations being due to the uncertainty of temperature measurements. This justifies the hypothesis of thermal steady-state for the following analyses.

Results of the “low heat flux” case are shown in Figure 4.73 and Figure 4.74:

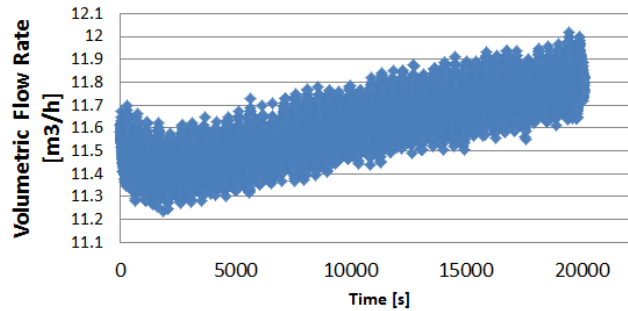


Figure 4.73 - "Low heat flux case" flow stability

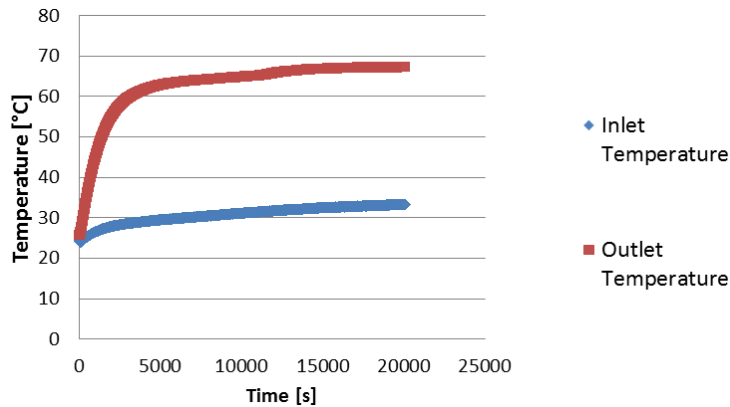


Figure 4.74 - "Low heat flux" case thermal transient evaluation

Again they show the same behavior of the flow rate as the “High Heat Flux” case. After a first decrease, the flow rate increases again of about  $0.06 \text{ (m}^3\text{/h)/h}$ . The flow rate resulted to be less stable than the previous case: however, since the measurements are done over a very short time compared to the global transient time (i.e. five minutes over several hours), this behavior is not of primary importance to assume flow stability during measurements. See the uncertainty evaluation to quantify this effect. As regards the temperature convergence evaluation, the flow tends to a fully steady-state condition. The measurements have been done again once all temperatures did not vary of more than  $0.1^\circ\text{C/h}$  (i.e. a variation of the outlet/inlet temperature difference of less than  $0.4\%/h$  with regard to its mean value). Again, to quantify the evolution of the

thermal transient, the SMA thermal power absorbed by the aluminum mockup at time “ $t$ ” has been plotted. Results are shown in Figure 4.75

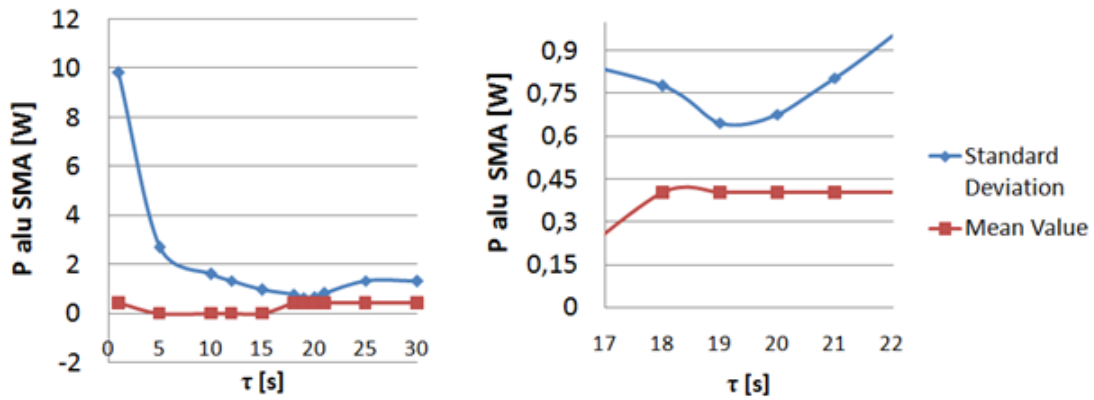


Figure 4.75 – “Low Heat Flux” case evaluation of thermal transient by mockup thermal power absorption

Once again, even when the fluctuations are less important, the standard deviation is always higher than the mean value. This means that the thermal power absorbed by the mockup is practically zero, the fluctuations being due to the uncertainty of temperature measurements. As previously mentioned these conditions are retained to perform a steady state thermal analysis.

### 3.4 EXPERIMENTAL UNCERTAINTY EVALUATION

As already mentioned, only measurements of temperature are available in the VHEGAS facility. Hence, the uncertainty evaluation has to be done for each measured temperature, and then propagated to derived values, such as the absorbed thermal power and heat flux.

Type K TCs have been used to measure temperatures. A typical standard deviation of such TCs is  $\pm 0.5^\circ\text{C}$  with respect to the measured temperature. However, the standard deviation of the set of measured values has to be added to have the total standard deviation  $\sigma$ . The uncertainty is again evaluated as three times the total measured uncertainty. Note that there are two invaluable uncertainties in inlet / outlet temperature and mean wall temperature measurements: the former is related to the actual position of the TCs, whereas the latter to the limited number of TCs position along the channel. Indeed, inlet/outlet TCs have been positioned by hand at the channel center point, with fine evaluation of their position inside the channel. By the way it is impossible to fully ensure the right desired position. Hence this uncertainty

will be neglected, even if it could play a role to explain eventual differences between numerical and experimental results. For the mean wall temperature, the wall could not be fully equipped with TCs. Hence there might be a bias in the measured mean wall temperature. Moreover, it has been already explained that the measured wall temperature is actually the temperature of a point 1 mm far from the wall. By the way this assumption is not supposed to result in major bias of the results<sup>xix</sup>. The final  $3\sigma$  uncertainty for inlet temperature, outlet temperature, 7<sup>th</sup> bend temperature, and average wall temperature is shown in Table 4.14 and Table 4.15.

	TC-related Standard Deviation	Measurement Statistical Standard Deviation	Mean Value $\pm$ Total $3\sigma$ Uncertainty
Inlet Temperature	0.5 °C	0.06 °C	43.0 $\pm$ 1.5°C
Outlet Temperature	0.5 °C	0.10 °C	180.9 $\pm$ 1.5 °C
7 <sup>th</sup> bend Temperature	0.5 °C	0.09°C	119.6 $\pm$ 1.5 °C
Mean wall Temperature	0.5 °C	0.12 °C	167.6 $\pm$ 1.5 °C

**Table 4.14 - "High heat flux" temperature uncertainties**

<sup>xix</sup> As an example, consider a heat flux of 11 kW/m<sup>2</sup> and an aluminum thermal conductivity of 240 W/(m°C). In 1 mm distance there is a supposed  $\Delta T$  of around 0.05°C, which is negligible compared to the other uncertainties.

	TC-related Standard Deviation	Measurement Statistical Standard Deviation	Mean Value $\pm$ Total $3\sigma$ Uncertainty
Inlet Temperature	0.5 °C	0.03 °C	33.3 $\pm$ 1.5°C
Outlet Temperature	0.5 °C	0.02 °C	67.2 $\pm$ 1.5 °C
7 <sup>th</sup> bend Temperature	0.5 °C	0.02 °C	51.5 $\pm$ 1.5 °C
Mean wall Temperature	0.5 °C	0.3 °C	64.4 $\pm$ 1.5 °C

Table 4.15 - "Low heat flux" temperature uncertainties

### 3.5 FINAL GLOBAL HEAT TRANSFER COEFFICIENT EVALUATION

#### 3.5.1 “High Heat Flux” Case

Given the uncertainties in Table 4.14 and the previously shown formulae, see in Table 4.16 the final propagate uncertainties for the derived variables of interest. The uncertainty on air physical properties and channel wetted surface is neglected.

	Mean Value $\pm$ Total $3\sigma$ Uncertainty
Volumetric Flow Rate	11.44 $\pm$ 0.12 m <sup>3</sup> /h
Absorbed thermal power	440 $\pm$ 8 W
Wall Heat Flux	13 832 $\pm$ 203 W/m <sup>2</sup>

Table 4.16 - "High heat flux" derived uncertainties

To evaluate the flow mean temperature, two ways are used. The first one is simply to assume a linear temperature evolution inside the channel, hence:

$$\bar{T}_{bulk} = \frac{T_{inlet} + T_{outlet}}{2} = 112\text{ }^{\circ}\text{C}$$

Where  $T_{inlet}$  is the temperature at the center of the channel inlet section and  $T_{outlet}$  is the temperature at the center of the channel outlet section. However, it could be that a nonlinear evolution occurs. Hence, temperature measurements inside the 7<sup>th</sup> bend (see Figure 4.64) have been used to plot the temperature evolution as a function of the linear position X between inlet and outlet section. Results are shown in Figure 4.76:

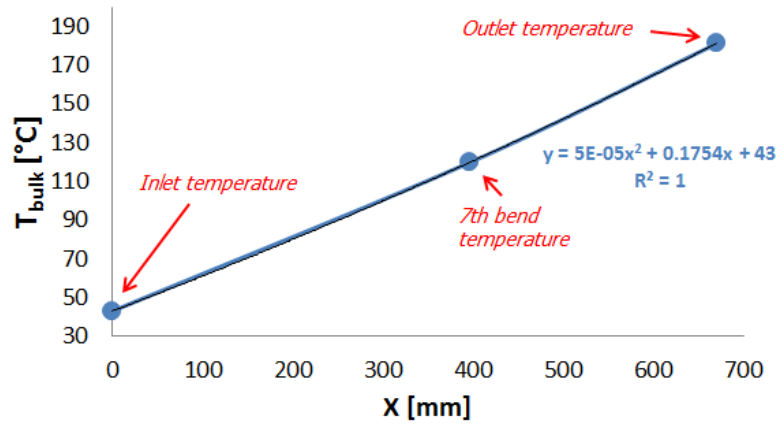


Figure 4.76–“High Heat Flux” case fluid temperature distribution inside the channel

The temperature evolution seems to be better represented by a parabola, where the quadratic term is positive: hence, the flow is slightly more heated up in the second half of the channel than in the first half. To calculate the average value in this case, we use the Lagrange theorem (where  $L=670$  mm):

$$\bar{T}_{bulk} = \frac{1}{L} \int_0^L (5 \cdot 10^{-5}x^2 + 0.1754x + 43)dx = 109.2^{\circ}\text{C}$$

Finally, it is possible to calculate the global heat transfer coefficient and its uncertainty. Note that the subscript “1” is used when a linear fluid temperature is supposed, whereas the subscript “2” is used when a quadratic evaluation is used:

$$h_1 = \frac{\phi}{(\bar{T}_{wall} - \bar{T}_{bulk})} = \frac{13\,832 (\pm 250) \text{ W/m}^2}{167.6 (\pm 1.9)^{\circ}\text{C} - 112 (\pm 2.1)^{\circ}\text{C}} = 249 \pm 16 \text{ W/m}^2\text{ }^{\circ}\text{C}$$

$$h_2 = \frac{\phi}{(\bar{T}_{wall} - \bar{T}_{bulk})} = \frac{13\,832 (\pm 250) \text{ W/m}^2}{167.6 (\pm 1.9)^{\circ}\text{C} - 109.2 (\pm 2.1)^{\circ}\text{C}} = 237 \pm 16 \text{ W/m}^2\text{ }^{\circ}\text{C}$$

See that the two calculated values slightly differ, suggesting that the way the average fluid temperature is evaluated is of primary importance for the following comparison with numerical data.

### 3.5.2 “Low Heat Flux” Case

Given the uncertainties in Table 4.15 and the previously shown formulae, see in Table 4.17 the final propagate uncertainties for the derived variables of interest..

	Mean Value $\pm$ Total $3\sigma$ Uncertainty
Volumetric Flow Rate	$11.8 \pm 0.2 \text{ m}^3/\text{h}$
Absorbed thermal power	$121.4 \pm 6.2 \text{ W}$
Wall Heat Flux	$3112 \pm 159 \text{ W/m}^2$

**Table 4.17 - "Low heat flux" derived uncertainties**

To evaluate the flow mean temperature, the same previously mentioned methods are used. The first one gives:

$$\bar{T}_{bulk} = \frac{T_{inlet} + T_{outlet}}{2} = 50.2 \text{ }^{\circ}\text{C}$$

Using the second methods, the measured temperature evolution inside the channel is studied. Results are shown in Figure 4.77:

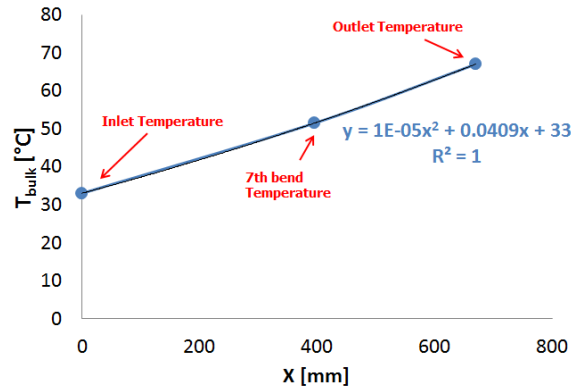


Figure 4.77 - “Low Heat Flux” case fluid temperature distribution inside the channel

Again the temperature evolution seems to be better represented by a parabola, where the quadratic term is positive: hence, the flow is slightly more heated up in the second half of the channel than in the first half. To calculate the average value in this case, we use the Lagrange theorem (where  $L=670$  mm):

$$\bar{T}_{bulk} = \frac{1}{L} \int_0^L (1 \cdot 10^{-5}x^2 + 0.049x + 33)dx = 48.2^\circ\text{C}$$

Finally, it is possible to calculate the global heat transfer coefficient and its uncertainty. Subscripts are used in the same way as for the previous case:

$$h_1 = \frac{\phi}{(\bar{T}_{wall} - \bar{T}_{bulk})} = \frac{3\,530 (\pm 180) \text{ W/m}^2}{64.4(\pm 1.5)^\circ\text{C} - 50.2(\pm 2.12)^\circ\text{C}} = 249 \pm 47 \text{ W/m}^2\text{C}$$

$$h_2 = \frac{\phi}{(\bar{T}_{wall} - \bar{T}_{bulk})} = \frac{3\,530 (\pm 180) \text{ W/m}^2}{64.4(\pm 1.5)^\circ\text{C} - 48.2(\pm 2.12)^\circ\text{C}} = 218 \pm 45 \text{ W/m}^2\text{C}$$

Note that the difference between the two heat transfer coefficients is larger because the  $\bar{T}_{wall} - \bar{T}_{bulk}$  is lower and hence even a small variation of one of the two temperatures plays a very important role for the final value of the heat transfer coefficient. See also that the heat transfer coefficient calculated by the first method is the same for both the “High Heat Flux” and for the “Low Heat Flux” cases. By the way this is not the case when dealing with the second method, where a more precise temperature distribution is considered and the actual heat flux distribution effects could potentially be described better. Finally see that, with regard the “High Heat Flux Case”, the heat transfer coefficient uncertainty is higher for the present case, since the  $1.5^\circ\text{C}$  single temperature uncertainty (which is fixed by the use of type K TCs) is more important when the mean temperature value is lower. By the way the two heat transfer coefficients are the same

(within the experimental uncertainty): in fact the difference between the heat transfer coefficient mean value is lower than twice the sum of the experimental uncertainties (see Figure 4.26), which is the criterion used so far to determine whether two experimental values can be considered the same or not.

### **3.6 CONCLUSIONS ON VHEGAS MEASUREMENTS**

The VHEGAS test section has been built to obtain experimental data to evaluate the global heat transfer coefficient of the innovative channel as well as of other channel geometries. Regarding the innovative channel geometry, two tests (high and low heat flux) have been carried out in order to determine the influence of near-wall thermal compressibility effects on the measured heat transfer coefficient. Measurements have been done after a careful evaluation of the thermal transient to ensure the stability of the thermal field. Experimental values of the heat transfer coefficient have been obtained in two different ways, trying to properly take into account the temperature evolution inside the innovative channel. The acquired database will be used to validate the numerical model in the next Chapter.

## **4. CONCLUSIONS**

The aim of the present chapter was to build a wide experimental database on the innovative channel to be used both for flow analysis and for the numerical model validation. Such an experimental necessity has been motivated in Chapter 2 and 3, where no real test case has been found in the literature. Hence, an aerodynamic database has been acquired by the LDV and PIV experiments. In particular, LDV experiment provided precise local measurements, whereas PIV experiment provided global pictures of the fluid stream. Design hypotheses have been carefully verified, to justify the measurement campaign strategies. Together with these data, thermal data have been obtained by the VHEGAS facility. These data are of primary importance since they can be used to verify the correctness of the thermal model and of the innovative channel performances.

Therefore, what it is still to be done is the flow analysis, to describe the phenomena occurring in the innovative channel (especially with regard to the effect of the mixing zones) and to obtain design correlations to show whether the innovative geometry is competitive with already existing compact heat exchanger technologies. This will be the goal of the next Chapter.



# Chapitre 5: Analyse de l'écoulement

Dans le chapitre 3, trois modèles de turbulence (SST, Stress Omega et ASST) ont été testés sur un certain nombre de cas test de base qui décrivent certains phénomènes potentiellement présents dans le canal innovant. En ce sens, la nécessité d'une base de données expérimentale spécifique a été soulignée. Les moyens nécessaires à l'établissement de cette base de données expérimentale ont été décrits dans le Chapitre 4, où les sections d'essais et une analyse préliminaire ont été détaillées.

L'objectif de ce chapitre est d'étudier l'écoulement de canal innovant et de donner un aperçu de la performance potentielle qui peut être obtenue. Plus précisément, la répartition de l'écoulement principal, ainsi que le mouvement secondaire présentent un intérêt pour l'écoulement dans un coude, ainsi que dans la zone de mélange. Avec la campagne expérimentale il n'était pas envisageable d'obtenir une description exhaustive de l'écoulement, et l'objectif était d'avoir suffisamment de données pertinentes pour valider le modèle numérique. Une fois validé, ce dernier nous a permis de décrire en détails l'écoulement dans le canal innovant.. Pour mettre en évidence cette approche, les résultats expérimentaux et numériques seront toujours affichés ensemble, sauf pour les variables qui n'ont pas été mesurées. Par conséquent, le choix est de sélectionner l'un des trois modèles décrits dans le chapitre 3 comme référence, en se basant sur les résultats présentés dans le chapitre 3 et sur une brève évaluation dans le premier paragraphe de ce chapitre.

Au final l'écoulement principal et secondaire sont analysés, avec les données expérimentales LDV et PIV et les résultats numériques du modèle ASST. Pour l'écoulement dans un coude, une région inhabituelle à vitesse élevée dans l'intérieur du coude est montrée alors que, pour l'écoulement secondaire dans le coude un tourbillon initial évoluant dans une structure à trois tourbillons est identifiée. Ce comportement est essentiellement dû à l'écoulement en entrée du coude provenant de la sortie de la zone de mélange. Dans la zone de mélange, le mélange est mis en évidence, du fait du champ de vitesse secondaire, de l'effet du coude et de l'entraînement visqueux de la vitesse d'écoulement secondaire du canal opposé.

Une fois le modèle aéraulique validé, la validation thermique a été faite en comparant le coefficient d'échange thermique calculé et expérimental, pour avoir un modèle numérique globalement fiable. Les résultats montrent que la valeur calculée du coefficient d'échange peut être comprise dans l'incertitude expérimentale.

Une fois expliqués les phénomènes d'écoulement à l'état stationnaire, le comportement thermo-hydraulique du canal innovant est étudié.

L'objectif final de ce travail étant de proposer un motif d'échange thermique innovant, des corrélations d'échange thermique et de pertes de charge sont fournies.

Avec les corrélations, une stratégie de comparaison de compacité est proposée: elle prend en compte les contraintes de dimensionnement, notamment le fait que les différentes technologies comparées ont la même puissance thermique échangée et les mêmes pertes de charge. Avec cette approche, il est montré que le motif innovant est le plus compact parmi les technologies d'échangeur de chaleur compact existantes dans le domaine industriel.

Une conception finale de l'échangeur de chaleur sodium-gaz d'ASTRID est proposée, démontrant qu'un gain d'environ 25% de compacité peut être acquis lors de l'adoption de la géométrie du canal innovant si on la compare à une technologie d'échangeur de chaleur compact à base de canaux droits traditionnels. De même une compacité supérieure peut être atteinte si le concepteur a des contraintes mécaniques et / ou de pertes de charge moins importantes.

# Chapter 5: Flow Analysis

## 1. INTRODUCTION

Chapter 3 has illustrated the development of a numerical model that could potentially be used to study the innovative channel flow. In particular, three turbulence models (i.e. the SST, Stress Omega and ASST) have been tested on a number of basic flows which potentially describe some of the several phenomena ongoing in the innovative channel. In this sense, the need of an experimental database has been underlined. The means to set this experimental database have been described in Chapter 4, where the test sections and some preliminary analysis have been detailed.

The aim of this section is to study the innovative channel flow and to provide an overview of the potential performance that can be obtained. Specifically, the principal flow distribution as well as the secondary motion are of interest for the in-bend flow, whereas the mixing description will be given for the mixing zone. Since the experimental campaign could not provide all the information needed to completely describe the flow, computations will be used as a mean of description. To validate this approach, experimental and numerical results will be always shown together, except for the variables that have not been measured. Therefore, the choice is to select one of the three models described in Chapter 3 as the reference one, based on the results shown in Chapter 3 and a brief evaluation in the next paragraph.

The final goal of this work being to propose an innovative heat transfer geometry, the heat transfer and pressure drop correlations will be provided. A comparison of the available technologies and the innovative channel will be finally done, to demonstrate the potential of the proposed geometry.

## 2. SELECTION OF THE REFERENCE MODEL FOR THE ANALYSIS

Section 5.1 has described the approach of retaining one of the three models shown in Chapter 3 as the reference one to be validated against experimental data and to be used to analyze the innovative channel flow. In this sense, the conclusions of Chapter 3 showed how the SST model provided quite good results on the tested cases, even if it cannot capture flow anisotropies (section 3.1) and turbulence-driven secondary motions (section 3.4). The Stress Omega model provided very good results for many of the tested cases but it failed in some special applications (section 3.2 and 3.5), raising

doubts on its applicability on complex flows. The ASST model, instead, provided superior results compared to the SST model due to the anisotropic formulation; moreover, its results were at least as good as those of the Stress Omega model or even better, since it could usefully be employed on all the selected test cases. To finally select the reference model, the three models are compared against LDV experimental data, where it is simpler to get detailed information. Given the noticed flow stability of Figure 3.24, steady state calculations have been run.

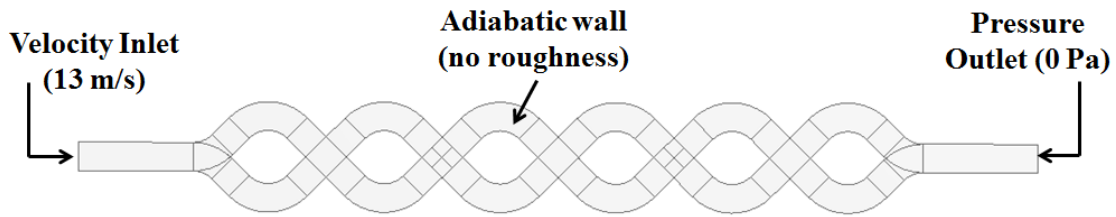


**Figure 5.1 - Innovative channel computation boundary conditions**

A velocity inlet (Dirichlet) and a gauge pressure equal to 0 Pa pressure outlet (Neumann) boundary conditions are used. The working fluid is air at atmospheric temperature and pressure. The solver is Pressure-based one and the Coupled pressure-velocity algorithm with pseudo-transient option is used. Gradients are evaluated through the Least-Squared method. Second Order Upwind Scheme is used for the spatial discretization of momentum, turbulent kinetic energy and turbulent dissipation rate transport equations.

Meshing convergence has been evaluated by comparing the average wall shear stress on the walls of the channel. Three successively refined meshes (hereafter named as A, B and C according to the refinement level of the near-wall first cell thickness) have been tested. A near-wall approach has been used to obtain proper  $Y^+$  values for the first cell. Table 5.1 shows the results of the convergence evaluation for the SST model:

Configuration	$Y^+$	$\tau_w$
A	2.5	1.001 Pa
B	1.2	0.984 Pa
C	0.7	0.988 Pa

**Table 5.1 - Innovative channel LDV geometry mesh convergence evaluation**

From values in Table 5.1, see that configuration C shows a converged wall shear stress solution. Based on these trends, we retained configuration C as the reference

meshing (difference with B configuration of 0.4%), which results to be a converged mesh for the Stress Omega and ASST models as well. See an example of C configuration in Figure 5.2. Note that the same approach in terms of  $y^+$  value and discretization schemes will be used for PIV channel as well. The only difference lies in the inlet boundary condition, which is a fully developed velocity profile, as shown in Chapter 4 section 2.4.1.

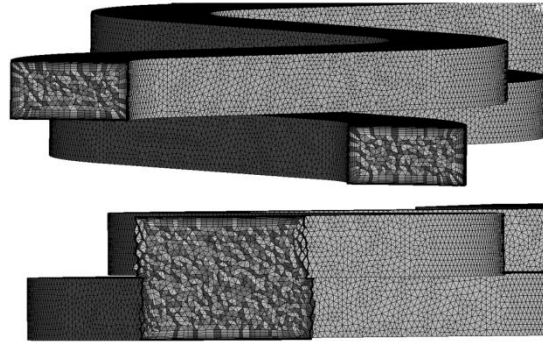


**Figure 5.2 - Innovative channel study reference mesh: bend (on top) and mixing zone (on bottom)**

To evaluate the three models, two velocity profiles and one Reynolds stress profile will be shown. They are taken from the “45°  $Y^*=0$ ”  $Z^*$  profile defined in Table 4.4 and the  $Y^*$  profile right in the middle of the mixing zone (Figure 5.3).

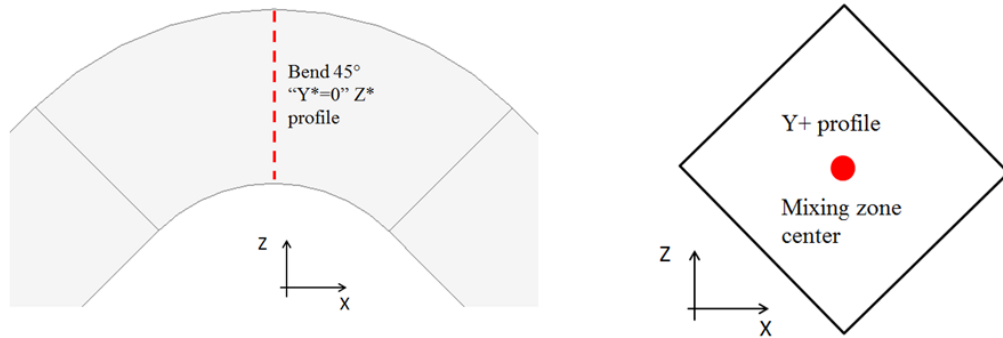


**Figure 5.3 - Chosen profiles for turbulence model comparison**

See the results of the comparison in Figure 5.4 to Figure 5.7.

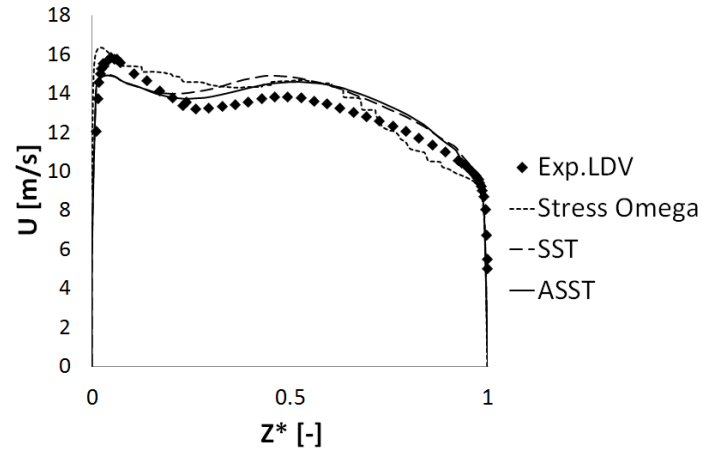


Figure 5.4 - Experimental vs numerical in-bend 45° Y0 profile principal velocity

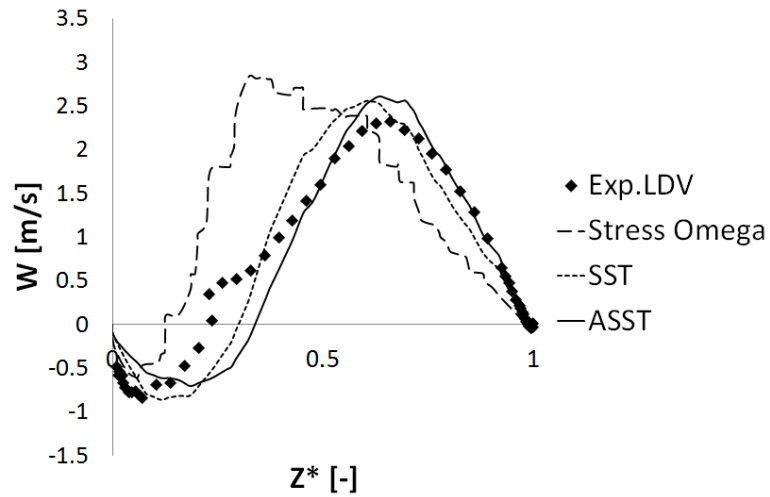


Figure 5.5 - Experimental vs numerical in-bend 45° Y0 profile radial velocity

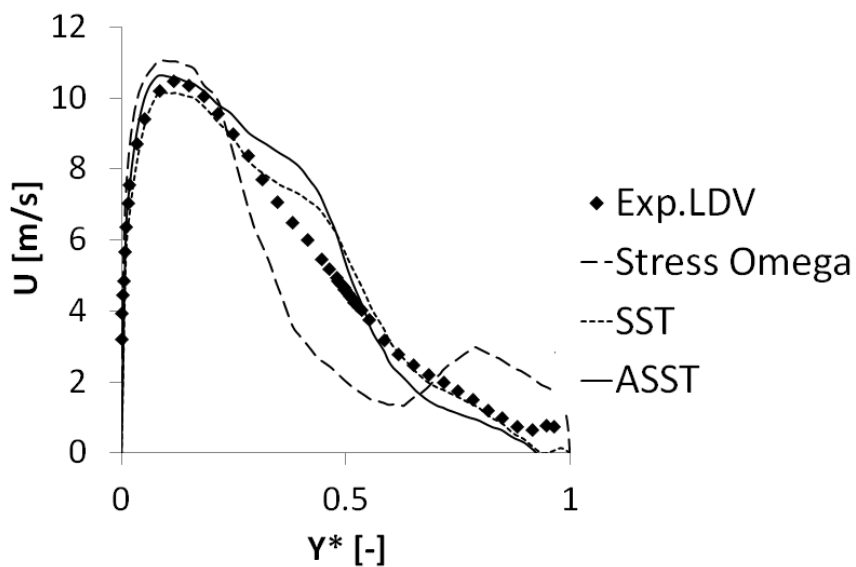
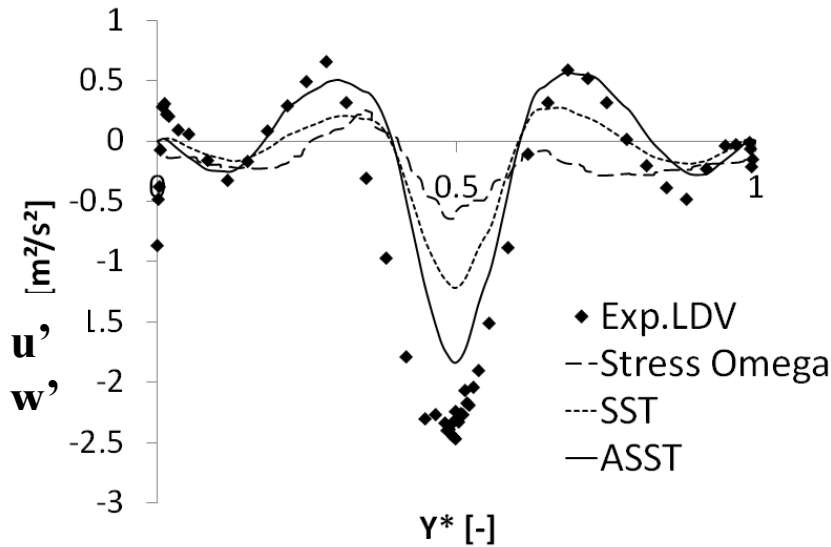


Figure 5.6 - Experimental vs numerical mixing zone central Y profile principal velocity



**Figure 5.7 - Experimental vs numerical mixing zone central Y profile  $u'w'$  mixed Reynolds stress**

Note that, even though the SST model provides very good results, it is the ASST model that provides the best overall results. In particular, see in Figure 5.4 that the U profile is slightly better predicted by the ASST model in the central region and that the W profile calculated by the ASST model is better in capturing the maximum and the boundary layer in the outer bend, despite a slightly worse prediction of the local minimum in the inner bend. As regards the mixing zone, the SST model gives slightly better results than the ASST near the mixing plane but the ASST model captures far better the mixed Reynolds stress  $u'w'$  all over the profile. We never mentioned the Stress Omega model's results because they are always poor: again, this could seem to be surprising, since it is a model which is supposed to better capture complex flows. Indeed, as already observed in Chapter 3, the ANSYS Fluent Stress Omega results are sometimes incorrect for complex flows and hence its application can be questioned. Before going through the flow analysis, it is useful to look at the distribution of the  $F_1$  function (see Chapter 3 for its definition), because it provides valuable information on the SST/ASST application in the fluid channel. Remember that when  $F_1=0$  the actual used model is a  $k-\varepsilon$  model, whereas for  $F_1=1$  it is a  $k-\omega$  model. Strictly speaking, intermediate values of the  $F_1$  function result in a hybrid model which could potentially provide incorrect and unphysical results, since the transport equation coefficients (found and evaluated based on basic test cases) also depend on  $F_1$  function. Figure 5.8 shows the  $F_1$  distribution in the “45°  $Y^*=0$ ”  $Z^*$  profile. See that the SST model is actually using a not-well-known model almost in the whole profile, where the average  $F_1$  value is around 0.75. In this

sense, the ASST model acts more properly, since its  $F_1$  function is practically always equal to one, resulting in using the  $k-\omega$  model in the whole profile. Both models use a  $k-\omega$  formulation in the boundary layer region, which is consistent with the  $F_1$  function formulation. Nevertheless, the  $k-\varepsilon$  model, which should be used in the high-Re region outside the boundary layer, is never used: this suggests that such a region is never detected by the models, even though this should not be physical.

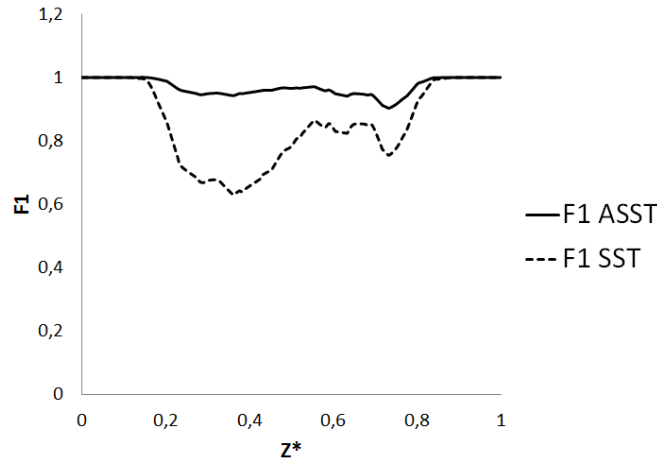


**Figure 5.8 - ASST vs SST model computed  $F_1$  function in the in-bend 45°  $Y_0$  profile**

To complete this analysis, see the  $F_1$  function values in the  $Y^*$  profile in the middle of the mixing zone (see Figure 5.9).

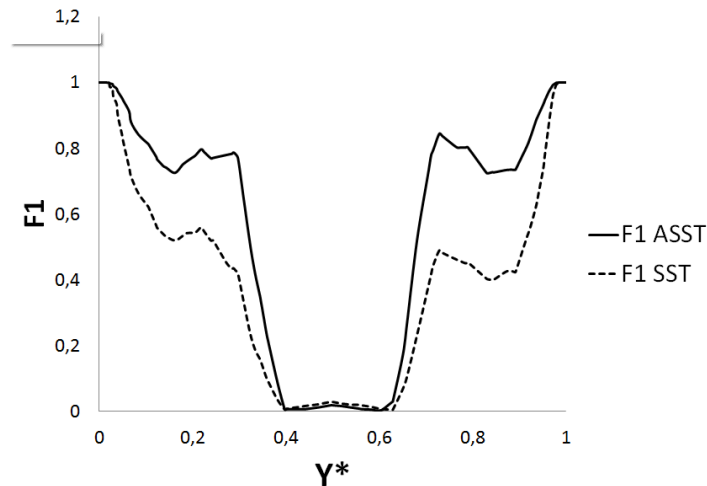


**Figure 5.9 - ASST vs SST model computed  $F_1$  function in the mixing zone central  $Y$  profile**

Again, both models use a  $k-\omega$  model ( $F_1=1$ ) in a thin region of the two boundary layers, whereas they use a  $k-\varepsilon$  model around the mixing plane. This is a first result compared to the bend case where the  $k-\varepsilon$  model is never used. Indeed, the mixing plane is supposed to be a high turbulence region where it is no surprising to find a  $k-\varepsilon$  modelling. Again,



note that the two models use a hybrid model between the boundary layers and the mixing planes. Still, the ASST results are somehow more proper, in the sense that a faster transition between the two models occurs. In fact, the smooth transition occurring in the SST model seems to result in a hybrid model in the majority of the profile. Nonetheless, the hybrid model provides very valuable results, especially for the velocity field. This is probably one of the characteristics of the SST model, which coefficients have been carefully tuned to provide good results for engineering application. Finally note that the anisotropic formulation of the ASST model improves the results both in the hybrid model and in the k- $\epsilon$  model regions.

See that, given these results, the flow analysis will be done with experimental data supported by ASST model's results.

### **3. MODEL VALIDATION AND FLOW ANALYSIS**

#### **3.1 IN-BEND FLOW**

##### **3.1.1 Principal flow**

Principal velocity analysis is of primary importance since principle flow field is responsible for the macroscopic phenomena occurring in the innovative channel. Indeed the analysis that will be shown in the current section corresponds to that of chapter 2 section 2.2, in which it has been shown how a wavy channel creates a fluid flow which characteristics strictly depend on the channel geometry. To investigate the in-bend flow, the LDV, PIV and ASST numerical data will be used. Anyway, since the Reynolds numbers in LDV and PIV experiments were different (see Chapter 3), the fluid flow is not supposed to be exactly the same for the two sets of experimental data. Nonetheless, provided that both flows were turbulent, minor differences as well as qualitative agreement are expected. For the sake of a better comprehension, only the velocity fields will be shown. For a comprehensive model validation refer to Appendix F.

Figure 5.10, Figure 5.11 and Figure 5.12 show the LDV vs ASST in bend Z\* principal velocity profiles for different Y\* values (refer to chapter 4, section 1.3.1).

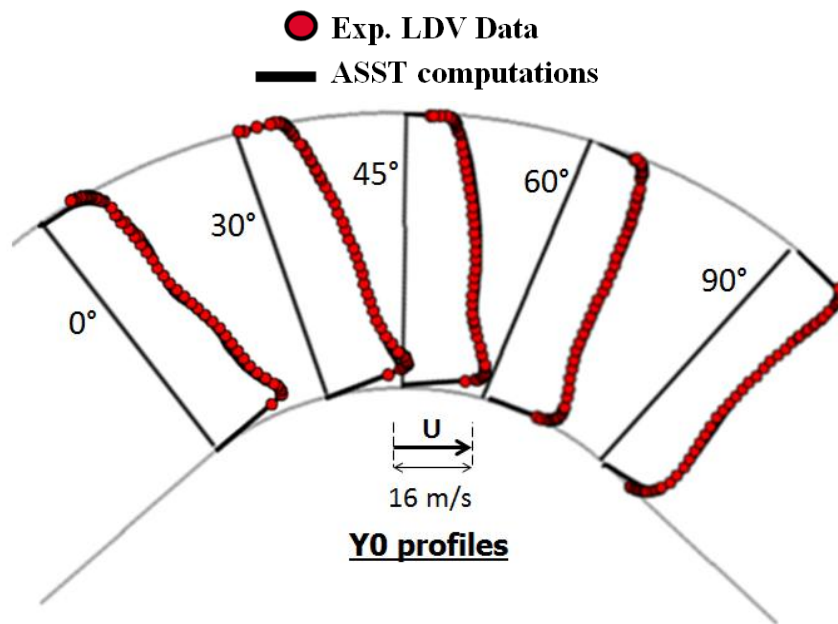


Figure 5.10 - LDV/ASST Y0 principal velocity profiles for in-bend flow

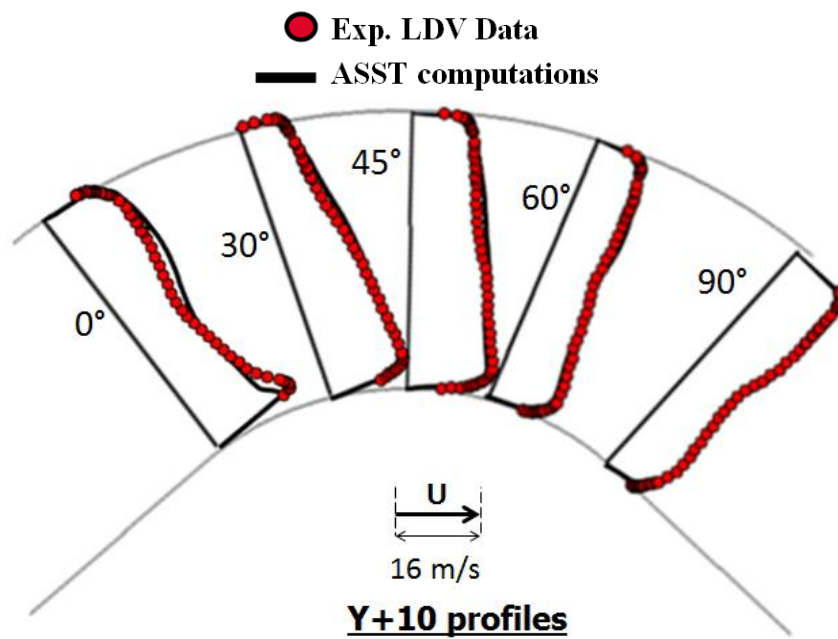
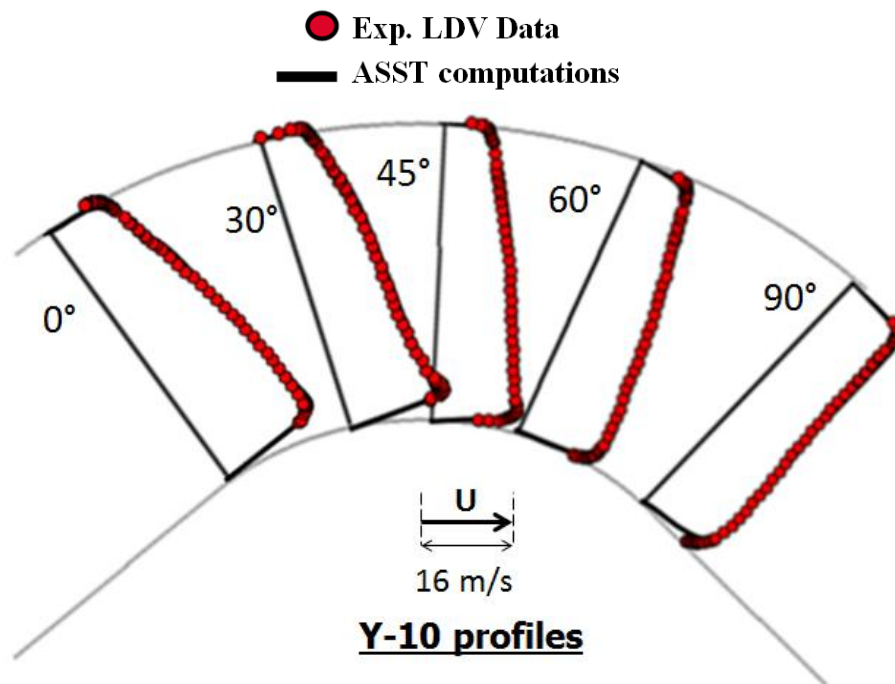


Figure 5.11 - LDV/ASST Y+10 principal velocity profiles for in-bend flow



**Figure 5.12 - LDV/ASST Y-10 principal velocity profiles for in-bend flow**

First of all, the ASST model provides very trustful results all over the bend region. What is immediately clear is that an unusual phenomenon is occurring, e.g. a high velocity region in the inner bend. This distribution contrasts with the usual velocity field in a curved bend, where the higher velocity region is in the outer part of the bend due to mass conservation (see Figure 3.21). Indeed the source of this behavior is to be searched in the mixing zone flow, since this phenomenon can be already observed at the bend inlet section (i.e.  $0^\circ$  profiles – see next paragraph). However, the in-bend pressure gradient tends to homogenize the flow: see that the outlet flow at bend  $90^\circ$  section is somehow smoother than the inlet flow. Indeed the outer bend acceleration results in a M-type velocity profile at the bend outlet, with the inner and outer bends still presenting relatively high velocity values, and the middle region having local lower values. In this sense, the curvature effects are, as expected, the same as a normal in-bend flow, with the only difference in the inlet conditions.

LDV database has not shown if separation occurs in such a flow. Remember that separation is potentially of primary importance for local heat transfer enhancement (see chapter 2, section 2.2). In this sense, PIV campaign gives useful insights. Figure

5.13, Figure 5.14 and Figure 5.15 compare PIV measurements and ASST computations on the PIV and LDV geometries in terms of velocity magnitude.

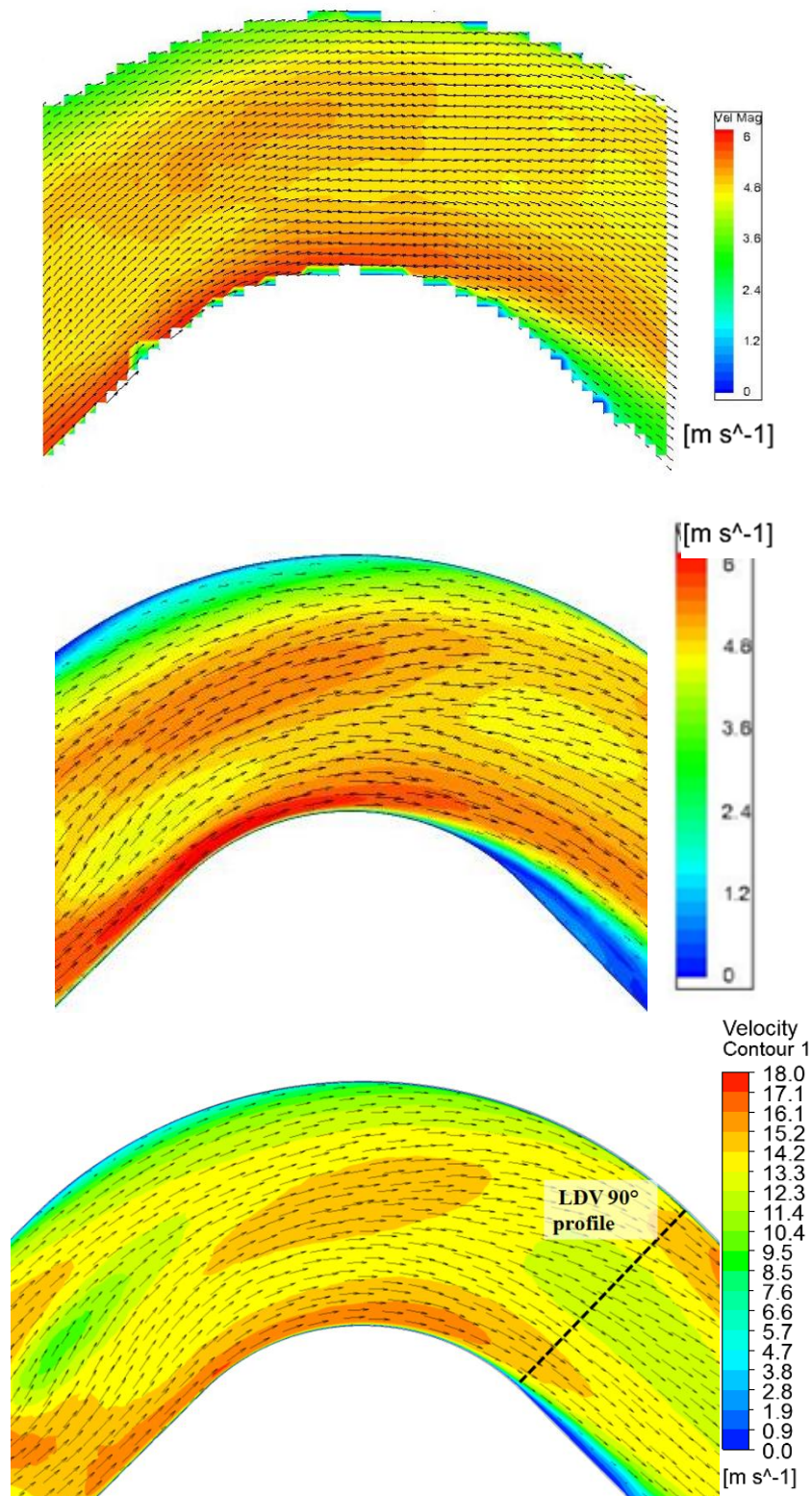


Figure 5.13 - Velocity field on bend middle plane comparison (PIV data on top, ASST computation on PIV channel geometry in the middle and ASST computation on LDV channel on the bottom at  $Y^*=15\text{mm}/30\text{mm}$ )



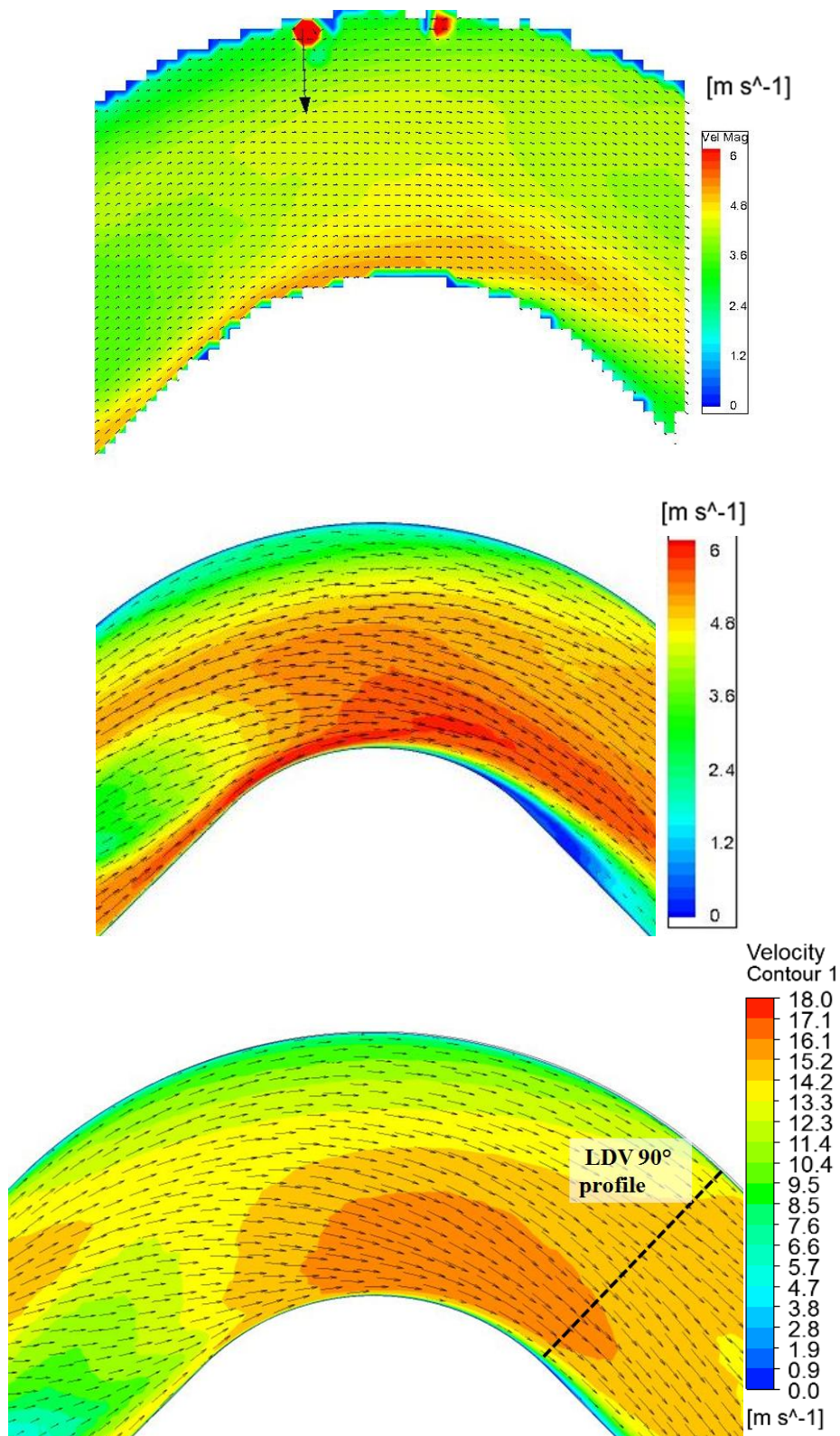
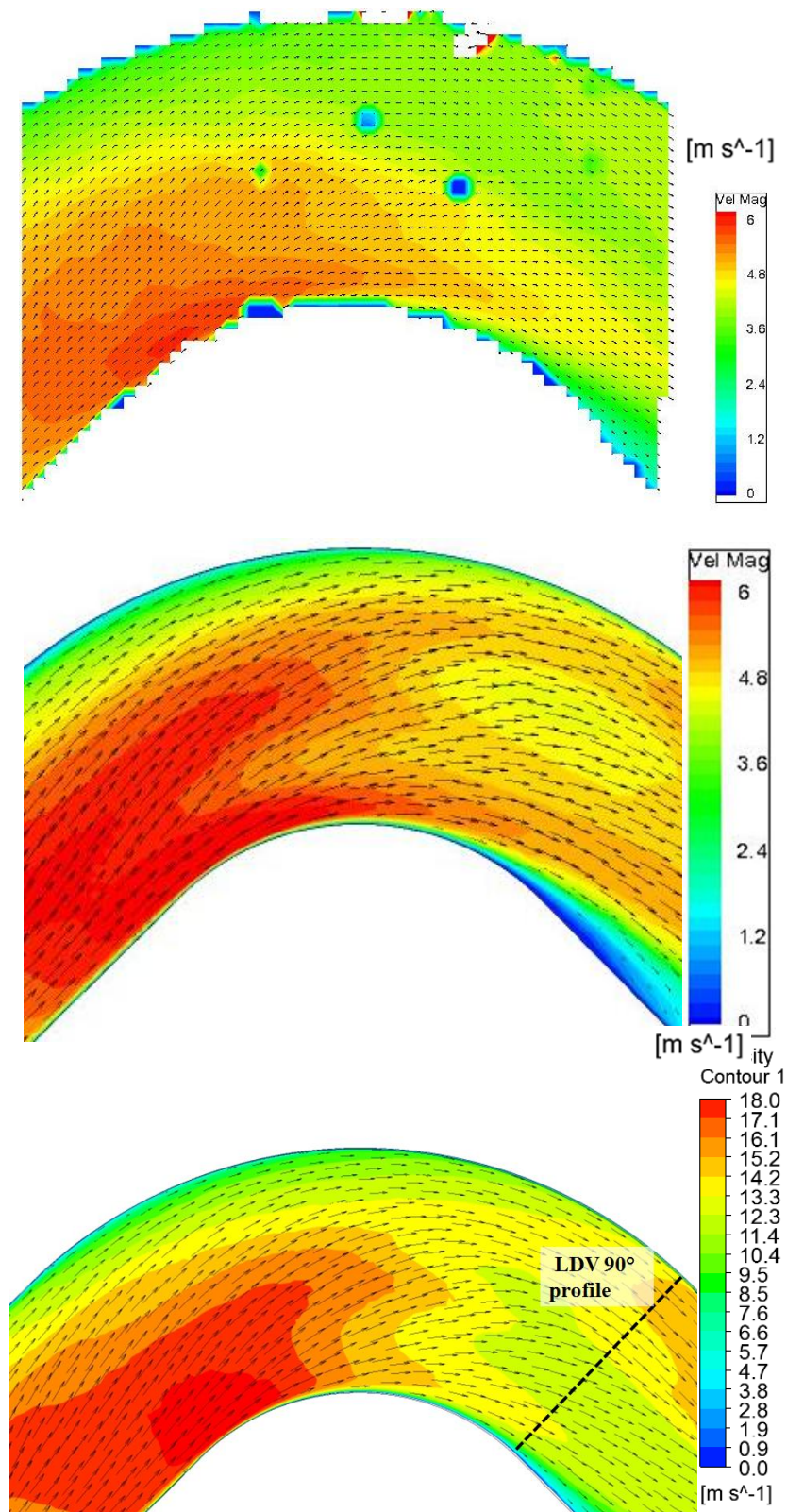


Figure 5.14 - Velocity field on bend middle plane plus 4 mm comparison (PIV data on top, ASST computation on PIV channel geometry in the middle and ASST computation on LDV channel on the bottom at 24mm/30mm)



**Figure 5.15 - Velocity field on bend middle plane minus 4 mm comparison (PIV data on top, ASST computation on PIV channel geometry in the middle and ASST computation on LDV channel on the bottom at 6mm/30mm)**

First of all see again that the LDV data behavior is the same as the PIV data, with a higher velocity region in the inner bend and in fluid core region. The latter is pushed towards the outer bend by the pressure gradient as expected. Generally, the velocity field is very well predicted by the ASST model, except for the zone close to the bend outlet. This is critical, since this is the region where separation seems to occur. Separation is not detected in PIV data. Anyway there is a low velocity region at inner bend outlet even in the PIV data, even though it was difficult to capture since it is very close to the wall, where PIV measurements are less trustworthy. Hence, since the two computations give the same results, we conclude that separation might occur, even though separation is always a very difficult phenomenon to be captured by computations. LDV experiments could not show it because separation would occur after the bend outlet 90° cross-section, which is the last one investigated by the LDV campaign (in this sense, the 90° profile is always shown in previous figures). Anyway, ASST computations on LDV channel flow show that separation occurs. By the way, even if separation did not occur, the low velocity region at inner bend outlet would result in local flow acceleration in the outer bend. This is again of particular interest for the heat transfer enhancement, as shown in chapter 2 section 2.2. Moreover, the fact that two high velocity regions in the inner bend inlet section and outer bend outlet section make us stating that a flow swirling (i.e. strong secondary motion) is occurring, which is a good feature for the innovative channel geometry since it can largely enhance heat transfer due to boundary layer detachment and hence to local accelerating zones. In this sense, the secondary flow field has to be studied, because it could result in high mixing level thanks to secondary motions.

### **3.1.2 Secondary flow**

Secondary motions are responsible for flow mixing and heat transfer enhancement due to their capability to act on the thermal boundary layer in a channel flow, reducing the effect of such a thermal barrier to effective heat transfer. We saw in Chapter 3 how secondary motions are always difficult to capture, especially the secondary motions of the second kind (i.e. turbulence drive, see chapter 3 section 3.4).

To study secondary motions in the in-bend flow, the radial velocity  $W$  measured in the LDV campaign will be shown together with the ASST results to validate the numerical model. In fact radial velocity value (either positive or negative, towards the outer or the



inner bend respectively) provide visual information about the flow motion in the radial direction. Therefore, a first trial of the secondary motion can be done with this velocity component. However, to complete the analysis, secondary motion vectors calculated by the validated ASST model will be shown as well. Figure 5.16 to Figure 5.20 show the results, with red dots being LDV experimental data and black solid lines being ASST computation results.

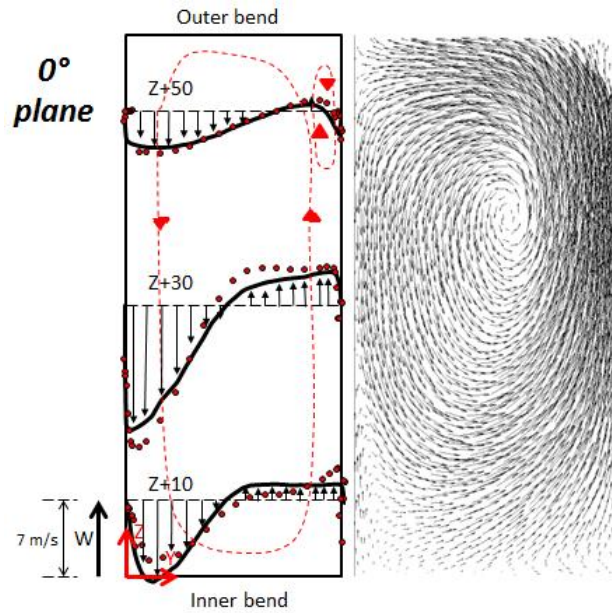


**Figure 5.16 - LDV/ASST data on radial velocity at bend  $0^\circ$  plane (on the left) and ASST computed secondary motions (on the right)**

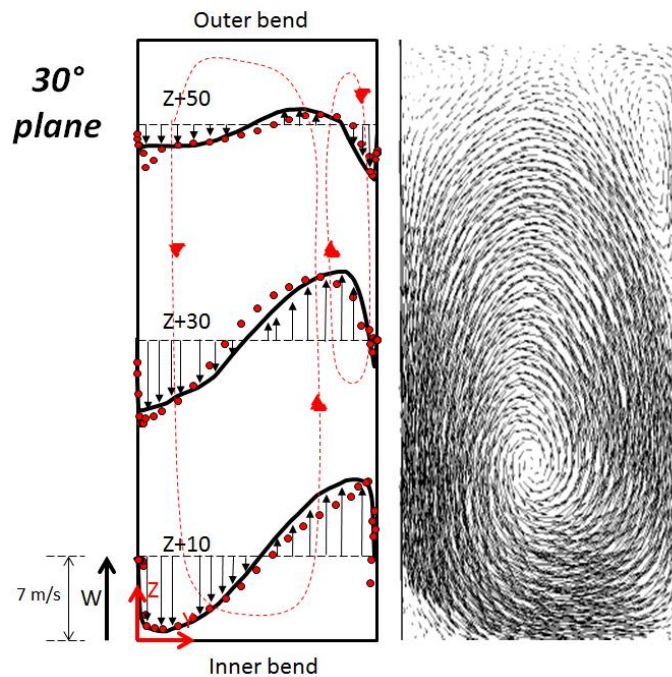


**Figure 5.17 - LDV/ASST data on radial velocity at bend  $30^\circ$  plane (on the left) and ASST computed secondary motions (on the right)**



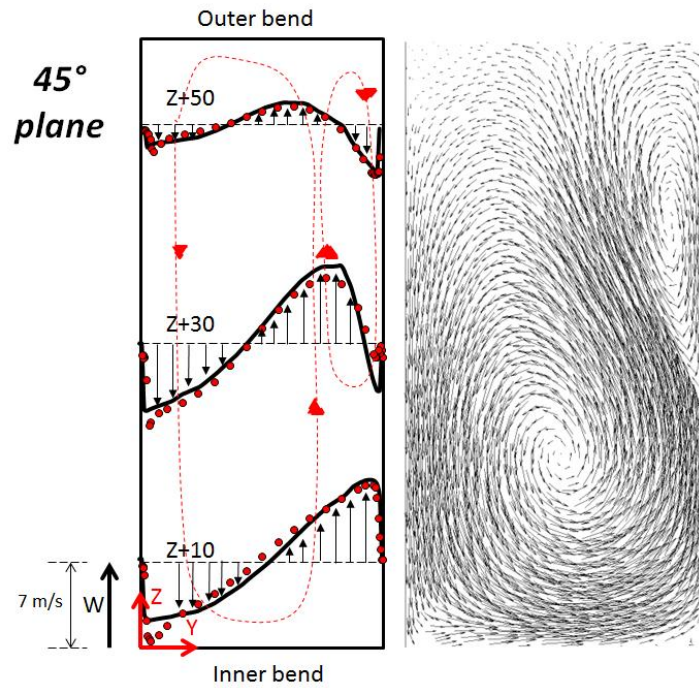


Figure 5.18 - LDV/ASST data on radial velocity at bend 45° plane (on the left) and ASST computed secondary motions (on the right)

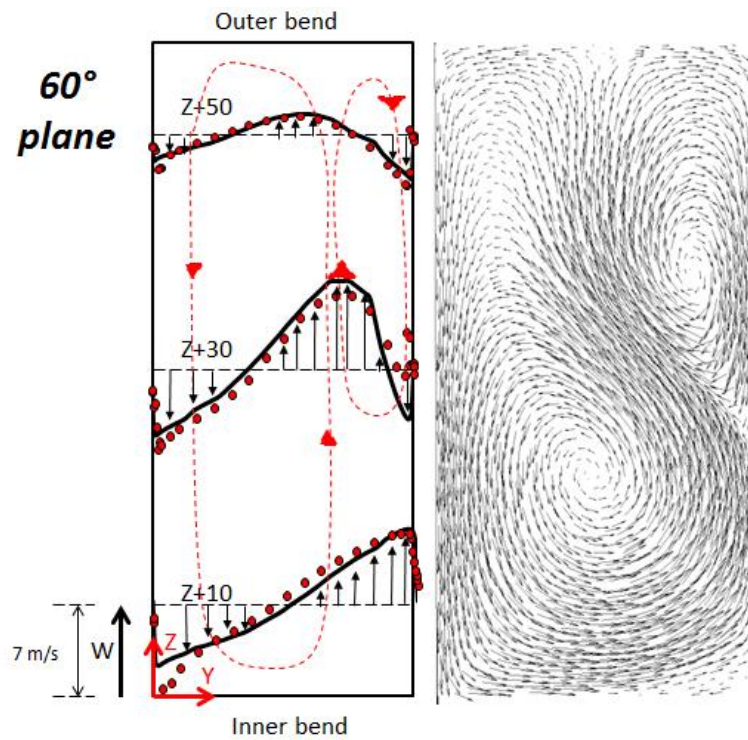
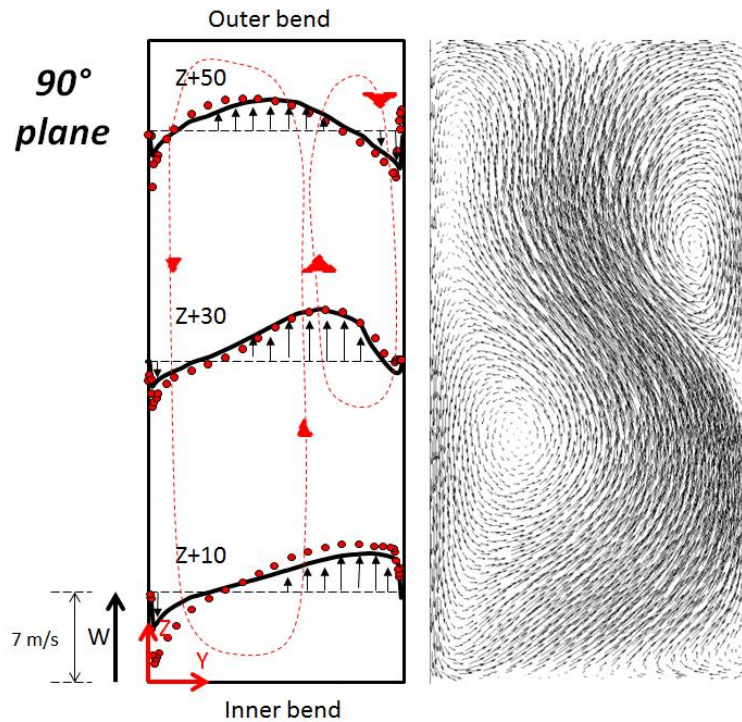


Figure 5.19 - LDV/ASST data on radial velocity at bend 60° plane (on the left) and ASST computed secondary motions (on the right)



**Figure 5.20 - LDV/ASST data on radial velocity at bend 90° plane (on the left) and ASST computed secondary motions (on the right)**

See that a vorticity component is already present in the bend inlet section (i.e. 0°) due to the mixing zone effects that will be shown in next paragraph. Moreover the maximum secondary velocity value in the bend inlet section is around 50% of the principal velocity). This shows that an effective swirling is already occurring at bend inlet, as already detected by principal flow field analysis. Compare, for example, this 50% of secondary to principal velocity ratio with the 5% value shown in chapter 3 section 3.3 for a 90° bend flow.

Note that a small corner vortex could be detected observing the experimental data at 0°. This corner vortex is slightly detected by the secondary motion vectors. Anyway note that at 30° the corner vortex is clear both in the LDV data and in the ASST computed streamlines. This vortex tends to grow up passing through the bend. At the bend outlet, it is almost of the same magnitude as the principal vortex. What is interesting to note is that there is a fair similitude between these results and the results of Adachi et al.<sup>108</sup> for a curved channel with rectangular cross-section of the same aspect ratio as ours. In fact, for a uniform shear inlet flow, they found a corner vortex at bend outlet as shown in Figure 5.21:

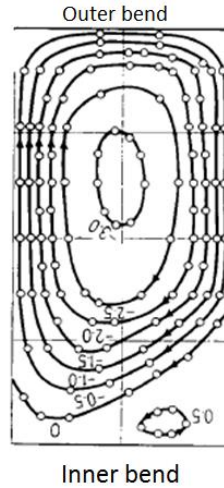


**Figure 5.21 - 90° bend secondary motion according to Adachi et al.**

Even if there are several differences between Adachi's and the innovative channel geometries (specifically the curvature with regard the rectangle minor dimension), it is surprising to find such a corner vortex at bend outlet. Moreover, the fact that Adachi et al. had a uniform shear inlet flow is somehow similar to the present case, where a non-zero shear velocity is given by the fluid flow coming out from the mixing zone (see it in next section). What really changes is the position of this corner vortex, which is at the inner bend for Adachi et al. while, in the innovative channel flow, it is rather on the outer bend, as shown in Figure 5.16 to Figure 5.20. Indeed the motivation for this difference has to be found in the opposite momentum distribution in the channel cross section. As already mentioned, for a standard inlet section the high momentum flow is in the outer part of the bend, whereas for the innovative channel it is in the inner bend (at least until separation, which would occur after the bend outlet 90° cross section). In this sense, the two corner vortices occur in a relative low momentum region of the fluid flow, where they can grow and stretch. By the way the explanation given by Adachi et al. about this corner vortex occurrence is the vorticity contained in the portion of the boundary layer. In fact, the Squire-Winter solution<sup>109</sup> describes the secondary motion streamlines in a bend through the following equation for the stream function  $\psi^{xx}$  in the system of coordinates given in Figure 3.21:

$$\frac{\partial^2 \psi}{\partial Z^{*2}} + \frac{\partial^2 \psi}{\partial Y^{*2}} = -\xi$$

<sup>xx</sup> The stream function  $\psi$  results in  $V_x = \frac{\partial \psi}{\partial y}$  and  $V_y = -\frac{\partial \psi}{\partial x}$

With the principal vorticity component  $\xi$  being:

$$\xi = -2\theta \frac{dU}{dY^*}$$

And  $\theta$  being the bend total angle (i.e.  $90^\circ = \pi/2$  for the present case).

Indeed see that the boundary layer vorticity is higher for the “z50” profile where the vortex occurs (red circle in Figure 5.22).

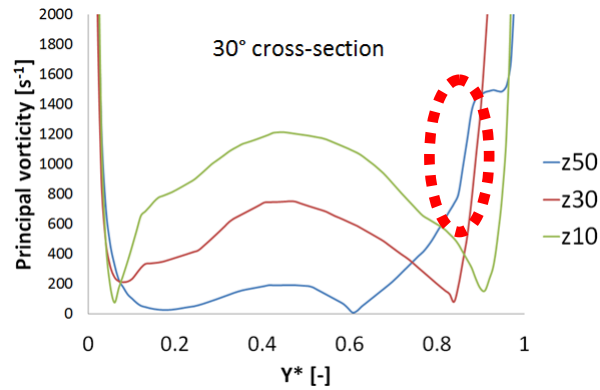


**Figure 5.22 - 30° plane ASST computed principal vorticity profiles**

Once assumed this explanation (which must be validated by the analysis of mixing zone outlet flow, in particular with regard to the uniform shear velocity profile), see that the corner vortex stretches under pressure gradient (as for Dean vortices) and becomes almost as large as the principal one at bend outlet. In  $90^\circ$  cross section, see that computation clearly shows a third vortex of the second kind (turbulence driven) appearing in the inner bend. This is not detected by the LDV data since that portion of the channel was not investigated. However we expect to find this three-vortices distribution at mixing zone inlet in next section. To summarize bend secondary flow, Figure 5.23 shows several secondary streamlines distribution in different positions of the bend:

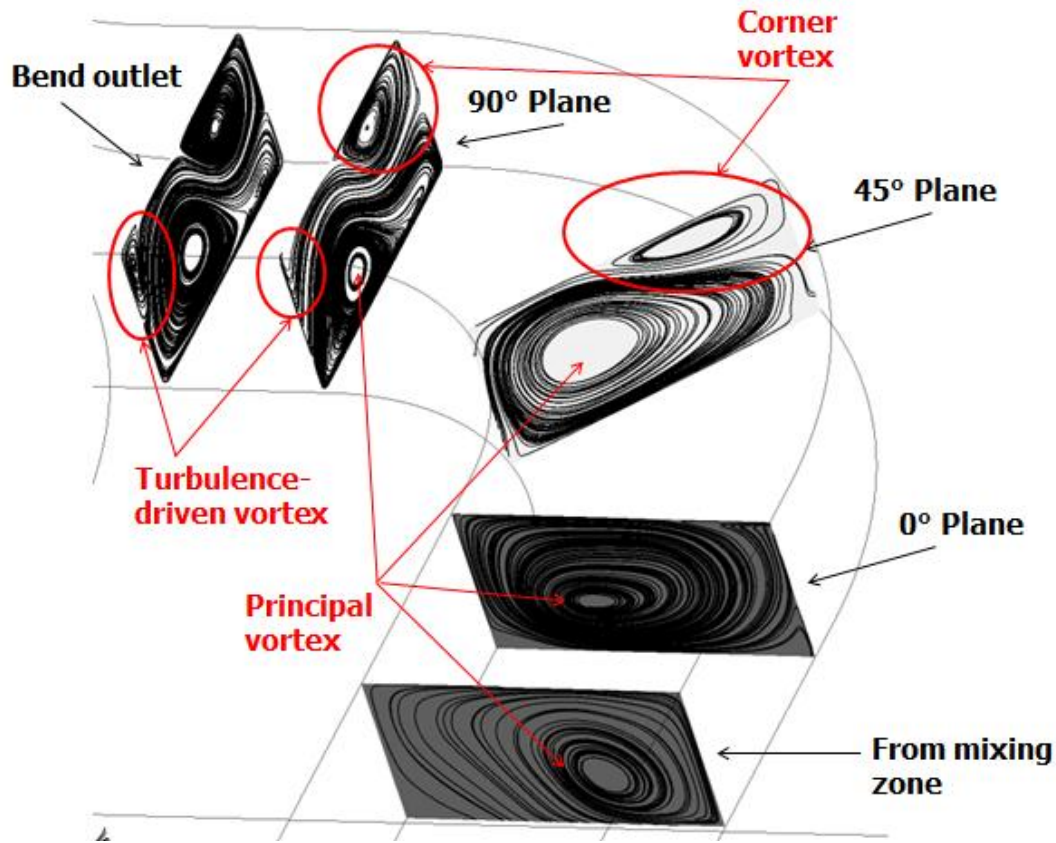


Figure 5.23 - In-bend flow ASST computed secondary motion evolution

### 3.2 MIXING ZONE FLOW

Mixing zone analysis is of primary importance to verify the hypothesis done in the previous paragraph on bend flow analysis and to show that actual mixing occurs. This phenomenon is supposed to be responsible for a large part of the heat transfer enhancement provided by the innovative channel, creating a real 3D flow with major thermal boundary layer detachment and mixing.

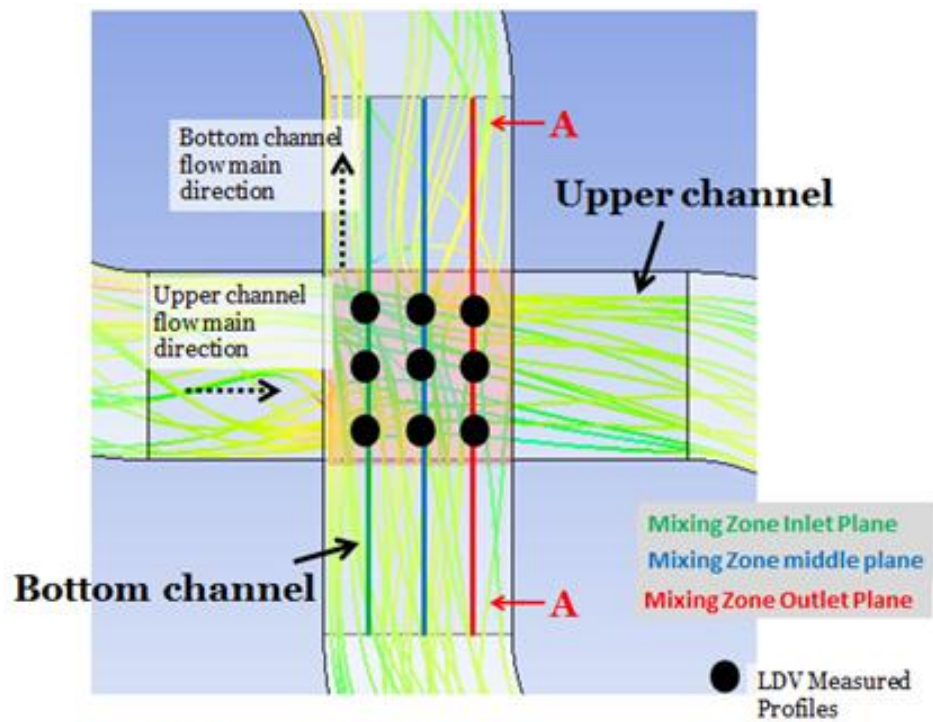
The inlet condition for the mixing zone is a flow with a principal velocity having two local maximum values and a secondary flow characterized by three different vortices.

To show the principal and secondary velocity field, we will present results for three planes measured by the LDV technique:

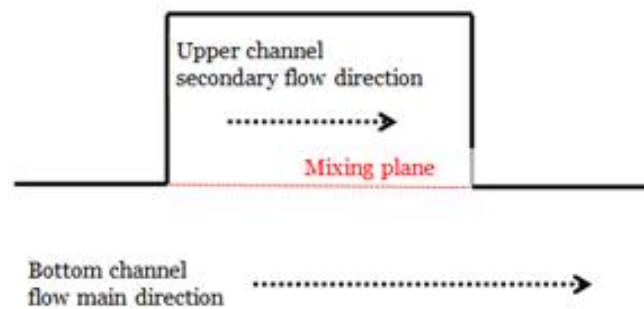
- The mixing zone inlet, meaning that this is the first measured plane the flow encounters when entering the mixing zone.
- The mixing zone middle plane.
- The mixing zone outlet, meaning that this is the last measured plane the flow encounters in the mixing zone before approaching the bend.

See Figure 5.24 for visual explanation.





A-A section



Bottom channel flow main direction

A-A section

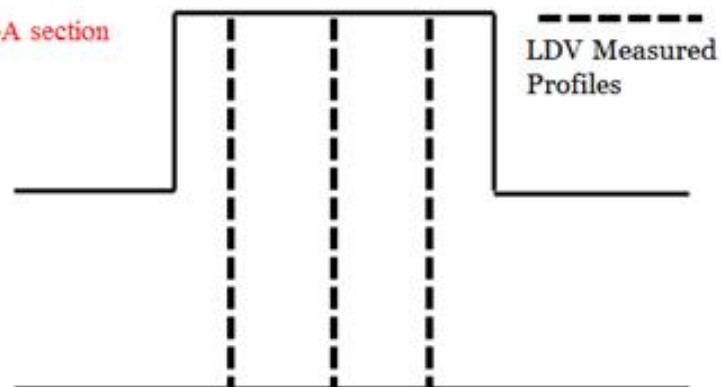
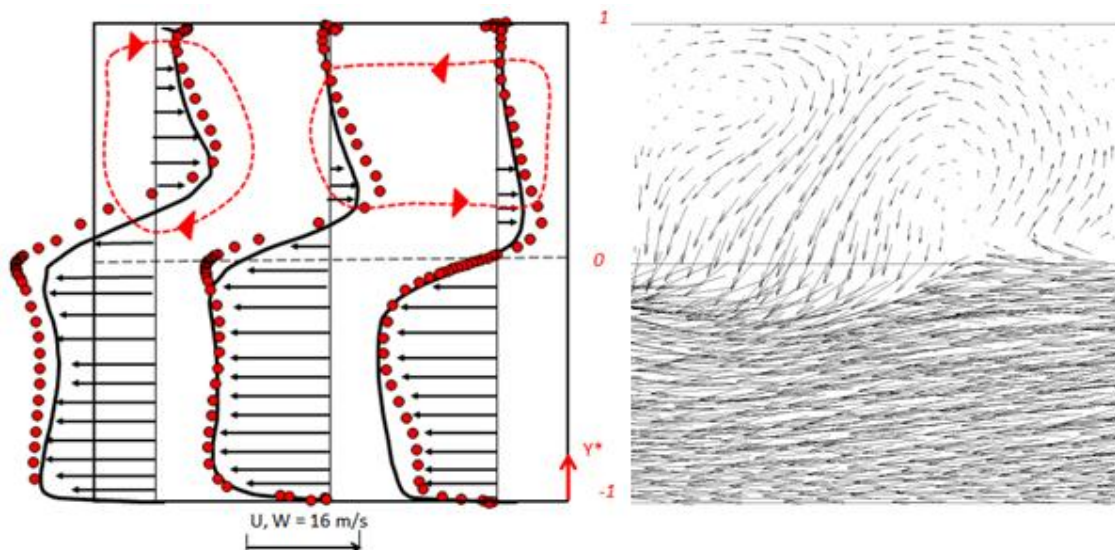


Figure 5.24 - Mixing zone investigated planes

To be formally correct, the three planes normal to those of Figure 5.24 should be studied as well, since they provide complementary information. However, planes of Figure 5.24 allow the study of the principal and secondary velocity at the same time due to flow symmetry shown in Chapter 4: in fact the shown velocity is the principal velocity for one of the two rectangular channels composing the innovative geometry (i.e. the bottom channel), and the radial velocity for the other one (i.e. the upper channel). However, due to flow symmetry, we can assume that the principal and radial velocity profiles are the same for the upper and bottom channel, resulting in no need to study them separately via the other normal planes.

Figure 5.25, Figure 5.26 and Figure 5.27 show the results for the already mentioned LDV measured profiles, together with ASST computations, which give the global velocity field on the shown plane. The upper part of such figures corresponds to the secondary velocity field, whereas the bottom part to the principal velocity field (as already explained no matter the considered channel due to flow symmetry).



**Figure 5.25 - LDV/ASST data on principal and radial velocity at mixing zone inlet plane (on the left) and ASST computed secondary velocity vectors (on the right)**

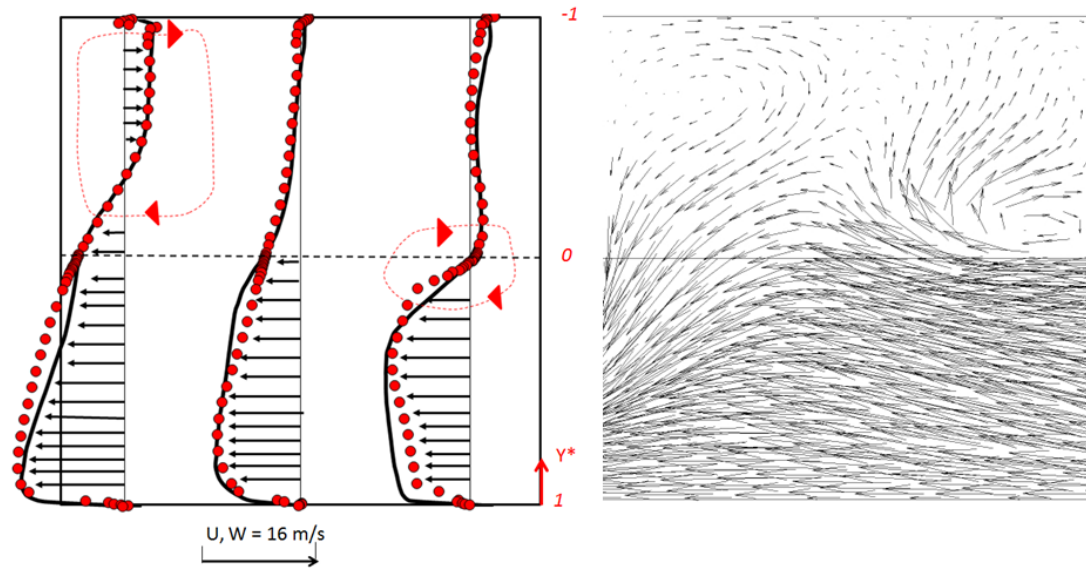


**Figure 5.26 - LDV/ASST data on principal and radial velocity at mixing zone middle plane (on the left) and ASST computed secondary velocity vectors (on the right)**

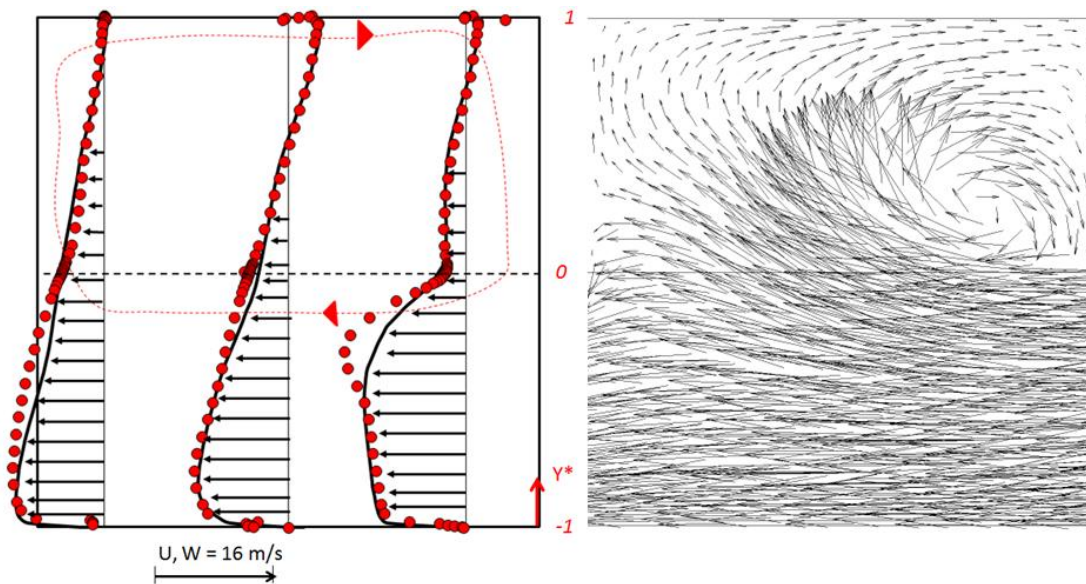


**Figure 5.27 - LDV/ASST data on principal and radial velocity at mixing zone outlet plane (on the left) and ASST computed secondary velocity vectors (on the right)**

Regarding the principal velocity, see how the flow entering the mixing zone keeps the two local maximum values structure. Mixing already occurs, since principal velocity streamlines of the bottom channel do penetrate in the upper channel and vice versa. This is due to the secondary velocity provided by secondary motions at bend exit, which provides the velocity component necessary to mass transport through the mixing plane. In particular, the three vortices structure of the secondary motions is still present. In this sense, the LDV data are clearer than computations, showing the well identified three vortices secondary motion distribution. However, the interaction between principal flow



in the bottom channel with secondary vortices of the upper channel results in a smoother principal velocity distribution in the mixing zone mixing plane and a corresponding destruction of the secondary motion structure. In this sense, penetration of bottom channel principal streamlines in the upper channel is more effective, demonstrating how effective mixing is occurring. This behavior is essentially due to two phenomena:

- principal flow inertia: the principal flow tends to pass through the mixing plane because of secondary velocity component (i.e. at least one velocity component is normal to the mixing plane), as already mentioned for flow in the inlet plane;
- flow viscous entrainment of the bottom channel principal flow by the upper channel secondary motion.

It is worth noting that this is a steady state analysis on the average velocity components measured by LDV technique and calculated by the ASST model. In fact, it has to be noted that velocity fluctuations are definitely higher around the mixing zone. This means that turbulence created by mass transfer through the mixing plane enhances even more the flow mixing and has to be added to the flow inertia and viscous entrainment to explain flow mixing. Velocity fluctuations (which are up to 50% of average principal velocity near the mixing plane) are shown in Appendix F<sup>XXI</sup>.

Regarding the principal flow at outlet plane, note the uniform shear velocity distribution, which is consistent with the hypothesis done in the previous paragraph to explain the corner vortex generation in the outer region of the bend. Secondary motion at mixing zone outlet plane clearly shows a difference from the precedent two planes: a corner vortex appears. To understand this phenomenon, it is useful to look at ASST computation results on mixing plane. Since no direct information on velocity field in mixing plane is available in the experimental database, we will first show PIV/ASST results to validate the analysis that will be done hereafter only with ASST numerical results (Figure 5.28 to Figure 5.32).

---

<sup>XXI</sup> In this sense questions rise on the applicability of a RANS approach to such turbulence level. Indeed the computed velocity field will contain some information about the flow characteristics; however, it has to be expected that the steady-state approach is definitely more limiting than the RANS approach itself, a transient approach (which is out of the scope of the present work, as already motivated in Chapter 2) could better account for such unsteadiness.

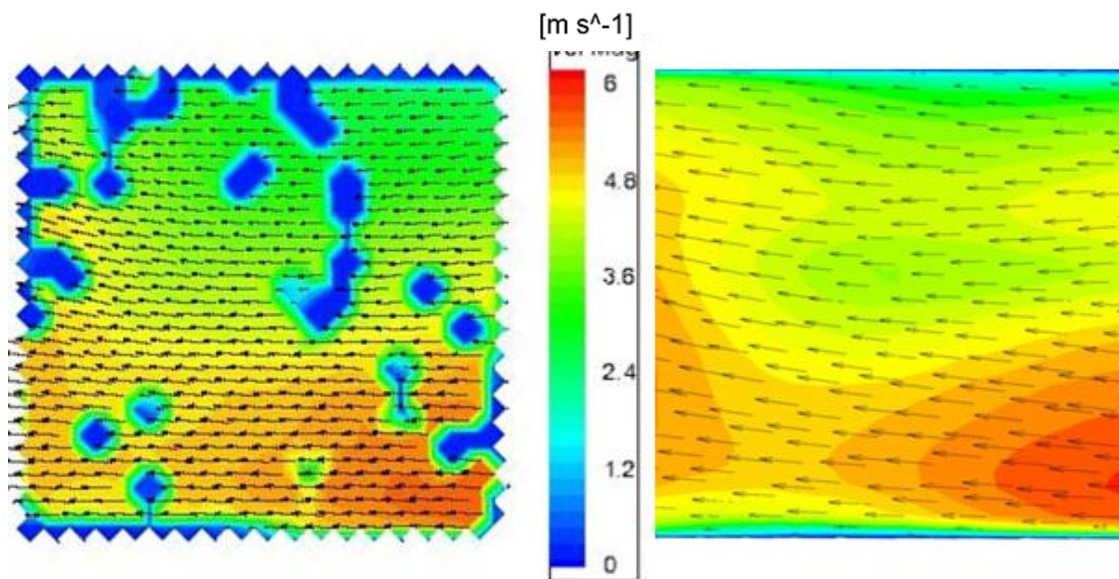


Figure 5.28 - PIV/ASST velocity field at mixing zone top channel middle + 8 mm plane

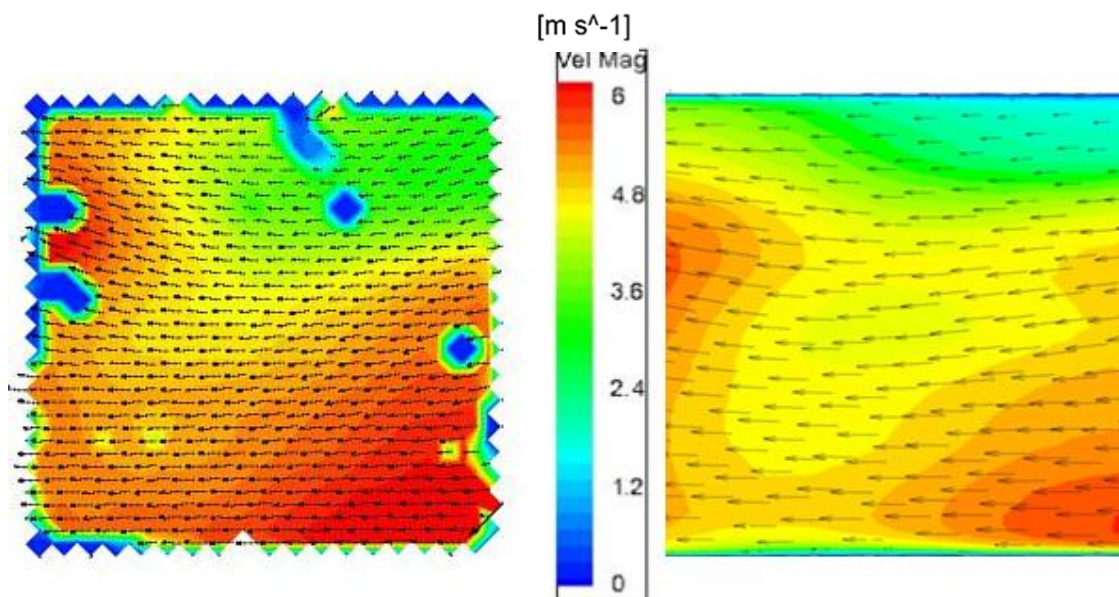


Figure 5.29 - PIV/ASST velocity field at mixing zone top channel middle + 4 mm plane

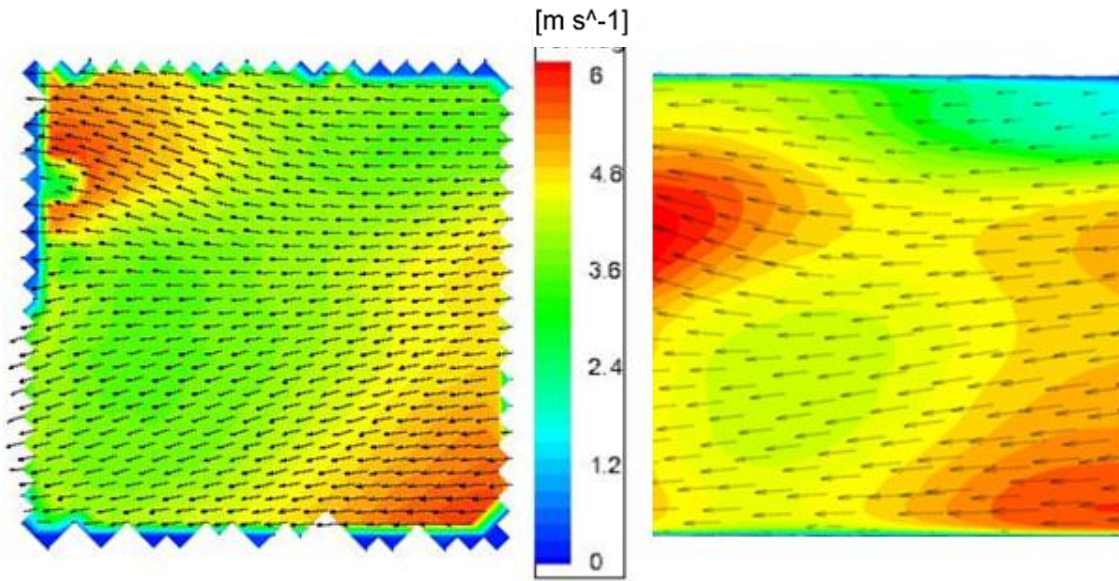


Figure 5.30 - PIV/ASST velocity field at mixing zone top channel middle plane

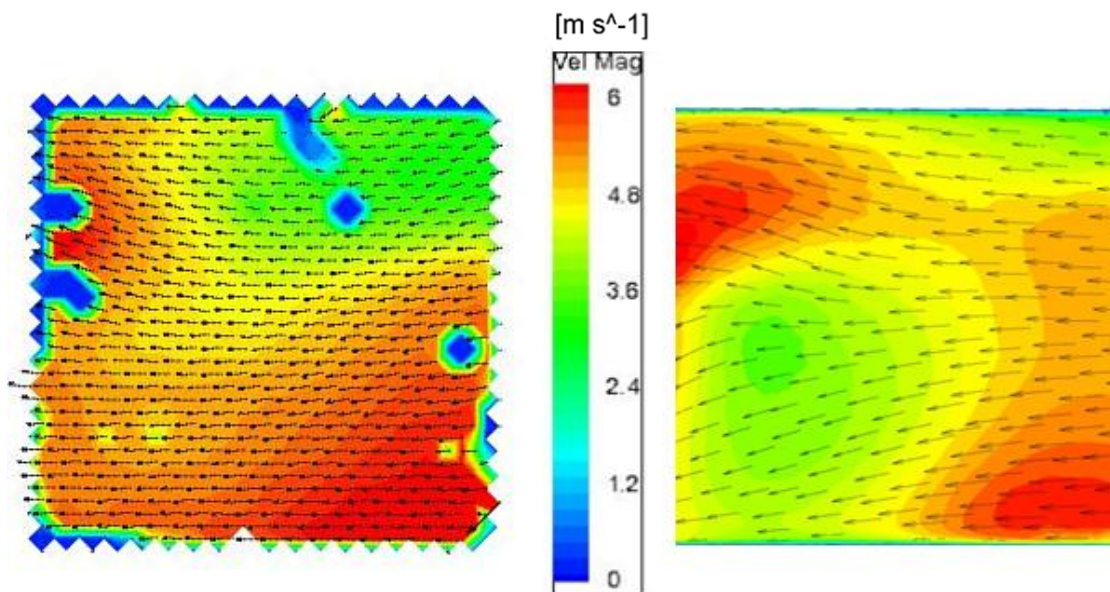
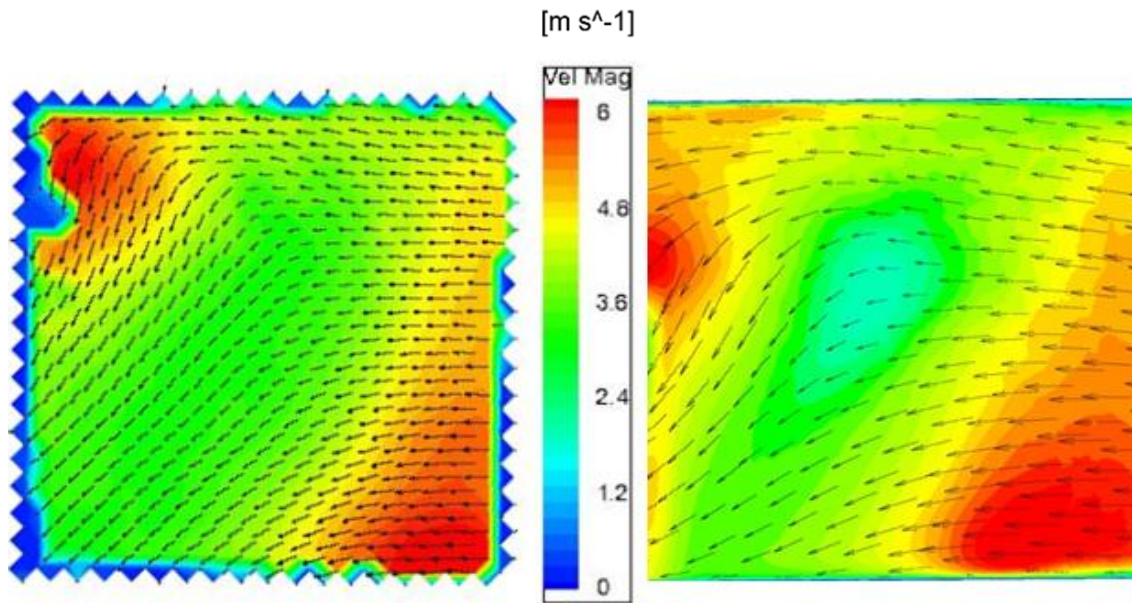


Figure 5.31 - PIV/ASST velocity field at mixing zone top channel middle - 4 mm plane





**Figure 5.32 - PIV/ASST velocity field at mixing zone top channel middle - 8 mm plane**

Once shown that ASST can capture the velocity field distribution in mixing zone (for velocity fluctuation, always refer to Appendix E) we can go through the analysis.

The physical explanation for the corner vortex generation in the mixing zone outlet plane is the vorticity generated by the velocity field in mixing plane. This vorticity is essentially due to the same reasons already mentioned: in fact, the bottom channel flow going upwards to the upper channel is entrained by the upper channel principal flow, which momentum is responsible for the entrainment. Of course, the same occurs for upper channel flow entrained by bottom channel due to its momentum. See that this results in a local high velocity region, shown in red in Figure 5.33. Since the velocity direction is somehow normal to the mixing plane<sup>xxii</sup>, this created the velocity gradients responsible for vorticity generation. Moreover, note how the corner vortex stretches and become the big inlet vortex already shown in the in-bend flow, since the wall effect is to concentrate the vorticity of that region of the mixing zone only in the whole upper channel. Hence, the corner vortex tends to stretch all over the rectangular cross-section, creating the principal secondary motion vortex at bend inlet. This also explains the swirling already occurring at bend inlet.

<sup>xxii</sup> At least one velocity component normal to the mixing plane is  $\neq 0$  due to occurring mixing.

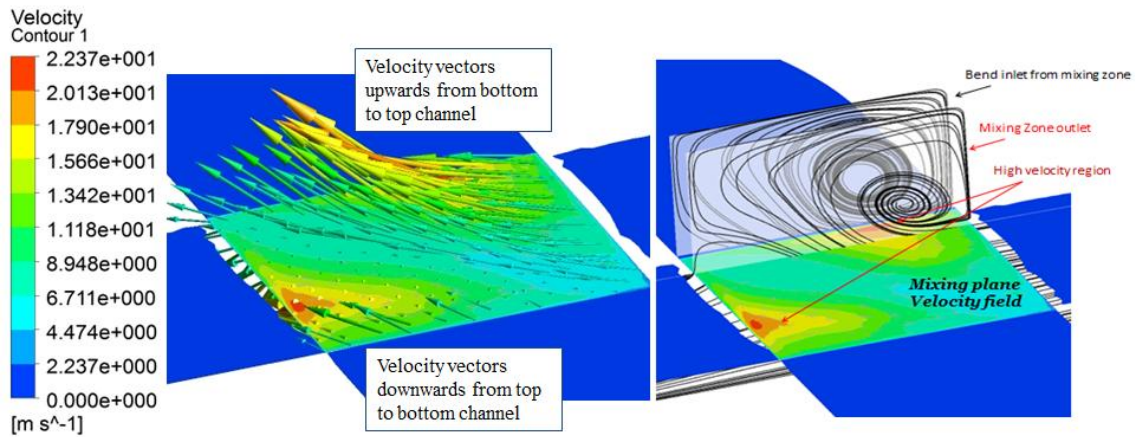


**Figure 5.33—Example of ASST computed velocity field and vectors at mixing plane and related secondary motion at bend inlet for LDV channel geometry**

### 3.3 THERMAL MODEL VALIDATION

Thermal model validation is of primary importance to evaluate the actual performance of the proposed innovative heat exchanger. In particular, if the pure aerodynamic validation has been done thanks to LDV and PIV database, for thermal validation “VHEGAS” facility data are available for comparison with numerical results.

As already mentioned in Chapter 3, the choice for the present work is to use a Simple Gradient Diffusion Hypothesis approach to model the turbulent heat flux. This approach is the simplest possible, but allows for numerically very stable computations and for acceptable results especially for channel flows. The turbulent Prandtl number is chosen to be equal to 0.85, to be consistent with its formulation for channel flow heat transfer.

#### 3.3.1 VHEGAS channel model description

Given the noticed VHEGAS tests’ flow stability of discussed in Chapter 4, steady state calculations have been run.

A mass flow rate inlet and a gauge pressure equal to 0 Pa pressure outlet boundary conditions are used. The working fluid is air at atmospheric pressure. A uniform wall heat flux is imposed to channel wall<sup>XXIII</sup>. Values of mass flow rate and wall heat flux are obtained from data in Table 4.16 for the “High Heat Flux” case and from Table 4.17 for the “Low Heat Flux” case. The inlet temperature is set to the experimental values, whereas the outlet temperature is calculated by the solver. The solver is always

<sup>XXIII</sup>See that this is the major difference between the real case channel and the numerical modeled one, since in the former the heat flux (both for the “High” and the “Low” heat flux cases is not necessarily uniform along the wall. We will show the effects of the heat flux actual distribution in the next paragraph.

Pressure-based one and the Coupled pressure-velocity algorithm with pseudo-transient option is used. Gradients are evaluated through the Green-Gauss node-centered method. Second Order Upwind Scheme is used for the spatial discretization of momentum, turbulent kinetic energy, turbulent dissipation rate and energy transport equations.

Meshing convergence has been evaluated by comparing the average wall shear stress on the walls of the channel. Three successively refined meshes (named as A, B and C according to the refinement level of the near-wall first cell thickness) have been studied. A near-wall approach has been used to obtain proper  $Y^+$  values for the first cell. Table 5.2 shows the results of the convergence evaluation for the SST model:

Configuration	$Y^+$	$\tau_w$
A	1.1	6.52 Pa
B	0.3	6.42 Pa
C	0.2	6.40 Pa

**Table 5.2 - VHEGAS channel geometry mesh convergence evaluation**

From values in Table 5.2, see that configuration B shows a converged wall shear stress. Hence, we retained configuration B as the reference meshing (difference with finer configuration C of 0.3%). See an example of B configuration in Figure 5.34.

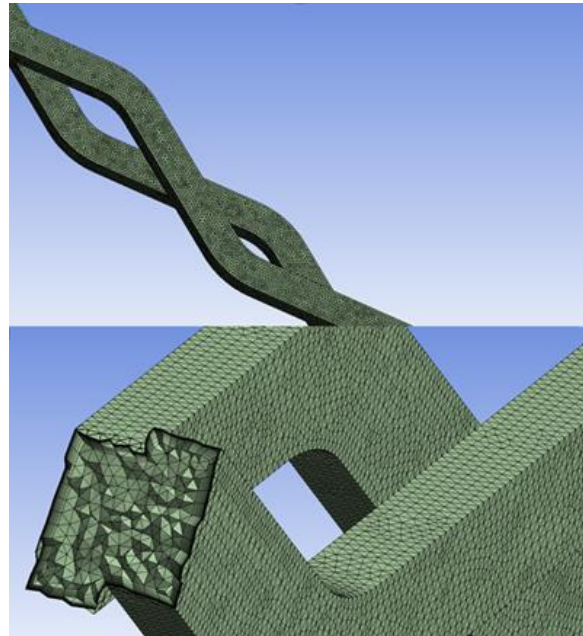


**Figure 5.34 - VHEGAS channel study reference mesh: bend (on top) and mixing zone (on bottom)**

Once determined the mesh convergence, both the “High Heat Flux” and the “Low Heat Flux” cases are studied. In particular, the same approach as the experimental tests is

retained, especially with regard to the locations for flow temperature evaluation, i.e. the actual position of the thermocouples inside the channel.

### 3.3.2 VHEGAS "High Heat Flux" case thermal validation

As already mentioned in Chapter 4, the measured heat transfer coefficient value is very sensitive to the fluid average temperature evaluation method used. Two strategies have been identified, i.e. supposing a linear evolution of the channel center temperature and hence  $\bar{T}_{bulk} = \frac{T_{inlet} + T_{outlet}}{2}$ , or a finer polynomial evolution obtained thanks to the 7<sup>th</sup> bend TC measured temperature. To be consistent with this approach, the same two methods are employed to evaluate the computed heat transfer coefficient.

The first method, i.e. supposing a linear evaluation of the center channel fluid temperature, gives the following result:

$$\bar{T}_{bulk} = \frac{T_{inlet} + T_{outlet}}{2} = \frac{43^{\circ}\text{C} + 171.6^{\circ}\text{C}}{2} = 107.3^{\circ}\text{C}$$

Therefore, the numerical heat transfer coefficient results to be:

$$h_1 = \frac{\phi}{(\bar{T}_{wall} - \bar{T}_{bulk})} = \frac{13\,382\text{ W/m}^2}{187.4^{\circ}\text{C} - 107.3^{\circ}\text{C}} = 173\text{ W/m}^2\text{C}$$

On the other hand, plotting the actual center channel temperature distribution, we obtain the results shown in Figure 5.35

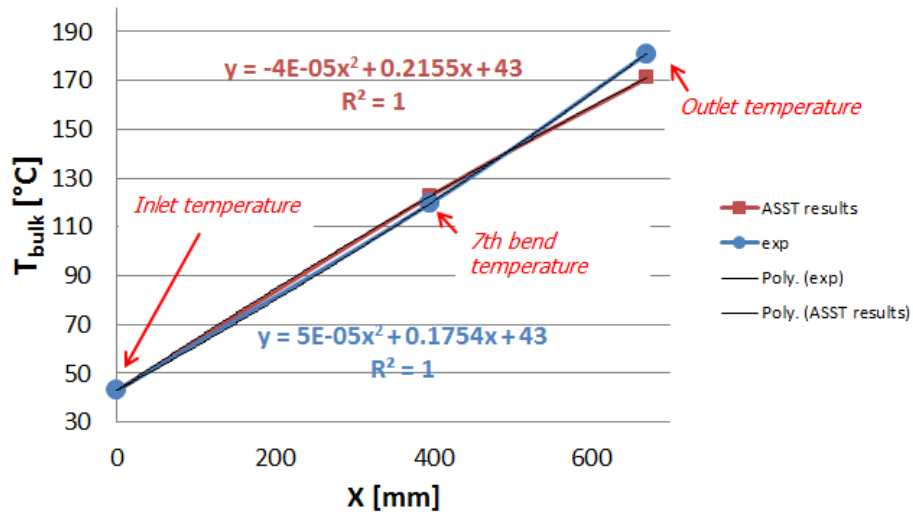


Figure 5.35 - VHEGAS "High Heat Flux" Case channel temperature evaluation comparison

It is worth noting that for ASST numerical computation, the fitting parabola has a negative quadratic term coefficient, suggesting that the fluid flow is heated up slightly more in the first half of the channel than in the second half. This is in contrast with the trend observed for the VHEGAS experimental data, where it was rather the second half

that contributed the most to flow heating up. This behavior is essentially due to the different heat flux distribution, with the uniform heat flux imposed on the numerical model channel resulting in a coherent more effective heating up where the flow is colder, i.e. in the first half of the channel. Hence, applying the Lagrange theorem in the found quadratic temperature evolution we obtain:

$$\bar{T}_{bulk} = \frac{1}{L} \int_0^L (-4 \cdot 10^{-5} x^2 + 0.2155x + 43) dx = 109.4^{\circ}C$$

(where L=670 mm), and a numerical heat transfer coefficient of:

$$h_2 = \frac{\phi}{(\bar{T}_{wall} - \bar{T}_{bulk})} = \frac{13\,382\, W/m^2}{187.4^{\circ}C - 109.4^{\circ}C} = 177\, W/m^2^{\circ}C$$

Table 5.3 summarizes the results of the present case analysis.

	$h_1 [W/m^2^{\circ}C]$	$h_2 [W/m^2^{\circ}C]$
VHEGAS exp. Value	249±16	237±16
ASST computed Value	173	177
(VHEGAS-ASST)/VHEGAS % Difference	-30.6 %	-25.2 %

**Table 5.3 - VHEGAS "High Heat Flux" Case numerical vs experimental heat transfer coefficient comparison**

See that the ASST results are always conservative with respect to the experimental results. In fact, even taking into account experimental uncertainties, it appears that ASST model results underestimate the actual heat transfer coefficient. However, it seems that the second method to evaluate the flow average temperature allows for somehow better results (i.e. lower difference), even if it cannot help to recover the right measured value. It is worth noting that near-wall thermal compressibility effects, that play an important role especially in the inlet region where the wall is much hotter than the fluid, have been neglected. To try to quantify these effects, the “Low Heat Flux” case is studied in the next paragraph. Lastly, see in Figure 5.36 the local heat transfer coefficient distribution, where the heat transfer coefficient is defined as:

$$h = \frac{\phi(x, y, z)}{(\bar{T}_{wall}(x, y, z) - T_{in})}$$

Values are taken from the second last bend and mixing zone. See that the bend low-velocity regions are responsible for a very low contribution to the heat transfer, as already demonstrated in Chapter 2. On the other hand, bend regions of local flow



acceleration present a relatively high heat transfer. However, it is in the mixing zone exit, where the fluid flow is mostly three-dimensional (see Figure 5.33), that the heat transfer coefficient has the maximum value. This demonstrates how the 3D flow mixing zones play a major role in heat transfer enhancement, as thought when the innovative channel has been proposed.

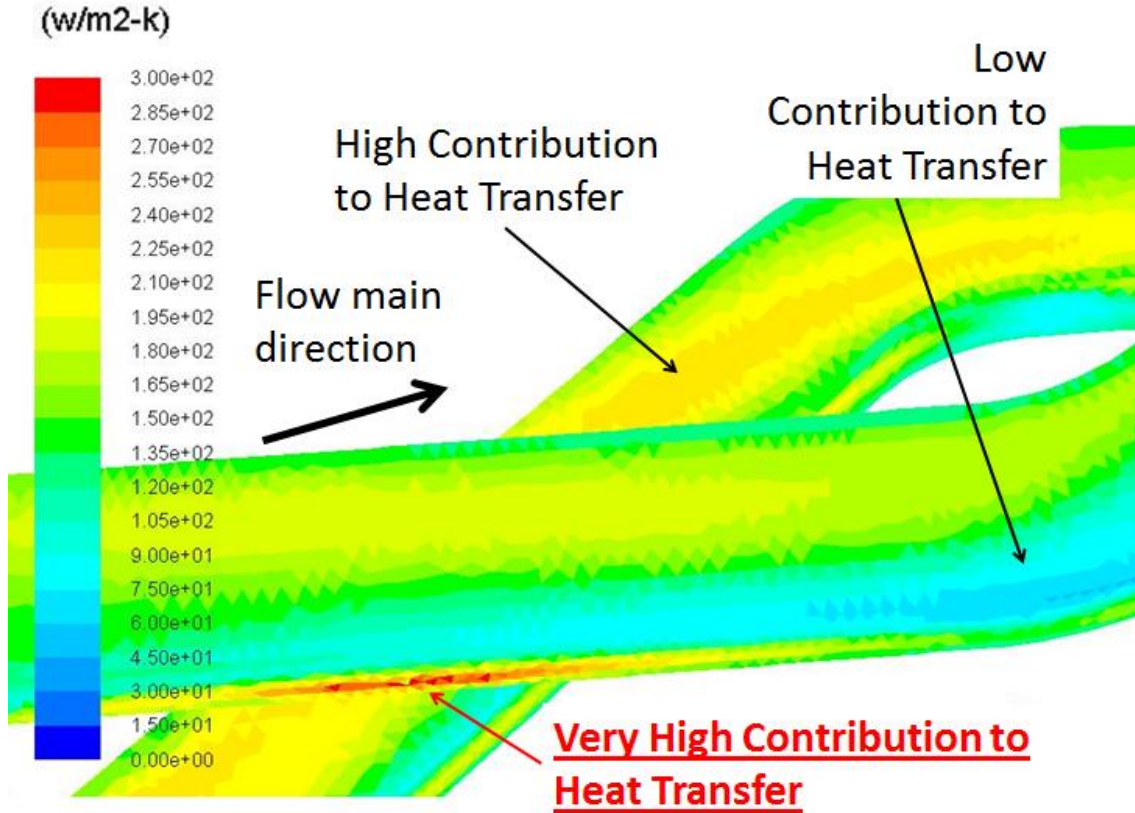


Figure 5.36 - VHEGAS "High Heat Flux" case local contribution to the heat transfer

### 3.3.3 VHEGAS "Low Heat Flux" case thermal validation

The present case is particularly interesting since the thermal gradients between wall and fluid temperatures are less than 25°C, which allows for neglecting near-wall thermal compressibility effects. Therefore, numerical results closer to experimental results are expected.

The first method for the evaluation of the flow mean temperature, i.e. supposing a linear evaluation of the center channel fluid temperature, gives the following result:

$$\bar{T}_{bulk} = \frac{T_{inlet} + T_{outlet}}{2} = \frac{33^{\circ}C + 67.4^{\circ}C}{2} = 48.7^{\circ}C$$

Therefore, the numerical heat transfer coefficient results to be:

$$h_1 = \frac{\phi}{(\bar{T}_{wall} - \bar{T}_{bulk})} = \frac{3\,530\, W/m^2}{69.1^{\circ}C - 48.7^{\circ}C} = 173\, W/m^2\cdot^{\circ}C$$

On the other hand, plotting the actual center channel temperature distribution, we obtain the results shown in Figure 5.37

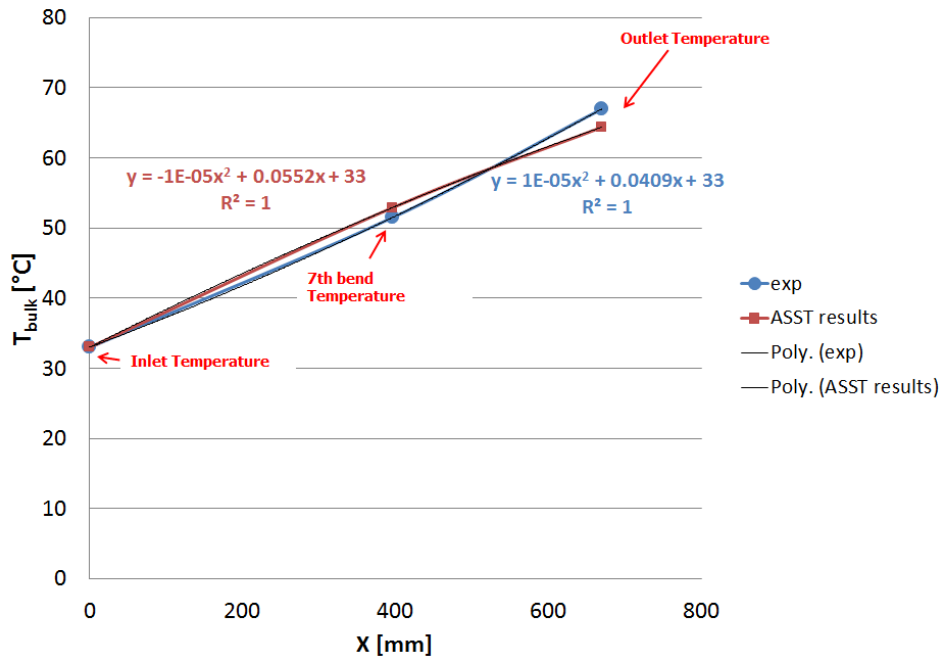


Figure 5.37 - VHEGAS "Low Heat Flux" Case channel temperature evaluation comparison

It is worth noting that once again numerical computation, the parabola fitting ASST numerical results has a negative quadratic term coefficient, confirming that the fluid flow is heated up slightly more in the first half of the channel than in the second half as an effect of the uniform heat flux boundary condition. Finally, applying the Lagrange theorem in the found quadratic temperature evolution we obtain:

$$\bar{T}_{bulk} = \frac{1}{L} \int_0^L (-1 \cdot 10^{-5}x^2 + 0.0552x + 33)dx = 50.2^{\circ}C$$

(where L=670 mm), and a numerical heat transfer coefficient of:

$$h_2 = \frac{\phi}{(\bar{T}_{wall} - \bar{T}_{bulk})} = \frac{3530 \text{ W/m}^2}{69.1^{\circ}C - 50.2^{\circ}C} = 187 \text{ W/m}^2\text{C}$$

Table 5.4 summarizes the results of the present case analysis.

	$h_1 [W/m^2\text{C}]$	$h_2 [W/m^2\text{C}]$
VHEGAS exp. Value	249 $\pm$ 47	218 $\pm$ 45
ASST computed Value	173	187
(VHEGAS-ASST)/VHEGAS % Difference	-30.6 %	-14.2 %

Table 5.4 - VHEGAS "Low Heat Flux" Case numerical vs experimental heat transfer coefficient comparison

As expected, ASST results for the present case are in better agreement with experimental results with respect to the previous case. In particular, it seems again that numerical results are conservative with respect to the experimental results. However, when the flow average temperature is evaluated based on the actual in-channel evolution, the obtained numerical heat transfer is within the experimental uncertainty range, with a mean value difference of only 14.2% with respect to the experimental value. This result is considered as satisfactory to validate the thermal model: in fact, once having a proper numerical model that does not neglect important phenomena such as near-wall thermal compressibility and once having correctly evaluated the effect of the different boundary condition i.e. the effect of the heat flux distribution on flow temperature, the model can provide results that are within the experimental uncertainty range. Therefore the conclusion is that the SGDH with turbulent Prandtl number equal to 0.85 can correctly reproduce the thermal performance of the innovative channel, especially if there are not excessive thermal gradients between wall and fluid temperatures. Lastly, see again in Figure 5.38 the local heat transfer coefficient distribution.

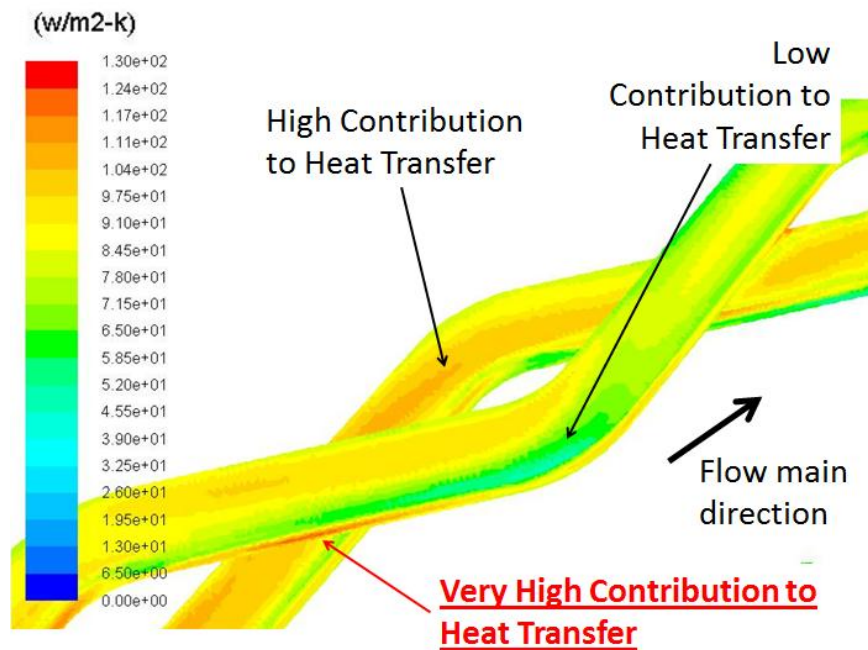


Figure 5.38 - VHEGAS "Low Heat Flux" case local contribution to the heat transfer

See that the results are qualitatively the same as the previous case, confirming the role of the mixing zone in enhancing the global heat transfer coefficient.

## 4. HEAT TRANSFER AND PRESSURE DROP CORRELATIONS

### 4.1 INTRODUCTION

Once validated the ASST model and studied the innovative channel flow, the actual performances have to be determined. In particular it is of primary interest to obtain information about pressure drop and heat transfer capabilities of the proposed geometry in order to demonstrate that the hypothesis made about heat transfer enhancement provided by the innovative channel are true and eventually compare it with other available technologies. Hence the aim of this section is to analyze the innovative channel to calculate friction factor and Nusselt number correlations.

### 4.2 NUMERICAL MODEL DEFINITION

The numerical approach is basically the same as the previous sections. In particular we use a single channel approach (which geometrical characteristics are listed in Table 5.5), the validated ASST turbulence model and a SGDH model for the turbulent heat flux. Again, the same meshing strategy of Chapter 5 Section 2 has been used to ensure meshing convergence. In particular the same  $y^+$  value (for a reference inlet  $Re = 50\,000$ ) has been retained in order to avoid near-wall-dependent effects. Nevertheless the reference mesh has always been used for all the calculations with different Reynolds numbers. Since the  $y^+$  value never passed the unity value, we kept the results for the analysis.

Reference geometry	
Angle	<b>45°</b>
Straight distance between bends	<b>7 mm</b>
Bend radius of curvature	<b>2.5 mm</b>
Total channel height	<b>2 mm</b>

**Table 5.5 – Reference innovative channel geometry for performance evaluation**

A velocity inlet and a gauge pressure equal to 0 Pa pressure outlet (with regard to 180 bar operating pressure) boundary conditions are used. A constant heat flux of 32.4 kW/m<sup>2</sup> is applied on channel walls. This value is a best-estimate value for the ASTRID sodium-gas heat exchanger heat flux on the gas side<sup>111</sup>. Flow inlet temperature is set at 350°C. The working fluid is nitrogen. Nitrogen temperature-dependent properties are taken from National Institute of Standards and Technology (NIST) Thermodynamic and Transport Properties of Refrigerants and Refrigerants Mixture database version 7.0

(REFPROP 7.0) available in ANSYS FLUENT. Note that wall roughness in the present analysis is neglected, even though it could play a role in the heat transfer<sup>XXIV</sup>. The solver is Pressure-based one and the Coupled pressure-velocity algorithm with pseudo-transient option is used. Gradients are evaluated through the Green-Gauss node-centered method. Second Order Upwind Scheme is used for the spatial discretization of momentum, turbulent kinetic energy, turbulent dissipation rate and energy transport equations.

Friction factor is calculated using the Darcy formula, i.e.

$$f = \frac{2\Delta p D_h}{\rho V^2 L}$$

Where  $\Delta p$  is the channel pressure drop,  $\rho$  is the fluid mean density,  $V$  is the flow average velocity,  $D_h$  is the channel hydraulic diameter and  $L$  is the linear distance between inlet and outlet.

Nusselt number is evaluated by:

$$Nu = \frac{h D_h}{\lambda}$$

Where  $h$  is the heat transfer coefficient,  $D_h$  the hydraulic diameter and  $\lambda$  the fluid thermal conductivity. The heat transfer coefficient is calculated as follows:

$$h = \frac{\phi}{(\bar{T}_{wall} - \bar{T}_{bulk})},$$

$\phi$  being the imposed constant heat flux,  $\bar{T}_{wall} = \frac{1}{S} \int_{wall} T dS$  and  $\bar{T}_{bulk} = \frac{1}{V} \int_{volume} T dV$ ,  $dS$  being the unit heat transfer surface  $S$  and  $dV$  the unit fluid volume  $V$ .

What is still to be determined is the number of bends necessary to obtain a fully converged solutions in terms of friction factor and heat transfer coefficient. In fact it has

---

<sup>XXIV</sup> To a first approximation, the final goal is to evaluate the channel intrinsic performance. Further effects can eventually be evaluated once shown the interest of the proposed geometry.

been demonstrated (Chapter 4) that the innovative channel flow is fully developed after four bends. Nonetheless this is not sufficient to avoid entry effects when dealing with friction factor and heat transfer coefficient evaluation. Therefore preliminary computations have been run to identify this number of bends for the present study. Results are shown in Figure 5.39 and in Figure 5.40.

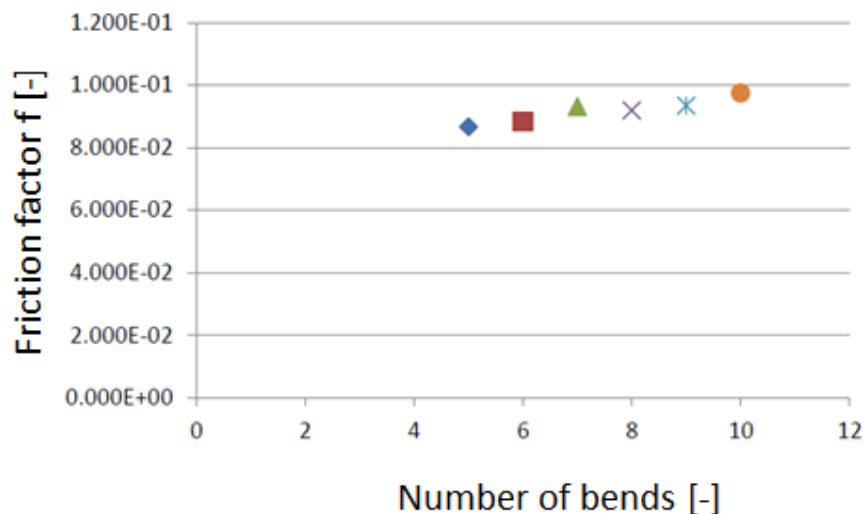


Figure 5.39 - Friction factor as a function of the number of bends for the innovative geometry

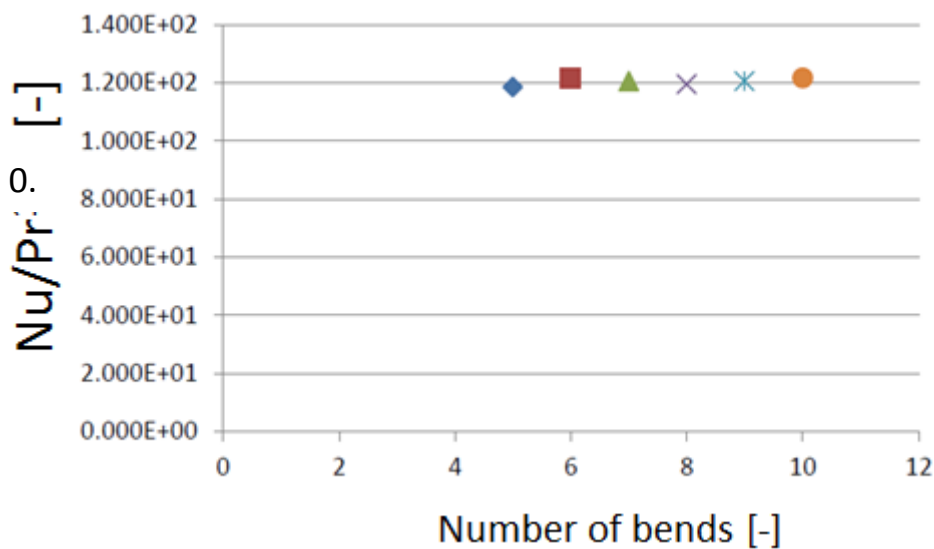


Figure 5.40 - Heat transfer coefficient as a function of the number of bends for the innovative geometry

See that there are no major differences in terms of heat transfer parameters as a function of the number of bends, whereas the friction factor seems to slightly increase (around 2%/bend). This effect is essentially due to single bend contribution to the total pressure

drop. In fact, if the fluid flow is fully developed after 4 bends, the single bend pressure drop from the 4<sup>th</sup> bend on will be the same. However, when the number of bends presenting a periodic flow is comparable to the number of bends necessary to flow development, entry effects provide a bias in the final pressure drop value, which is no longer linearly proportional to the number of bends. Therefore it would be necessary a number of bends much higher than 4 to be able to neglect these entry effects, i.e. to have a negligible increase of the friction factor value with regard to the number of bends. By the way, this would result in a too much big computational domain for the purpose of the present work. Therefore the final choice is to use eight bends for the analysis, trying to obtain a converged friction factor and heat transfer variables without resulting in excessive time-consuming calculations.

### 4.3 HYDRAULIC DIAMETER DEFINITION

It is worth defining properly the hydraulic diameter, since it determines the non-dimensional numbers and the parameters of interest for the following analysis. In fact, if there is no issue in defining the hydraulic diameter for wavy channels, we already underlined how it is more difficult to do it for a complex flow (see Chapter 2 Section 1.3).

In the present case, there are two different regions, where the hydraulic diameter could be defined differently:

- The bend region, where the hydraulic diameter should be defined based on the rectangular cross-section;
- The mixing zones, where the hydraulic diameter might be defined based on the squared cross-section, even if the definition of cross-section and wetted perimeter would not be clear due to occurring mixing.

The innovative channel hydraulic diameter definition should possibly include both the previous definitions.

Remember the classical hydraulic diameter definition for a channel flow:

$$D_h = \frac{4A}{p}$$

With A the channel cross section and p the wetted perimeter. This definition can be generalized<sup>xxv</sup> as follows:

$$D_h = \frac{4A}{p} \cdot \frac{L_c}{L_c} = \frac{4V}{S}$$

Where  $L_c$  is the actual channel length (i.e. the developed curved length for a wavy channel), V is the channel volume and S is the channel wetted surface. For the innovative channel flow, it is more useful to use this formulation rather than the classical one, since in this way the hydraulic diameter can be considered as the volume average of all the possible hydraulic diameter values depending on the channel position (i.e. bend or mixing zone). Note that for straight or wavy channels the  $D_h$  final value do not change with the general formulation with regard to the traditional one.

By the way the channel volume and wetted surface are generally not available information. Therefore it is useful to look for an approximation capable to provide a quantitative evaluation of the hydraulic diameter. Based on different innovative channel geometries (identified by the specific inclination angle and bend longer side), the hydraulic diameter has been calculated with the generalized formula thanks to Computer Aided Design (CAD) tools. See the values of the quantity  $D_h/D$  (D being the bend longer side) in Figure 5.41.

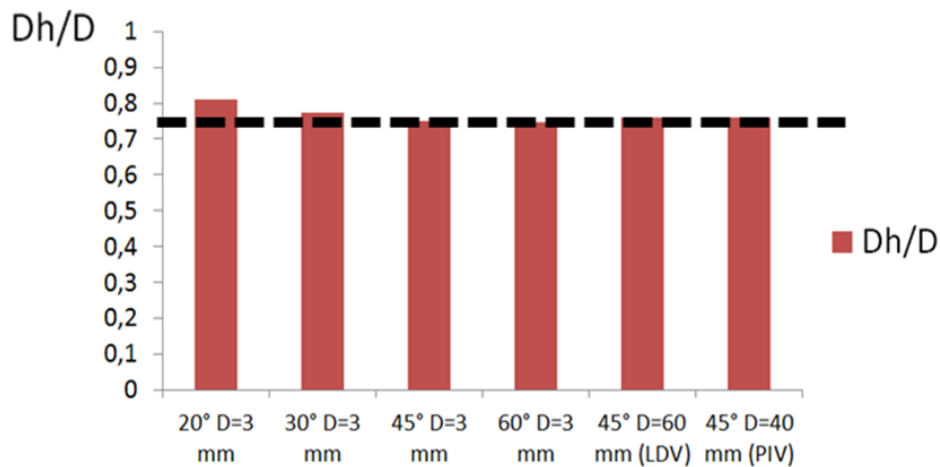


**Figure 5.41 - Innovative channel hydraulic diameter**

<sup>xxv</sup> The exercise is straightforward for the case of a straight channel.



See that it results always  $D_h \approx \frac{3}{4}D$ . Hence, since  $D$  is generally known due to design consideration and plate width needs (see Chapter 2 section 9.1), we will use the approximation  $D_h = \frac{3}{4}D$  as the reference value for the innovative channel hydraulic diameter. It has to be immediately noted that, for the same fluid properties, plate width and flow velocity, the innovative channel Reynolds number differs from that of a wavy or straight channel. Anyway it is of primary importance to use this formulation because it takes into account the actual wetted (i.e. heat transfer) area enlargement factor that potentially results in a better compactness of the component. In fact, for the same total component volume  $V$ , the innovative channel presents a higher heat transfer surface than other geometries, resulting in the lower hydraulic diameter definition. Note also that the found expression for the innovative channel hydraulic diameter evaluation is strictly valid for single channel as that of the LDV or PIV experimental mock-up. This is not the actual case for the complete geometry (see Figure 2.43 in Chapter 2), where several channels meet in different zones. However, it is still useful to approximate the hydraulic diameter through the found expression to better represent the higher surface per unit volume corresponding to the innovative geometry. See that generally the difference between the actual hydraulic diameter inferred from CAD means and the approximation proposed is around 6-7%. It is expected by the author that this difference can be as high as 10% when dealing with the real complete geometry having several parallel channels.

#### 4.4 HEAT TRANSFER AND PRESSURE DROP CORRELATIONS

As already explained, correlations will be extracted from numerical computation results. In particular we will look for two correlations as follows:

$$f = ARe^{-\alpha}$$

$$\frac{Nu}{Pr^{0.4} \left( \frac{T_{bulk}}{T_{wall}} \right)^{0.47}} = BRe^{\beta}$$

If there is nothing to be noted for the diabatic friction factor correlation, see that the formulation for the heat transfer correlation allows to:

- Be independent of the fluid (through the ratio to the Prandtl number);
- Take into account properly turbulent effects (see Prandtl number superscript equal to 0.4 with regard to information in Chapter 1, i.e. Figure 2.20);
- Take into account significant variations of the fluid properties with the bulk to wall temperature ratio<sup>xxvi</sup>.

Table 5.6 shows the influence of thermal gradients for the computed flow conditions, to demonstrate that, for current computations, thermal gradient effects are negligible to a first approximation. This is also very important with regard to thermal calculation correctness, as previously shown. Final correlations are shown in Figure 5.42 and Figure 5.43.

Re	$\bar{T}_{bulk} - \bar{T}_{wall} [^{\circ}\text{C}]$	$\left(\frac{\bar{T}_{bulk}}{\bar{T}_{wall}}\right)^{0.47}$
20000	13.6	0.990
30000	9.7	0.993
40000	8.0	0.994
50000	6.7	0.995
60000	5.8	0.996

Table 5.6 – Influence of thermal gradients for 45° innovative channel geometry flow

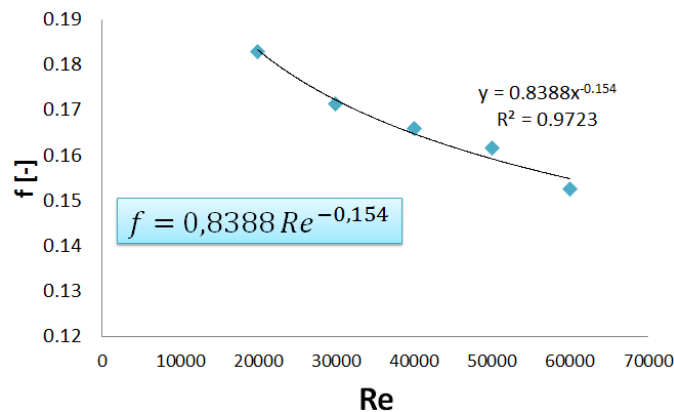
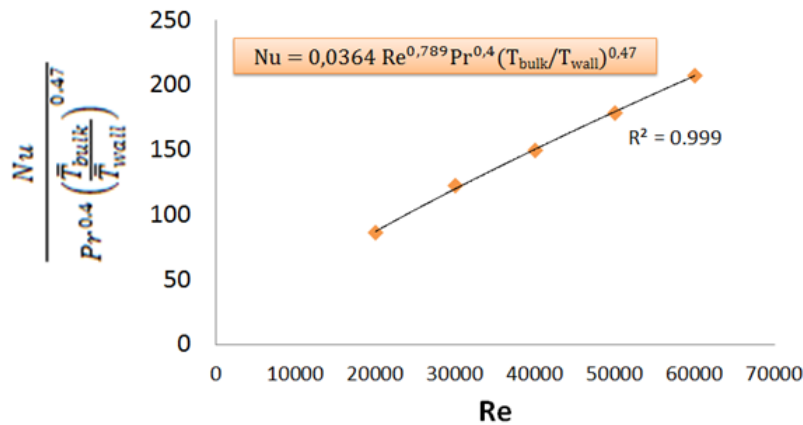


Figure 5.42 - Friction factor correlation for innovative channel with  $\alpha=45^{\circ}$  and  $D=2$  mm

<sup>xxvi</sup> The superscript equal to 0.47 is valid for heating flow, which is the case for the current analysis. Otherwise, for cooling flow, no correction is needed, i.e. the superscript would be equal to 0 (see N.E.TODREAS and M.S.KAZIMI, “Nuclear Systems Vol.1 – Thermal-hydraulic fundamentals”, CRC Press, 2011). Note also that the same reference specify that another very common correction factor, i.e.  $(\mu/\mu_w)^{0.14}$  is to be used when dealing with liquids. However, since the contribution of the correction factor to the Nusselt number is often negligible, the choice is formally interesting but of less practical application.



**Figure 5.43 – Nusselt number correlation for innovative channel with  $\alpha=45^\circ$  and  $D=2$  mm**

As an exercise, the same correlations are computed for a different channel, which is supposed to have lower pressure drop (which is of interest for the compactness comparison shown in the next section). This second test case is defined by the following geometrical parameters (Table 5.7), representing a scaling-down of the VHEGAS channel geometry:

Second test geometry	
Angle	<b><math>20^\circ</math></b>
Straight distance between bends	<b>14 mm</b>
Bend radius of curvature	<b>6 mm</b>
Total channel height	<b>3 mm</b>

**Table 5.7 – Alternative innovative channel geometry for performance evaluation**

Again, Table 5.8 shows the influences of thermal gradients on the tested geometry flow conditions, to demonstrate that, for current computations, thermal gradient effects are negligible to a first approximation and hence that numerical results can be considered as quite accurate. Final correlations are shown in Figure 5.44 and Figure 5.45 and heat transfer and friction factor differences are listed in Table 5.9 and Table 5.10 (differences of friction factor and heat transfer coefficient are presented because two geometries with different hydraulic diameters are compared).

Re	$\bar{T}_{bulk} - \bar{T}_{wall}$ [°C]	$\left(\frac{\bar{T}_{bulk}}{\bar{T}_{wall}}\right)^{0.47}$
20000	21.2	0.985
30000	16.4	0.988
40000	12.4	0.991
50000	10.5	0.992
60000	9.1	0.993

**Table 5.8 - Influence of thermal gradients for  $20^\circ$  innovative channel geometry flow**

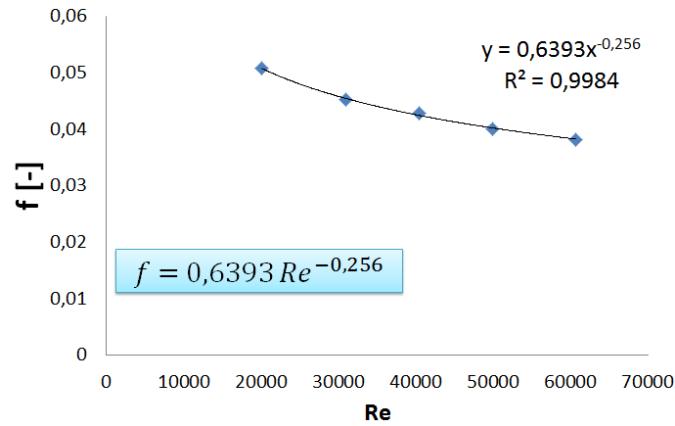


Figure 5.44 - Friction factor correlation for innovative channel with  $\alpha=20^\circ$  and  $D=3$  mm

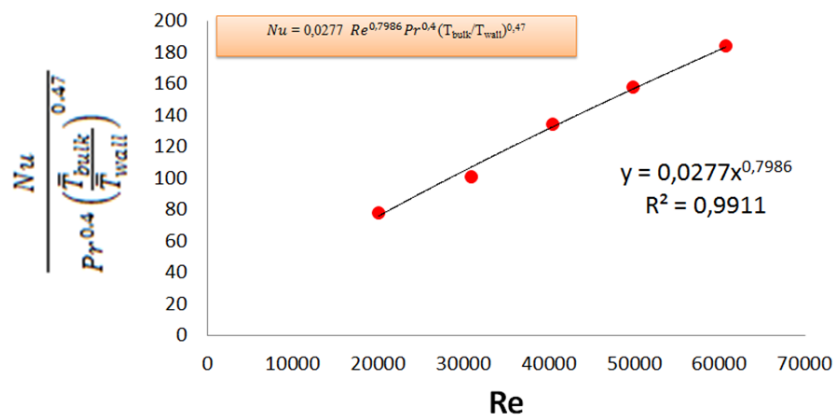


Figure 5.45 - Nusselt number correlation for innovative channel with  $\alpha=20^\circ$  and  $D=3$  mm

Re	f 45° [Pa]	f 20° [Pa]	(f <sub>20°</sub> -f <sub>45°</sub> )/f <sub>45°</sub> %
20000	0.171	0.051	-237.9
30000	0.183	0.045	-304.3
40000	0.166	0.043	-287.9
50000	0.162	0.040	-302.8
60000	0.153	0.038	-299.6

Table 5.9–Friction factor difference between innovative channel with  $\alpha = 45^\circ$  and  $\alpha=20^\circ$

Re	h 45° [W/(m²K)]	h 20° [W/(m²K)]	(h <sub>20°</sub> -h <sub>45°</sub> )/h <sub>45°</sub> %
20000	2375	1531	-35,6
30000	3339	1971	-41,0
40000	4071	2615	-35,8
50000	4861	3076	-36,7
60000	5637	3578	-36,5

Table 5.10 – Heat transfer coefficient difference between innovative channel with  $\alpha = 45^\circ$  and  $\alpha=20^\circ$

See that there is a dramatic decrease of friction factor for the  $20^\circ$  geometry with regard to the  $45^\circ$  geometry: there is a factor of about 5 between the two, whereas the decrease

in the heat transfer coefficient for the 20° geometry is much slighter than that of the 45° geometry. Moreover, see in Table 5.11 the obtained correlations with regard to classical straight tube Blasius' and Dittus-Boelter-McAdams' correlations<sup>xxvii</sup>:

Geometry	Friction factor correlation	Heat transfer correlation
Innovative channel $\alpha=45^\circ$ D=2 mm	$f = 0.8388Re^{-0.154}$	$Nu = 0.0364Re^{0.789}Pr^{0.4}$
Innovative channel $\alpha=20^\circ$ D=3 mm	$f = 0.6393Re^{-0.256}$	$Nu = 0.0277Re^{0.7986}Pr^{0.4}$
Straight tube	$f = 0.316Re^{-0.25}$ (Blasius)	$Nu = 0.023Re^{0.8}Pr^{0.4}$ (Dittus Boelter McAdams)

**Table 5.11 - Correlation comparison**

It is worth noting that the difference between the straight tube and the 20° innovative channel is essentially in the multiplying coefficient both for heat transfer and friction factor: this means that the 20° innovative channel has a friction factor about two times higher than that of a straight channel, whereas the heat transfer coefficient is only 20% higher. Comparison is more complicated for 45° innovative geometry. Anyway results of Table 5.9 and Table 5.10 show that the 45° geometry presents very important pressure drop and a slightly higher heat transfer coefficient. In this sense, it is of primary importance to determine which geometry provides the most compact design for given design constraints, or whether the high pressure drop given by the innovative geometry is acceptable or not. This analysis will be done in the next section.

These correlations can be used by designers to design compact heat exchangers. Nevertheless, as already explained, these correlations have been obtained for a single innovative channel, whereas there are many parallel channels in the real case, where additional mixing zone are created when two innovative channels meet (see Figure 2.43). To better account for the real case, computations have been done for a three-channel geometry, as shown in Figure 5.46 (see the added mixing zone when two bends meet). The single channel geometry is the same as the previously described 45° geometry in Table 5.5; the three channels are separated by a 2 mm distance between the straight parts between two following bends of the same channel.

---

<sup>xxvii</sup> See that corrections for variations of fluid properties have been neglected in Table 5.11, aiming to show the different values of the coefficients in the correlations.

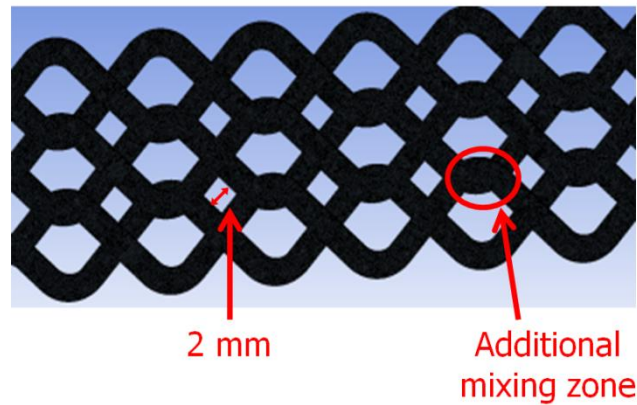


**Figure 5.46 - Triple innovative channel description**

The same meshing, modelling and post-processing approach previously described has been used. In particular the pressure drops have been evaluated in the center channel, trying to account for enhanced mixing and decreased wetted surface of the real channel case. Same for the heat transfer evaluation, for which average bulk and wall temperature have been calculated for the center channel<sup>xxviii</sup>. Differences between pressure drop (the channel geometry being the same of the reference 45° single channel) and heat transfer coefficient from single and triple channel geometry simulations are shown in Table 5.12 and in Table 5.13. Design correlations are shown in Figure 5.47 and in Figure 5.48.

Re	$\Delta P$ single [Pa]	$\Delta P$ triple [Pa]	$(\Delta P_{\text{triple}} - \Delta P_{\text{single}}) / \Delta P_{\text{single}} \%$
20000	7118	9679	26.5
30000	16180	22500	28.1
40000	26030	36645	29.0
50000	39790	57194	30.4
60000	54160	81066	33.2

**Table 5.12 - Pressure drop difference between single and triple innovative channel with  $\alpha = 45^\circ$  and  $\alpha = 20^\circ$**

<sup>xxviii</sup> Note that the two side-channels do not represent the real case, since additional mixing zones are created only when they meet the centre channel. To properly account for additional mixing zone a large number of parallel channels should be used. Here, to keep the strategies used so far in the thesis as well as to limit the model size, three channels have been used to provide some information about actual performance for the real case heat exchanger.

Re	h single [W/(m <sup>2</sup> K)]	h triple [W/(m <sup>2</sup> K)]	(h <sub>triple</sub> -h <sub>single</sub> )/h <sub>single</sub> %
20000	2375	2525	6.3
30000	3339	3553	6.4
40000	4071	4334	6.5
50000	4861	5199	6.9
60000	5637	6001	6.5

Table 5.13 – Heat transfer coefficient difference between single and triple innovative channel with  $\alpha = 45^\circ$  and  $\alpha = 20^\circ$

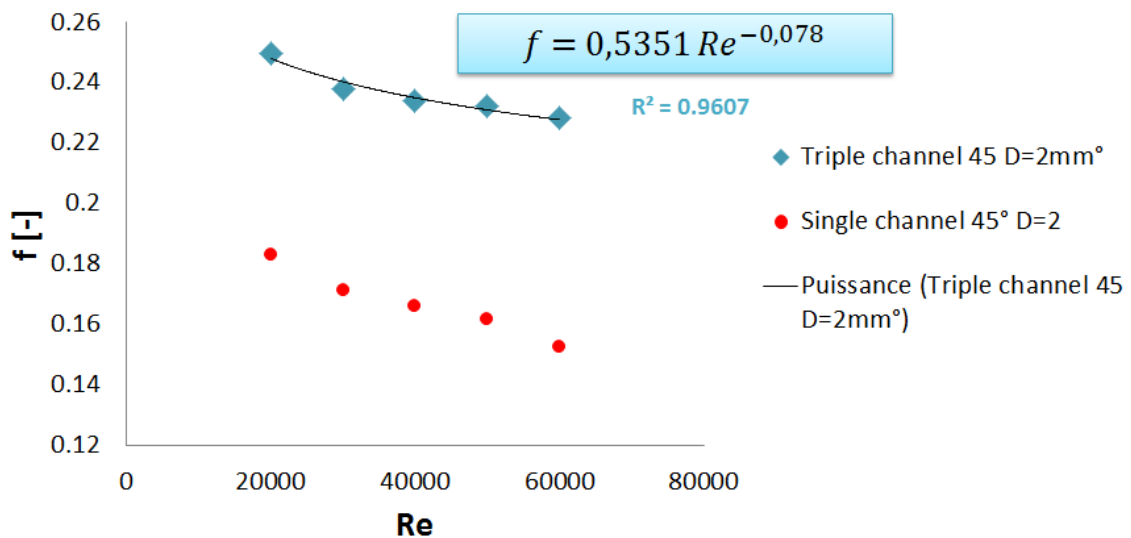


Figure 5.47 - Friction factor correlation for triple innovative channel with  $\alpha=45^\circ$  and  $D=2$  mm

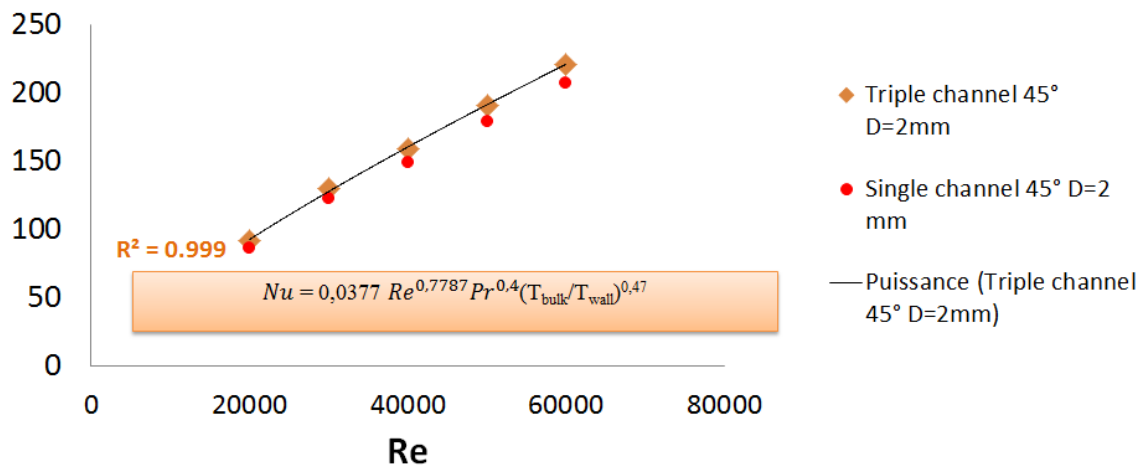


Figure 5.48 – Nusselt number correlation for triple innovative channel with  $\alpha=45^\circ$  and  $D=2$  mm

The triple channel pressure drop is sensibly higher than the single channel pressure drop (around 30%). This is essentially due to additional mixing zones, where fluid streams meet and provide additional hydraulic resistance. For the same reason, heat transfer

coefficient is higher, but less than the relative pressure drop increase (around 6 to 7%). Again the fundamental arising question is whether the innovative geometry provides superior compactness for given performance. Specifically it is still to be demonstrated if the higher pressure drop is acceptable or not for the design constraints defined in Chapter 1. This evaluation is done in the next paragraph.

## **5. COMPARISON OF DIFFERENT HEAT EXCHANGER TECHNOLOGIES**

### **5.1 PRELIMINARY CONSIDERATIONS**

The previous section has shown how it is of primary importance to determine which geometry is the most compact one for given performance, in order to demonstrate its industrial interest<sup>XXIX</sup>. Chapter 2 presented three criteria that are widely used in the industry. Indeed some defaults in these formulations have also been identified, suggesting that a proper criterion should be proposed. In fact, while it has been shown that the pumping power per unit volume is supposed to better compare different technologies, on the other hand its formulations could be improved, since the volume is not properly expressed. There is another reason why this criterion could fail in comparing such compact heat exchanger technologies. In fact, it has been clearly shown that the innovative geometry is far more resistive (i.e. higher pressure drop) than a straight channel geometry. For a single channel approach (such as that used in the present work), fixing the channel pumping power would mean fixing the reference channel velocity, i.e. the reference channel Reynolds number. Since the innovative channel is more resistive, there are only two ways to fix the pumping power to a desired value, constant for all geometries to be compared: either decreasing the channel flow rate or decreasing the channel length. Both of them deteriorate the heat transfer, since the former results in a decreased channel Reynolds number, whereas the latter in a reduced heat transfer surface. The final result could easily be a lower compactness for the innovative channel if compared to the straight channel. As it will be shown, this is not the real case. Hence, a new compactness criterion is to be determined to properly analyze this important aspect.

It is worth noting that, if the question is which geometry provides the most compact design, performance (in terms of exchanger thermal power and pressure drop and mass

---

<sup>XXIX</sup> Compactness can be defined as thermal power per unit volume.



flow rate) must be fixed, to verify which geometry has the lower volume. This approach is formally correct, since it takes into account designer's necessity to determine the size of a component for a given load. Determining the size of a plate heat exchanger is an iterative process: in fact, if the designer wants to use a more resistive technology (with pumping power fixed to a given value), for a given total mass flow rate and total length, the channel flow rate is decreased through an increase of the number of plates and hence the number of channels. However this increases also the heat transfer surface, resulting in a potentially higher exchanged thermal power. Hence the total channel length (giving the pressure drop, see Darcy formula) has to decrease to meet the desired thermal load. The final design point has the right number of plates and total length giving the desired performance. Figure 5.49 shows the illustrated design process:

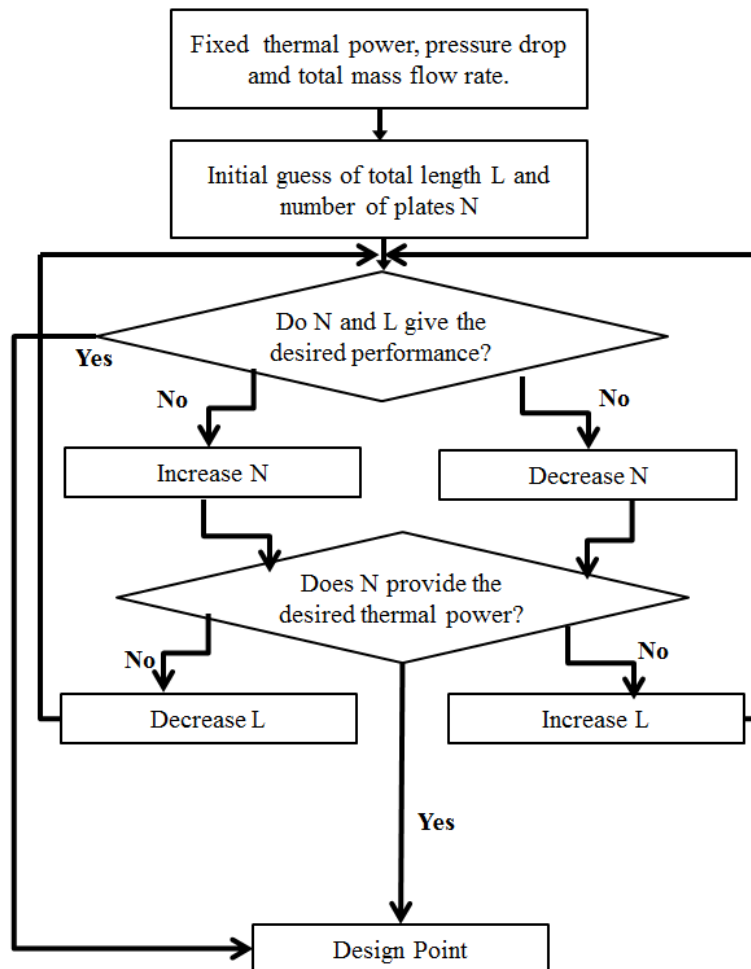


Figure 5.49 - Compact heat exchanger design process

Finally, trying to represent the design process, we will adopt the following strategy to define a comparison criterion: given a global heat exchanger description as that of Figure 5.50, the following assumptions and design goals are made at the global component scale, hence including both sides of the heat exchanger:

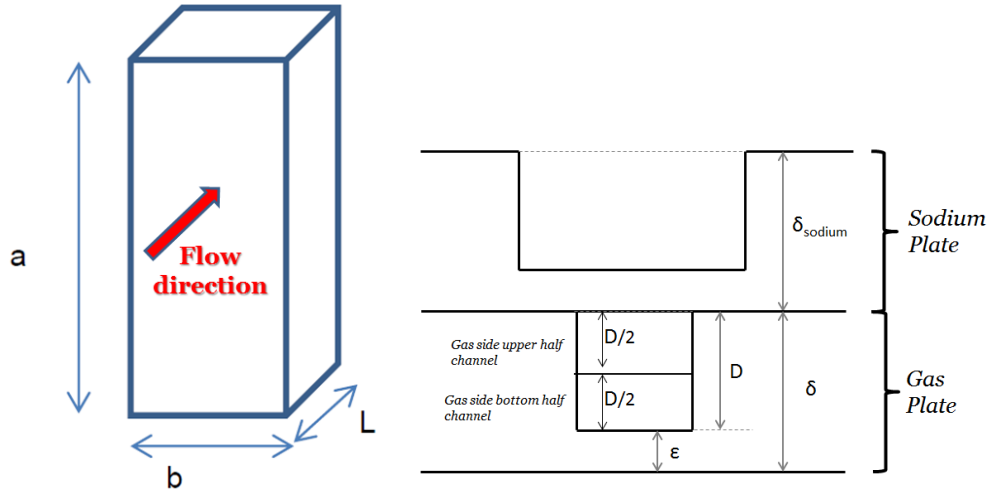


Figure 5.50 - Compact heat exchanger major dimensions

1. Same thermal power  $P_{th}$  exchanged ( $=24$  MW);
2. Same pressure drop  $\Delta p$  ( $= 1$  bar for the gas-side of the heat exchanger);
3. Same total mass flow rate  $\Gamma$  (both for gas and sodium side);
4. Same total component width (i.e. dimension “b”);
5. Fixed distance between two channels “d”;
6. Fixed total thickness of the sodium plate  $\delta_{sodium}$ .

Hypotheses 4 and 5 are necessary to simplify the analysis. Regarding the “a” dimension (see Figure 5.50), it can be demonstrated that  $a \propto N\delta$ , where  $N$  is the number of gas side plate and  $\delta$  the gas side plate total thickness equal to  $D+\epsilon$ . In fact it has already been explained in Chapter 2 Section 9.1 that the sodium side is neglected in the present analysis since it has a minor role on the global thermal resistance. Hence we only take into account the volume of the gas side of the heat exchanger. However this assumption does not change the validity of the adopted approximation about the “a” dimension: since sodium and gas plates are superposed each other, it results that  $N=N_{gas} \approx N_{sodium}$ . Hence it would be  $a = N\delta + N_{sodium} \delta_{sodium} \approx N(\delta + \delta_{sodium}) \propto N\delta$ . Finally, it results that, the volume  $V$  of the component, which is equal to  $abL$ , is only a function of the total length  $L$  (given by the desired pressure drop value) and of the number of plates

of the heat exchanger gas side  $N$ , since the gas side plate total thickness  $\delta$  is constant due to considerations in Chapter 2 Section 9.1 and hypothesis 5. Together with these two parameters, the total channel height  $D$  (remember that  $D=D_h$  for a straight or PCHE channel but  $D \propto D_h$  for the innovative channel) is the third parameter to take into account since it gives the total channel thickness (i.e.)  $\delta=D+\varepsilon$ , the number of channel per plate (i.e.  $N_c=b/(D+d)$ , see hypothesis 5), the channel cross section  $A_0$  (i.e.  $A_0=D^2$  for a squared cross section) as well as the Reynolds number values to be considered into friction factor and heat transfer correlations. Next section will demonstrate that, knowing  $N$ ,  $L$  and  $D$  it is possible to correctly compare different geometries.

## 5.2 COMPACTNESS COMPARISON STRATEGY

Figure 5.49 showed the iterative design process of a compact heat exchanger to meet a fixed performance in terms of exchanged thermal power  $P_{th}$  and pressure drop  $\Delta p$ . It essentially consists of varying the total length and number of plates of the component, for a fixed total channel height  $D$ , to meet the design goals.

As it will be shown, writing the pressure drop and thermal power equations, we can express these two equations in terms of three unknowns, specifically  $N$ ,  $L$  and  $D$ . One unknown is of particular interest: in fact  $D$  can be fixed by the designer in order to have a certain plate thickness (see Chapter 2). To confirm that, remember that this strategy has already been adopted when determining the innovative channel rectangular shape in Chapter 2. In fact, the rectangular cross-section of the single wavy channel was chosen to keep the total plate width (see also hypothesis 4) and cross-section with regard to a reference PCHE or straight channel with squared cross-section. Therefore we can fix a given  $D$  value and finally have two equations (pressure drop and exchanged thermal power) and two unknown to be determined ( $N$  and  $L$ ). The problem has always a physical solution, since the exchanged thermal power and pressure drop always assume non-zero values. Therefore the comparison strategy will consist of writing  $L$  as a function of the pressure drop and number of plates i.e.  $L = L(\Delta p, N)$  and as a function of the exchanged thermal power and number of plates i.e.  $L = L(P_{th}, N)$ . Since the two design constraints must be respected at the same time, there must be a design point corresponding to the intersection point  $(L, N)$  such as  $L(\Delta p, N) = L(P_{th}, N)$ ,  $P_{th}$ ,  $\Delta p$  and  $D$  being fixed.

In particular, with respect to Figure 5.49, it is expected that  $L(\Delta p, N)$  is a function increasing with  $N$ : this is due to the fact that, for a fixed pressure drop, increasing the number of plates results in decreasing the mass flow rate per channel i.e. the channel Reynolds Number and hence the channel pressure drop. Since we want the pressure drop to be constant, the only way to recover the desired pressure drop value would be to increase  $L$ . On the other hand, it is expected that  $L(P_{th}, N)$  is a function decreasing with  $N$  increasing: in fact, for a fixed thermal power to be exchanged, increasing the number of plates would results in increasing the heat transfer area: hence, even if the channel Reynolds number decreases, the thermal power would likely exceed the fixed desired value. Hence the component length should be shortened to meet the design goal in terms of thermal power. Figure 5.51 illustrates these two trends and the design point.

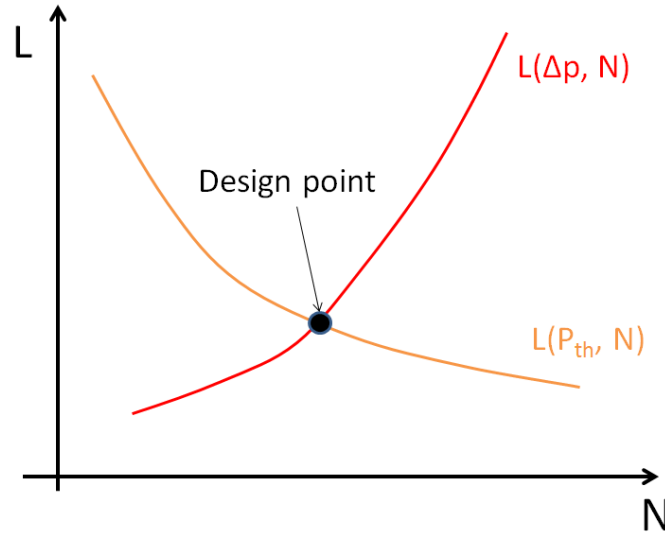


Figure 5.51 - Compactness comparison strategy illustration

Therefore write:

$$P_{th} = US_{gas} \Delta T_m$$

Where  $U$  is the total heat transfer coefficient,  $S_{gas}$  is the heat transfer surface of the gas side of the heat exchanger (which can be calculated based on the generalized definition of hydraulic diameter) and  $\Delta T_m$  is a temperature difference, that we define using the log-mean temperature definition. Now write all the terms as a function of the unknown, hence, neglecting the high temperature gradients correction factor:

$$\begin{aligned}
P_{th} &= U 4 \frac{V_{gas}}{D_h} \cdot LMTD = \\
&= U \frac{4NN_c A_0 L_c}{D_h} LMTD = \\
&= U \frac{4NN_c A_0 L \frac{L_c}{L}}{D_h} LMTD \rightarrow \\
L &= \frac{P_{th} D_h \frac{L}{L_c}}{4NN_c A_0 L \cdot U \cdot LMTD}
\end{aligned}$$

$$\frac{\lambda}{D_h} B Re^\beta Pr^{0.4}$$

Where  $\lambda$  is the fluid average thermal conductivity,  $V_{gas} = N \cdot N_c \cdot A_0 \cdot L_c$  is the gas total volume,  $N_c$  is the number of channels per plate,  $A_0$  is the single channel cross section i.e. equal to  $D^2$  for a squared cross section and LMTD is the log mean temperature difference<sup>xxx</sup> and  $\frac{L_c}{L}$  is the ratio between the actual channel length and the straight distance between heat exchanger inlet and outlet. It takes into account the heat transfer surface gain provided by wavy channels<sup>xxxi</sup>.

Now the total heat transfer coefficient is equal to:

$$U = \frac{1}{\frac{S_{gas}}{h_{gas}} + \frac{\varepsilon}{\lambda_{steel}} \frac{S_{gas}}{S_{steel}} + \frac{1}{h_{sodium}} \frac{S_{gas}}{S_{sodium}}}$$

See that  $\varepsilon$  is the plate's residual thickness,  $S_{steel} = 2NbL$  is the total steel heat transfer surface,  $h_{sodium} = \frac{\lambda_{sodium}}{D_{h,sodium}} Nu_{sodium} = \frac{\lambda_{sodium}}{D_{h,sodium}} (5 + 0.025Pe_{sodium}^{0.8})$  is the sodium side heat transfer coefficient and  $S_{sodium} = NN_{c,sodium} p_{sodium} L$  is the total sodium side heat transfer area. Note that  $p_{sodium}$  is the perimeter of the single straight channel

---

<sup>xxx</sup>The LMTD or Logarithmic Mean Temperature Difference is a widely used parameter when dealing with heat exchanger. For the a heat exchanger with two ends A and B it is defined as  $LMTD = \frac{\Delta T_A - \Delta T_B}{\ln \frac{\Delta T_A}{\Delta T_B}}$ .

<sup>xxxi</sup>In fact, the ratio is equal to one for a straight channel, whereas for wavy channel it is larger than one, meaning that in a fixed linear distance between inlet and outlet, a wavy geometry provides a higher heat transfer surface. With the hypothesis of bend curvature radius far smaller than the straight distance between two bends, it can be easily demonstrated that  $\frac{L_c}{L} = 1/\cos\alpha$ .

of sodium,  $N_{c,sodium}$  is the number of channel per plate of sodium and the hypothesis of  $N_{gas}=N_{sodium}=N$  is still used. Hence write:

$$\begin{aligned}
L &= \frac{P_{th} D_h \frac{L}{L_c}}{4NN_c A_0 \cdot U \cdot LMTD} = \\
&= \frac{P_{th} D_h \frac{L}{L_c}}{4NN_c A_0 \cdot \left[ \frac{1}{\frac{1}{h_{gas}} + \frac{\varepsilon}{\lambda_{steel} S_{steel}} + \frac{1}{h_{sodium} S_{sodium}}} \right] \cdot LMTD} = \\
&= \frac{P_{th} D_h \frac{L}{L_c}}{4NN_c A_0 \cdot \left[ \frac{1}{\frac{1}{h_{gas}} + \frac{\varepsilon}{\lambda_{steel} \frac{4NN_c A_0 L_c}{D_h 2NbL}} + \frac{1}{h_{sodium} \frac{4NN_c A_0 L_c}{D_h NN_{c,sodium} p_{sodium} L}}} \right] \cdot LMTD} = \\
&= \frac{P_{th} D_h \frac{L}{L_c}}{4NN_c A_0 \cdot \left[ \frac{1}{\frac{1}{h_{gas}} + \frac{\varepsilon}{\lambda_{steel} \frac{2N_c A_0 L_c}{D_h bL}} + \frac{1}{h_{sodium} \frac{4N_c A_0 L_c}{D_h N_{c,sodium} p_{sodium} L}}} \right] \cdot LMTD} = \\
&= \frac{P_{th} D_h \frac{L}{L_c}}{4NN_c A_0 \cdot \left[ \frac{1}{\frac{1}{h_{gas}} + \frac{\varepsilon}{\lambda_{steel} \frac{2N_c A_0 L_c}{D_h bL}} + \frac{1}{h_{sodium} \frac{4N_c A_0 L_c}{D_h N_{c,sodium} p_{sodium} L}}} \right] \cdot LMTD} = \\
&= \frac{P_{th} D_h \frac{L}{L_c}}{4NN_c A_0 \cdot \left[ \frac{1}{\frac{D_h}{\lambda_{gas} Nu_{gas}} + \frac{\varepsilon}{\lambda_{steel} \frac{2N_c A_0 L_c}{D_h bL}} + \frac{D_{h,sodium}}{\lambda_{sodium} Nu_{sodium} \frac{4N_c A_0 L_c}{D_h N_{c,sodium} p_{sodium} L}}} \right] \cdot LMTD} = \\
&= \frac{P_{th} D_h \frac{L}{L_c}}{4NN_c A_0 \cdot \left[ \frac{1}{\frac{D_h}{\lambda_{gas} Re \beta Pr^{0.4}} + \frac{\varepsilon}{\lambda_{steel} \frac{2N_c A_0 L_c}{D_h bL}} + \frac{D_{h,sodium}}{\lambda_{sodium} (5+0.025 Pe_{sodium}^{0.8} \frac{4N_c A_0 L_c}{D_h N_{c,sodium} p_{sodium} L}}} \right] \cdot LMTD}
\end{aligned}$$

For the moment, we have kept the Reynolds number as it is in the found expression. However, the Reynolds number can be written as:

$$Re = \frac{\Gamma D_h}{N N_c A_0 \mu}$$

Both for gas and sodium side. Hence we can finally write:

$$P_{th} D_h \frac{L}{L_c} / 4 N N_c A_0 \cdot LMTD$$

$$= \left[ \frac{1}{\lambda_{gas} B \left( \frac{\Gamma D_h}{N N_c A_0 \mu} \right)^\beta Pr^{0.4} + \frac{\varepsilon}{\lambda_{steel}} \frac{2 N_c A_0 L_c}{D_h b L} + \frac{D_{h,sodium}}{\lambda_{sodium} (5 + 0.025 \left( Pr \frac{\Gamma D_h}{N N_c A_0 \mu} \right)_{sodium}^{0.8} \frac{4 N_c A_0 L_c}{D_h N_{c,sodium} p_{sodium} L}} \right]$$

Note that  $L \propto 1/D$ , therefore it results that  $L(P_{th}, N)$  decreases when N increases, as already anticipated previously.

The pressure drops can be also expressed as:

$$\Delta p = f \frac{L}{D_h} \frac{1}{2} \rho V^2 = f \frac{L}{D_h} \frac{1}{2} \rho \frac{Re^2 \mu^2}{\rho^2 D_h^2} = A \frac{L}{D_h^3} \frac{1}{2} \rho \frac{Re^{2-\alpha} \mu^2}{\rho^2} =$$

$$= A \frac{L}{D_h^3} \frac{1}{2} \frac{Re^{2-\alpha} \mu^2}{\rho} = A \frac{L}{D_h^3} \frac{1}{2} \frac{\mu^2}{\rho} \left( \frac{\Gamma D_h}{N N_c A_0 \mu} \right)^{2-\alpha} =$$

$$= AL \frac{1}{2} \frac{\mu^2}{\rho} \left( \frac{\Gamma}{N_c A_0 \mu} \right)^{2-\alpha} \frac{1}{N^{2-\alpha} D_h^{-(1+\alpha)}}$$

Again, see that the combination of all the different term is specific of the considered geometry, due to the dependency on the superscript  $\alpha$  and on the fixed D dimension. Hence, these quantities are of primary interest for a quantitative comparison of different geometries.

Finally, write the total component length as:

$$L(\Delta p, N) = N^{2-\alpha} D_h^{1+\alpha} \frac{2 \rho \Delta p}{A \mu^2 \left( \frac{\Gamma}{N_c A_0 \mu} \right)^{2-\alpha}}$$

Since  $0 < \alpha < 2$ , see that  $L(\Delta p, N)$  increases if N increases, as previously explained.

These considerations demonstrate the validity of the approach shown in Figure 5.51. As a final comment before showing the results of the proposed approach see that this is

based upon actual performance of the heat exchanger. It could be stated that this is less practical than the compactness criteria shown in Chapter 2. However, as it has already been detailed, those criteria do not respect the real design alternatives available for a designer i.e. Figure 5.49. Moreover, it has been demonstrated that  $L(P_{th}, N)$  and  $L(\Delta p, N)$  expressions depend on actual geometries and hence that any comparison which is not based on the actual performance results in a loss of information that likely provides incorrect results. By the way, using this approach allows for comparing different geometries with different D dimensions since all quantities (i.e.  $D_h$ ,  $N_c$ ,  $A_0$ ) can be known once fixed a value for D). Therefore, the generality of this approach is something important to be pointed out. The final design point, not having an analytical solution, needs to be found either graphically or numerically via bisection techniques.

### 5.3 PERFORMANCE COMPARISON

With the correlations obtained in the previous section it is possible to compare the compactness of different technologies, in particular:

1. 45° innovative channel shown in Table 5.5;
2. 20° innovative channel shown in in Table 5.7;
3. Three parallel innovative channels as the one in Figure 5.46;
4. Straight channel with squared cross-section with  $D=2.5$  mm;
5. PCHE 45 wavy channel with squared cross-section with  $D= 2$  mm.

The geometries are chosen to show two different innovative channel geometries, the real-case three parallel innovative channel geometry, the simplest possible straight tube and a PCHE channel, which is as a third geometry of interest. Note that correlations for PCHE channel are taken from reference<sup>110</sup>. Reference heat exchanger performances are taken from ASTRID sodium-gas heat exchanger illustrated in Chapter 1. Results are shown in Figure 5.52.



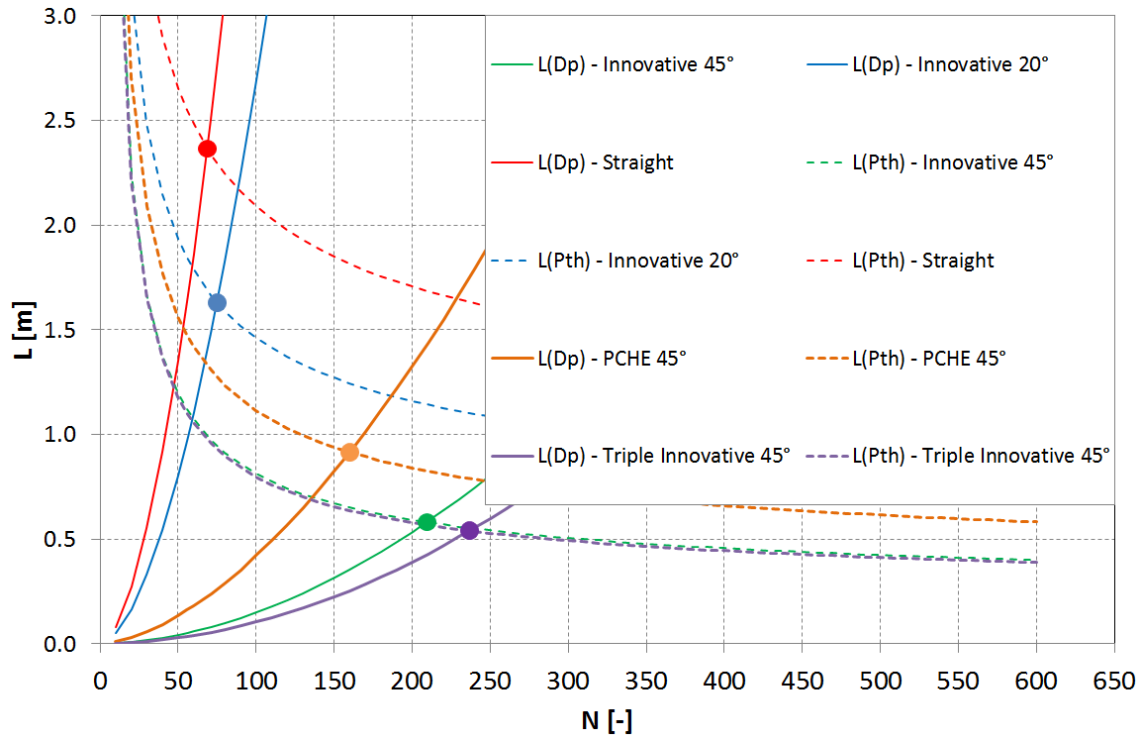


Figure 5.52 - Different technologies performance comparison

To better visualize the compactness, see the obtained whole component compactness values in Table 5.14.

	Straight channel	Single innovative channel 45°	Triple innovative channel 45°	Single Innovative channel 20°	PCHE channel 45°
Compactness [MW/m <sup>3</sup> ]	<b>20</b>	<b>28</b>	<b>27</b>	<b>25</b>	<b>23</b>
% with regard to Straight channel	/	<b>+40%</b>	<b>+35%</b>	<b>+25%</b>	<b>+15%</b>

Table 5.14 - Compactness comparison of different geometries for ASTRID Sodium-Has Heat Exchanger conditions

The innovative channel geometry presents always the higher compactness. The obtained gain is impressive, up to 25% for the 20° case, and 40% for the 45° case. Indeed it is worth noting that these 25% and 40% gains are not supposed to be the real ones, since the comparison between the single and the triple innovative channel with 45° angle clearly shows that the real case being more resistive, some percent of compactness gain

could be lost. Hence, even if a value of 35% for the 45° innovative channel geometry and 20% (author's best estimate) for the 20° geometry are foreseen as the more real ones, anyway it represents an important result. Note that the drawback of additional pressure drop created by the additional mixing zones for the real channel case (see Figure 5.46) could be eliminated if the distance between innovative channels is large enough to allow for having separated channel not intersecting each other on their bends. However, this presumably high distance would deteriorate the global component compactness. In any way, the innovative channel compactness improvement is even more impressive when looking at the PCHE, which is an existing technology more and more used in the industry when dealing with heat exchangers. PCHE at 45° seems to provide a smaller gain, compared to the innovative channel geometry. See that it could be considered as illogical that the innovative geometry, which is the most resistive among the studied geometries, is always the most compact one. Indeed this is not surprising at all: in fact, a more resistive geometry leads the designer to reduce the heat exchanger length (as shown) to meet the pressure drop value goal. This is obviously favorable if the heat exchanger can deal, in that lower volume, the same thermal load. The major parameter of interest for a compact heat exchanger is therefore the heat transfer surface to volume ratio, which is higher for the innovative channel, as shown in Chapter 5 section 4.3. Hence it is clear that the interest given by the innovative geometry is due to the fact that the global length has to be reduced to meet the pressure drop value, reducing the total volume of the component keeping the right heat transfer surface. Even if additional plates are to be added (see Figure 5.49) the final design point is always more compact than any other known industrial technology. This is obviously more true if the number of plates to be added is not excessive: in fact in that case, too short plates would be designed, which could be a potential drawback for other design constraints such as thermal-mechanical resistance. As a final comment see that, based on purely thermal-hydraulic considerations, the most compact geometry is that of 45°  $D=2\text{mm}$ .

## **6. PROPOSED DESIGN FOR ASTRID Na/N<sub>2</sub> HEAT EXCHANGER**

The previous section showed some correlations and the different geometry comparison for innovative channel-, PCHE- and straight tube-based compact heat exchangers. It has

been clarified that, due to the higher heat transfer surface per unit volume and to its thermal-hydraulic behavior, the innovative channel provides the most compact solution between the other cited. Hence, it is of interest to apply the found correlations to the design of the Sodium-Gas heat exchanger foreseen for ASTRID.

Having shown that the most compact geometry is that with  $D=2\text{mm}$  and a  $45^\circ$  angle with respect to flow main direction, it would be obvious to retain this geometry as the reference one. However, due to mechanical constraints about maximum thermal load and deformation, it seems that this geometry provide a component which is even “too compact” to respect the other design constraints. Hence, the  $20^\circ$  angle geometry has been chosen as the reference one. Design has been done with validated finite difference code developed at CEA<sup>111</sup> and the final result is compared with the straight tube-based design, to show the gain in compactness that can be obtained by using the innovative channel geometry. Heat exchanger global performance (which is the same for the shown components) is shown in Table 5.15, with a single machined plate shown in Figure 5.53 and a possible full component visualization shown in Figure 5.54.

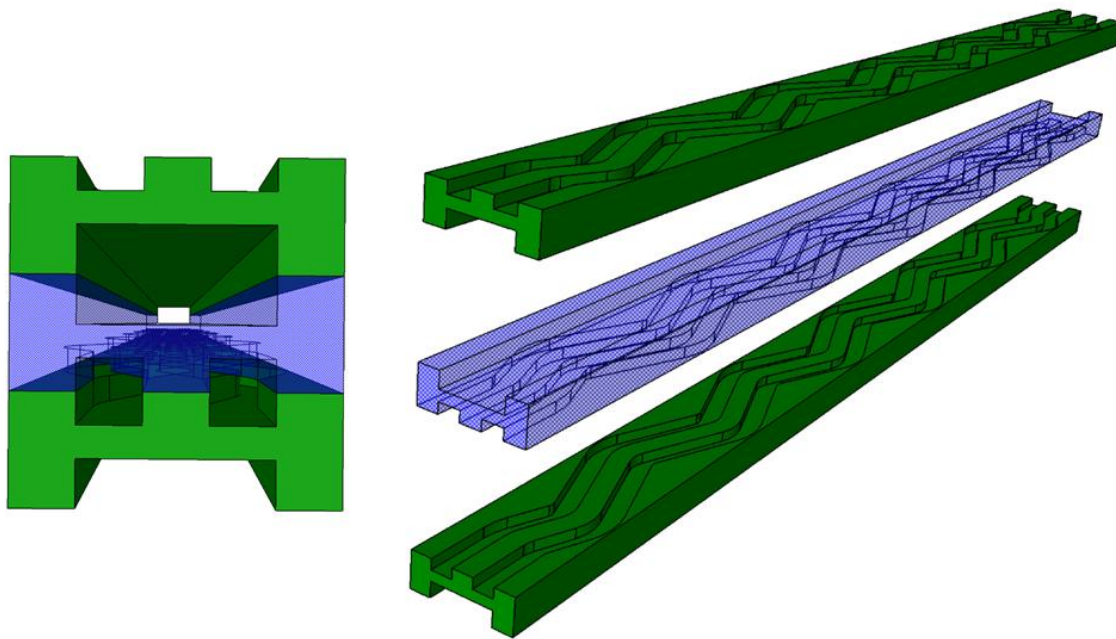


**Figure 5.53 - Single machined plate for innovative channel geometry based ASTRID Sodium-gas heat exchanger**

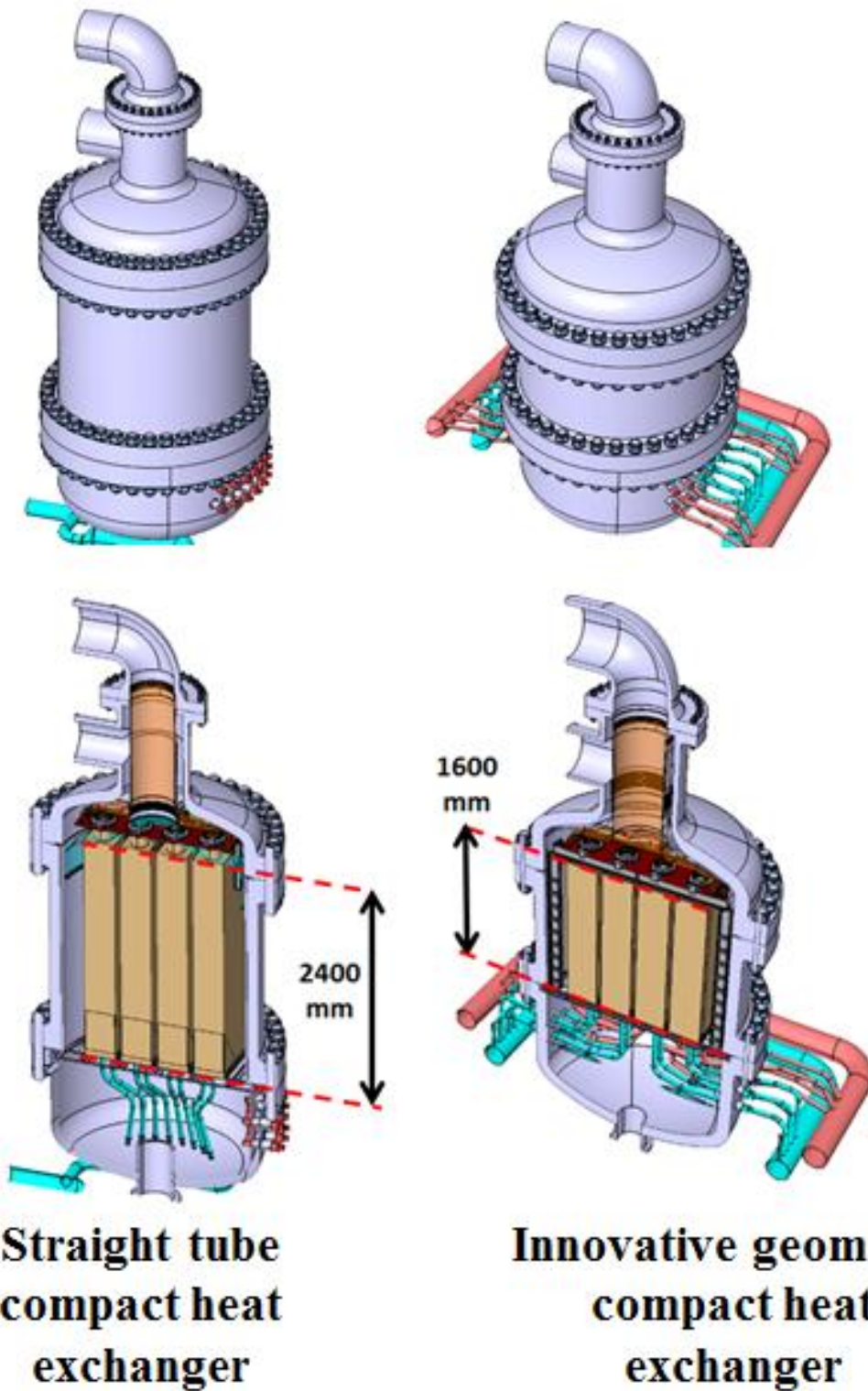


Figure 5.54 - ASTRID Sodium-gas heat exchanger design comparison (note that horizontal dimensions are not to scale)

Paramètres					
Puissance thermique	MWth	190		191	
Pression SCE (bar)		180		180	
Compacité composant (estimée) (MW/m <sup>3</sup> )		4.7		3,2	
mélange de gaz (%He / % N <sub>2</sub> )		0	/ 100	0	/ 100
Nombre de module		8		8	
Compacité thermique module	MW/m <sup>3</sup>	24		18	
poids composant estimé	Tonne	184		264	
<b>Na</b>					
<b>Thermohydraulique</b>					
Température Entrée / Sortie (°C)		530	/ 345.8	530	/ 345,4
Débit total / par composant (kg/s)		3189	/ 797.2	3189	/ 797,2
Pertes de charge (bar)		0.03		0,04	
Nu		5+0,025Pe <sup>0.8</sup>		5+0,025Pe <sup>0.8</sup>	
f		c.Re <sup>-d</sup>		c.Re <sup>-d</sup>	
c / d		0.0791	/ 0.25	0,0791	/ 0,25
<b>Caractéristiques Fluide</b>					
Cp J/(Kg.K)		1270.6		1270,6	
ρ kg/m <sup>3</sup>		844.3		844,4	
λ W/(m.K)		69.3		69,3	
μ Pa.s		2.58E-04		2,58E-04	
<b>Gaz</b>					
<b>Thermohydraulique</b>					
Température Entrée / Sortie (°C)		311	/ 515	310	/ 515
Débit total / par composant (Kg/s)		3.23E+03	/ 808.25	3,23E+03	/ 808,25
Pertes de charge (bar)		1.00		0,98	
Nu		a.Re <sup>b</sup> .Pr <sup>1/3</sup>		a.Re <sup>b</sup> .Pr <sup>1/3</sup>	
a / b		0.028	/ 0.7986	0,023	/ 0,8000
f		c.Re <sup>-d</sup>		c.Re <sup>-d</sup>	
c / d		0.6393	/ -0.2560	0,0791	/ -0,2500
<b>Caractéristiques Fluide</b>					
Cp J/(Kg.K)		1132.6		1132,6	
ρ kg/m <sup>3</sup>		81.0		81,0	
λ W/(m.K)		0.0528		0,0528	
μ Pa.s		3.35E-05		3,34E-05	
<b>Caractéristiques du module</b>					
Longueur (m)		1.63		2,39	
largeur plaque (m)		1		1	
hauteur (m)		0.608		0,54	
Nb de plaques		152		144	
Section de passage Na / N <sub>2</sub> (m <sup>2</sup> )		0.171	/ 0.137	0,162	/ 0,113
Surface d'échange Na / N <sub>2</sub> (m <sup>2</sup> )		279	/ 422	387	/ 430
Volume Na / gaz (m <sup>3</sup> )		0.279	/ 0.237	0,387	/ 0,269
poids (kg)		5287		7062	
<b>Motif corrugation</b>					
<b>Na</b>					
Epaisseur plaques mm		4.0		4,0	
hauteur canal mm		3.0		3,0	
Largeur canal mm		6.0		6,0	
Ep. Ligament canal mm		2.00		2,00	
Dh mm		4.00		4,00	
<b>Gaz</b>					
Epaisseur plaques mm		4.00		3,50	
Angle de corrugation °		40		0	
hauteur canal mm		3.00		2,50	
largeur canal mm		3.00		2,50	
Ep. Ligament canal mm		2.00		1,50	
Dh mm		2.250		2,500	

Table 5.15 - Design comparison of the ASTRID Sodium-Gas Heat Exchanger (innovative channel geometry on the left and straight tube geometry on the right)<sup>111</sup>

The design is based on an eight-module heat exchanger. Actual dimensions show the gain in compactness shown in Table 5.15. In particular, note how the proposed comparison approach, even if employs several simplifying assumptions, can give a very good prediction of the final design point in terms of number of plates and total component length. In fact, see in Figure 5.52 that both the component length and number of gas plates (i.e. half of the total number of plates in Table 5.15) are very well predicted by the proposed approach for the  $20^\circ$  innovative channel case, whereas slightly higher differences are found for the straight channel case due to the different heat transfer and pressure drop correlations used for data in Table 5.15 (i.e. Pethukov-Gnielinski correlations instead of Blasius and Dittus-Boelter-McAdams)<sup>111</sup>. In any case, always remember that the used correlations for the design of the innovative channel geometry with  $\alpha=20^\circ$  are those shown in Table 5.11, which do not take into account the actual geometry with several parallel channels. Since it has demonstrated that the innovative real geometry (i.e. several innovative single channels intersecting each other on their bends) is slightly less compact than the innovative single channel geometry (see Table 5.15), it can be stated that the proposed design is slightly optimistic and that a lower gain would be achieved. However, as a last comment, remember that the  $20^\circ$  geometry has been chosen due to the nuclear-related mechanical constraints. This means that, for an application which requires less strict mechanical performance or pressure drop constraints, a dramatic gain in compactness could be obtain by more compact geometries, i.e. the previously mentioned  $D=2\text{mm } 45^\circ$  one.

## 7. CONCLUSIONS

In the present Chapter the analysis of the innovative channel flow has been done, to identify the physical phenomena ongoing in the channel as well as its thermal-hydraulic performance.

Principal and secondary flow has been analyzed, with LDV and PIV experimental data and ASST numerical results. For the bend flow, an unusual high velocity region in the inner bend has been shown, whereas for the secondary flow an initial vortex evolving in a three vortices structure has been identified. This behavior is essentially due to the inlet bend flow coming from the mixing zone outlet. In the mixing zone, actual occurring mixing has been demonstrated, due to secondary velocity field from the bend outlet and to viscous entrainment of the opposite channel secondary flow velocity.

Once explained the steady-state flow phenomena, thermal hydraulic behavior of the innovative channel has been studied. Correlations for friction factor and Nusselt number for various geometries have been obtained. With the correlations, a new compactness comparison has been proposed: it takes into account design constraints, in particular the fact that different compared technologies have the same exchanger thermal power and pressure drop. With this approach, it has been shown that the innovative channel is the most compact one among the most important existing industrial compact heat exchanger technologies.

A final ASTRID Sodium-gas heat exchanger design has been proposed, which demonstrates that 25% compactness can be gained when adopting the innovative channel geometry if compared to a traditional straight-tube-based compact heat exchanger technology. Even higher compactness can be achieved if the designer has less important mechanical and/or pressure drop constraints.

# Chapitre 6: Conclusions et Perspectives

Dans le cadre du programme CEA R&D pour développer un prototype industriel de RNR-Na, nommé ASTRID, une technologie d'échangeur de chaleur compact innovante est en cours de développement pour l'utilisation d'un système de conversion de l'énergie à cycle Brayton. L'objectif de ce travail de thèse a consisté à mettre en place un travail de recherche visant à évaluer le potentiel, en termes d'efficacité thermique et de résistance aérodynamique, de motifs d'échange innovant.

Parmi les technologies existantes d'échangeurs de chaleur compacts, l'échangeur de chaleur à tôles embouties (PSHE), a été identifié car il offre potentiellement la solution la plus compacte. La conclusion de l'étude bibliographique nous a permis de comprendre qu'un écoulement complexe 3-D des PSHEs permet d'augmenter de manière significative les performances de transfert de chaleur. D'autre part, la faible résistance mécanique de cette technologie est souvent considérée comme trop limitative pour une application industrielle plus large pour des écoulements à haute pression. Dans ce cadre, il existe une technologie d'échangeur de chaleur compact qui peut potentiellement supporter cette différence de pression: la technologie d'échangeur de chaleur à circuit imprimé (PCHE). Par conséquent, afin d'augmenter la compacité globale du composant un canal innovant est proposé. Le canal peut être considéré comme le résultat de la superposition de deux canaux ondulés type PCHE en opposition de phase.

Afin de fournir un modèle numérique physiquement cohérent, et industriellement utilisable, un nouveau modèle de turbulence à viscosité turbulente non linéaire nommé "Anisotropic Shear Stress Transport" model (ASST) a été développé et implémenté dans le solveur ANSYS FLUENT ®. Il a été démontré que le modèle ASST peut fournir une alternative intéressante aux modèles plus complexes (par exemple les modèles type transport des tensions de Reynolds) pour une variété d'écoulements, donnant des résultats globaux qui sont au moins aussi bons que ceux du modèle Stress Omega, beaucoup plus coûteux en temps de calcul.

Compte tenu de l'innovation de la géométrie actuelle, aucun cas-test de validation n'a été trouvé dans la littérature pour être pleinement applicable à la géométrie innovante.



Ainsi, deux sections expérimentales ont été utilisées pour obtenir une base de données aérodynamique fiable. La campagne de Vélocimétrie Laser à franges (LDV) nous a permis d'acquérir une très grande base de données sur les vitesses d'écoulement et les fluctuations de vitesse dans plusieurs régions du canal innovant. D'autre part, un banc d'essai de Vélocimétrie Laser par images de particules (PIV) a été utilisé pour étudier les phénomènes globaux qui se produisent dans le canal innovant qui n'ont pas été observés au cours de la campagne LDV.

Ensuite, l'analyse numérique de l'écoulement avec le modèle développé ASST dans le canal innovant a été faite avec les données d'entrées des expérimentations afin d'évaluer la performance du modèle. Une fois validée, la modélisation a permis d'étudier en détails le comportement aéraulique du canal innovant.

Pour la partie thermique, l'installation "VHEGAS" a été construite pour mesurer le coefficient de transfert de chaleur global dans le canal innovant. Le modèle ASST est utilisé avec un modèle thermique SGDH; ils ont été validés avec les données expérimentales de "VHEGAS", en montrant que le coefficient de transfert de chaleur calculé se situe dans la plage d'incertitude expérimentale ( $\pm 20\%$ ).

Le modèle ASST est donc validé d'un point de vue thermo-hydraulique. Par conséquent, les corrélations pour le coefficient de frottement et le nombre de Nusselt pour différentes géométries peuvent être calculées. En comparant différentes géométries, il a été montré que la géométrie innovante est la plus compacte parmi les autres technologies d'échangeur de chaleurs compacts.

Enfin, une conception de l'échangeur de chaleur sodium-gaz d'ASTRID a été proposée, démontrant qu'un gain de compacité de 25% peut être acquis lors de l'adoption de la géométrie du canal innovant par rapport à une technologie d'échangeur de chaleur compact à base de canaux droits plus classiques.

Ce travail constitue une première étape pour l'évaluation d'une géométrie de transfert de chaleur innovant qui peut fournir à la fois une très grande compacité et une résistance mécanique élevée. Même si le travail accompli jusqu'à présent a fourni des informations précieuses, de nombreux points restent encore à être approfondis.

Le nouveau modèle ASST de turbulence proposé couple le modèle SST avec une formulation non-linéaire d'ordre deux des tensions de Reynolds. Cependant, comme il

a été mentionné dans le Chapitre 3, une formulation d'ordre trois saurait mieux rendre compte du swirling, qui est un phénomène survenant dans le canal innovant, comme on l'a souligné dans le chapitre 5.

L'approche de modélisation de ce travail a été basée sur des modèles de turbulence RANS. Cependant, d'autres modèles plus fins peuvent être utilisés pour étudier les caractéristiques d'écoulement des canaux innovants. Si la LES pourrait être une solution difficile à cause du temps de calcul très élevée, le modèle SAS pourrait fournir une solution très intéressante, car l'approche URANS permettrait d'étudier l'écoulement des fluides dans la décomposition du spectre des fréquences. Cette décomposition pourrait montrer les contributions instationnaires au transfert de chaleur, notamment au niveau des zones de mélange.

Dans le cadre d'une étude locale, il serait intéressant d'améliorer l'approche de modélisation thermique. En raison de contraintes de temps, seule une validation globale a pu être faite dans ce travail de thèse. Toutefois, afin de mieux mettre en évidence les contributions locales au transfert thermique, un banc d'essai spécifique doit être conçu et construit, probablement à grande échelle pour être en mesure d'utiliser un grand nombre de thermocouples sans perturber l'écoulement du fluide. Cette analyse locale peut être numériquement étudiée par un modèle à flux de chaleur turbulent algébrique (EAHFM), ce qui pourrait mieux expliquer le transfert de chaleur, en particulier dans un écoulement très turbulent tel que celui des canaux innovants grâce aux fluctuations du flux de chaleur turbulent dans les trois dimensions.

Pour effectuer une optimisation de la géométrie, une étude paramétrique approfondie sur le paramètre géométrique du canal innovant devrait être faite. Une première étude paramétrique a été effectuée en utilisant le modèle SST et le modèle de SDGH. Cependant, les corrélations d'échange thermique et de pertes de charge calculées doivent être mises à jour en utilisant au moins le modèle ASST couplé au modèle SDGH en fonction des résultats de la validation thermique.

« Last but not least », il sera très intéressant de comparer différentes sections de canaux innovants pour vérifier si une section de passage du fluide rectangulaire donnant une section transversale totale carrée est la meilleure possible en termes de

performance. En fait, le motif innovant pourrait se décliner en différentes sections de canal ondulé, soit triangulaire, semi-circulaire, trapézoïdale, carrée, etc. Le comportement thermo-hydraulique de ces canaux innovants mérite d'être étudié pour déterminer le meilleur candidat. Même si certaines sections transversales peuvent être considérés comme «exotiques» et industriellement irréalisables, la section semi-circulaire ou semi-élliptique semble être très intéressante en raison de sa possible fabrication par usinage électrochimique.

# Chapter 6: Conclusions and Perspectives

## 1. CONCLUSIONS

In the framework of CEA R&D program to develop an industrial prototype of Sodium-cooled Fast Reactor, the present thesis aimed to propose an innovative compact heat exchanger technology to provide solid technological basis for the utilization of a Brayton Gas-power conversion system, in order to avoid the energetic sodium-water interaction if a traditional Rankine cycle was used. The design of the gas-side (which determines the heat transfer resistance of the heat exchanger) of the Sodium-gas heat exchanger has been the object of the present work. Compact technologies are necessary for the present application because of the low heat transfer capacity of the gas foreseen, i.e. nitrogen. Among the compact heat exchanger existing technologies, Plate Stamped Heat Exchanger (PSHE), has been identified since it potentially provides the most compact solution. Therefore the present work started studying the PSHE technology, to investigate its thermal-hydraulic behavior and to understand the physical phenomena providing the efficient heat transfer.

The conclusion of the bibliographic review led us to understand that the complex 3-D flow of the PSHEs makes it possible to significantly increase the heat transfer performances of the component (see Section 2.2). On the other hand, the low mechanical resistance of this technology is often seen as too limiting for a wider industrial application for high-pressure flow such as that of a nuclear reactor loop. In fact, if PSHEs provide a relatively high heat transfer coefficient, on the other hand, they do not seem to be able to provide sufficiently good mechanical resistance to withstand working conditions (temperature and pressure) foreseen for ASTRID. In this sense it does exist a compact heat exchanger technology that can potentially stand this pressure difference: the Printed Circuit Heat Exchanger (PCHE) technology, using diffusion bonding as welding process.

Hence, in order to increase the heat transfer coefficient (and the global compactness) the basic idea of this work is to design a channel where the fluid flow is as much three-dimensional as possible.

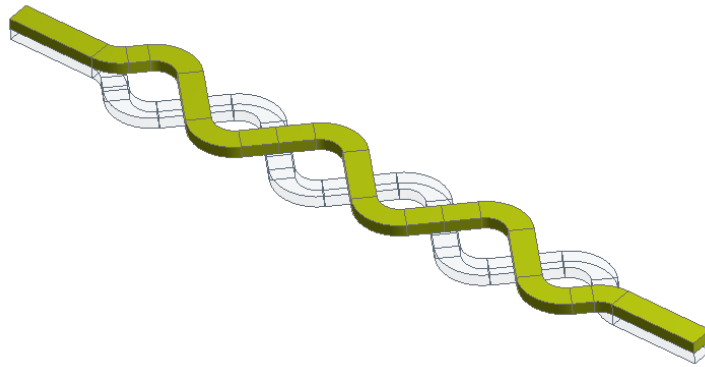


**Figure 2.48 - Superposed channels identification**

In particular the channel can be thought as the result of the superposition of two single PCHE wavy channels in phase opposition (white and yellow in Figure 2.41), as Figure 2.42 shows. Note always in Figure 2.42 two of the possible fluid streams inside the channel (in green and orange) and compare them with the 3D fluid stream in a PSHE shown in Figure 2.11 and Figure 2.13)

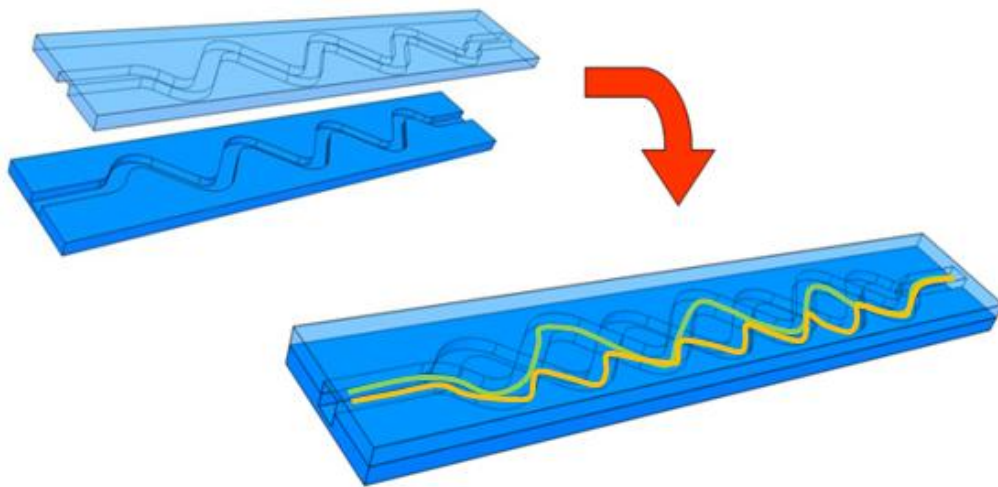


**Figure 2.49 - Innovative geometry concept**

The innovative channel geometry has to be studied numerically and experimentally to demonstrate its industrial interest and the actual compactness gain, if present.

Therefore, to numerically provide a physically-consistent model, a new non-linear eddy viscosity named Anisotropic Shear Stress Transport (ASST) model has been developed and implemented into the available solver ANSYS FLUENT ®. It presents the beneficial feature to be a fully realizable model, which means that spurious and non-physical turbulent characteristics are avoided thanks to mathematical and physical

considerations. It has been demonstrated that the ASST model can provide a valuable alternative to more complex models (i.e. Reynolds Stress Transport models) for a variety of flows, giving global results that are at least as good as those of the Stress Omega model. Moreover, it keeps a very shorter computational time than the Stress Omega model, resulting to be a very good option for the desired industrial tool to potentially describe the innovative channel flow.

Given the innovation of the present geometry, no actual test case has been found in the literature to be fully applicable to the present study. So, two experimental sections have been used to acquire an extensive aerodynamic database. The Laser Doppler Velocimetry (LDV) campaign allowed us acquiring a very large database on flow velocities and velocity fluctuations in several regions of the innovative channel. These data are helpful for the numerical model validation, since they give a full representation of the fine phenomena occurring in the fluid flow bulk as well as in the boundary layer. On the other hand, a Particle Image Velocimetry (PIV) technique has been used to study global phenomena occurring in the innovative channel flow that have not been observed during the LDV campaign and that have been discussed. To give a further double-check to the PIV with regard to LDV measurements, a comparison of velocity profiles in equivalent geometrical places has been shown, demonstrating that the two velocity profiles are almost identical, even though Reynolds numbers were different and hence no exact consistency could be expected.

Then, the analysis of the innovative channel flow has been done, to identify the physical phenomena ongoing in the channel as well as its thermal-hydraulic performance.

Principal and secondary flow has been analyzed, with LDV and PIV experimental data and ASST numerical results. For the bend flow, an unusual high velocity region in the inner bend has been shown, whereas for the secondary flow an initial vortex evolving in a three vortices structure has been identified, and it has been shown that this behavior is due to the inlet bend condition from the mixing zone. Here, high mixing has been demonstrated, due to secondary velocity field from the bend outlet and to viscous entrainment of the opposite channel secondary flow velocity.

Once explained the steady-state flow phenomena, thermal hydraulic behavior of the innovative channel has been studied.

To do that, the VHEGAS facility has been built to investigate the innovative channel global heat transfer coefficient. The ASST model used with a SGDH thermal model has been validated against VHEGAS experimental data, showing that, under proper conditions, the computed heat transfer coefficient lies within the experimental uncertainty range. Hence, once having done the validation of the pure aerodynamic and the coupled thermal-hydraulic model, correlations for friction factor and Nusselt number for various geometries could be obtained. With the correlations, a compactness comparison strategy has been developed: it takes into account design constraints, in particular the fact that different compared technologies have the same exchanger thermal power and pressure drop. With this strategy, it has been shown that the innovative channel is the most compact one among the most important existing industrial compact heat exchanger technologies.

A final ASTRID Sodium-gas heat exchanger design has been proposed, which demonstrates that a 25% compactness can be gained when adopting the innovative channel geometry if compared to a traditional straight-tube-based compact heat exchanger technology. Even higher compactness can be achieved if the designer has less important mechanical and/or pressure drop constraints.

## **2. PERSPECTIVES**

The present work represents a first step for the assessment of an innovative heat transfer geometry which can provide both a very high compactness and high mechanical resistance to pressure gradients between the two sides of the heat exchanger. Even though the work done so far has provided valuable information, many points are still to be investigated further.

1. The new proposed ASST turbulence model coupled the linear SST model with a 2<sup>nd</sup> order non-linear Reynolds stress formulation. However, as it has been mentioned in Chapter 3, a 3<sup>rd</sup> order formulation would better account for flow swirling, which is an occurring phenomenon in the innovative channel, as highlighted in Chapter 5. For example, Baglietto et al. proposed the following 3<sup>rd</sup> order formulation, which could be a starting point for ASST model improving:

$$\begin{aligned}
\rho \overline{u_i u_j} &= \frac{2}{3} \rho k - \mu_t S_{ij} + \rho C_1 k \tau^2 \left( S_{ik} S_{kj} - \frac{1}{3} \delta_{ij} S_{kl} S_{kl} \right) \\
&+ \rho C_2 k \tau^2 \left( \Omega_{ik} \Omega_{kj} - \frac{1}{3} \delta_{ij} \Omega_{kl} \Omega_{kl} \right) + \rho C_3 k \tau^2 (\Omega_{ik} S_{kj} + \Omega_{jk} S_{ki}) \\
&+ \rho C_4 k \tau^3 (S_{ki} \Omega_{lj} + S_{kj} \Omega_{li}) S_{kl} + \rho C_5 k \tau^3 (S_{kl} S_{kl} - \Omega_{kl} \Omega_{kl}) S_{ij}
\end{aligned}$$

Where  $C_1$ ,  $C_2$  and  $C_3$  coefficients are the same as those in Chapter 3 and

$$C_4 = C_\mu \frac{-2.2}{15+8S+S^2}, C_5 = C_\mu \frac{-2.0}{15+8S+S^2}.$$

2. The modeling approach of the present work has been that of RANS turbulence models. However, other finer models could be used to investigate innovative channel flow characteristics that RANS models hardly show. If LES could be a tough solution due to the very high computational time required, the SAS model<sup>112</sup> could provide a very interesting solution, since the URANS approach would allow to study the fluid flow under frequency spectrum decomposition. This decomposition could potentially show unsteadiness contributions to heat transfer, information loosen by the RANS averaging adopted in the present work.
3. In the framework of a better local flow investigation, it would be interesting to improve the thermal modeling approach. Due to time constraints, only a global validation could be done during the present work. However, to better highlight local contributions to heat transfer, a proper facility should be designed and built, likely on large scale to be able to use a large number of TCs without perturbing the fluid flow. This local analysis could be numerically studied by an Explicit Algebraic Heat Flux Model (EAHFM), which could better explain the heat transfer, especially in a very turbulent flow such as that of the innovative channel thanks to the fluctuating turbulent heat flux contribution in the three dimensions.
4. In order to perform a geometry optimization, an extensive parametric study on the innovative channel geometrical parameters should be done. In particular, referring to Figure 2.47, the parameters of interest are  $\alpha$ ,  $L/D$  and  $R/D$ . A first parametric study had been done using the SST model and the SGDH model<sup>113</sup>. However, the computed heat transfer and friction factor correlations should be updated using at least the ASST model coupled to the SDGH model to obtain better results.



5. Last but not least, it will be very interesting to compare different innovative channel geometries to verify if the assumption done in Chapter 2 of a rectangular cross section giving a total squared cross section is the best possible. In fact, the innovative channel can be thought as the superposition of very different single channel cross sections, i.e. triangular, hemi-circular, trapezoidal, squared, etc (see Figure 6.1). Thermal-hydraulic behavior of such innovative channels is worth being studied to determine the best candidate. Even if some cross-sections might be considered as “exotic” and industrially unfeasible, the hemi-circular cross-section appears to be very interesting due to its possible fabrication via chemical machining.

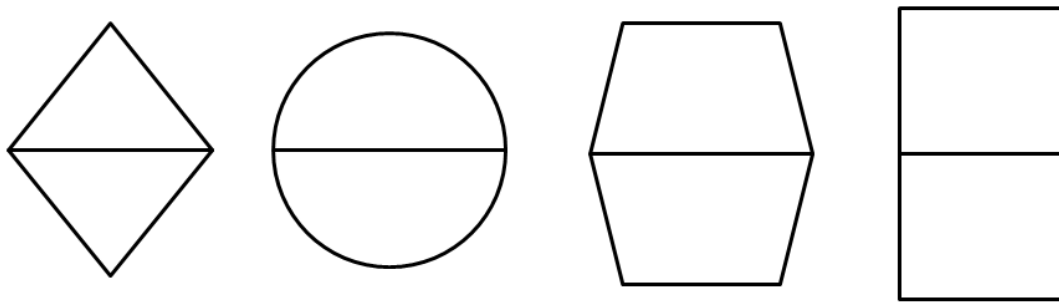


**Figure 6.1 - Possible innovative channel cross-section geometries to be studied**

## APPENDIX A – DIFFERENTLY DEFINED PSHE CORRELATION CONVERSION FACTORS

It is important to show the correlation between the definition of Nusselt number and friction factor, using the hydraulic diameter or the equivalent diameter.

It is straightforward that  $D_h = \frac{D_e}{\phi}$ ; therefore there will be the same relation for the two differently defined Reynolds and Nusselt numbers: in particular it will be  $Re_h = \frac{Re_e}{\phi}$  and  $Nu_h = \frac{Nu_e}{\phi}$ , with obvious meaning of the subscripts “h” and “e”. The opposite is for the definition of the friction factor, which depends on the inverse of the hydraulic/equivalent diameter. Hence:

$$f_h \propto \frac{1}{D_h}, f_e \propto \frac{1}{D_e} \rightarrow f_e = \phi \cdot f_h$$

Now consider the general type of correlation for Nusselt number and friction factor (See Correlations):

$$Nu = B \cdot Pr^c \cdot Re^d$$

$$f = A \cdot Re^{-b}$$

Since we want:

$$Nu_e = B_e \cdot Pr^c \cdot Re_e^d, Nu_h = B_h \cdot Pr^c \cdot Re_h^d$$

$$f_e = A_e \cdot Re_e^{-b}, f_h = A_h \cdot Re_h^{-b}$$

Write:

$$Nu_h = B_h \cdot Pr^c \cdot Re_h^d \rightarrow Nu_e = \phi \cdot B_h \cdot Pr^c \cdot Re_h^d = \phi \cdot B_h \cdot Pr^c \cdot \frac{Re_e^d}{\phi^d} = \phi^{1-d} \cdot B_h \cdot Pr^c \cdot Re_e^d \rightarrow$$

$$B_e = \phi^{1-d} \cdot B_h$$

And

$$f_h = A_h \cdot Re_h^{-b} \rightarrow f_e = \phi \cdot A_h \cdot Re_h^{-b} = \phi \cdot A_h \cdot \frac{Re_e^{-b}}{\phi^{-b}} = \phi^{1+b} \cdot A_h \cdot Re_e^{-b} \rightarrow$$

$$A_e = \phi^{1+b} \cdot A_h$$

## APPENDIX B – ANISOTROPIC FORMULATIONS OF THE REYNOLDS STRESS TENSOR

We have seen in Chapter 3 that the Reynolds stress tensor in anisotropic formulations can be expressed in two different ways, specifically Eq.22 and Eq.34 which use the velocity gradients and the strain rate and rotation rate tensors to express second order terms respectively. The two formulations can be linked in the following way: each second order term of the tensor formulation (i.e. pure strain, mixed strain-rotation, pure rotation) can be expressed in terms of pure velocity gradient product. Then it is sufficient to correlate the coefficients of each term to link the two formulations. Therefore:

$$\begin{aligned}
 C_1 S_{ik} S_{kj} &= \frac{C_{NL1}}{(C_{NL4} + C_{NL5} \cdot S^3)} \left( \frac{\partial U_i}{\partial x_k} + \frac{\partial U_k}{\partial x_i} \right) \left( \frac{\partial U_k}{\partial x_j} + \frac{\partial U_j}{\partial x_k} \right) = \\
 &= \frac{C_{NL1}}{(C_{NL4} + C_{NL5} \cdot S^3)} \left( \frac{\partial U_i}{\partial x_k} \frac{\partial U_k}{\partial x_j} + \frac{\partial U_i}{\partial x_k} \frac{\partial U_j}{\partial x_k} + \frac{\partial U_k}{\partial x_i} \frac{\partial U_k}{\partial x_j} + \frac{\partial U_k}{\partial x_i} \frac{\partial U_j}{\partial x_k} \right) \\
 C_2 [\Omega_{ik} S_{kj} + \Omega_{jk} S_{ki}] &= \frac{C_{NL2}}{(C_{NL4} + C_{NL5} \cdot S^3)} \left[ \left( \frac{\partial U_i}{\partial x_k} - \frac{\partial U_k}{\partial x_i} \right) \left( \frac{\partial U_k}{\partial x_j} + \frac{\partial U_j}{\partial x_k} \right) + \left( \frac{\partial U_j}{\partial x_k} - \frac{\partial U_k}{\partial x_j} \right) \left( \frac{\partial U_k}{\partial x_i} + \frac{\partial U_i}{\partial x_k} \right) \right] = \\
 &= \frac{C_{NL2}}{(C_{NL4} + C_{NL5} \cdot S^3)} \left( 2 \frac{\partial U_i}{\partial x_k} \frac{\partial U_j}{\partial x_k} - 2 \frac{\partial U_k}{\partial x_i} \frac{\partial U_k}{\partial x_j} \right) \\
 C_3 \Omega_{ik} \Omega_{jk} &= \frac{C_{NL3}}{(C_{NL4} + C_{NL5} \cdot S^3)} \left( \frac{\partial U_i}{\partial x_k} - \frac{\partial U_k}{\partial x_i} \right) \left( \frac{\partial U_j}{\partial x_k} - \frac{\partial U_k}{\partial x_j} \right) = \\
 &= \frac{C_{NL3}}{(C_{NL4} + C_{NL5} \cdot S^3)} \left( \frac{\partial U_i}{\partial x_k} \frac{\partial U_j}{\partial x_k} - \frac{\partial U_i}{\partial x_k} \frac{\partial U_k}{\partial x_j} - \frac{\partial U_k}{\partial x_i} \frac{\partial U_j}{\partial x_k} + \frac{\partial U_k}{\partial x_i} \frac{\partial U_k}{\partial x_j} \right)
 \end{aligned}$$

Note that the four second order gradient terms found are the same used in Shit et al. formulation. Again, it is sufficient to correlate the coefficients of second order gradient formulation to those of strain and rotation rate tensor formulation to obtain the correct link between the two. Note that it can already be stated that the A2 coefficient must be equal to the  $C_{NL4}$  coefficient and that  $C_{NL5} = 1$ .

Term	Velocity gradient formulation coefficient	Strain and rotation rate tensor formulation coefficient
$\frac{\partial U_i}{\partial x_k} \frac{\partial U_k}{\partial x_j}$	$C_{\tau 1}$	$C_{NL1} - C_{NL3}$
$\frac{\partial U_k}{\partial x_i} \frac{\partial U_j}{\partial x_k}$	$C_{\tau 1}$	$C_{NL1} - C_{NL3}$
$\frac{\partial U_i}{\partial x_k} \frac{\partial U_j}{\partial x_k}$	$C_{\tau 2}$	$C_{NL1} + 2C_{NL2} + C_{NL3}$
$\frac{\partial U_k}{\partial x_i} \frac{\partial U_k}{\partial x_j}$	$C_{\tau 3}$	$C_{NL1} - 2C_{NL2} + C_{NL3}$

See the different values of the coefficients in the two formulations for the model proposed by Shih et al.:

Velocity gradient formulation coefficient	Strain and rotation rate tensor formulation coefficient
$C_{\tau 1} = -4$	$C_{NL1} = \mathbf{0.75}$
$C_{\tau 2} = 13$	$C_{NL2} = \mathbf{3.75}$
$C_{\tau 3} = -2$	$C_{NL3} = \mathbf{4.75}$
$A_2 = 1000$	$C_{NL4} = \mathbf{1000}$

Note that the  $C_{NL2}$  coefficient has been increased by Baglietto et al. up to eleven. Other coefficients have been slightly modified. This formulation still respects realizability conditions, since:

Velocity gradient formulation coefficient	Strain and rotation rate tensor formulation coefficient
$C_{\tau 1} = -3.7$	$C_{NL1} = \mathbf{0.8}$
$C_{\tau 2} = 27.3$	$C_{NL2} = \mathbf{11}$
$C_{\tau 3} = -16.7$	$C_{NL3} = \mathbf{4.5}$
$A_2 = 1000$	$C_{NL4} = \mathbf{1000}$

With the new coefficients it results that realizability conditions are respected:

$$2C_{\tau 1} + C_{\tau 2} + C_{\tau 3} = 2 \cdot (-3.7) + 27.3 - 16.7 = 3.2 > 0$$

$$C_{\tau 2} = 27.3 > 2 \cdot (-16.7) = -33.4$$

$$C_{\tau 4} = A_2 = 1000 > 0$$

Hence the model of Baglietto et al.(with modified coefficients) is fully realizable as well, providing physical positive principal Reynolds stresses values, which can potentially improve complex flow modelling and description.

## APPENDIX C – EXAMPLE OF LDV CALIBRATION FILE

```
# application/x-assa
# calibration file

[Etalonnage]
Numéro=44
Date=2013-10-28
NbCanaux=2
Canaux=514,488,0
Interfranges=3.70047e-06,3.5326e-06,0
sdInterfranges=9.63382e-09,8.97233e-09,0
MatriceL1=0.00524428,0.999998,0
MatriceL2=0,0,1
MatriceL3=1.00417,-0.00548003,0
sdMatriceL1=0.00389577,2.2714e-05,0
sdMatriceL2=0,0,0
sdMatriceL3=3.42137e-05,0.00357572,0
Bragg=10 MHz,10 MHz,10 MHz
sdBragg=0.001 MHz,0.001 MHz,0.001 MHz
# "Comment" peut comporter plusieurs lignes.
Comment=RAS
```

```
[DataLink]
nCWord=0
```

```
[DataLink0]
Nom=HP
Type=OFF
A0=0.0
A1=1.0
A2=0.000000
A3=0.000000
A4=0.000000
Unité=V
Précision=3
```

```
[DataLink1]
Nom=Mic1
Type=OFF
A0=0.0
A1=1.0
A2=0.000000
A3=0.000000
A4=0.000000
Unité=V
Précision=3
```

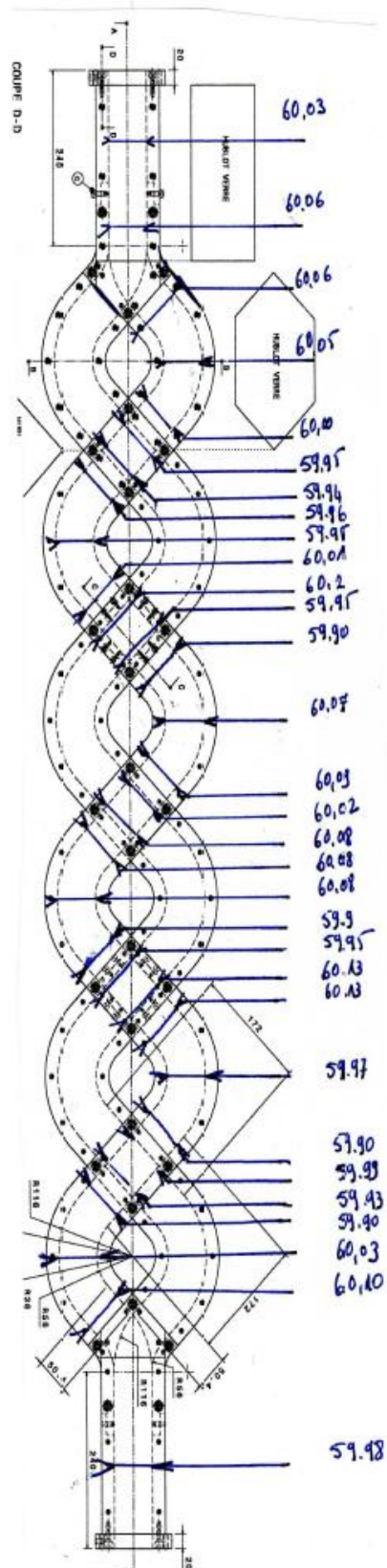
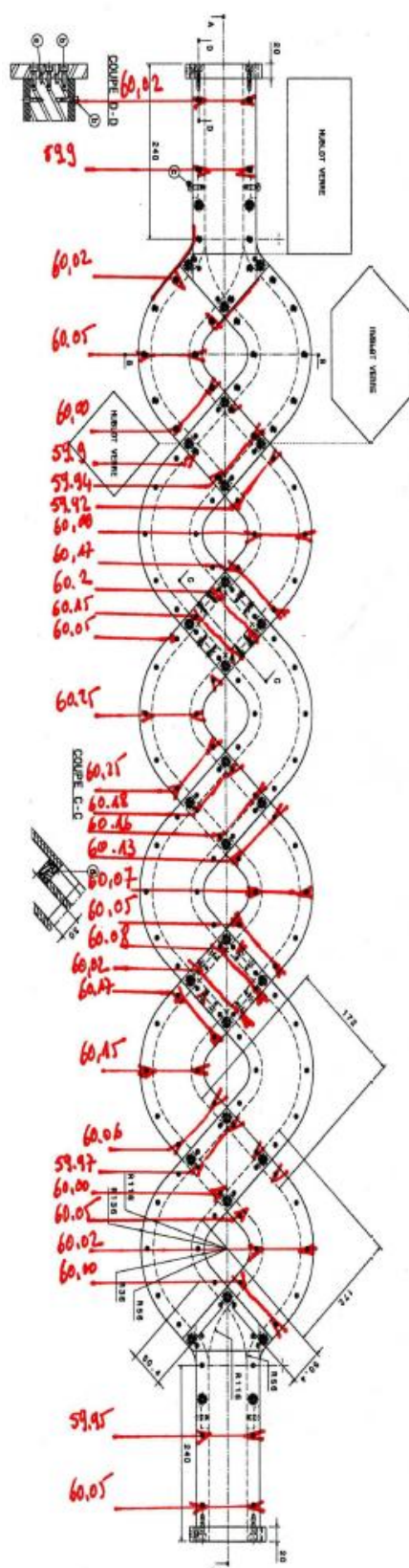
```
[DataLink2]
Nom=Mic2
Type=OFF
A0=0.0
```

```
A1=1.0
A2=0.000000
A3=0.000000
A4=0.000000
Unité=V
Précision=3
```

```
[DataLink3]
Nom=Compteur
Type=OFF
A0=0.0
A1=1.0
A2=0.000000
A3=0.000000
A4=0.000000
Unité=#
Précision=0
```

```
[Banc]
# Changement d'unités de la position du volume de mesure
# selon  $\text{new\_xi} = \text{ai} * \text{old\_xi} + \text{bi}$ 
# sachant que old_xi est toujours en mètre.
# Les bi sont réservés à des décalages fortuits.
A=1000.,1000.,1000.
B=0.,0.,0.
Unité=mm
# Passage entre le repère Vélocimètre et le repère Maquette
# Translation d'origine entre repère vélocimètre et repère
maquette
# Coordonnées du zéro maquette dans le repère vélocimètre
OvOm=0.,0.,0.
# Matrice de passage entre les repères Déplacement
#  $V(Rv) = MD V(Rd)$ 
MatriceDL1=-1.0,0.0,0.0
MatriceDL2=0.0,1.0,0.0
MatriceDL3=0.0,0.0,-1.0
# Matrice de passage entre les repères Vitesse
#  $V(Rm) = MV V(Rv)$ 
MatriceVL1=1.0,0.0,0.0
MatriceVL2=0.0,1.0,0.0
MatriceVL3=0.0,0.0,1.0
```

## APPENDIX D –LDV MOCKUP DIMENSIONS VERIFICATION





**Rappel :**

Plaque : PMMA Coule, Transparent

Dimensions : 157,28\*1501,6 , épaisseur 10

2 trous de centrage, Ø10

Poissage optique sur les surfaces usinées

Vue de dessus  
Échelle : 1/3

Vue de face  
Échelle : 1/3

Détail A  
Échelle : 2/3

Détail B  
Échelle : 2/3

Vue latérale gauche  
Échelle : 1/3

Vue latérale droite  
Échelle : 1/3

PROJET :  
SUD PACA  
Rapport PIV  
Plaque Direct Laser  
1220 001 003

Direction de l'Armement Nucléaire  
Département de Technologie Nucléaire  
OED

SUD PACA  
Rapport PIV  
Plaque Direct Laser  
1220 001 003

## APPENDIX F – ASST VS VELOCITY FLUCTUATIONS MEASUREMENTS COMPARISON

The goal of the present appendix is to present the experimental data versus ASST computation results in order to provide further information on ASST model validation on the innovative channel case. Data of velocity fluctuations will be shown, to demonstrate ASST model capability to represent turbulent phenomena in the innovative channel as well as to illustrate which regions of the innovative channel present higher turbulence.

First, see the comparison of the  $u'$  and  $w'$  components measured by LDV. Note that shown results are taken in the same profiles as Figure 5.16 and Figure 5.20 for in-bend flow and Figure 5.25, Figure 5.26 and Figure 5.27 for mixing zone flow. Hence, as already mentioned, red dots represent experimental data and solid black lines the computational results.

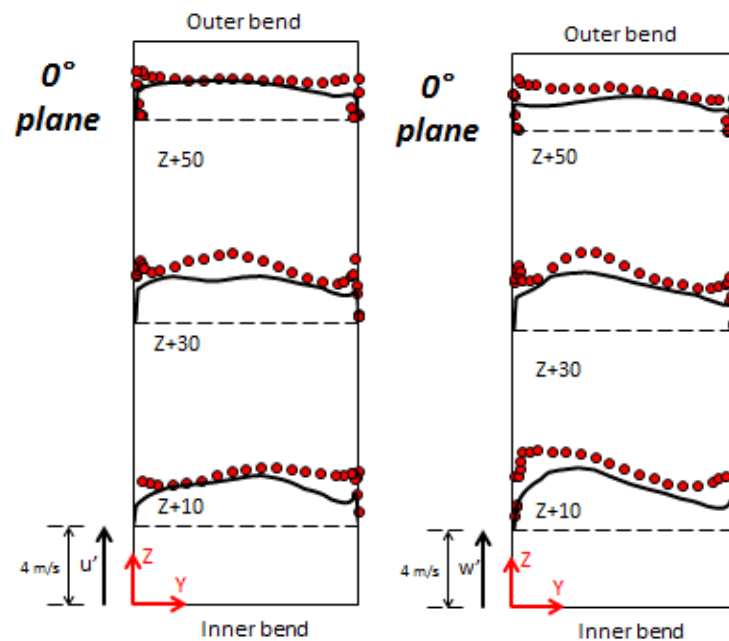


Figure E. 1 - Bend 0° plane LDV vs ASST principal (left) and radial (right) velocity fluctuation

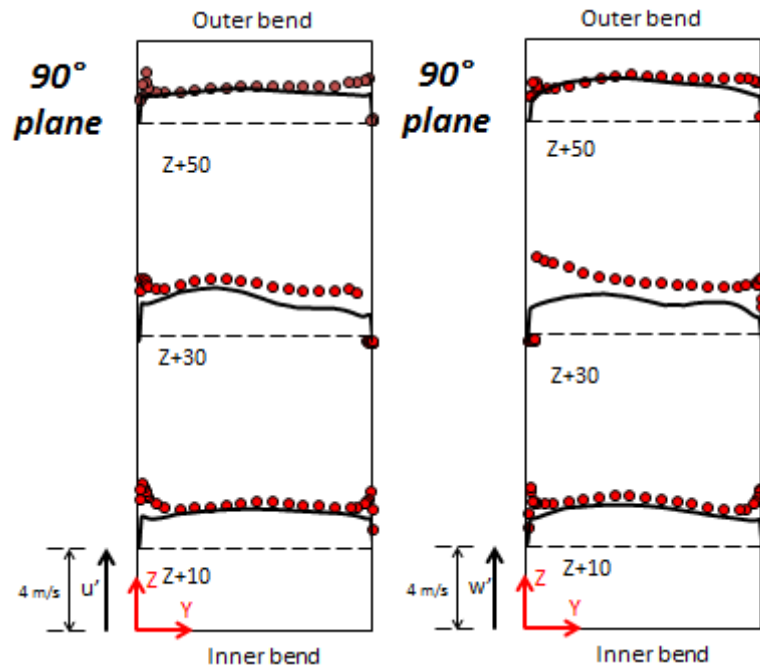


Figure E. 2 - Bend 90° plane LDV vs ASST principal (left) and radial (right) velocity fluctuation

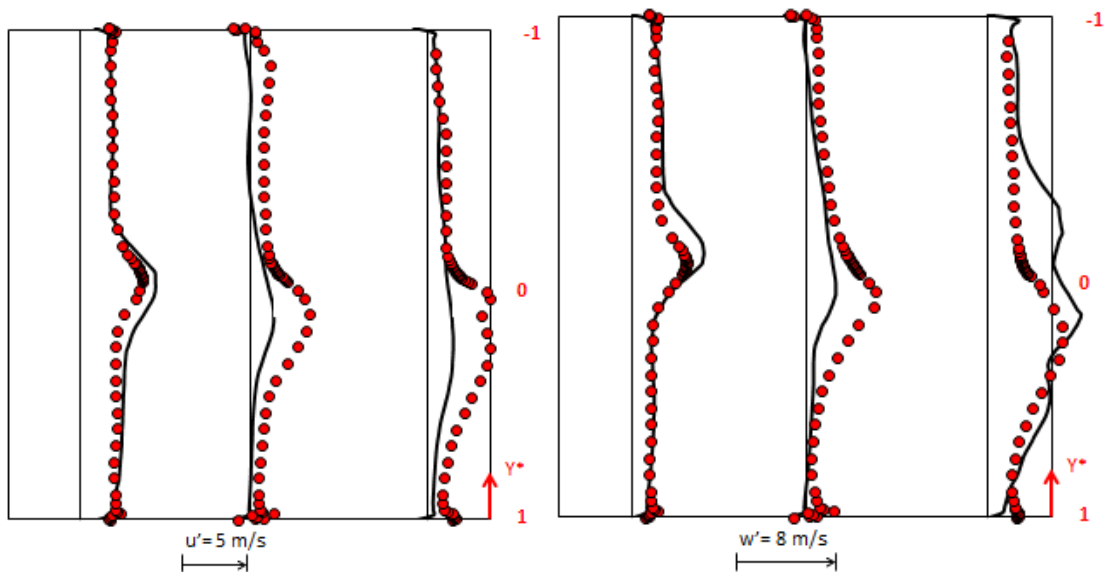
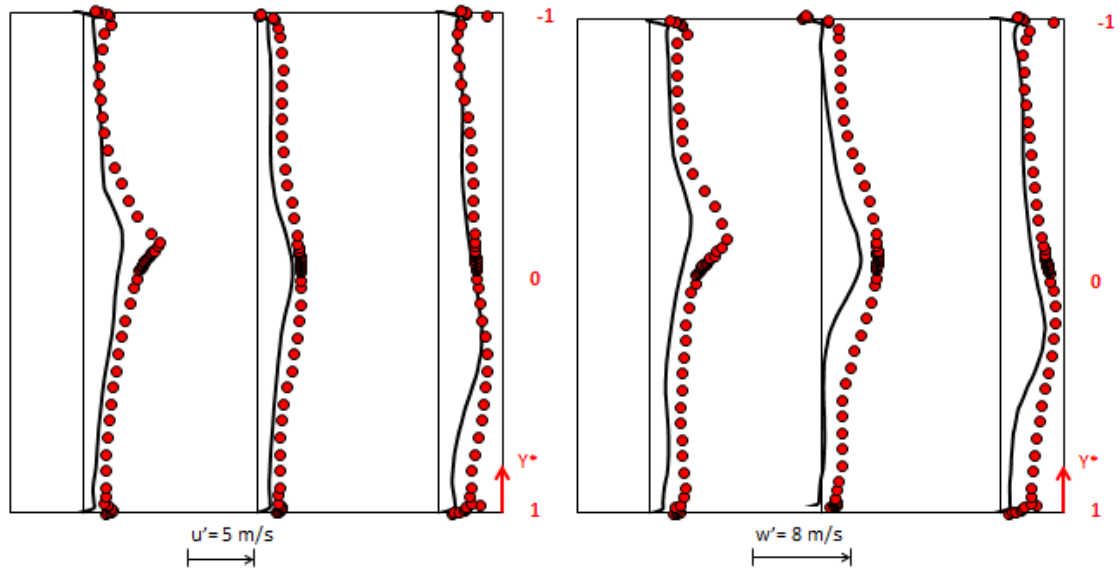
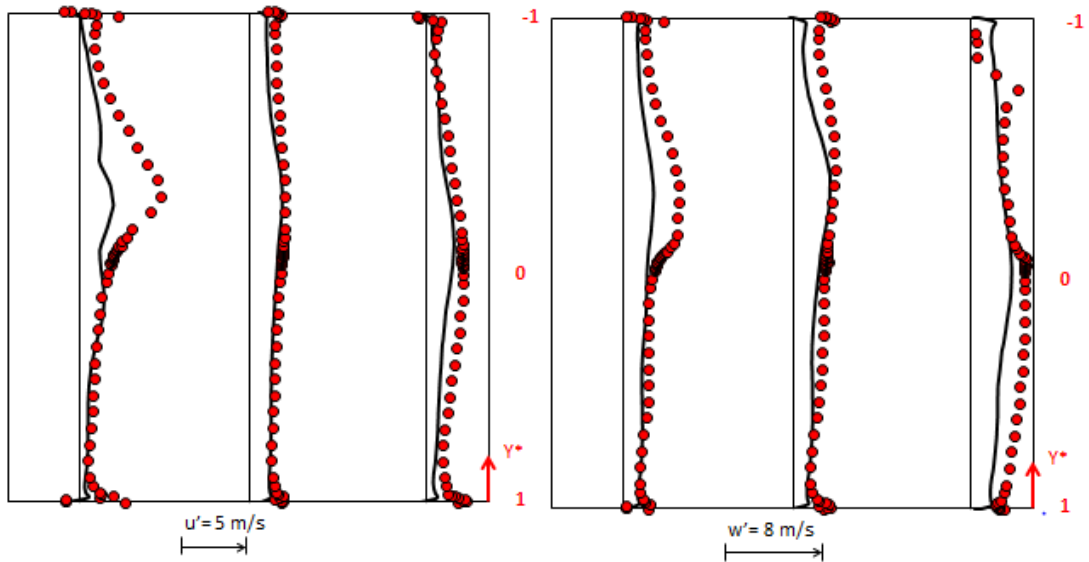


Figure E. 3 - Mixing zone inlet plane LDV vs ASST principal (left) and radial (right) velocity fluctuation



**Figure E. 4 - Mixing zone middle plane LDV vs ASST principal (left) and radial (right) velocity fluctuation**



**Figure E. 5 - Mixing zone outlet plane LDV vs ASST principal (left) and radial (right) velocity fluctuation**

As a general conclusion, the ASST can capture the velocity fluctuations order of magnitude both in the bend and in the mixing zone. However, if the differences in the velocity fluctuations in bend boundary layers could be explained (as already explained) by the absence of a low-Re formulation, which results in a poor description of the velocity fluctuation peak even for a straight channel flow case (see Chapter 3), note that there are still differences even in the bulk region. However, due to the shown high swirling behavior of the in-bend flow, it could be stated that a third-order anisotropic formulation of the Reynolds stress tensor (taking into account swirling in a more proper

way) might provide better results. A third-order formulation often results however in a poorer model numerical behavior. Moreover, PhD thesis timing and planning led to implement and validate only a second-order formulation, with the third-order formulation left for future work.

As regards the mixing zone, see again that the velocity fluctuations general trend is very well represented by the ASST model. Nevertheless the model seems to fail in reproducing the peak close to the mixing plane, where the two fluid streams meet. It is not straightforward to find the right reason for this velocity fluctuation underestimation. Anyway one point has to be underlined: a RANS modeling like the present one is formally based on the scale separation assumption, i.e. the larger eddies contain the turbulent kinetic energy dissipated by the smallest eddies. This is not the case for the mixing zone flow: in fact, largest eddies in fluid bulk (as those shown in chapter 5 section 3.1.2) meet and result in high dissipation rates. The  $\omega$ -transport equation has been developed to describe smallest eddy dissipation. Hence it could not be applied as it is for this flow case. Indeed a finer scale approach i.e. the Scale Adaptive Simulation (SAS) could provide valuable information in this sense.

The same validation on velocity fluctuations will be done for PIV data on planes shown in Chapter 5. In particular, the comparison will be done in the same planes shown in Figure 5.28 to Figure 5.32.

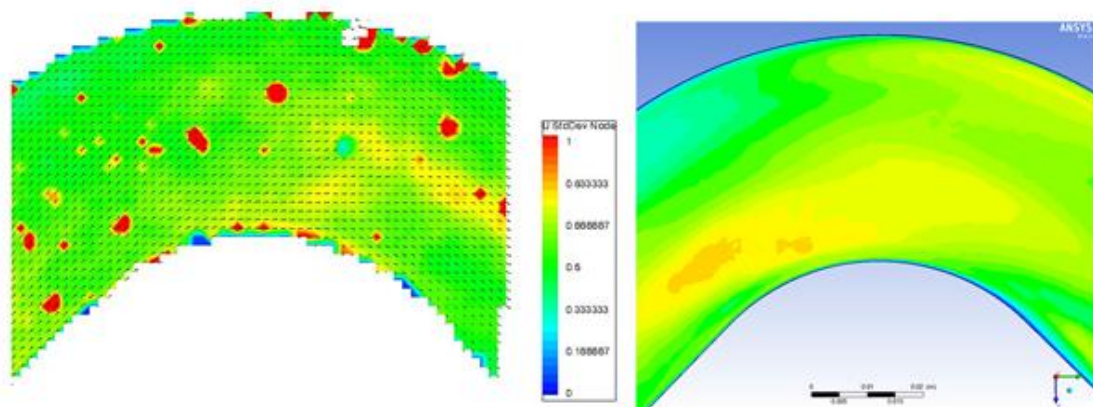


**Figure E. 6 - Bend middle plane + 4 mm plane PIV vs ASST  $u'$  fluctuation**

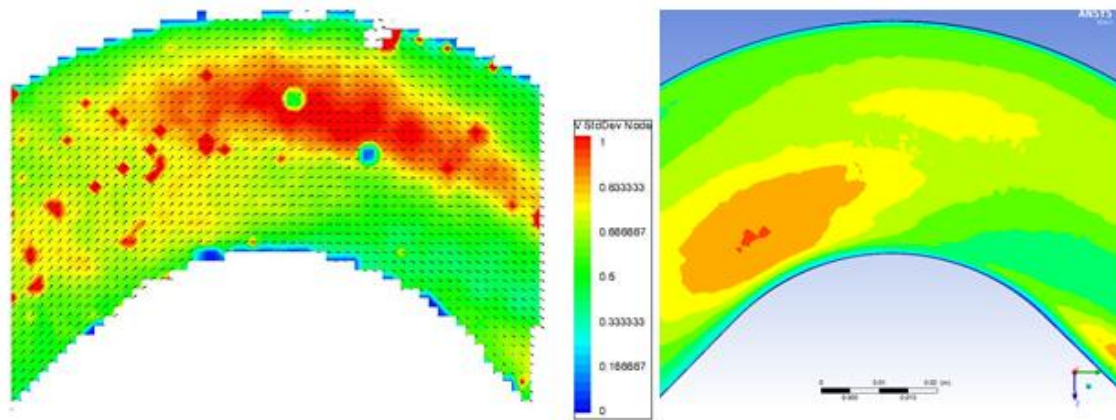


**Figure E. 7 - Bend middle plane + 4 mm plane PIV vs ASST  $v'$  fluctuation**

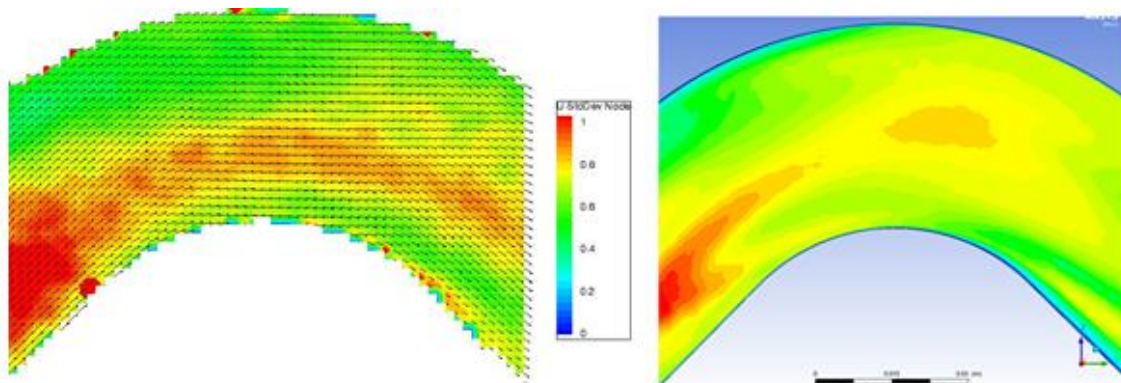


**Figure E. 8 - Bend middle plane PIV vs ASST  $u'$  fluctuation**

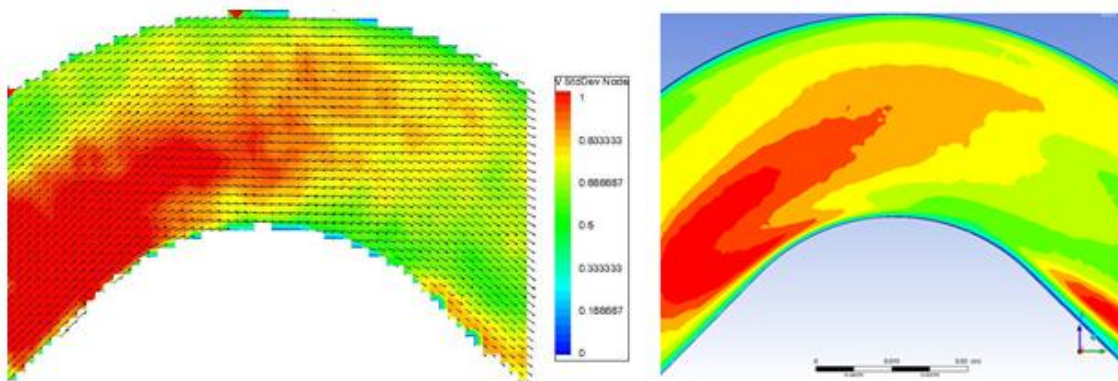


**Figure E. 9 - Bend middle plane PIV vs ASST  $v'$  fluctuation**



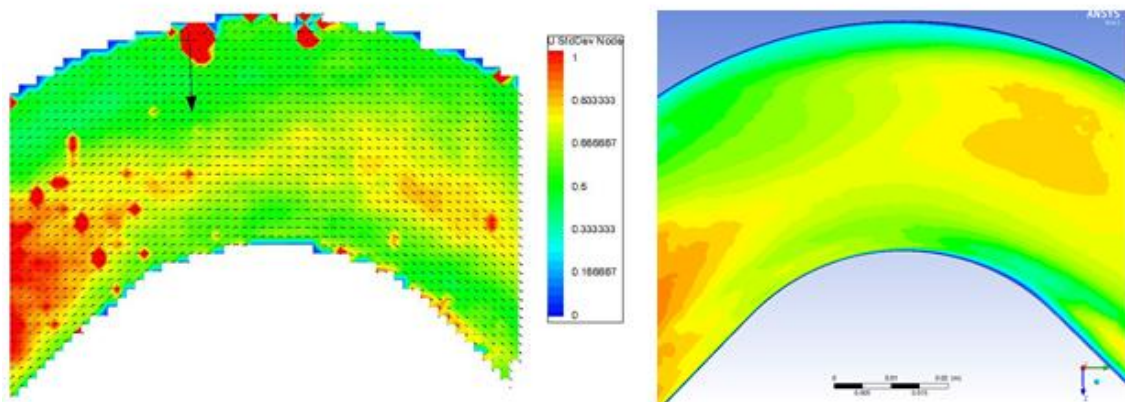


Figure E. 10 - Bend middle plane - 4 mm plane PIV vs ASST  $u'$  fluctuation

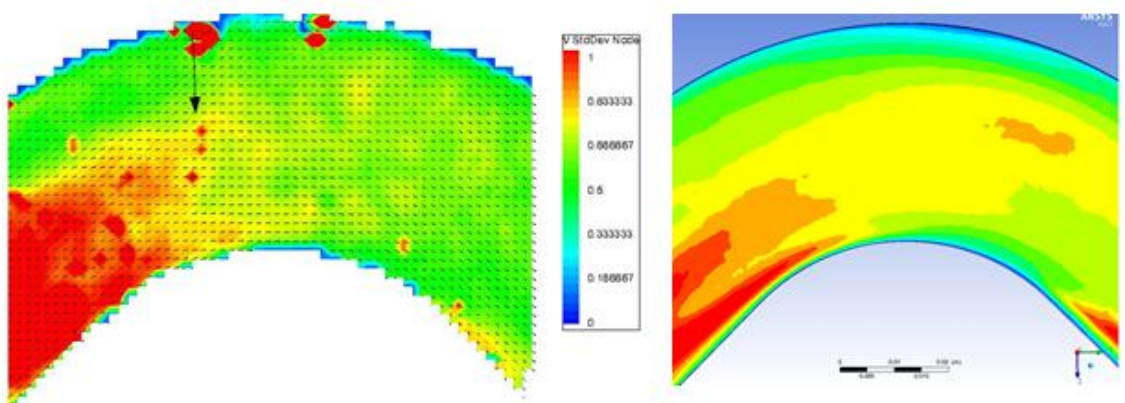


Figure E. 11 - Bend middle plane - 4 mm plane PIV vs ASST  $v'$  fluctuation

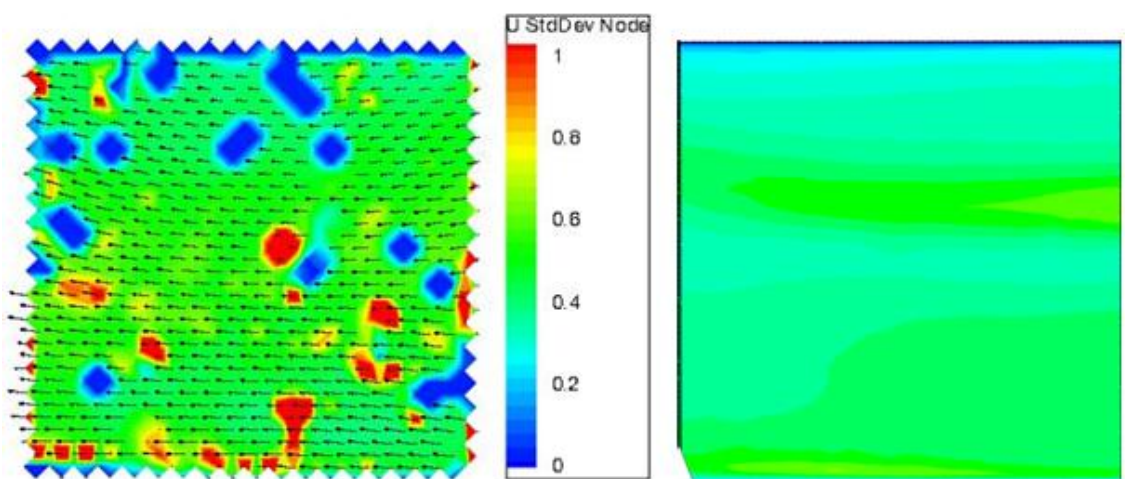


Figure E. 12 - Mixing zone top channel middle plane +8 mm plane PIV vs ASST  $u'$  fluctuation

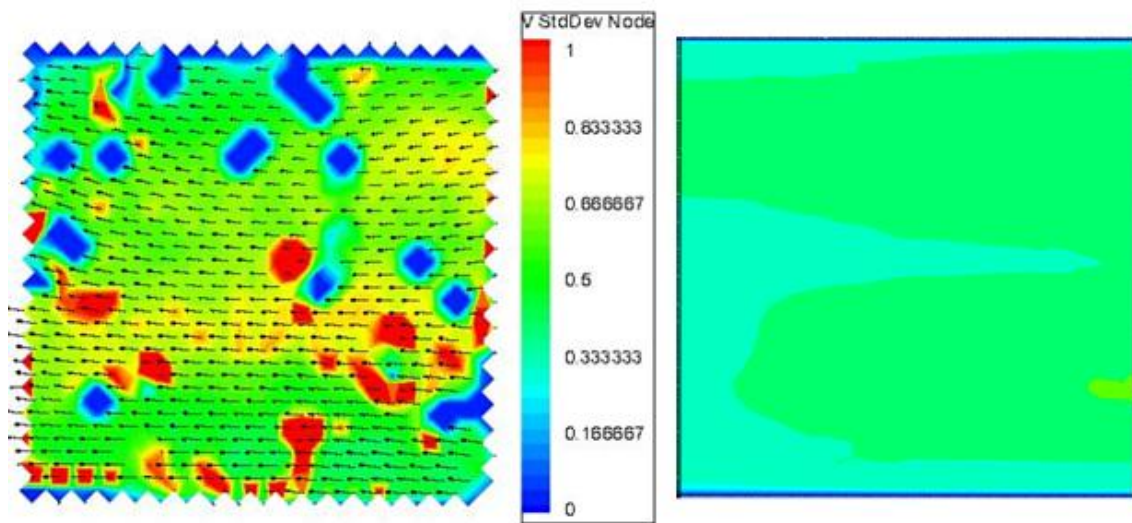


Figure E. 13 - Mixing zone top channel middle plane +8 mm plane PIV vs ASST  $v'$  fluctuation

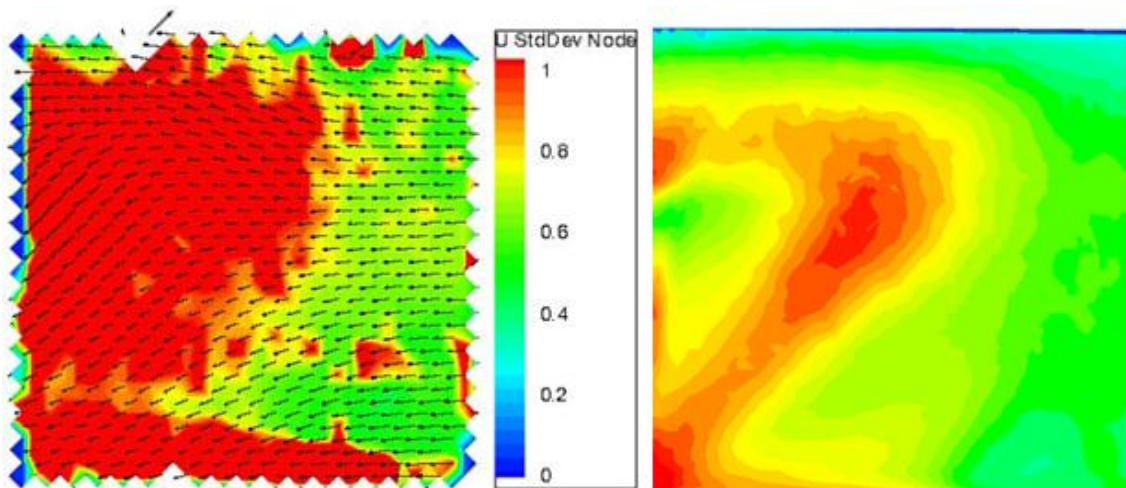


Figure E. 14 - Mixing zone top channel middle plane +4 mm plane PIV vs ASST  $u'$  fluctuation

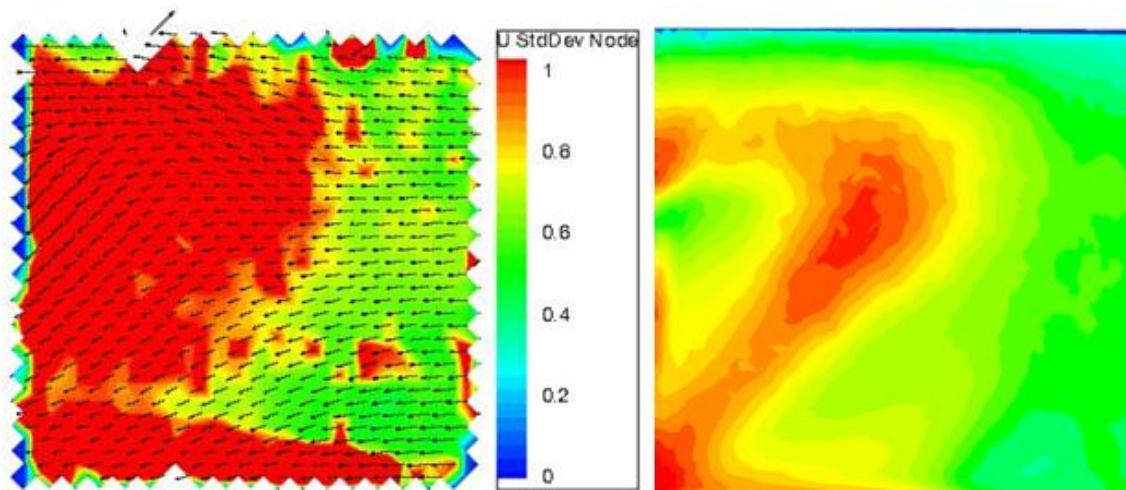


Figure E. 15 - Mixing zone top channel middle plane +4 mm plane PIV vs ASST  $v'$  fluctuation



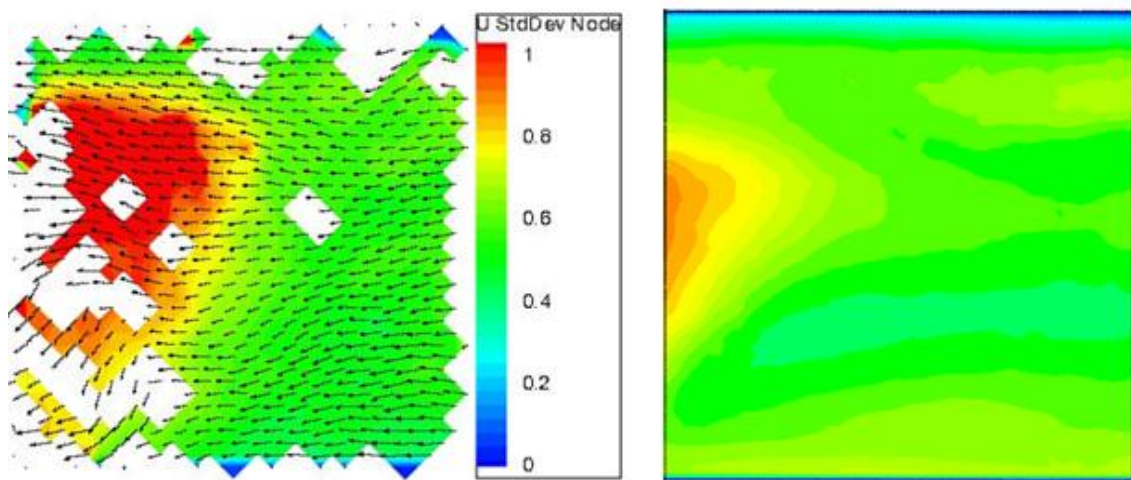


Figure E. 16 - Mixing zone top channel middle plane PIV vs ASST  $u'$  fluctuation

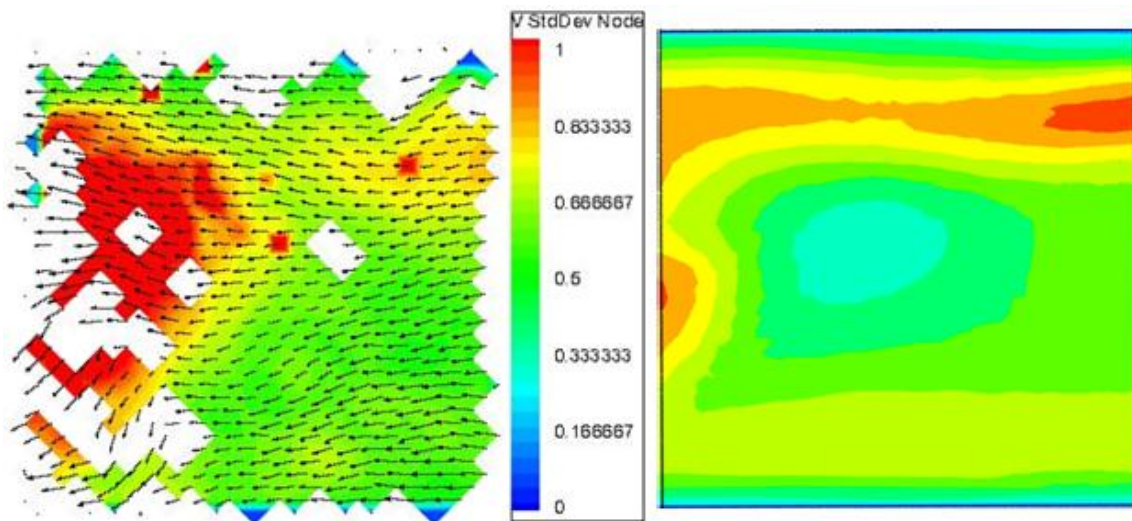


Figure E. 17 - Mixing zone top channel middle plane PIV vs ASST  $v'$  fluctuation

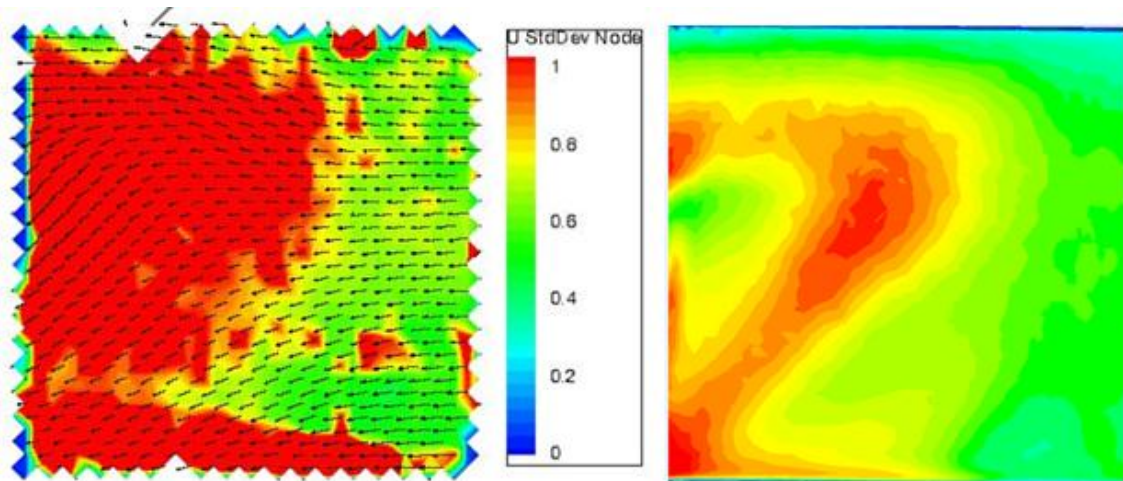


Figure E. 18 - Mixing zone top channel middle plane – 4 mm plane PIV vs ASST  $u'$  fluctuation

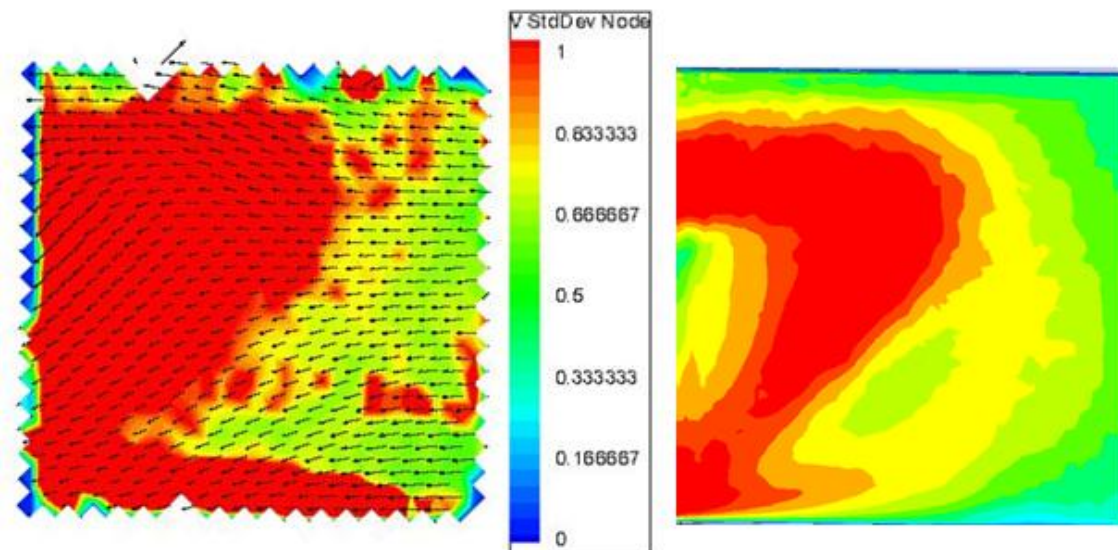
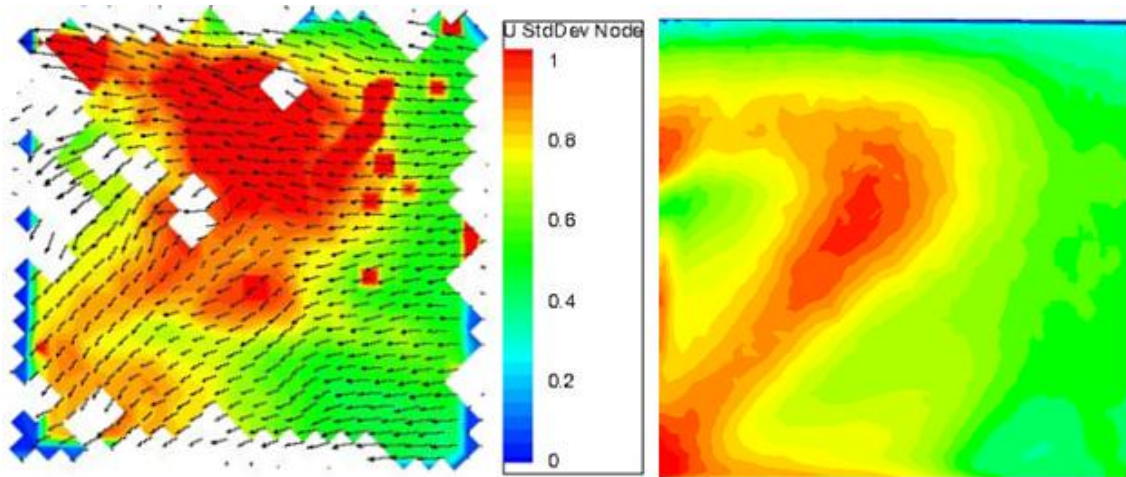
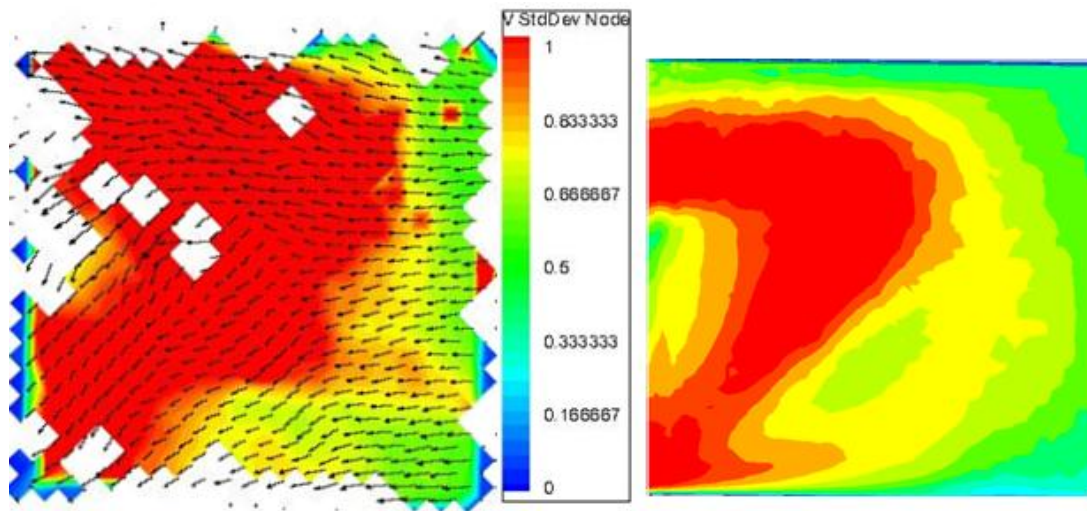


Figure E. 19 - Mixing zone top channel middle plane – 8 mm plane PIV vs ASST  $v'$  fluctuation



**Figure E. 20 - Mixing zone top channel middle - 8 mm plane PIV vs ASST  $u'$  fluctuation**



**Figure E. 21 - Mixing zone top channel middle -8 mm plane PIV vs ASST  $v'$  fluctuation**

Given the not perfect statistical convergence of the PIV data, it is more difficult to provide insightful information on ASST model behavior. Nevertheless, see that ASST computation results agree quite well with PIV experimental data, suggesting that the agreement could be even better considering a higher number of pictures per each measurement. As already mentioned in Chapter 4, the major discrepancies in terms of experimental uncertainties are localized in small regions of the measured zones: hence, it is not surprising that the ASST model can provide a fair description of the velocity fluctuation global shape.



## REFERENCES

---

- <sup>1</sup>Key World Energy Statistics 2012, International Energy Agency, 2012
- <sup>2</sup> World Nuclear Power Reactors 2007-08 and Uranium Requirements, World Nuclear Association, 2008-06-09.
- <sup>3</sup> Nuclear Energy Agency, Nuclear Energy Data, Nuclear Development 2013
- <sup>4</sup>Nuclear Energy Agency, Nuclear Energy Today 2<sup>nd</sup> Edition, Nuclear Development 2012
- <sup>5</sup> CEA – ELECNUC, Nuclear power plants in the world, 2012
- <sup>6</sup> P.Le Coz, J.F.Sauvage and J.P.Serpantie, « Sodium-cooled Fast Reactors : the ASTRID plant project », Proceedings of ICAPP 2011 – Nice, France, May 2-5, 2011, paper 11249, pp.419-425
- <sup>7</sup> P.Sciora et al., « Low Void Effect Core Design Applied on 2400 MWth SFR reactor », Proceedings of ICAPP 2011 – Nice, France, May 2-5, 2011, paper 11048, pp.487-495
- <sup>8</sup> F.Varaine et al., « Pre-conceptual design study of ASTRID core », Proceedings of ICAPP'12, Chicago, USA, June 24-28, 2012, paper 12173, pp.572-579
- <sup>9</sup> M.Saez et al., « The use of gas based energy conversion cycles for sodium fast reactors », Proceedings of ICAPP'08, Anaheim, USA, June 8-12, 2008, paper 8037, pp.565-573
- <sup>10</sup> S.Carnevali, C.Proust, M.Soucille, « Unsteady aspects of sodium-water-air reaction », Chemical Engineering Research and Design 91, pp.633-639, 2013
- <sup>11</sup> S.Carnevali, « Unsteady aspects of sodium-water reaction », PhD thesis, Université de Technologie de Compiègne, France, October 2012
- <sup>12</sup> L.Cachon, A.Morcillo, « ASTRID : faisabilité des échangeurs du SCE gaz et programme R&D associé », NT DEN/CAD/DTN/STPA/LCIT/2010-041, Novembre 2010
- 13 Shah R.K. and Focke W.W., “Plate Heat Exchangers and their design theory”, Heat transfer-Seattle - American Institute of Chemical Engineers (AIChE) Symposium Series 225, Vol.79, pp.227-254, 1983
- 14 Kakaç S., Liu H., “Heat Exchangers: Selection, Rating, and Thermal Design”, Chap. 10, CRC Press, 1992
- 15 Kumar, “The plate heat exchanger: construction and design”, First UK National Conference in Heat Transfer, Vol.2, pp.1275-1288, 1984
- 16 Bond M.P., “Plate Heat Exchangers for Effective Heat Transfer”, Chem.Eng., pp.162-167, 1981
- 17 B.Thonon, “Design method for plate evaporators and condensers”, 1st International Conference on Process Intensification for the Chemical Industry, Vol.18, pp.37-47, BHR Group Conference Series Publication, 1995
- 18 Muley A., Manglik R.M., “Experimental study of turbulent flow heat transfer and pressure drop in a plate heat exchanger with chevron plates”, Journal of heat transfer, Vol.121, pp. 110-117; 1999
- 19 I. Gherasim, N. Galanis, C.T. Nguyen, “ Effects of smooth longitudinal passages and port configuration on the flow and thermal fields in a plate heat exchanger”, Applied Thermal Engineering 31 (2011) 4113-4124
- 20 R.L. Heavner, H. Kumar, A.S.Wanniarachchi, “Performance of an industrial heat exchanger: effect of chevron angle”, AIChE Symposium, Vol.89, n.295, pp. 262-267, 1993

- 
- 21 Charre et al., "General model for plate heat exchanger performance prediction", *Journal of enhanced heat transfer*, Vol. 9, pp. 181-186, 2002
  - 22 W.W.Focke, J.Zachariades, I.Olivier., "The effect of the corrugation inclination angle on the thermohydraulic performance of plate heat exchangers", *Int. J. Heat Mass Transfer*. Vol. 28, No. 8, pp. 1469-1479, 1985
  - 23 W.W.Focke, P.G.Knibbe, "Flow visualization in parallel-plate ducts with corrugated walls", *J.Fluid.Mech.* (1986) vol. 165, pp. 73-77
  - 24 Zhang, Tian, "Simulation and analysis of flow pattern in cross-corrugated plate heat exchangers", *Journal of Hydrodynamics, Ser.B*, 2006,18(5): 547-551
  - 25 Gaiser, Kottke, "Effects of wavelength and inclination angle on the homogeneity of local heat transfer coefficients in plate heat exchangers", *Heat Transfer 1998, Proceedings of the 11th IHTC*, Vol.6, August 23-28, 1998, Kyongju, Korea
  - 26 Hessami, "An experimental investigation of the performance of cross-corrugated plate heat exchangers", *Journal of enhanced heat transfer*, Vol.10 N°4, pp.379-393, 2003
  - 27 GRETh, TM11 – Perte de pression et transfert de chaleur dans les échangeurs à plaques en simple phase, Manuel technique, 24 juin 1999
  - 28 Metwally, Manglik, "Enhanced heat transfer due to curvature-induced lateral vortices in laminar flows in sinusoidal corrugated-plate channels", *International Journal of Heat and Mass Transfer* 47 (2004) 2283–2292
  - 29 Xin, Tao (1988): "Numerical prediction of laminar flow and heat transfer in wavy channel of uniform cross-sectional area", *Numerical Heat Transfer*, 14:4, 465-481
  - 30 Oyakawa et al., "The effect of the channel width on heat transfer augmentation in a sinusoidal wavy channel", *JSME International Journal, Series II*, Vol.32, n°3, pp.403-410, 1989
  - 31 Gradeck, Hoareau, Lebouche, « Local analysis of heat transfer inside corrugated channel », *International Journal of Heat and Mass Transfer* 48 (2005) 1909–1915
  - 32 Thonon, Vidil, Marvillet, "Recent Research and developments in plate heat exchangers", *Journal of enhanced heat transfer*, Vol.2, n°1-2, pp. 149-155, 1995
  - 33 Gradeck, Hoareau, Lebouche, « Local analysis of heat transfer inside corrugated channel », *International Journal of Heat and Mass Transfer* 48 (2005) 1909–1915
  - 34 Snyder et al., « Heat transfer enhancement in a serpentine channel », *International Journal of Heat and Mass Transfer*, Vol.36, n°12, pp.2965-2976, 1993
  - 35 Martin, "A theoretical approach to predict the performance of chevron-type heat exchangers", *Chemical Engineering and Processing* 35 (1996) 301-310
  - 36 Mazen M. Abu-Khader, « Better thermal calculations using modified generalized Leveque equations for chevron plate heat exchangers », *International Journal of Green energy*, Vol.4, pp. 351-366, 2007
  - 37 Dovic et al., "Generalized correlations for predicting heat transfer and pressure drop in plate heat exchanger channels of arbitrary geometry", *International Journal of Heat and Mass Transfer* 52 (2009) 4553–4563
  - 38 Lee et al. "The effect of aspect ratio on turbulent flow heat transfer and pressure drop in a plate heat exchanger", *International Journal of Heat Exchangers*, Vol.I, pp.113-124, 200, ISSN 1524-5608
  - 39 Savostin, A. F., and Tikhonov, A. M., "Investigation of the Characteristics of Plate-Type Heating Surfaces", *Teploenergetika*, Vol.17, n.9, pp. 75-78, 1970
  - 40 Okada et al., "Design and heat transfer characteristics of new plate heat exchanger", *Heat transfer-Japanese research*, Vol.1, pp.90-95, 1972

- 
- 41 A. Cooper, "Recover More Heat with Plate Heat Exchangers", Chemical Engineer, Vol. 285, pp.280-285, May 1974
- 42 G. Rosenblad and A. Kullendorff, "Estimating Heat Transfer Rates from Mass Transfer Studies on Plate Heat Exchanger Surfaces", Wärme-und- Stoffübertragung 8 (1975) 187-191
- 43 Marriott, J. "Performance of an Alfaflex plate heat exchanger", Chemical Engineering Progress, Vol.73, n.2, pp.73-78, 1977
- 44 Price, Fattah, "Hydrodynamic characteristics of a Plate Heat Exchanger Channel", Trans. Inst. of Chem. Eng., Vol.56, pp.217-228, 1978
- 45 Tovazhnyanski L.L. et al., « Heat Transfer and Hydraulic Resistance in Channels of Plate Heat Exchangers », Energetika, Vol.9, pp.123-125, 1980
- 46 Chisholm D., Wanniarachchi A.S., « Maldistribution in Single-Pass Mixed-Channel Plate Heat Exchanger », Compact Heat Exchangers for Power and Process Industries, HTD- Vol.201, ASME, New York, pp.95-99, 1992
- 47 Talik A.C. et al., « Heat Transfer and Pressure Drop Characteristics of a Plate Heat Exchangers », Proc. ASME/JSME Thermal Engineering Joint Conference, Maui, Hawaii, 1995
- 48 Wanniarachchi et al., "Approximate correlations for chevron-type plate heat exchangers », HTD Vol. 314, 1995 National Heat Transfer Conference, Vol. 12, ASME 1995
- 49 Kanaris et al., "Flow and Heat Transfer Prediction in a Corrugated Plate Heat Exchanger using a CFD Code », Chem. Eng. Technol. 2006, 29, No. 8, 923–930
- 50 Abu-Khader; "Better Thermal Calculations Using Modified Generalized Leveque Equations for Chevron Plate Heat Exchangers", International Journal of Green Energy, 4:4, 351-366 (2007)
- 51 Khan et al., "Experimental investigation of single phase convective heat transfer coefficient in a corrugated plate heat exchanger for multiple plate configurations", Applied Thermal Engineering 30 (2010) 1058–1065
- 52 Akturk et al., "Experimental investigation of the characteristics of a chevron-type gasketed plate heat exchanger", 6th International Advanced Technologies Symposium (IATS'11), 16-18 May 2011, Elazığ, Turkey
- 53 Kapustenko et al., "The Heat and Momentum Transfers Relation in Channels of Plate Heat Exchangers", 14th International Conference on Process Integration, Modelling and Optimisation for Energy Saving and Pollution Reduction 8-11 May 2011 - Florence, Italy, paper 89
- 54 Gherasim et al., "Heat transfer and fluid flow in a plate heat exchanger part I. Experimental investigation », International Journal of Thermal Sciences 50 (2011) 1492-1498
- 55 Maslov A.M., Kovalenko L.M., « Hydraulic Resistance and Heat Transfer in Plate Heat Exchangers », Molochnaya Promyshlennost, N.10, pp.20-22, 1972
- 56 Tovazhnyanski L.L. et al., « Heat Transfer and Hydraulic Resistance in Channels of Plate Heat Exchangers », Energetika, Vol.9, pp.123-125, 1980
- 57 O'Brien and Sparrow; "Corrugated-Duct heat transfer, pressure drop and flow visualization", Journal of heat transfer, vol.104, pp.410-416, 1982
- 58Croce, D'Agaro, "Numerical analysis of forced convection in plate and frame heat exchangers", International Journal of numerical methods for heat and fluid flow, Vol.12, n°6, pp.756-771
- 59 H. Blomerius, N. K. Mitra (2000): Numerical investigation of convective heat transfer and pressure drop in wavy ducts, Numerical Heat Transfer, Part A: Applications, 37:1, 37-54
- 60 Zhang, "Numerical study of periodically fully developed flow and heat transfer in cross-corrugated triangular channels in transitional flow regime", Numerical Heat Transfer, Part A, 48: 387–405, 2005
- 61 Lei Zhang & Defu Che (2011): Influence of Corrugation Profile on the Thermalhydraulic Performance of Cross-Corrugated Plates, Numerical Heat Transfer, Part A: Applications, 59:4, 267-296

- 
- 62 Ciofalo, Stasiek, Collins, Investigation of flow and heat transfer in corrugated passages-II Numerical simulations, In1 J Heat Transf. Vol. 39.No. 1, pp. 165-192, 1996
- 63 Jain et al., "A New Approach to Numerical Simulation of Small Sized Plate Heat Exchangers With Chevron Plates", Journal of Heat Transfer March 2007, Vol. 129, pp. 291-297
- 64 Etemad and Sundén, "CFD-analysis of fully developed turbulent flow and heat transfer in a unitary cell of a cross corrugated plate pattern heat exchanger", Proceedings of HT2007, 2007 ASME-JSME Engineering Summer heat transfer conference, pp. 531-540, July 8-12 2007, Vancouver, British Columbia, Canada
- 65 S. Freund, S. Kabelac, "Investigation of local heat transfer coefficients in plate heat exchangers with temperature oscillation IR thermography and CFD", International Journal of Heat and Mass Transfer 53 (2010) 3764-3781
- 66 Weizhe Han, Khaled Saleh, Vikrant Aute, Guoliang Ding, Yunho Hwang, Reinhard Radermacher, "Numerical simulation and optimization of single-phase turbulent flow in chevron-type plate heat exchanger with sinusoidal corrugations", HVAC&R Research, Vol.17, N° 2, pp.186-197, 2011
- 67 Gherasim et al., "Heat transfer and fluid flow in a plate heat exchanger. Part III: Assessment of laminar and two-equation turbulent models", International Journal of Thermal Sciences 50 (2011) 1499-1511
- 68 Lei Zhang and Defu Che, "Turbulence models for fluid flow and heat transfer between cross-corrugated plates", Numerical Heat Transfer, Part A, 60: 410-440, 2011
- 69 Jain et al., "A New Approach to Numerical Simulation of Small Sized Plate Heat Exchangers With Chevron Plates", Journal of Heat Transfer March 2007, Vol. 129, pp. 291-297
- 70 K.M.Stone, "Review of literature on heat transfer enhancement in compact heat exchangers", ACRC TR-105, August 1996
- 71 R.K.Shah and A.L.London, "Laminar Flow Forced Convection in Ducts", Advances in Heat Transfer, J.Thomas, F.Irvine and P.Hartnett ed. Academic Press, 1978
- 72 J. G. Soland, J. W. M. Mack and W. M. Rohsenow, Performance Ranking of Plate-Fin Heat Exchanger Surfaces, Transactions of the ASME Journal of Heat Transfer, Vol. 100, pp. 514-519, 1978.
- <sup>73</sup> L.Cachon, "Avant Projet Sommaire des échangeurs de chaleur du SCE gaz d'ASTRID", NT DEN/CAD/DTN/STPA/LCIT/2011-056, Février 2012
- <sup>74</sup> S.Christin, « ASTRID – Etude de tenue thermomécanique des PSHE sodium/gaz », NT DEN/CAD/DTN/STPA/LCIT 2012-039, October 2012
- <sup>75</sup> HEATRIC Inc. [http://www.heatric.com/superior\\_performance.html](http://www.heatric.com/superior_performance.html)
- <sup>76</sup> K.Gezielus, "Design of Compact Intermediate Heat Exchangers for Gas Cooled Fast Reactors", MSc Thesis, Massachusetts Institute of Technology, Cambridge USA, June 2004
- <sup>77</sup> Thomas Schmerber, "Calculs CFD sur des échangeurs thermiques Sodium/Gaz pour ASTRID", Rapport de stage ST50 – Printemps 2011, UTBM – Université de Technologie de Belfort-Montbéliard
- <sup>78</sup> D.C.Wilcox, "Turbulence Modeling for CFD", DCW Industries, 2006
- <sup>79</sup> S.Castris, B.Aupoix, « Density corrections for turbulence models », Aerospace Science and Technology, Vol.4, pp.1-11, 2000
- <sup>81</sup> D.C.Wilcox, "Turbulence Modeling for CFD", DCW Industries, 1998

- 
- <sup>81</sup>F.R.MENTER, M.Kuntz, R.Langtry, “*Ten years of industrial experience with the SST Turbulence model*”, Turbulence, Heat and Mass Transfer 4, Begell House, Inc., 2003
- <sup>82</sup>B.E.Launder and D.B.Spalding, “*Lectures in Matematical Models of Turbulence*”, Academic Press, 1972
- <sup>83</sup>J.Kim, P.Moin, R.Moser, “*Turbulence Statistics in fully developed channel flow at low Reynolds number*”, J.Fluid Mech. Vol.56, pp.337-351, 1987
- <sup>84</sup>J.Laufer, “The structure of turbulence in fully developed pipe flow”, NACA report 1174
- <sup>85</sup>D.M.Driver and H.L.Seegmiller, “*Features of a reattaching turbulent shear layer in divergent channel flow*”, AIAA Journal Vol.23, N° 2, pp.163-171, 1985
- <sup>86</sup>A.Huser, S.Biringen, “*Direct numerical simulation of turbulent flow in a square duct*”, J.Fluid Mech., v. 257, pp. 65-95, 1993
- <sup>87</sup>F.Mantlik, J.Heina, J.Chervenka, “*Results of local measurements of hydraulic characteristic in triangular pin bundle*”, UJV-3778-R, Rzez, Czech Republic, 1976.
- <sup>88</sup>P.A.Durbin, “Limiters and wall treatments in applied turbulence modeling”, Fluid Dyn. Res. Vol. 41, pp.1-18, 2009
- <sup>89</sup>C.G.Speziale, “*On Nonlinear  $k-\ell$  and  $k-\varepsilon$  Models of Turbulence*”, J.Fluid Mech., Vol.178, pp.459-475, 1987
- <sup>90</sup>T.H.SHIH, J.ZHU and J.L.LUMLEY, “*A Realizable Reynolds Stress Algebraic Equation Model*”, NASA TM 105993
- <sup>91</sup>T.J.CRAFT, B.E.Launder and K.Suga, “*Prediction of turbulent transitional phenomena with a nonlinear eddy-viscosity model*”, Int. J. Heat and Fluid Flow 18: 15-28, 1997
- <sup>92</sup>A.Hellsten and S.Laine, “*Explicit Algebraic Reynolds-Stress Modelling in Decelerating and Separating Flows*”, AIAA Paper 2000-2313, 2000
- <sup>93</sup>S.WALLIN and A.V.JOHANSSON, “*An explicit algebraic Reynolds stress model for incompressible and compressible turbulent flows*”, J.Fluid Mech (2000), vol.43, pp.89-132
- <sup>94</sup>F.R.Menter, A.V.Gabaruk, Y.Egorov, “*Explicit Algebraic Reynolds Stress Models for Anisotropic Wall-Bounded Flows*”, EUCASS – 3rd European Conference for Aero-Space Sciences, Versailles (France), July 6-9 2009
- <sup>95</sup>E.Baglietto, H.Ninokata, T.Misawa, “*CFD and DNS methodologies development for fuel bundle simulations*”, Nuclear Engineering and Design, Vol. 236, pp.1503-1510, 2006
- <sup>96</sup>P.Bradshaw, D.H.Ferris, N.P.Atwell, “*Calculation of Boundary Layer development using the turbulent energy equation*”, Journal of Fluid Mechanics, Vol.28, No 3, pp.593-616, 1967
- <sup>97</sup>J.Kim and P.Moin, “*Transport of passive scalars in a turbulent channel flow*”, Turbulent Shear flows, edited by J.C.André et al., Vol.6, pp.85-96, 1989
- <sup>98</sup>B.J.Daly, F.H.Harlow, “*Transport Equations in turbulence*”, Physics of Fluids, Vol.13, pp.2634-2649, 1970
- <sup>99</sup>S.Thangam and C.G.Speziale, “*Turbulent flow past a backward facing step: a critical evaluation of two-equation models*”, AIAA Journal, Vol.30, No 5, pp.1314-1320, 1992



- 
- <sup>100</sup>Y.G.Lai, R.M.C.So and H.S.Zhang, "*Turbulence-Driven Secondary Flows in a Curved Pipe*", Theoret.Comput. Fluid Dynamics, Vol.3, pp.163-180, 1991
- <sup>101</sup>F.R.Menter, "Two-equation eddy viscosity turbulence models for engineering applications", AIAA Journal Vol.32, No 8, August 1994
- <sup>102</sup>J.C.Vogel and J.K. Eaton. "Combined Heat Transfer and Fluid Dynamic Measurements Downstream of a Backward-Facing Step". J. Heat Transfer. Vol. 107.922-929. 1985.
- <sup>103</sup> A.M.K.P.Taylor, J.H.Whitelaw and M.Yianneskis, "*Measurements of laminar and turbulent flow in a curved duct with thin inlet boundary layer*", NASA Contractor Report 3367, 1981
- <sup>104</sup>B.E.Launder, "*Numerical computation of convective heat transfer in complex turbulent flows: time to abandon wall functions?*", Int.J.Heat Mass Transfer, Vol.27, N.9, pp. 1485-1491, 1984
- <sup>105</sup>W.R.Dean, "*Note on the motion of fluid in a curved pipe*", Proc.Roy.Soc. A, Vol. 85, pp.208-223, 1911
- <sup>106</sup>F. Micheli, "Étalonnage d'un Vélocimètre Laser à Franges", ONERA RT 1/15062 DMAE, 2013
- <sup>107</sup>F. Micheli, M. Lavieille, P. Millan. "ASSA, un outil de référence pour le traitement du signal en vélocimétrie laser", Congrès Francophone de Techniques Laser, CFTL 2006, Toulouse, 19- 22 septembre, 2006. [hathor.onera.fr/dmae/velocimetrie-laser-assa](http://hathor.onera.fr/dmae/velocimetrie-laser-assa)
- <sup>108</sup>T. ADACHI et al., "Secondary flows in curved ducts of rectangular cross-section", Bulletin of the JSME, Vol.20, N° 143, May 1977
- <sup>109</sup>H.B.SQUIRE and K.G.WINTER, « The secondary flow in a cascade of aerofoils in a non-uniform stream », Royal Aircraft Establishment, Report N° AERO 2317, March 1949
- <sup>110</sup>C.GALATI, intern at CEA/DEN/CAD/DTN/STCP/LCIT, Personal Communication
- <sup>111</sup>L.CAHON, R&D Engineer at CEA/DEN/CAD/DTN/STCP/LCIT and Head of Power conversion system R&D within the TECNA project, Personal Communication
- <sup>112</sup>Y.EGOROV, F.Menter, « Development and Application of SST-SAS Turbulence Model in the DESIDER Project », Advances in Hybrid RANS-LES Modelling, Notes on Numerical Fluid Mechanics and Multidisciplinary Design, Vol.97, pp. 261-270, 2008
- <sup>113</sup>J.NAVE, « Modélisation CFD d'un motif d'échange innovant pour l'ECSG d'ASTRID », CEA/DEN/CAD/DTN/STPA/LCIT/NT/2013-026-INDICE A, Diffusion Restreinte, 2013

# **Contribution Expérimentale et numérique à l'amélioration de l'échange thermique des échangeurs de chaleur compacts à plaques**

Résumé : Dans le cadre du programme CEA R&D pour développer un prototype industriel de Réacteur à Neutrons Rapides refroidi au Sodium (RNR-Na), cette thèse vise à proposer une technologie d'échangeur de chaleur compact innovant. Afin d'augmenter la compacité globale du composant la conception est réalisée d'un canal: il peut être considéré comme le résultat de la superposition de deux canaux ondulés en opposition de phase. Afin de fournir un modèle numérique physiquement cohérent, un nouveau modèle de turbulence à viscosité turbulente non linéaire nommé modèle ASST a été développé et implémenté dans le solveur ANSYS FLUENT ®. Il a été démontré que le modèle ASST peut fournir une alternative intéressante aux modèles plus complexes. Pour valider le modèle ASST, deux montages expérimentaux ont été réalisés, dont un utilisant la Vélocimétrie Laser à franges et l'autre la Vélocimétrie Laser par images de particules. Pour la validation thermique, l'installation "VHEGAS" a été construite. Une fois le modèle ASST validé, les performances pour différentes géométries peuvent être étudiées. Enfin, il a été montré que la géométrie innovante est la plus compacte parmi les autres technologies d'échangeurs de chaleur compacts type PCHE.

Mots clés : Motif d'échange innovant, CFD, modèle ASST, LDV, PIV, transfert thermique, échangeurs thermiques à plaques

---

## **Experimental and numerical contribution to heat transfer enhancement in compact plate heat exchangers**

Abstract : In the framework of CEA R&D program to develop an industrial prototype of Sodium-cooled Fast Reactor, the present thesis aimed to propose an innovative compact heat exchanger technology. In order to increase the global compactness the basic idea of this work is to design a channel where the fluid flow is as much three-dimensional as possible. In particular the channel can be thought as the result of the superposition of two undulated channels in phase opposition. To numerically provide a physically-consistent model, a new non-linear eddy viscosity named Anisotropic Shear Stress Transport (ASST) model has been developed and implemented into the available solver ANSYS FLUENT. To validate the numerical model, two experimental sections have been used to acquire an extensive aerodynamic database, whereas, to validate the thermal modeling approach, the VHEGAS facility has been built. Once having validated the ASST model, correlations for friction factor and Nusselt number for various geometries could be obtained. Finally, it has been shown that the innovative channel is the most compact one among the most important existing industrial compact heat exchanger technologies.

Keywords: Innovative heat exchanger, CFD, ASST model, LDV, PIV, heat transfer, plate heat exchanger